Global Fits of Supersymmetric Models after LHC Run 1

Kees Jan de Vries

High Energy Physics
Blackett Laboratory
Imperial College London

A thesis submitted to Imperial College London
for the degree of Doctor of Philosophy

May 2015

To Johan, my parents, my grandparents, Erik, Jaqueline, and Thulan

Abstract

In this thesis up-to-date global fits are presented of four benchmark models within the R-parity conserving Minimal Supersymmetric extension of the Standard Model (MSSM): the constrained MSSM (CMSSM) and two Non-Universal Higgs Mass (NUHM) models, for which soft supersymmetry-breaking input parameters are defined at the Grand Unified Theory (GUT) scale, as well as a 10-parameter phenomenological MSSM model (pMSSM10) for which the input parameters are defined at the $M_{SUSY} \equiv \sqrt{m_{\tilde{t}_1} \cdot m_{\tilde{t}_2}}$ scale. These global fits take into account experimental constraints from flavour physics, electroweak precision observables, the anomalous magnetic dipole moment of the muon, cosmological constraints on the dark matter relic density, direct detection experiments for dark matter, properties of the Higgs boson, and searches for supersymmetric particles from Run 1 of the LHC with 20 fb^{-1} of proton proton collisions at $\sqrt{s} = 8$ TeV. This thesis contains a careful assessment of the impact of experimental constraints on the parameter spaces of the models. Predictions for physical observables and the corresponding prospects for future runs of the LHC, as well as other experiments, are discussed in detail. Novel features of the global fits of the CMSSM, NUHM1, and NUHM2 presented in this thesis include a comprehensive characterisation of the annihilation processes that bring the dark matter relic density in the cosmologically allowed range. The global fit of the pMSSM10 is the first global fit of a pMSSMn model that fully implements searches for supersymmetric particles from Run 1 of the LHC. The validation of these implementations is discussed in detail.

Declaration

I hereby declare that the work in this thesis was carried out by myself between October 2011 and May 2015. Work of others is referenced explicitly throughout this thesis.

– *Kees Jan de Vries May 2015*

Copyright Declaration

Acknowledgments

First and foremost, I would like to thank my parents, Saskia Smeenk and Hans de Vries, who have supported me throughout my life and encouraged me to do my best regardless of the outcome. I have truly enjoyed my studentship at Imperial College London, thanks to all the great friends that I met here in London. The research has been great fun (most of the time) and I am grateful for the patience and great supervision from Oliver Buchmueller, John Ellis, and Jad Marrouche, and the opportunities they have given me. I have had the pleasure to collaborate closely with the members of the MasterCode Collaboration. I also gratefully acknowledge the European Research Council for their financial support throughout my studentship.

During the completion of this thesis I have received very valuable feedback from Emanuele Bagnaschi, Oliver Buchmueller, Matthew Citron, John Ellis, Ben Krikkler, Bjoern Penning, Kazuki Sakurai, and Seth Senz for which I am very grateful. I would also like to thank my grandparents who have hosted (and spoiled) me for two week during the writing process. Finally, I would like to thank my girlfriend Jaqueline Chang for supporting me and bearing with me throughout the (sometimes tough) write-up of this thesis.

Contents

List of Figures

List of Tables

Chapter 1

Introduction

At the time of completing this thesis the Large Hadron Collider (LHC) has started Run 2 colliding protons at an unprecedented centre-of-mass energy of $\sqrt{s} = 13$ TeV. This marks the beginning of the next chapter in the field of High Energy Physics that tries to answer the question "What are the constituents of the Universe and how do they interact?". The Standard Model (SM) of Particle Physics, with the addition of neutrino masses, is the current best understanding and successfully describes presently known phenomena in sub-atomic physics. With the discovery of the Higgs boson at the LHC in July 2012 [1, 2] its full particle content has been established, a journey that required decades of searches at various collider experiments. However, there are important outstanding issues that suggest or even necessitate physics beyond the SM. The SM does not account for the dark matter in the Universe as parametrised in the standard model of Big Bang cosmology (ΛCDM) [3]. Furthermore, the SM Higgs boson receives quadratically divergent loop contributions to its mass, requiring finely-tuned cancellations to 1 part in 10^{30}, see e.g. Ref. [4].

A very popular theory that can address these outstanding issues is supersymmetry (SUSY), a symmetry that relates fermions and bosons that differ in spin by a half integer. The SM can be supersymmetrised by extending it with an additional Higgs doublet and a supersymmetric partner for all SM particles. This constitutes the particle content of the Minimal Supersymmetric extension of the Standard Model (MSSM) [5, 6].[1] If the lightest supersymmetric particle (LSP) is neutral and R-parity (to be defined) is conserved, then the MSSM naturally provides a dark matter candidate. The quadratic divergences to the Higgs mass are naturally cancelled by loop contributions from the supersymmetric scalar partners of the SM fermions, leaving only logarithmic divergences, see e.g. [4]. Another

[1] Other extensions are also possible. However, they are not considered in this thesis.

appealing feature of SUSY extensions of the SM is that the gauge couplings measured at the electroweak scale tend to unify at the so-called Grand Unified Theory (GUT) energy scale $M_{GUT} \sim 2 \times 10^{16}$ GeV [7], whereas in the SM they do not.

These considerations have led to an ongoing quest to find supersymmetric particles. One of the challenges is that, even if the (R-parity conserving) MSSM were to describe Nature, its parameters are currently unknown. The topic of this thesis is establishing preferred parameters (to be defined) and corresponding predictions in four benchmark models, namely the constrained MSSM (CMSSM [8]), two non-universal Higgs mass (NUHM [9]) models, and the pMSSM10, a restricted version of the phenomenological MSSM (pMSSM [10]) with 10 parameters. In the CMSSM and the NUHM models input parameters are specified at the GUT scale, whereas in the pMSSM input parameters are specified at the SUSY breaking scale of $\mathcal{O}$(TeV). The preferred parameters of these models are established by performing global fits using constraints from flavour physics [11–16], electroweak precision observables [17–20], the anomalous magnetic dipole moment of the muon [21], cosmological constraints on the dark matter relic density [3], direct detection experiments for dark matter [22, 23], properties of the Higgs boson [24], and searches for SUSY particles during Run 1 of the LHC with 20 fb^{-1} of proton proton collisions at $\sqrt{s} = 8$ TeV [25, 26].

It should be emphasized that performing frequentist (or Bayesian) global fits in order to establish unknown model parameters is a common practice in High Energy Physics. Examples are global fits of electroweak parameters by e.g. Gfitter [20], and predictions, such as the masses of the top quark and the Higgs boson, often precede discoveries, cf. the top right panel in Fig. 3 of Ref. [27], which displays the profile likelihood function for the mass of the Higgs boson before and after its discovery. Other examples are global fits of elements of the CKM matrix, e.g. by CKM Fitter [28] (frequentist) or UT Fit [16] (Bayesian). Likewise, many groups have performed frequentist global fits of the CMSSM and NUHM, e.g. Fittino [29–32] and MasterCode [33–44], or Bayesian global fits, e.g. BayesFit [45–48] and SuperBayes [49–56]. Some (of these) groups have also performed global fits of pMSSMn models [57–60].

Throughout his studentship the author participated in the `MasterCode` Collaboration. He contributed to the analysis of the global fits of the CMSSM and NUHM1 in Refs. [41,42]. He played a key role in an overhaul of the `MasterCode` framework in order to facilitate, among other things, to interface it with the `MultiNest` package [61–63]. The `MultiNest` sampling algorithm replaced the previously used Metropolis algorithm [64] and allowed to accurately sample the parameter spaces of the NUHM2 and pMSSM10, which have a

larger dimensionality than the CMSSM and NUHM1. Using the overhauled `MasterCode` framework the author performed and analysed the global fits of the CMSSM and NUHM1 in Ref. [43] and the NUHM2 in Ref. [44] in line with the previous analyses by the `MasterCode` Collaboration. The authors largest original contribution is performing and analysing the global fit of the pMSSM10 presented in Ref. [60]. He lead the implementation of constraints from direct searches for SUSY particles performed by ATLAS and CMS during Run 1 of the LHC and had a major contribution in determining the focus and content of this analysis. Finally, the author made contributions to studies in Refs. [65–67], although these are not discussed in this thesis.

The work presented in this thesis is mainly based on [43, 44, 60]. Novel features of the analysis of the CMSSM, NUHM1, and NUHM2 presented in this thesis include a comprehensive characterisation of the annihilation processes that bring the dark matter relic density in the cosmologically allowed range. The global fit of the pMSSM10 is the first global fit of a pMSSMn model that fully incorporates searches for SUSY particles during Run 1 of the LHC.

This thesis is structured as follows. In chapter 2 the MSSM is defined, and the CMSSM, NUHM1, NUHM2 and pMSSM10 are specified. Relevant physical observables are discussed: masses of SUSY particles, the dark matter relic density, elastic dark matter scattering off nuclei, the anomalous magnetic dipole moment of the muon, electroweak precision observables, and flavour physics observables.

Chapter 3 introduces frequentist confidence intervals and regions for parameters and physical observables, and specifies how these may be constructed using profile likelihood functions. Then the χ^2 function (equivalent to the likelihood function) is detailed, paying particular attention to the implementation of the searches for SUSY particles in light of the pMSSM10. The algorithm used to sample the parameters spaces is discussed, and the parameter ranges that have been considered in the scans.

The results of the global fits of the CMSSM, NUHM1, and NUHM2 are discussed in chapter 4. First a characterisation is developed of the annihilation processes that bring the dark matter relic density in the cosmologically allowed range. Then the preferred parameters regions of the CMSSM, the variation of the χ^2 throughout the parameter space, as well as predictions for physical observables and prospects for future experiments are discussed according to this characterisation. The second part of this chapter contains the comparison between global fits of the NUHM1 and NUHM2 with that of the CMSSM, following a similar structure as the first part.

The global fit of the pMSSM10 is discussed in chapter 5, starting with the variation

of the χ^2 function in the parameter space, with a particular emphasis on the impact of the constraints from searches for SUSY particles and the interplay with other constraints. General features of the mass spectra are discussed and a few benchmark model points are described in detail. Other physical observables are discussed, in particular the prospects for future underground experiments for the direct detection of dark matter through elastic scattering. The next topic is the extrapolation of the purely phenomenologically defined model parameters to energies at the GUT scale and the departure from the universality of these parameters is assessed. The penultimate topic is the prospects for future searches at the LHC with 300 and 3000 fb^{-1} at 14 TeV. Detailed maps of the decay chains are provided along with some projection of future sensitivities. The final topic is some prospects for future e^+e^- colliders.

The summary and conclusions of this thesis are given in chapter 6.

Chapter 2

Theory

This chapter is intended to introduce the relevant theoretical background for this thesis and relies heavily on the "A Supersymmetry Primer" [68] (a pedagogical introduction to supersymmetry), as well as other references. After a short review of the Standard Model we introduce the MSSM, its particle content and relevant properties. Then we introduce the models that we consider in this thesis: the CMSSM, the NUHM1, the NUHM2 and the pMSSM10. The remaining part of this chapter is dedicated to the discussion of the physical observables that are of relevance for our global fits.

2.1 Standard Model

The Standard Model (SM) of particle physics describes our present day understanding of the fundamental constituents of matter and their interactions. With the discovery of the Higgs boson reported in July 2012 [1, 2], the full particle content has been established: three generations of quarks and leptons, which constitute the matter, along with the photon, $W^{\pm}$ and Z bosons, and gluons, which mediate the "forces" among these matter particles. The SM is extremely predictive and it has withstood decades of continuous testing to very high accuracy.

More formally, the SM is a renormalisable gauge-invariant quantum field theory. The gauge group is given by $SU(3)_C \times SU(2)_L \times U(1)_Y$ and left- and right-handed components of the fermion fields (quarks and leptons) transform differently. By consequence, parity is broken and explicit mass terms would break gauge-invariance, as would explicit mass terms for gauge bosons. This is circumvented by the spontaneous breaking of $SU(2)_L \times U(1)_Y$ into $U(1)_{\text{e.m.}}$, as a result of a non-zero vacuum expectation value (VEV) of the Higgs field,

giving mass to the fermions and the Z and $W^{\pm}$ bosons. Finally, in the quark sector the mass eigenstates differ slightly from the gauge-eigenstates and this mixing is parametrised by the CKM-matrix.

2.2 The Minimal Supersymmetric Extension of the Standard Model

In this section we describe the Minimal Supersymmetric extension of the Standard Model (MSSM). We refer to Ref. [68] for an in depth and pedagogic review and emphasize that this section is merely intended to specify the language that will be used in the rest of this thesis.

To supersymmetrise the SM, its field content needs to be extended with an additional Higgs doublet to obtain the so-called two Higgs doublet model (2HDM). Each 2HDM field needs to be embedded in a supermultiplet and their gauge transformations properties are listed in Table 2.1. Note that by convention the fermion fields are all written as left-handed two component Weyl spinors. Therefore right handed spinors appear as their hermitian conjugates. This way the gauge transformation properties manifest the gauge invariance of the Lagrangian. For completeness we also state here the nomenclature for SUSY particles, which we interchangeably refer to as sparticles. Supersymmetric parters of fermions acquire the prefix "s", e.g. sfermions, squarks, sleptons, stau, stop, sbottom, etc. The SUSY partners of (gauge) bosons acquire the suffix "ino", e.g. Bino, Wino, gluino, Higgsino etc. The Bino, Wino and Higgsino gauge eigenstates mix to become the "electroweakinos", namely "neutralinos" and "charginos". Finally, we refer to the lightest supersymmetric particle as the LSP.

A supersymmetric renormalisable quantum field theory is specified by the field content and their gauge transformation properties, such as listed in Table 2.1, and the so-called superpotential [68]. The superpotential for the MSSM is given by

$$W_{\text{MSSM}} = \bar{U}\mathbf{y_u}QH_u - \bar{D}\mathbf{y_d}QH_d - \bar{E}\mathbf{y_e}LH_d + \mu H_u H_d, \tag{2.1}$$

where $H_u,\ H_d,\ Q,\ L,\ \bar{U},\ \bar{D},\ \bar{E}$ are the chiral superfields corresponding to the supermultiplets listed in Table 2.1, $\mathbf{y_{u,d,e}}$ denote the 3×3 Yukawa matrices (which determine the masses and CKM mixing angles of the SM quarks and leptons after electroweak symmetry breaking), and μ is called the Higgsino mass parameter. Note that Eq. 2.1 is written in

Superfield	$SU(3)_C,\, SU(2)_L,\, U(1)_Y$	**2HDM Particle**	Spin	**SUSY Partner**	Spin
Q	$(\mathbf{3}, \mathbf{2}, \frac{1}{6})$	$(u\ d)_L$	$\frac{1}{2}$	$(\tilde{u}\ \tilde{d})_L$	0
$\bar{U}$	$(\bar{\mathbf{3}}, \mathbf{1}, -\frac{2}{3})$	$u_R^\dagger$	$\frac{1}{2}$	$\tilde{u}_R^*$	0
$\bar{D}$	$(\bar{\mathbf{3}}, \mathbf{1}, \frac{1}{3})$	$d_R^\dagger$	$\frac{1}{2}$	$\tilde{d}_R^*$	0
L	$(\mathbf{1}, \mathbf{2}, -\frac{1}{2})$	$(\nu\ e_L)$	$\frac{1}{2}$	$(\tilde{\nu}\ \tilde{e}_L)$	0
$\bar{E}$	$(\mathbf{1}, \mathbf{1}, 1)$	$e_R^\dagger$	$\frac{1}{2}$	$\tilde{e}_R^*$	0
H_u	$(\mathbf{1}, \mathbf{2}, +\frac{1}{2})$	$(H_u^+\ H_u^0)$	0	$(\tilde{H}_u^+\ \tilde{H}_u^0)$	$\frac{1}{2}$
H_d	$(\mathbf{1}, \mathbf{2}, -\frac{1}{2})$	$(H_d^0\ H_d^-)$	0	$(\tilde{H}_d^0\ \tilde{H}_d^-)$	$\frac{1}{2}$
W	$(\mathbf{1}, \mathbf{3}, 0)$	$W^\pm\ W^0$	1	$\tilde{W}^\pm\ \tilde{W}^0$	$\frac{1}{2}$
B	$(\mathbf{1}, \mathbf{1}, 0)$	B^0	1	$\tilde{B}$	$\frac{1}{2}$
G	$(\mathbf{8}, \mathbf{1}, 0)$	g	1	$\tilde{g}$	$\frac{1}{2}$

Table 2.1: *Field content of the MSSM. Fermion fields are listed as left-handed two component Weyl spinors. Therefore right-handed fields appear as the hermite conjugate.*

terms of superfields and can be expanded in terms of the particle and sparticles. Also note that all family indices are suppressed.

As said, the gauge transformation properties in Table 2.1, together with the superpotential W would determine the interactions and masses of all particles in a fully supersymmetric renormalisable field theory. However, a realistic phenomenological model must contain breaking of supersymmetry. This SUSY breaking could for example originate from extending the MSSM with new particles and interactions at very high mass scales rendering the theory fully supersymmetric. This theory should be spontaneously broken, so that the low-energy effective Lagrangian (of the MSSM) is "softly" broken. "Soft" symmetry breaking refers to the requirement that the SUSY breaking part of the Lagrangian only contains mass terms and coupling parameters with positive mass dimension, in order to avoid reintroducing quadratically divergent contributions to the Higgs mass [68]. The

soft SUSY breaking part of the Lagrangian is given by [68]

$$\begin{aligned}\mathcal{L} = &-\frac{1}{2}\left(M_1\tilde{B}\tilde{B} + M_2\tilde{W}^A\tilde{W}^A + M_3\tilde{g}^X\tilde{g}^X + \text{c.c.}\right)\\ &-\left(\tilde{u}\mathbf{a_u}\tilde{Q}H_u - \tilde{\bar{d}}\mathbf{a_d}\tilde{Q}H_d - \tilde{e}\mathbf{a_e}\tilde{L} + \text{c.c.}\right)\\ &-\tilde{Q}^\dagger\mathbf{m_Q^2}\tilde{Q} - \tilde{L}^\dagger\mathbf{m_L^2}\tilde{L} - \tilde{u}^\dagger\mathbf{m_u^2}\tilde{u} - \tilde{d}^\dagger\mathbf{m_d^2}\tilde{d} - \tilde{e}^\dagger\mathbf{m_e^2}\tilde{e}\\ &-m_{H_u}^2H_u^*H_u - m_{H_d}^2H_d^*H_d - (bH_uH_d + \text{c.c.}).\end{aligned} \tag{2.2}$$

The first line contains the Bino, Wino, and gluino mass terms, where M_1, M_2, and M_3 denote their respective soft SUSY breaking parameters (indices run over adjoint representation indices $A = 1, 2, 3$ and $X = 1 \ldots 8$). The second line consists of the trilinear scalar interactions, where $\mathbf{a_{u,d,e}}$ are each complex 3×3 complex matrices in family space and have dimension [mass]. The third line lists the squark and slepton mass terms and $\mathbf{m^2_{Q,\bar{u},\bar{d},L,\bar{e}}}$ are each 3×3 hermitian matrices in family space. The last line contains the SUSY breaking contributions to the Higgs potential, see section 2.5.1.

It is important to note that the soft SUSY breaking part of the MSSM Lagrangian, Eq. 2.2, introduces a vast number ($\mathcal{O}(100)$ [69]) of physical parameters (masses, phases and mixing angles) in addition to the ones that are present in the SM. However, most of these would induce flavour-changing neutral interactions or $\mathcal{CP}$-violating effects that are subject to severe experimental constraints on e.g. BR($\mu \to e\gamma$) in the lepton sector and kaon mixing [68, 70]. This justifies considering models that fulfil (at some input scale) the following assumptions:

- The mass squared matrices $\mathbf{m^2_{Q,\bar{u},\bar{d},L,\bar{e}}}$ are diagonal,
- the trilinear coupling matrices are proportional to the corresponding Yukawa coupling matrices, i.e. $\mathbf{a_{u,d,e}} = A_{u,d,e}\mathbf{y_{u,d,e}}$,
- the (resulting) soft SUSY breaking parameters M_1, M_2, M_3, A_u, A_d, and A_e are real.

Note that these assumptions drastically limit the number of free parameters. In section 2.3 and section 2.4 we define the models that are studied in this thesis. However, before we turn to these models, we discuss two other important topics: R-parity and the renormalisation group equations (RGEs).

2.2.1 *R*-Parity

In the SM all interactions conserve baryon number B and lepton number L, and B- and L-violating processes have indeed never been seen experimentally. If these numbers were not conserved, it would most notably mean that the proton could decay, whereas the lower bound on its lifetime is known to be $> 10^{32}$ years [68]. The superpotential in Eq. 2.1 could in principle be extended with L- and B-violating terms (in a way in which the Lagrangian would still be gauge-invariant and renormalisable), but this is clearly unwanted.

The baryon number that is assigned to the supermultiplets in Table 2.1 is B=+1/3 for Q_i, B=−1/3 for $\bar{U}_i$ and $\bar{D}_i$, and B=0 for all others. The lepton number that is assigned to the supermultiplets in Table 2.1 is L=+1 for L_i, L=−1 for $\bar{E}_i$ and L=0 for all others. With these assignments, R-parity for a particle of spin s is defined as

$$P_R = (-1)^{3(\mathrm{B}-\mathrm{L})+2s}.$$

It is easy to verify that all "2HDM" particles in Table 2.1 have even R-parity ($P_R = +1$), whereas their SUSY partners have odd R-parity ($P_R = -1$).

As said, the MSSM is defined to conserve R-parity. This has a number of important consequences. First of all, there is no mixing between R-parity even and odd particles, and every interaction vertex contains an even number of R-parity odd particles. Secondly, the lightest supersymmetric particle (LSP) has $P_R = -1$ and is hence stable. Therefore an electrically neutral LSP would be a good candidate to account for the non-baryonic dark matter in the Universe, since it would interact only weakly with ordinary matter. Finally, particles would be produced in even numbers in collider experiments, and each of which would subsequently decay to a state that has an odd number of supersymmetric particles.

2.2.2 Renormalisation Group Equations

In order to calculate physical observables near the electroweak scale, the gauge couplings, superpotential parameters, and soft SUSY breaking parameters need to be evolved from the input scale using the renormalisation group equations (RGEs). It is beyond the scope of this thesis to discuss these RGEs in detail. Instead we refer again to Ref. [68] for a more complete description and list some observations that will facilitate later discussions in this thesis.

The first observation is that the values of the coupling constants measured at low energies are consistent with unification at a mass scale of $M_{\mathrm{GUT}} \sim 2 \times 10^{16}$ GeV, called

the Grand Unified Theory (GUT) scale, cf. Ref. [7]. This observation is an inspiration for model builders to define theories at the GUT scale.

The second observation is that at the one-loop level the RGEs imply that [68]

$$\frac{M_1}{g_1^2} = \frac{M_2}{g_2^2} = \frac{M_3}{g_3^2} \tag{2.3}$$

at any RG scale. Since the coupling constants unify at the GUT scale it is a popular assumption that also the gauge masses unify and we consider a number of these models in this thesis, cf. section 2.3.

Finally, we note that the RG running of the first- and second-generation sfermion mass-squared parameters get contributions proportional to the relevant gauge couplings and gaugino masses as well as from a quantity S [68]

$$S \equiv m_{H_u}^2 - m_{H_d}^2 + \mathrm{Tr}\left[\mathbf{m_Q^2} - \mathbf{m_L^2} - 2\mathbf{m_u^2} + \mathbf{m_d^2} + \mathbf{m_e^2}\right]. \tag{2.4}$$

Third generation sfermion mass-squared parameters also receive contributions due to their large Yukawa couplings in addition to those from gauginos and S. We provide some approximate equations for the sfermion mass-squared parameters in the case of unifying assumptions on the GUT scale.

2.3 The Constrained MSSM and Non-Universal Higgs Models

In this thesis we first consider a set of models that are inspired by the unification of the gauge couplings at the GUT scale $\sim 2 \times 10^{16}$ GeV. In these theories the soft SUSY breaking parameters of Eq. 2.2 are given as follows.

The gaugino masses unify and are set to a common value $m_{1/2}$

$$M_1 = M_2 = M_3 \equiv m_{1/2}.$$

One important consequence is that with this definition Eq. 2.3 is satisfied (approximately) at any RG scale, so that at the TeV scale the gaugino mass parameters satisfy [68]

$$M_3 = \frac{\alpha_s}{\alpha} \sin^2\theta_W M_2 = \frac{3}{5}\cos^2\theta_W M_1,$$

which results in the approximate ratios of the gaugino mass parameters

$$M_1 : M_2 : M_3 \approx 1 : 2 : 6. \tag{2.5}$$

Then, there is the drastic simplification of the scalar mass matrices in Eq. 2.2 that are assumed to be

$$\mathbf{m}_{\mathbf{Q}}^{\mathbf{2}} = \mathbf{m}_{\bar{\mathbf{u}}}^{\mathbf{2}} = \mathbf{m}_{\bar{\mathbf{d}}}^{\mathbf{2}} = \mathbf{m}_{\mathbf{L}}^{\mathbf{2}} = \mathbf{m}_{\bar{\mathbf{e}}}^{\mathbf{2}} = m_0^2 \mathbf{1}.$$

This unifying assumption can be motivated by the possibility that there is a unified theory with only one gauge group under which all sfermions transform in the same representation with a unified coupling. At lower energies this gauge group is spontaneously broken into the standard model gauge group $SU(3) \times SU(2) \times U(1)$.

The possibility of relaxing the universality assumptions for the soft SUSY breaking parameters $m_{H_u}^2$ and $m_{H_d}^2$ leads to define three models that we consider in this thesis:

$$\begin{aligned}
&m_{H_u}^2 = m_{H_d}^2 = m_0^2 \quad \text{CMSSM}, \\
&m_{H_u}^2 = m_{H_d}^2 \neq m_0^2 \quad \text{NUHM1}, \\
&m_{H_u}^2 \neq m_{H_d}^2 \neq m_0^2 \quad \text{NUHM2},
\end{aligned}$$

where CMSSM [8] stands for "constrained MSSM", and NUHM abbreviates Non-universal Higgs Mass [9]. Note that for the CMSSM and NUHM1 the expression for S in Eq. 2.4 vanishes and it remains small under RG running [68]. In the NUHM2 this is no longer true due to $m_{H_u}^2 \neq m_{H_d}^2$.

With unifying assumptions for m_0 and $m_{1/2}$ on the GUT scale, the running for the first two generation sfermion soft SUSY breaking mass-squared parameters can parametrised, to a good approximation, as [68]:

$$\begin{aligned}
m_{\tilde{q}}^2 &= m_0^2 + \frac{1}{36}K_1 + K_2 + K_3, \\
m_{\tilde{u}}^2 &= m_0^2 + \frac{4}{9}K_1 + K_3, \\
m_{\tilde{d}}^2 &= m_0^2 + \frac{1}{9}K_1 + K_3, \\
m_{\tilde{l}}^2 &= m_0^2 + \frac{1}{4}K_1 + K_2, \\
m_{\tilde{e}}^2 &= m_0^2 + K_1,
\end{aligned} \tag{2.6}$$

where K_i parametrise the contributions due to the RG running proportional to the gaugino

mass parameters and approximate numerical values are given by [68]

$$K_1 \approx 0.15 m_{1/2}^2, \qquad K_2 \approx 0.5 m_{1/2}^2, \qquad K_3 \approx (4.5 \text{ to } 6.5) m_{1/2}^2.$$

The third generation sfermion mass-squared parameters also get these gauge contributions, as well as contributions due their large Yukawa and soft trilinear couplings.

Note that Eq. 2.6 naturally yields squark masses-squared parameters larger than those of the sleptons due to gluino contribution (K_3). There is also a splitting between left- and right-handed scalars due to the different coefficients for the Bino contribution K_1 and (the absence of) a Wino contribution K_2. To illustrate the RG running of the sfermion and gaugino masses we display their values as a function of the energy scale (obtained using `SOFTSUSY-3.3.9` [71]) in Fig. 2.1 for a model point in the CMSSM with input parameters $m_0 = 400$ GeV, $m_{1/2} = 1000$ GeV, $A_0 = 3000$ GeV, and $\tan\beta = 10$: M_1 (black), M_2 (grey), M_3 (light grey), and the square root of the mass-squared parameters of sleptons (red), third-generation squarks (green), and first- and second-generation squarks (blue).

Turning back to the remaining parameters, the trilinear couplings are proportional to the Yukawa matrices with a unified soft SUSY breaking parameter A_0

$$\mathbf{a_u} = A_0 \mathbf{y_u}, \qquad \mathbf{a_d} = A_0 \mathbf{y_d}, \qquad \mathbf{a_e} = A_0 \mathbf{y_e}.$$

There are two more parameters, b and μ, that have not yet been defined. However, $|\mu|$ is constrained by the Z mass and b is traded for the ratio of the VEVs $\tan\beta = v_u/v_d$. We note that, in general, the sign of μ needs to be specified, although in this thesis we consider only positive μ to facilitate the desirable SUSY contributions to $(g-2)_\mu$, cf. section 2.5.4.

We would like to point out here that the additional freedom in choosing $m_{H_u}^2$ and $m_{H_d}^2$ in the NUHM models is equivalent to freedom in choosing M_A and μ. This can be understood from the conditions for electroweak symmetry breaking, which are given at tree level by [72]

$$\begin{aligned} M_A(Q) &= m_{H_d}^2(Q) + m_{H_u}^2(Q) + 2\mu^2(Q), \\ \mu^2(M_Z) &= \frac{m_{H_d}^2(M_Z) - m_{H_u}^2(M_Z)\tan^2\beta + \frac{1}{2}(1-\tan^2\beta)}{\tan^2\beta - 1}, \end{aligned}$$

where Q is the SUSY breaking scale $\sqrt{m_{\tilde{t}_1} \cdot m_{\tilde{t}_2}}$.

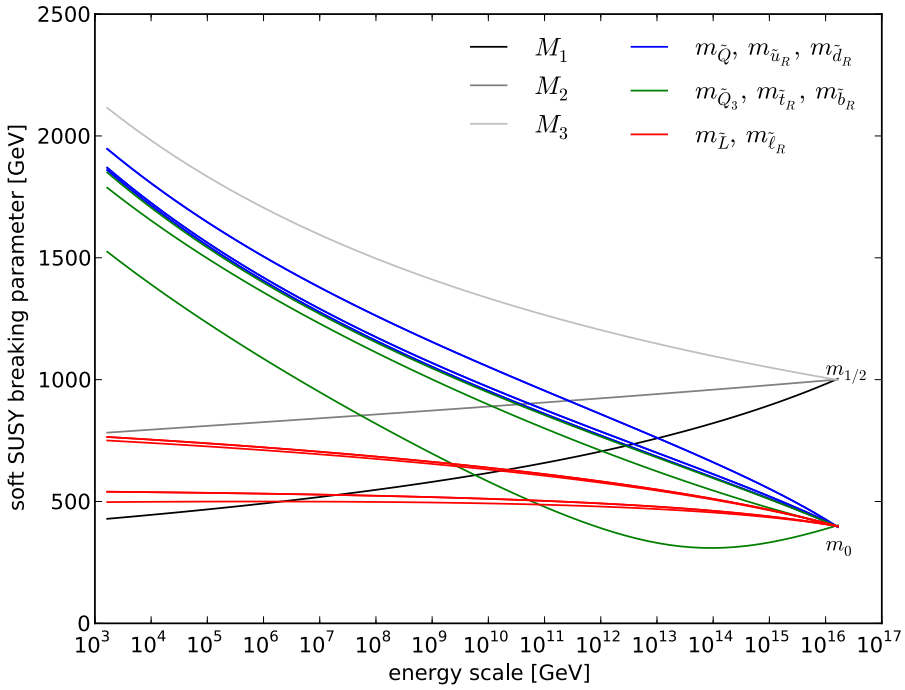

Figure 2.1: *Example of RG running (using* `SOFTSUSY-3.3.9` *[71]) of soft SUSY breaking sfermion and gaugino mass parameters in the CMSSM with input parameters* $m_0 = 400$ GeV, $m_{1/2} = 1000$ GeV, $A_0 = 3000$ GeV, *and* $\tan\beta = 10$*: M_1 (black), M_2 (grey), M_3 (light grey), and the square root of the mass-squared parameters of sleptons (red), third-generation squarks (green), and first- and second-generation squarks (blue).*

2.4 The Phenomenological MSSM

The phenomenological MSSM (pMSSM) makes no unification hypothesis at the GUT scale, but specifies μ and the soft SUSY breaking parameters of Eq. 2.2 at the SUSY breaking scale $M_{\text{SUSY}} \equiv \sqrt{m_{\tilde{t}_1} m_{\tilde{t}_2}}$. Motivated by the considerations in section 2.2 the pMSSM is defined by [10]

- The three (real) gaugino mass parameters

$$M_1, \quad M_2, \quad M_3.$$

- The trilinear couplings are proportional to the Yukawa couplings

$$\mathbf{a_u} = A_u \mathbf{y_u}, \qquad \mathbf{a_d} = A_d \mathbf{y_d}, \qquad \mathbf{a_e} = A_e \mathbf{y_e},$$

where $A_{u,d,e}$ are real.

- The squared mass matrices are diagonal and the first and second generation unify, so that

$$\mathbf{m}_{\mathbf{Q}}^{\mathbf{2}} = \mathrm{diag}(m_{\tilde{q}}^2, m_{\tilde{q}}^2, m_{\tilde{Q}}^2), \quad \mathbf{m}_{\tilde{\mathbf{u}}}^{\mathbf{2}} = \mathrm{diag}(m_{\tilde{u}}^2, m_{\tilde{u}}^2, m_{\tilde{t}}^2), \quad \mathbf{m}_{\tilde{\mathbf{d}}}^{\mathbf{2}} = \mathrm{diag}(m_{\tilde{d}}^2, m_{\tilde{d}}^2, m_{\tilde{b}}^2),$$
$$\mathbf{m}_{\mathbf{L}}^{\mathbf{2}} = \mathrm{diag}(m_{\tilde{l}}^2, m_{\tilde{l}}^2, m_{\tilde{L}}^2), \quad \mathbf{m}_{\tilde{\mathbf{e}}}^{\mathbf{2}} = \mathrm{diag}(m_{\tilde{e}}^2, m_{\tilde{e}}^2, m_{\tilde{\tau}}^2).$$

- The remaining parameters are

$$M_A, \quad \tan\beta, \quad \mu,$$

  which, together with the condition from electroweak symmetry breaking fix $m_{H_u}^2$, $m_{H_d}^2$, b [10].

2.4.1 pMSSM10

In this thesis we consider a 10-parameter version of this 19-parameter model, which we call the pMSSM10. For this model we assume

- unified left- and right-handed first and second generation masses

$$m_{\tilde{q}} = m_{\tilde{u}} = m_{\tilde{d}} \equiv m_{\tilde{q}_{12}},$$

- unified left- and right-handed third generation squark masses

$$m_{\tilde{Q}} = m_{\tilde{t}} = m_{\tilde{b}} \equiv m_{\tilde{q}_3},$$

- unified left- and right-handed first-, second-, and third-generation slepton masses

$$m_{\tilde{L}} = m_{\tilde{\tau}} = m_{\tilde{l}} = m_{\tilde{e}} \equiv m_{\tilde{\ell}},$$

- unified trilinear couplings

$$A_u = A_d = A_e \equiv A.$$

This set of parameters allows to explore SUSY scenarios that are free of the GUT scale unification induced relations between M_1, M_2, and M_3, and the squark and slepton sectors.

The choice of unifying assumptions keeps the dimensionality of the parameter space restricted.

2.5 Observables

2.5.1 Mass Spectrum

Higgs Masses

The scalar potential for the Higgs scalar fields in the MSSM is given by [73]

$$\begin{aligned} V = \; & (m_{H_u}^2 + |\mu|^2)|H_u|^2 + (m_{H_d}^2 + |\mu|^2)|H_d|^2 + b(\epsilon_{ab} H_u^a H_d^b + \text{h.c.}) \\ & + \frac{1}{8}(g^2 + g'^2)\left(|H_u|^2 - |H_d|^2\right)^2 + \frac{1}{2} g^2 |H_u^\dagger H_d|^2, \end{aligned}$$

where H_u and H_d denote the two Higgs doublets, $m_{H_u}^2$, $m_{H_d}^2$, and b are soft SUSY breaking parameters, μ is the Higgsino mass parameter, g and g' are the $SU(2)$ and $U(1)$ gauge couplings, and ϵ is the antisymmetric tensor with $\epsilon_{12} = -1$.

The minimum of this scalar potential has to break the $SU(2)_L \times U(1)_Y \to U(1)_{\text{EM}}$. To this end the doublet fields H_u and H_d acquire vacuum expectation values (VEVs) v_u and v_d (their ratio is denoted as $\tan\beta = v_u/v_d$) so that the doublets can be decomposed as

$$\begin{aligned} H_u &= \begin{pmatrix} H_u^0 \\ H_u^- \end{pmatrix} = \begin{pmatrix} v_u + \frac{1}{\sqrt{2}}(\phi_u^0 - i\chi_u^0) \\ -\phi_u^- \end{pmatrix} \\ H_d &= \begin{pmatrix} H_d^+ \\ H_d^0 \end{pmatrix} = \begin{pmatrix} \phi_d^+ \\ v_d + \frac{1}{\sqrt{2}}(\phi_d^0 + i\chi_d^0) \end{pmatrix}. \end{aligned}$$

When the electroweak symmetry is broken, three of the eight degrees of freedom (G^0 and $G^\pm$ as defined below) become the longitudinal polarizations of the Z and $W^\pm$ vector bosons. The other five degrees of freedom become the $\mathcal{CP}$-odd A scalar, the $\mathcal{CP}$-even neutral h^0 and H^0 scalars, and the charged $H^\pm$ scalars. It turns out that at tree level, the Higgs sector is fully described by $\tan\beta$ and the mass of the A scalar, M_A. The mass

eigenstates are obtained from the gauge eigenstates via [73]

$$\begin{pmatrix} H^0 \\ h^0 \end{pmatrix} = \begin{pmatrix} \cos\alpha & \sin\alpha \\ -\sin\alpha & \cos\alpha \end{pmatrix} \begin{pmatrix} \phi_u^0 \\ \phi_d^0 \end{pmatrix},$$
$$\begin{pmatrix} G^0 \\ A^0 \end{pmatrix} = \begin{pmatrix} \cos\beta & \sin\beta \\ -\sin\beta & \cos\beta \end{pmatrix} \begin{pmatrix} \chi_u^0 \\ \chi_d \end{pmatrix},$$
$$\begin{pmatrix} G^\pm \\ H^\pm \end{pmatrix} = \begin{pmatrix} \cos\beta & \sin\beta \\ -\sin\beta & \cos\beta \end{pmatrix} \begin{pmatrix} \phi_u^\pm \\ \phi_d^\pm \end{pmatrix},$$

where the mixing angle α is determined by

$$\tan 2\alpha = \tan 2\beta \frac{M_A^2 + M_Z^2}{M_A^2 - M_Z^2}, \qquad -\frac{\pi}{2} < \alpha < 0,$$

and the masses are given by [68, 73]

$$\begin{aligned} M_A^2 &= |\mu|^2 + m_{H_u}^2 + m_{H_d}^2 \\ M_{h^0,H^0}^2 &= \frac{1}{2}\left[M_A^2 + M_Z^2 \mp \sqrt{(M_A^2 + M_Z^2)^2 - 4M_Z^2 M_A^2 \cos^2 2\beta}\right], \\ M_{H^\pm}^2 &= M_A^2 + M_W^2. \end{aligned} \tag{2.7}$$

Note that from Eq. 2.7 it follows that at tree level $M_h < M_Z|\cos 2\beta|$. However, radiative corrections can add tens of GeV, see e.g. [74], although an upper bound of $M_h \lesssim 135$ GeV is found in e.g. [75]. For a review on radiative corrections in the Higgs sector we refer to Ref. [76]. Eq. 2.61 in this review highlights the fact that the M_h is mainly dependent on $X_t/M_{\tilde{t}}$ (where $X_t := A_t - \mu/\tan\beta$) and Fig. 2.2 of this review illustrates the dependence.

Neutralino and Chargino Masses

To avoid superfluous citations we state here that the equations and discussion in this subsection are again based on Ref. [68]. As a results of electroweak symmetry breaking the neutral and charged Bino, Wino and Higgsino gauge-eigenstates mix and constitute the neutralino and chargino mass eigenstates.

The part of the Lagrangian that gives mass to the neutralinos is given by

$$\mathcal{L} = -\frac{1}{2}(\psi^0)^T \mathbf{Y} \psi^0 + \text{c.c.},$$

where $(\psi^0)^T = (\tilde{B},\ \tilde{W}^0,\ \tilde{H}_d^0,\ \tilde{H}_u^0)$ are the gauge-eigenstates, and

$$\mathbf{Y} = \begin{pmatrix} M_1 & 0 & -c_\beta s_W M_Z & s_\beta s_W M_Z \\ 0 & M_2 & c_\beta c_W M_Z & -s_\beta c_W M_Z \\ -c_\beta s_W M_Z & c_\beta c_W M_Z & 0 & -\mu \\ s_\beta s_W M_Z & -s_\beta c_W M_Z & -\mu & 0 \end{pmatrix},$$

where we used common abbreviations $s_\beta = \sin\beta$, $c_\beta = \cos\beta$, $s_W = \sin\theta_W$, and $c_W = \cos\theta_W$. The matrix $\mathbf{Y}$ can be diagonalised by an orthogonal matrix $\mathbf{N}$ such that, $\mathbf{NYN}^{-1} = \mathrm{diag}(m_{\tilde{\chi}_1^0},\ m_{\tilde{\chi}_2^0},\ m_{\tilde{\chi}_3^0}\ , m_{\tilde{\chi}_4^0})$, where $\tilde{\chi}_i^0$ denote the neutralino mass-eigenstates. By convention, the index is ordered such that $m_{\tilde{\chi}_1^0} < m_{\tilde{\chi}_2^0} < m_{\tilde{\chi}_3^0} < m_{\tilde{\chi}_4^0}$ and they are obtained from the gauge-eigenstates via

$$\tilde{\chi}_i^0 = \mathbf{N}_{ij}\psi_j^0. \tag{2.8}$$

A limit that we will often encounter is when $M_Z \ll |\mu \pm M_1|,\ |\mu \pm M_2|$, in which case the elements that scale with M_Z can be treated as perturbations of the neutralino mixing matrix, so that the neutralino mass eigenstates are very nearly Bino-like ($\tilde{\chi}_{i_1}^0 \approx \tilde{B}$), Wino-like ($\tilde{\chi}_{i_2}^0 \approx \tilde{W}^0$) and Higgsino-like $\tilde{\chi}_{i_3}^0, \tilde{\chi}_{i_4}^0 \approx (\tilde{H}_u^0 \pm \tilde{H}_d^0)/\sqrt{2}$ and their masses are given by

$$\begin{aligned} m_{\tilde{\chi}_{i_1}^0} &= M_1 - \frac{M_Z^2 s_W^2 (M_1 + \mu \sin 2\beta)}{\mu^2 - M_1^2} + \dots\ , \\ m_{\tilde{\chi}_{i_2}^0} &= M_2 - \frac{M_Z^2 (M_2 + \mu \sin 2\beta)}{\mu^2 - M_2^2} + \dots\ , \\ m_{\tilde{\chi}_{i_3}^0} &= |\mu| + \frac{M_Z^2 (I - \sin 2\beta)(\mu + M_1 c_W^2 + M_2 s_W^2)}{2(\mu + M_1)(\mu + M_2)} + \dots\ , \\ m_{\tilde{\chi}_{i_4}^0} &= |\mu| + \frac{M_Z^2 (I + \sin 2\beta)(\mu - M_1 c_W^2 - M_2 s_W^2)}{2(\mu - M_1)(\mu - M_2)} + \dots\ . \end{aligned} \tag{2.9}$$

These equations (from [68]) assume that M_1 and M_2 are real and positive and μ is real with sign $I = \pm 1$. We used subscripts $i_1 \dots i_4$ to highlight that no hierarchy is assumed here. However, in the GUT models $M_1 \approx 0.5 M_2$ and low mass spectra in our global fits usually have a Bino LSP. In this case $M_1 < M_2 \ll |\mu|$ and the neutralino mass states follow the same order as listed in Eq. 2.9.

The part of the Lagrangian that gives mass to the charginos is given by

$$\mathcal{L} = -\frac{1}{2}(\psi^{\pm})^T \begin{pmatrix} 0 & \mathbf{X}^T \\ \mathbf{X} & 0 \end{pmatrix} \psi^{\pm} + \text{c.c.}$$

where $(\psi^{\pm})^T = (\tilde{W}^+,\ \tilde{H}_u^+, \tilde{W}^-,\ \tilde{H}_d^-)$ again denote the gauge eigenstates and

$$\mathbf{X} = \begin{pmatrix} M_2 & \sqrt{2}s_\beta M_W \\ \sqrt{2}c_\beta M_W & \mu \end{pmatrix}.$$

This matrix can be diagonalised by two unitary 2×2 matrices $\mathbf{U}$ and $\mathbf{V}$ as $\mathbf{U}^*\mathbf{X}\mathbf{V}^{-1} = \text{diag}(m_{\tilde{\chi}_1^\pm}, m_{\tilde{\chi}_2^\pm})$. Here $m_{\tilde{\chi}_{1,2}^\pm}$ are the mass eigenstates of the mixture of gauge-eigenstates obtained via

$$\begin{pmatrix} \tilde{\chi}_1^+ \\ \tilde{\chi}_2^+ \end{pmatrix} = \mathbf{V} \begin{pmatrix} \tilde{W}^+ \\ \tilde{H}_u^+ \end{pmatrix}, \qquad \begin{pmatrix} \tilde{\chi}_1^- \\ \tilde{\chi}_2^- \end{pmatrix} = \mathbf{U} \begin{pmatrix} \tilde{W}^- \\ \tilde{H}_d^- \end{pmatrix}.$$

The masses are explicitly given by

$$m^2_{\tilde{\chi}_1^\pm},\ m^2_{\tilde{\chi}_2^\pm} = \frac{1}{2}\left\{ |M_2|^2 + |\mu|^2 + M_W^2 \mp \sqrt{(|M_2|^2 + |\mu|^2 + 2M_W^2)^2 - 4|\mu M_2 - M_W \sin 2\beta|^2} \right\}.$$

In the limit of Eq. 2.9 the chargino masses are given by

$$\begin{aligned} m_{\tilde{\chi}_{i_1}^\pm} &= M_2 - \frac{M_W(M_2 + \mu \sin 2\beta)}{\mu^2 - M_2^2} + \dots\ , \\ m_{\tilde{\chi}_{i_2}^\pm} &= |\mu| + \frac{M_W I(\mu + M_2 \sin 2\beta)}{\mu^2 - M_2^2} + \dots\ . \end{aligned}$$

An interesting observation is that in this limit $m_{\tilde{\chi}_{i_1}^\pm} \approx m_{\tilde{\chi}_{i_2}^0}$ so that the $\tilde{\chi}_1^\pm$ is nearly degenerate with the $\tilde{\chi}_2^0$ when the LSP is Bino-like. Furthermore, $m_{\tilde{\chi}_{i_3,i_4}^0}$ and $m_{\tilde{\chi}_{i_2}^\pm}$ are close to the absolute value of the Higgsino mass parameter μ.

Sfermion Masses

The sfermion mass terms of the MSSM Lagrangian are given by [77]

$$\mathcal{L} = -\frac{1}{2}\left(\tilde{f}_L^\dagger, \tilde{f}_R^\dagger\right) \begin{pmatrix} M_L^2 + m_f^2 & m_f X_f^* \\ m_f X_f & M_R^2 + m_f^2 \end{pmatrix} \begin{pmatrix} \tilde{f}_L \\ \tilde{f}_R \end{pmatrix},$$

where we denote

$$
\begin{aligned}
M_L^2 &= M_{\tilde{F}}^2 + M_Z^2 \cos 2\beta (I_3^f - Q_f s_W^2), \\
M_R^2 &= M_{\tilde{F}'}^2 + M_Z^2 \cos 2\beta Q_f s_W^2), \\
X_f &= A_f - \mu^* \{\cot\beta, \tan\beta\},
\end{aligned}
$$

where $\cot\beta$ and $I_3^f = \frac{1}{2}$ ($\tan\beta$ and $I_3^f = -\frac{1}{2}$) corresponds to up-type squarks (down-type squarks and sleptons), and $M_{\tilde{F},\tilde{F}'}$ denote the left-handed and right-handed soft SUSY breaking mass parameters respectively, and Q_f is the electromagnetic charge. Note that the mixing due to off-diagonal elements is manifestly small for first and second generation sfermions and we therefore refer to their mass eigenstates as the $\tilde{f}_R$ and $\tilde{f}_L$. In case of real μ and A parameters, the mass matrices of the third generation sfermions are diagonalised with a rotation matrix $\mathbf{U}_{\tilde{f}}$, so that the mass eigenstates are obtained via

$$
\begin{pmatrix} \tilde{f}_1 \\ \tilde{f}_2 \end{pmatrix} = \mathbf{U}_{\tilde{f}} \begin{pmatrix} \tilde{f}_L \\ \tilde{f}_R \end{pmatrix},
$$

and the mass eigenvalue are given by

$$
m_{\tilde{f}_{1,2}}^2 = m_f^2 + \frac{1}{2}\left\{ M_L^2 + M_R^2 \mp \sqrt{(M_L^2 - M_R^2)^2 + 4m_f^2 |X_f|^2} \right\}.
$$

Finally, we comment that the sneutrino masses are given by [71]

$$
m_{\tilde{\nu},i}^2 = (\mathbf{m_L^2})_{ii} + \frac{1}{2} M_Z^2 \cos 2\beta.
$$

2.5.2 Dark Matter Relic Density

The current understanding of cosmology is summarised in the standard model of Big Bang cosmology (ΛCDM), which assumes that gravitation is described by General Relativity, that the Universe is a spatially-flat and expanding, and that its constituents are dominated by cold dark matter (CDM) and a cosmological constant (Λ) at late times [3]. Assuming this model the cold dark matter density is measured to be $\Omega_{\mathrm{CDM}} h^2 = 0.112$ with a few percent accuracy [3]. Here Ω denotes the ratio of the density to the "critical density" (the density for which the Universe is flat) and h is the reduced Hubble constant ($h^2 \approx 0.5$) that is related to the Hubble constant by $H_0 = 100h$ (km/s)/Mpc.

In this thesis we assume that the lightest neutralino is the LSP and that it fully accounts

for the present day density of cold dark matter. To fulfil this density, the neutralino must have (co)annihilated at appropriate rates as we now describe. As can be read in Refs. [68] and [78], it is plausible that sparticles and SM particles coexisted in the early Universe in thermal equilibrium when temperatures exceeded the neutralino mass $T \gg m_{\tilde{\chi}_1^0}$. As the Universe cooled and expanded, the heavier sparticles could no longer be produced and hence they annihilated or decayed to the lightest neutralino. Some fraction of these neutralinos annihilated to SM particles. If there are other sparticles that are only slightly heavier than the neutralino, then they were in thermal equilibrium with the neutralinos and present in almost equal numbers. In this case, it is possible that a sizable fraction of the neutralinos coannihilated with these other particles. As a result of these annihilations and the expanding Universe, the density decreased, and hence also the annihilation rate decreased. Eventually, the neutralino experienced a "freeze out" as a result of this small annihilation rate and further expansion of the Universe. This is the relic dark matter density that we see today.

In a given model of supersymmetry appropriate (co)annihilation processes are required to bring the dark matter relic density into the cosmologically allowed range. If no (co)annihilation took place, then the relic density would exceed the measured value, whereas too efficient (co)annihilation would yield a density that is too low. The relic density could thereby be off by multiple orders of magnitude [79]. The SUSY spectrum therefore needs to allow for one or more (co)annihilation mechanisms, which we will refer to as dark matter (DM) mechanisms. In the remaining of this section we describe the DM mechanisms that are relevant for this thesis.

Bulk Region

The bulk region is the region of the parameter space that has the properties that the neutralino is mostly Bino-like and that at least one of the sfermions is not too heavy, in particular the $\tilde{e}_R$, $\tilde{\mu}_R$, and $\tilde{\tau}_1$. In this region, the neutralino annihilates to a pair of SM particles such as a pair of fermions via t-channel exchange of a sfermion, as is shown in Fig. 2.2.

The name "bulk" dates from the time before $\Omega_{\text{CDM}}h^2$ was accurately known and there was only an upper bound on the relic density from the requirement that it needs to be less than the "critical density" and before LEP placed lower limits [80] on sparticle masses [68]. At that time the bulk region corresponded to the main allowed region in the parameter space. After LEP, the remaining bulk region in the CMSSM was located at $m_0 \lesssim 100$ GeV

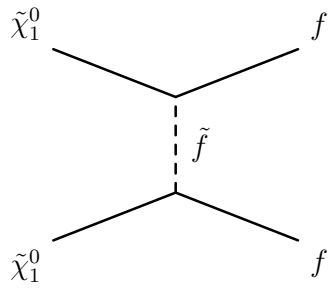

Figure 2.2: *Feynman diagram corresponding to the bulk region.*

and $m_{1/2} \lesssim 250$ GeV [68]. The LHC Run 1 searches have excluded this region [25, 26].

Sfermion Coannihilation

Sfermion coannihilation can occur when the LSP is mostly Bino-like and sfermions have nearly degenerate masses. More specifically, in the case of stau coannihilation and slepton coannihilation the respective sfermion masses are few GeV above the LSP mass. However, in the case of the stop, this mass difference can be higher, e.g. ~ 50 GeV for moderate ratios of $A_0/m_0 = 2.2$, as can be seen from Fig. 7 (top left) in Ref. [81]. As mentioned above, in the case that sfermions and neutralinos have a nearly degenerate mass, they will have coexisted in the early Universe in similar numbers. Therefore sfermions and neutralinos coannihilated, but sfermions also annihilated with other sfermions. Throughout this thesis we will refer extensively to the stau coannihilation mechanism, and to a lesser degree to the stop coannihilation and slepton coannihilation mechanisms. In Fig. 2.3 we show the relevant diagrams.

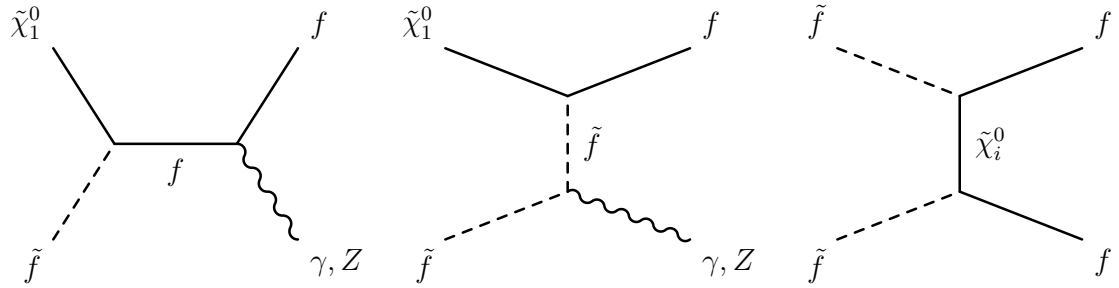

Figure 2.3: *Feynman diagrams corresponding to the sfermion coannihilation region.*

A/H, h and Z Funnels

The A/H funnel and h funnel regions are characterised by the LSP being mostly Bino-like and $2 \cdot m_{\tilde{\chi}_1^0} \sim M_{A,H,h}$. Note that in the case of the h funnel this implies $m_{\tilde{\chi}_1^0} \sim 62.5$ GeV. As we will see in chapter 4, in the GUT scale models this annihilation mechanism is already excluded by implicit bounds from searches for gluinos. However, in the pMSSM10 it is still possible. The diagram for this process is given in Fig. 2.4

We note here that there is a similar diagram for the Z funnel. As for the h funnel, the gluino bound from the LHC excludes this possibility in the GUT models. However, we will encounter the Z funnel in the pMSSM10.

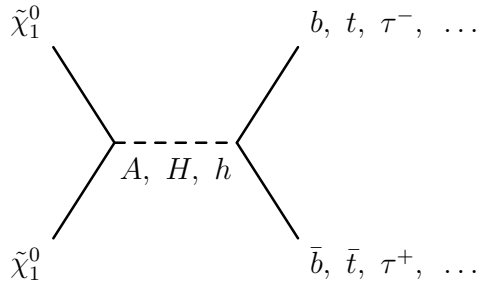

Figure 2.4: *Feynman diagram corresponding to the A/H funnel region.*

A Hybrid of Stau Coannihilation and A/H Funnel

As we will see in chapter 4, there are large regions in the CMSSM, NUHM1 and NUHM2 parameter space where the stau coannihilates with the neutralino, but where also the $2 \cdot m_{\tilde{\tau}_1} \sim M_A$. In this case the stau also annihilates with other another stau via the A/H funnel. In this thesis we refer to this mechanism as the "hybrid" mechanism. The diagram for this process is shown in Fig. 2.5.

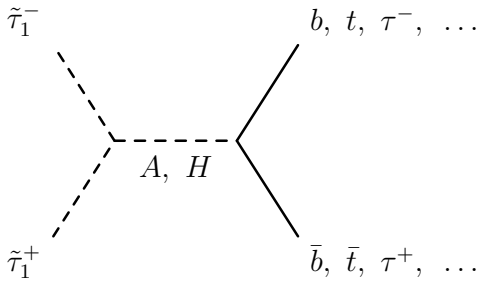

Figure 2.5: *Feynman diagram corresponding to the hybrid region.*

$\tilde{\chi}_1^\pm$ Coannihilation

The relic density can also be fulfilled via the $\tilde{\chi}_1^\pm$ coannihilation mechanism, which occurs when the $\tilde{\chi}_1^\pm$ and $\tilde{\chi}_2^0$ have nearly degenerate masses with the LSP. When the LSP is mainly Higgsino, the $\tilde{\chi}_1^\pm$ coannihilation can be too efficient to explain the present day DM density. To avoid the annihilation being too efficient, the $m_{\tilde{\chi}_1^0}$ needs take high values of $\mathcal{O}(1000\text{ GeV})$. Alternatively the LSP needs to be Bino-like. The corresponding diagrams are given in Fig. 2.6.

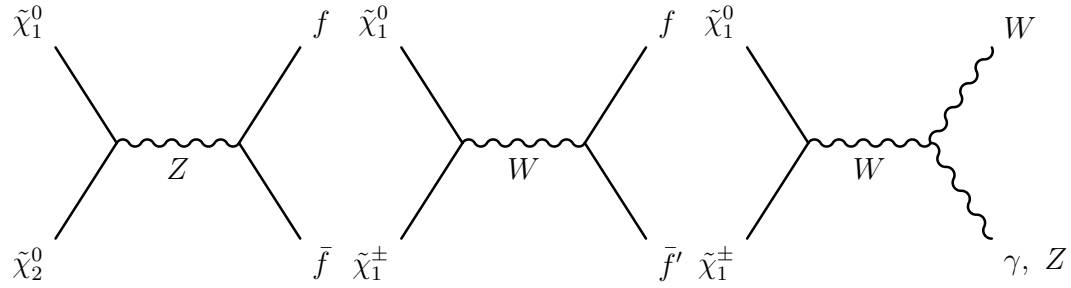

Figure 2.6: *Feynman diagrams corresponding to the $\tilde{\chi}_1^\pm$ coannihilation region.*

Focus Point

The focus point region usually refers to the region in the CMSSM where the RGEs have "focussing" properties [82] when μ is low for high values of m_0 [68]. In this situation $\mu \sim M_1$, which results in a sizable Higgsino component of the LSP. We note here that $\tilde{\chi}_1^\pm$ coannihilation can occur under these conditions, cf. our discussion in the beginning of chapter 4. However, in this thesis we consistently refer to the focus point region when $\mu \ll m_0$ and when $\tilde{\chi}_1^\pm$ coannihilation is not the dominant annihilation mechanism. With this definition the main mechanisms are t-channel exchange of the stop and t-channel chargino exchange (the corresponding diagram is displayed in Fig. 2.7). For a more in-depth discussion we refer to section III in Ref. [83].

2.5.3 Neutralino Scattering off Nuclei

An important probe for SUSY is the direct search for elastic scattering of Weakly Interacting Massive Particles (WIMPs) off nuclei. We assume these WIMPs to be the lightest neutralino. In this section we discuss how the event rate in such experiments arises from the spin-dependent (SD) and spin-independent (SI) contributions to the total neutralino-nucleus

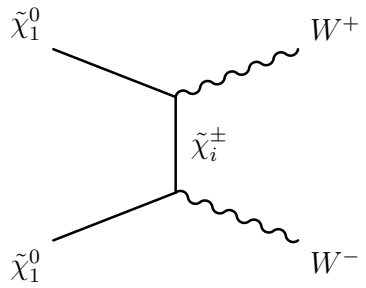

Figure 2.7: *Example of a Feynman diagram corresponding to the focus point.*

scattering cross-section, as well as the dominant uncertainties. This discussion is mainly based on Refs. [78] and [84].

Basic ingredients that enter in the calculation of this rate are 1) an astrophysical model for the number density and the velocity distribution of the neutralinos in the Milky Way, and 2) a model for the neutralino-nucleus interaction. Common assumptions for the astrophysical model, cf. Ref. [85], are that the local neutralino mass density is $\rho_0 = 0.3$ GeV/cm^3, the neutralinos are located in an isothermal non-rotating sphere (the halo) and their velocity distribution $f_1(v)$ is Maxwellian (where velocities are truncated above some escape velocity, e.g. $v_{\rm esc} = 544$ km/s [86]), whereas the Earth moves through this halo at a speed close to the circular speed of the Sun around the Galactic centre $v_0 \approx 220$ km s^{-2}, with some annual modulation due the Earth's orbit around the Sun. The interaction of the neutralinos is expressed as the "standard" zero momentum transfer cross-section σ_0 together with a form factor that is dependent on the momentum transfer $F(Q)$. With the assumptions above, the differential rate with respect to Q is given by

$$\frac{\mathrm{d}R}{\mathrm{dQ}} = \frac{\sigma_0 \rho_0}{2 m_{\tilde{\chi}_1^0} m_{\mathrm{r}}^2} \mathrm{F}^2(Q) \int_{v_{\min}}^{\infty} \frac{f_1(v)}{v} \mathrm{d}v$$

where $m_{\mathrm{r}} = m_{\tilde{\chi}_1^0} m_{\mathrm{N}} / (m_{\tilde{\chi}_1^0} + m_{\mathrm{N}})$ is the reduced mass, m_{N} is the mass of the target nucleus, and $v_{\min} = \sqrt{Q m_{\mathrm{N}} / 2 m_{\mathrm{r}}^2}$.

In the following we discuss the SUSY contributions to σ_0. The main contributions to the neutralino-nucleus cross-section comes from: elastic scattering via t-channel Z exchange, s- and u-channel squark exchange and t-channel h/H-exchange. Their respective diagrams are given in Fig. 2.8. It is also possible to scatter off gluons via loops, see e.g. chapter 7.3 in Ref. [78], although we do not consider this possibility as the effect is generally small [60].

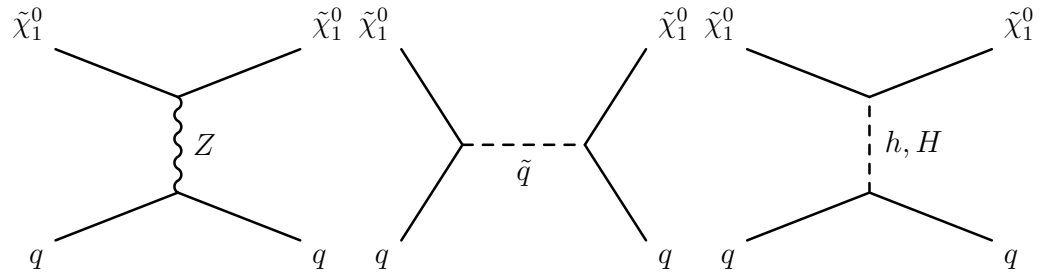

Figure 2.8: *Feynman diagram corresponding to the scattering of the neutralino off quarks within the nucleon.*

These diagrams contribute to the low-energy effective four-fermi Lagrangian [84]

$$\mathcal{L} = \alpha_{2i}\bar{\chi}\gamma^{\mu}\gamma^{5}\chi\bar{q}_i\gamma_{\mu}\gamma^{5}q + \alpha_{3i}\bar{\chi}\chi\bar{q}q,$$

where α_{2i} and α_{3i} are given in Ref. [84], γ^{μ} and γ^{5} are gamma matrices, we suppressed the superscripts and subscripts of the neutralino, and the Lagrangian is summed over the generations and $i = 1$ corresponds to up-type and $i = 2$ to down-type quarks. The first term corresponds to SD scattering and the second to SI scattering. The t-channel Z-exchange contributes only to the SD amplitude, the s- and u-channel squark exchange contributes to both the SD and SI amplitudes, and the t-channel h, H-exchange contributes to the SI amplitude. For a pedagogical review on the derivation and classification of SD and SI low-energy effective Lagrangians from renormalisable theories we refer to Ref. [87].

The general neutralino-nucleus SD cross-section can be written as [78]

$$\sigma^{\mathrm{SD}} = \frac{32}{\pi} G_{\mathrm{F}}^2 m_{\mathrm{r}}^2 \Lambda^2 J(J+1).$$

Here J denotes the total angular momentum of the nucleus, G_{F} the Fermi coupling constant, whereas

$$\Lambda \equiv \frac{1}{J}(a_p \langle S_p \rangle + a_n \langle S_n \rangle),$$

where $\langle S_p \rangle$ ($\langle S_n \rangle$) denote the expectation value of the spin content of the proton (neutron) group in the nucleus, and

$$a_p = \sum_q \frac{\alpha_{2q}}{\sqrt{2}G_{\mathrm{F}}} \Delta_q^{(p)}, \quad \text{and} \quad a_n = \sum_q \frac{\alpha_{2q}}{\sqrt{2}G_{\mathrm{F}}} \Delta_q^{(n)},$$

where $\Delta_q^{(N)}$ parametrises the quark spin content of the nucleon.

The SI cross-section is given by [78]

$$\sigma^{\rm SI} = \frac{4m_{\rm r}^2}{\pi}\left[Zf_p + (A-Z)f_n\right]^2, \tag{2.10}$$

where Z is the atomic number, A is the atomic weight, and for $N = n$ or p

$$\frac{f_N}{m_N} = \sum_{q=u,d,s} f_{T_q}^{(N)}\frac{\alpha_{3q}}{m_q} + \frac{2}{27}f_{TG}^{(N)}\sum_{q=c,b,t}\frac{\alpha_{3q}}{m_q},$$

where the nucleonic matrix elements are given by

$$f_{T_q} \equiv \langle N|m_q\bar{q}q|N\rangle\,, \quad \text{and} \quad f_{TG} = 1 - \sum_{q=\rm u,d,s} f_{T_q}^{(N)}.$$

We went into this much detail to point out some relevant properties of the SI and SD cross-sections. First of all, the SD interaction is manifestly dependent on the angular momentum J of the nucleus and the spin content of the nucleons. In the SI interaction, on the other hand, the neutralino "couples to the mass" of the nucleus, since usually $f_p \simeq f_n$ and hence $\sigma^{\rm SI} \propto A^2 \propto m_{\rm N}^2$. An important consequence is that heavy target nuclei, such as Xenon, are more sensitive to the SI interactions than to SD interactions. In this thesis we therefore only consider SI interactions. The contributions from SUSY to the SI cross-section are generally small if the LSP is almost purely Bino or Higgsino, but can become sizable when it is more mixed.

We would also like to remark that (in the limit where $f_p = f_n$) the $\sigma^{\rm SI}$ of a general nucleus is related to that of a single proton $\sigma_p^{\rm SI}$ by

$$\sigma^{\rm SI} = \sigma_p^{\rm SI}\frac{m_{\rm r}^2}{m_{{\rm r},p}^2}A^2,$$

where we denoted $m_{{\rm r},p}^2$ as the reduced masses of the proton, which reduces to the proton mass m_p if $m_{\tilde{\chi}_1^0} \gg m_p$. Hence, given an astrophysical model, the target material and mass, the acceptance of the experiment, and the exposure time, one can calculate the expected number of events as a function of $m_{\tilde{\chi}_1^0}$ and $\sigma_p^{\rm SI}$ using Eq. 2.5.3.

Finally, we would like to point out that the main uncertainty in the SI cross-section comes from pion-nucleon sigma term $\Sigma_{\pi N}$ and from the parameter ς_0 (which is related via the strange scalar density $y = (1 - \varsigma_0/\sigma_{\pi N})$) [84]. This can be seen from the fact that $f_{T_{u,d}} \propto \Sigma_{\pi N}$ and $f_{T_s} \propto \Sigma_{\pi N} y$. In our calculations we assume $\Sigma_{\pi N} = 50 \pm 7$ MeV

and $\sigma^0 = 36 \pm 7$ MeV (as was done in Ref. [39]), and propagate these errors to obtain an uncertainty on the SI cross-section using the code that was used in Ref. [84].

2.5.4 The Anomalous Dipole Moment of the Muon

The magnetic moment $\vec{\mu}$ of a Dirac fermion of mass m is related to its intrinsic spin $\vec{S}$ via the gyromagnetic ratio g:

$$\vec{\mu} = g\left(\frac{q}{2m}\right)\vec{S}.$$

The Dirac equation yields that $g = 2$ exactly. However g receives loop corrections that are quantified by $a = \frac{g-2}{2}$. The leading order loop correction for the electron (from the photon loop) was first calculated by Schwinger in 1947 [88]. Today the anomalous dipole moment of the electron a_e is the most precisely measured [89] and calculated [90] quantity in Nature, with agreement over 12 significant digits.

The story is a little different for the muon anomalous magnetic moment a_μ. Here the most precise experimental measurement of a_μ is from the Muon E821 Anomalous Magnetic Moment Measurement at Brookhaven National Lab (BNL) [21]. They found that $a_\mu = (11,659,208.0 \pm 5.4_{\text{stat.}} \pm 3.3_{\text{sys.}}) \times 10^{-10}$, reaching a 0.54 ppm precision. This measurement improved the previous measurements at CERN [91] by a 14-fold in precision.

The SM prediction of a_μ^{SM} receives contributions from QED, electroweak, and hadronic contributions:

$$a_\mu^{\text{SM}} = a_\mu^{\text{QED}} + a_\mu^{\text{EW}} + a_\mu^{\text{Had}}.$$

Representative diagrams are given in Fig. 2.9

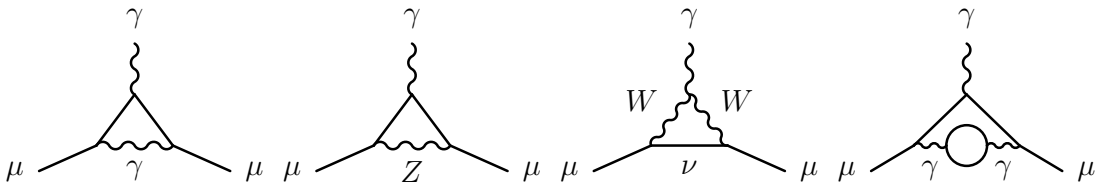

Figure 2.9: *Feynman diagrams corresponding to SM contributions to* $(g-2)_\mu$.

For more details on the SM theory predictions, we refer to the review in "Review of Particle Physics" [17]. We use $a_\mu^{\text{SM}} = (11,659,177.8 \pm 6.1) \times 10^{-10}$ for the the SM

calculation [92], leading to a discrepancy of 3.4σ.

We now turn to the contributions from SUSY. Representative diagrams are given in Fig. 2.10.

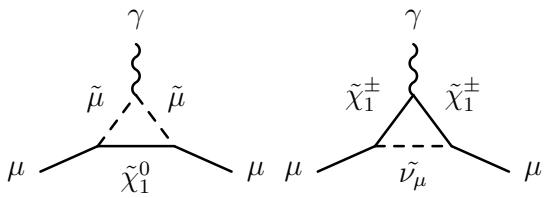

Figure 2.10: *Feynman diagrams corresponding to SUSY contributions to* $(g-2)_\mu$.

The SUSY contribution a_μ^{SUSY} can be sizable when smuons and charginos have masses of $O(100\text{ GeV})$ and therefore account for the difference between the SM prediction and the experimental value, although charginos do not necessarily have to contribute, cf. Ref. [93]. This can be illustrated with some of the analytic formulas for restricted cases from this reference, e.g. when $M_1 \ll M_2, \mu$ and $m_{\tilde{\mu}_R} \approx m_{\tilde{\mu}_L} \approx 2 \cdot M_1$ (Eq. 1.24):

$$a_\mu^{\text{SUSY}} = 18 \tan\beta \left(\frac{100\text{ GeV}}{m_{\tilde{\mu}}}\right)^3 \left(\frac{\mu - A_\mu \cot\beta}{1000\text{ GeV}}\right) 10^{-10}.$$

where the contribution comes from the Bino loop (the left diagram in Fig. 2.10).

2.5.5 Electroweak Precision Observables

Electroweak precision observables (EWPO), such as M_W and Z-pole observables (see below), are known with an accuracy at the per cent level or better [17, 18]. As such, they constrain new physics and can serve to discriminate between SUSY and SM quantum effects [73].

We now describe the Z-pole observables, which were measured at high precision at the electron-positron colliders LEP and SLC with data taken at the Z resonance [18]. The process of $e^+e^- \to f\bar{f}$ (where $f \neq e$) gives rise to observables and pseudo-observables as detailed below, cf. section 1.5 in Ref. [18].

Inclusive Quantities: Cross-Sections and Partial Widths

- The Z mass M_Z,
- the total decay width Γ_Z,
- the hadronic pole cross-section $\sigma^0_{\rm had} \equiv \frac{12\pi}{M_Z^2}\frac{\Gamma_{ee}\Gamma_{\rm had}}{\Gamma_Z^2}$,
- the ratio of hadronic to leptonic decay $R^0_l \equiv \Gamma_{\rm had}/\Gamma_{ll}$,
- ratio of partial decay width into $q\bar{q}$ to the total hadronic width $R^0_q = \Gamma_{q\bar{q}}/\Gamma_{\rm had}$, where $q = b, c$.

Asymmetries and Effective Fermionic Weak Mixing Angle

- The asymmetry parameters $\mathcal{A}_f \equiv 2\frac{{\rm Re}(g_{\rm Vf}/g_{\rm Af})}{1+{\rm Re}(g_{\rm Vf}/g_{\rm Af})^2}$, where $g_{\rm Vf}$ and $g_{\rm Vf}$ are the effective vector and axial vector couplings,
- the forward backward asymmetries $A^{0,f}_{\rm FB} = \frac{3}{4}\mathcal{A}_e\mathcal{A}_f$,
- the effective fermionic weak mixing angle $\sin^2\theta^f_{\rm eff}$.

Observables labelled with a superscript 0 are so-called pseudo-observables. They are derived from measured quantities and constructed to facilitate the theoretical interpretation, e.g. $\sigma_{\rm had}$ is the measured quantity whereas $\sigma^0_{\rm had}$ is the pole cross-section derived from the measurement. The asymmetry parameters $\mathcal{A}_f$ are also derived quantities.

For a pedagogic review of contributions to EWPO in the MSSM we refer to Ref. [73]. In this reference it was found that M_W and $\sin^2\theta^\ell_{\rm eff}$ vary significantly with respect to their experimental uncertainties, with the overall mass of SUSY particles (see e.g. Fig. 3.10 and 3.11 in this reference).

2.5.6 Flavour Physics Observables

Flavour physics observables may also be modified by SUSY quantum effects. In our fits we consider the B-meson decays $B_{s,d} \to \mu^+\mu^-$, $B \to X_s\gamma$, $B \to \tau\nu$, $B \to X_s\ell\ell$ [94], the K-meson decays $K \to \mu\nu$, and $K \to \pi\nu\bar{\nu}$ [95], observables related to $B - \bar{B}$ mixing ΔM_{B_s}, $\frac{\Delta M^{\rm EXP/SM}_{B_s}}{\Delta M^{\rm EXP/SM}_{B_d}}$, and $\Delta\epsilon_K$ [95]. It turns out that rare decays $B_{s,d} \to \mu^+\mu^-$, and $B \to X_s\gamma$ are particularly important in constraining our models and we discuss them below. For the

other flavour observables we refer to Refs. [96, 97] and the references given above for more details.

Diagrams for both SM and SUSY contributions to $B_{s,d} \to \mu^+\mu^-$ are given in Fig. 2.11 [98]. In the SM this Flavour Changing Neutral Current (FCNC) decay goes via the Z penguin top loop (75%) and the box diagrams (24%) and is helicity suppressed [98]. It is well known that SUSY contributions can enhance the branching ratio by a factor of $\mathcal{O}(100)$, cf. Ref. [99]. Eqs. 11 and 12 in Ref. [96] provide formulas for this enhancement in the case that squarks are heavy, so that the only relevant contributions are from the effective tree-level Higgs-mediated neutral currents. In this case the enhancement is proportional to $\propto \tan\beta^3/M_A^2$. This illustrates that $B_{s,d} \to \mu^+\mu^-$ is in general strongly dependent on M_A and $\tan\beta$.

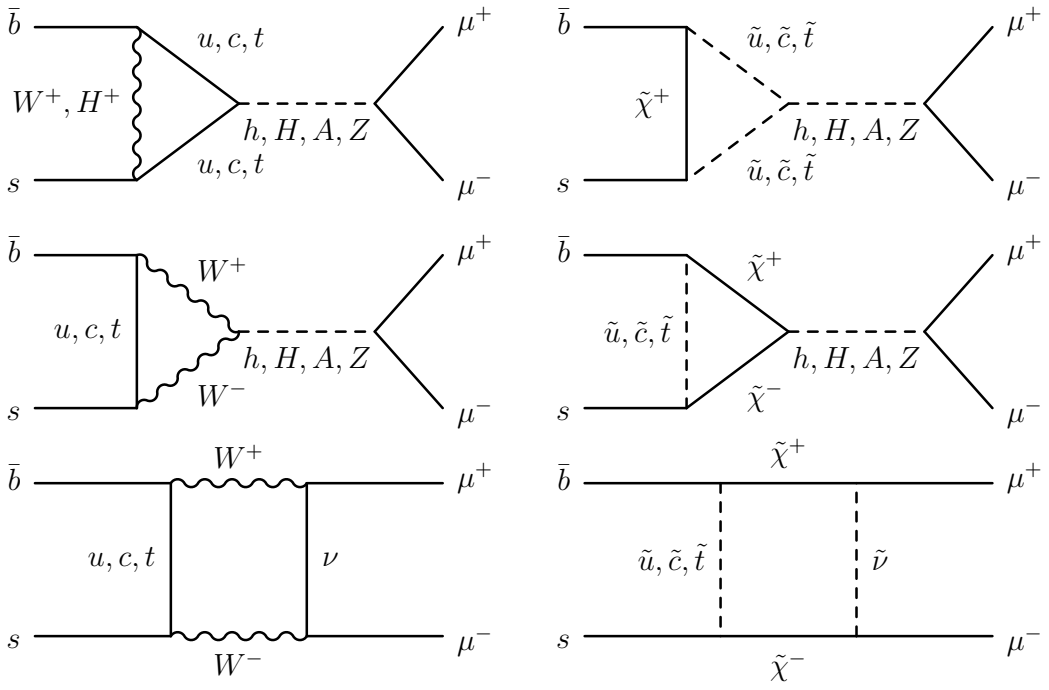

Figure 2.11: *Feynman diagrams contributing to* $B_{s,d} \to \mu^+\mu^-$.

Another important decay is $B \to X_s\gamma$. As is also discussed in Ref. [96], for $B \to X_s\gamma$ there is no effective tree-level contribution. Therefore, in the limit of heavy squarks, the contributions from the chargino squark loops may not be negligible compared to the heavy Higgs loops. For negative A_U these contributions can even partially cancel each other.

Chapter 3

Method

In order to explore our supersymmetric models we establish frequentist confidence intervals and regions for the model parameters and corresponding predictions for physical observables. Frequentist refers to the classical interpretation of probability being the frequency of an event in a large number of trials and confidence intervals are constructed as prescribed by Neyman [100].

A frequentist assumes that the physical observables O_i are random variables that are distributed according to a probability function $f(O_i|\theta)$ that depends on unknown parameters θ and that their measured values $O_{i,\text{meas.}}$ are the outcome of drawing one sample from each of these random variables. Given these measured values the likelihood function $\mathcal{L}(\theta)$ is defined as $\mathcal{L}(\theta) \equiv f(O_{i,\text{meas.}}|\theta)$. The likelihood function gives rise to the $\chi^2(\theta)$ function: $\chi^2(\theta) \approx -2\ln\mathcal{L}(\theta) + \text{const.}$ where the normalisation constant is irrelevant. Hence, constructing the $\chi^2(\theta)$ function is equivalent to defining the probability function $f(O_i|\theta)$ and as such the underlying model that describes Nature.

In this thesis the χ^2 function is given by[1]

$$\chi^2(\theta) \equiv \sum_i \left(\frac{O_{i,\text{meas.}} - O_{i,\text{pred.}}(\theta)}{\sigma(O_i)}\right)^2 + \sum_j \left(\frac{\theta^{\text{SM}}_{j,\text{meas.}} - \theta^{\text{SM}}_{j,\text{nuis.}}}{\sigma(\theta^{\text{SM}}_{j,\text{meas.}})}\right)^2 + \sum_k \chi^2_{k,\text{non-Gaussian}}, \quad (3.1)$$

where $O_{i,\text{pred.}}(\theta)$ are the predicted values for the observables, $\sigma(O_i)$ is total uncertainty, namely the experimental and theoretical uncertainties added in quadrature, and $\theta_{k,\text{nuis.}}$ are the SM nuisance parameters $\{m_t,\ \Delta\alpha^{(5)}_{\text{had}}(M_Z),\ M_Z\}$ that are allowed to vary in the fit whilst being constrained according to their measured values and uncertainties. We refer to

[1] We note here that the first term in the Eq. 3.1 is the limit obtained from the more general formula $(O_{i,\text{meas.}} - O_{i,\text{pred.}}(\theta))V^{-1}_{ij}(O_{j,\text{meas.}} - O_{j,\text{pred.}}(\theta))$, if the inverse covariance matrix V^{-1} is diagonal.

the terms in the first two summations as "Gaussian" constraints, since they correspond to a Gaussian or normal distribution of $f(O_i|\theta)$. We refer to the other constraints, that do not follow this simple formula, as "non-Gaussian".

We describe how confidence intervals and regions can be constructed using the profile likelihood function in section 3.1. In subsequent sections we provide details on the implementations of constraints that contribute in Eq. 3.1: in section 3.2 we specify the observables and measurements that constitute the Gaussian constraints; in section 3.3 we detail the implementation of the non-Gaussian constraints based on two-dimensional experimental limits; in section 3.4 we carefully explain how the searches for SUSY particles at the LHC have been implemented in the case of the pMSSM10. After the detailed description of the χ^2 function we discuss in section 3.5 the algorithm and the strategy used to sample the parameter space sufficiently in order to obtain reliable profile likelihood functions. We also provide the scan ranges for the input parameters. We conclude in section 3.6 with a brief description of the `MasterCode` framework, which is used to perform the global fits.

3.1 Confidence Intervals and Regions

In this section we summarise the construction of confidence intervals, which is a common practice in High Energy Physics. We refer to chapter 38 of "Review of Particle Physics" [17] for more details, in particular section 38.3.2.1 where the profile likelihood ratio is defined, and 38.4.2 where confidence intervals are discussed.

We now discuss how confidence intervals are constructed following the approach by Neyman [100]. Assume n random variables $X_1 \dots X_n$ that depend on l parameters $\theta_1 \dots \theta_l$ that are distributed according to a probability density function $f(x_1 \dots x_n|\theta_1 \dots \theta_l)$. The confidence interval for, for instance, θ_1 at confidence level α is determined by functions $\underline{\theta}(X)$ and $\bar{\theta}(X)$ that satisfy[2]

$$P\{\underline{\theta}(X) \leq \theta_1^0 \leq \bar{\theta}(X)|\theta_1^0\} = \alpha, \tag{3.2}$$

i.e. the probability that the true value of a parameter $\theta_1 = \theta_1^0$ lies between $\bar{\theta}(X)$ and $\underline{\theta}(X)$ is equal to α. Note in particular that $\underline{\theta}(X)$ and $\bar{\theta}(X)$ are random variables that are

[2]Note that in High Energy Physics it is common to formulate the requirement as $P\{\underline{\theta}(X) \leq \theta_1^0 \leq \bar{\theta}(X)|\theta_1^0\} \geq 1-\alpha$. The inequality is motivated by the use of random variables that take discrete values so that the exact equality may not necessarily be reached. The choice of $1-\alpha$ is motivated by the desire to reject null hypothesis.

fixed by an observed $X = E$. Assuming a test statistic T, the construction of $\underline{\theta}(X)$ and $\bar{\theta}(X)$ is equivalent to constructing a θ_1 dependent acceptance region $W_{\theta_1} = [t^-, t^+]$ such that $P\{t \in W_{\theta_1}|\theta_1\} = \alpha$. With this definition the confidence interval is defined as the parameter points for which the test statistic evaluated on the data falls in W_{θ_1}.

In High Energy Physics it is common to use the profile likelihood function[3] as the test statistic

$$t(\theta) = -2 \ln \frac{\mathcal{L}(\theta, \hat{\hat{\nu}})}{\mathcal{L}(\hat{\theta}, \hat{\nu})}, \tag{3.3}$$

where (this time) θ denote the parameters of interest, and ν the remaining parameters and $\hat{\hat{\nu}}$ is the conditional maximum likelihood estimator (MLE) for a given parameter θ, whereas $\hat{\theta}$ and $\hat{\nu}$ are unconditional MLEs. This is convenient, since Wilks' theorem states that t approaches a χ^2 distribution in the limit that the data sample is large [17]. Note that substituting our χ^2 function in Eq. 3.1 into Eq. 3.3 yields

$$t(\theta) = \chi^2(\theta, \hat{\hat{\nu}}) - \chi^2(\hat{\theta}, \hat{\nu}) = \chi^2(\theta, \hat{\hat{\nu}}) - \chi^2_{\text{min}} \equiv \Delta\chi^2(\theta). \tag{3.4}$$

We would like to stress the importance of this relation for this thesis, since most of the results are presented in terms of these profile likelihood functions. If we assume that Wilks' theorem holds, then the profile likelihood functions provide the confidence intervals for n parameters and/or physical observables of interest at confidence level α when $\Delta\chi^2 \leq \Delta\chi^2(\alpha, n)$ and some typical values are given in Table 3.1.

α (%)	$\Delta\chi^2(\alpha, 1)$	$\Delta\chi^2(\alpha, 2)$
68	0.99	2.27
68.3	1	2.30
95	3.84	5.99
95.4	4	6.18
99	6.63	9.21
99.7	9	11.82

Table 3.1: *Values for $\Delta\chi^2(\alpha, n)$ that define the acceptance region $\Delta\chi^2 \leq \Delta\chi^2(\alpha, n)$ for a confidence level of α assuming a χ^2-distribution for n degrees of freedom.*

We now define some of the terminology and procedures that we use consistently throughout this thesis. We refer to 68% CL intervals (regions) where $\Delta\chi^2 < 1$ ($\Delta\chi^2 < 2.30$)

[3]Strictly speaking this is minus two times the log of the profile likelihood ratio. Here and in the rest of this thesis we will refer to this test statistic as the "profile likelihood function" or simply "profile likelihood".

and to 95% CL intervals (regions) where $\Delta\chi^2 < 4$ ($\Delta\chi^2 < 5.99$) for one- (two)-dimensional profile likelihood functions.[4] We interchangeably refer to two-dimensional profile likelihood functions as "planes". All one- (two)-dimensional profile likelihood functions displayed in this thesis are consistently obtained as follows. The displayed parameter or observable range(s) is (are) divided in 100 (100×100) equally spaced bins and in each bin the point in the sample with the lowest χ^2 value is found. For one-dimensional profile likelihood functions we typically display the $\Delta\chi^2$ for each point, cf. Eq. 3.4. For two-dimensional profile likelihood functions we typically display the $\Delta\chi^2 = 2.30$ and $\Delta\chi^2 = 5.99$ level contours as red and blue lines respectively, and the location of the point the minimises the χ^2 over the full sample is indicated with a green star. This point is referred to as the best-fit point.

3.2 χ^2 Function Part I: Gaussian Constraints

We first discuss the experimental constraints that contribute to the χ^2 function given in Eq. 3.1 as Gaussian terms. Their contribution for an observable O_i that has a measured value $O_{i,\text{meas.}}$ and a predicted value $O_{i,\text{pred.}}(\theta)$ for parameters θ is given by

$$\chi^2 = \left(\frac{O_{i,\text{meas.}} - O_{i,\text{pred.}}(\theta)}{\sigma(O_i)} \right)^2 , \tag{3.5}$$

where $\sigma(O_i)$ is the 1σ uncertainty, namely the sum in quadrature of experimental and theoretical uncertainties. Eq. 3.5 applies to nominal Gaussian constraints, whereas in case of an upper (lower) limit it only applies when $O_{i,\text{pred.}}(\theta) > O_{i,\text{meas.}}$ ($O_{i,\text{pred.}}(\theta) < O_{i,\text{meas.}}$). For each of the Gaussian constraints we specify the measured value, the experimental and theoretical uncertainties and the calculations that lead to the predicted value.

3.2.1 LEP Mass Lower Limits

The ALEPH, DELPHI, L3, OPAL experiments at LEP have placed 95% CL lower limits on the masses of SUSY particles [80]. In our fits we take these into account as lower limits and their numeric values are given in Table 3.2. We note that the lower limit on the lightest neutralino was derived assuming GUT relations between the soft SUSY breaking

[4] This is to avoid cumbersome descriptions in the text, although we recognise that it would be more correct to refer to these $\Delta\chi^2$ values as 68.3% (68.3%) and 95.4% (95%) CL respectively.

gaugino mass parameters [101]. For this reason this constraint is applied in scans of the CMSSM, NUHM1 and NUHM2, but not in the case of the pMSSM10.

Observable	Constraint
$\tilde{q}$	> 90 GeV
$\tilde{\ell}$	> 90 GeV
$\tilde{\nu}_\ell$	> 90 GeV
$\tilde{\chi}_1^\pm$	> 103 GeV
$\tilde{\chi}_1^0$(SUGRA)	> 50 GeV

Table 3.2: *LEP 95% CL lower limits on SUSY particle masses.*

3.2.2 Top Mass

The top mass serves as a SM input parameter to the MSSM spectrum calculation and is therefore treated it as a nuisance parameter. As such it is allowed to vary, but constrained by a χ^2 contribution according to its measured value, cf. Eq. 3.1. In our fits we take the value of the top mass as given in a table provided by the Gfitter Collaboration [19], cf. Ref. [20]:

$$m_t = 173.2 \pm 0.87 \text{ GeV}.$$

3.2.3 The Light Higgs Boson

The discovery of the (lightest) Higgs boson by ATLAS [1] and CMS [2] is a great triumph of the LHC Run 1. One of the most accurately measured and also most constraining properties of the lightest Higgs boson is its mass. In our fits of the CMSSM, NUHM1, and NUHM1 we use

$$M_h = 125.7 \pm 0.4_{\text{EXP}} \pm 1.5_{\text{SUSY}} \text{ GeV},$$

which was available at the time of writing [43] and [44]. In our analysis of the pMSSM10 we updated this constraint to the recent world average based on a combination of ATLAS and CMS using 5 (20) fb^{-1} of data taken at $\sqrt{s} = 7$ (8) GeV [24]

$$M_h = 125.09 \pm 0.24_{\text{EXP}} \pm 1.5_{\text{SUSY}} \text{ GeV}.$$

For the calculation of the lightest Higgs mass, we use `FeynHiggs-2.10.0` [75, 102–106]. In our fits we assume a theoretical uncertainty of 1.5 GeV, which is a conservative,

but accurate estimate of the point-by-point uncertainty that can be calculated using `FeynHiggs-2.10.0`.

In our analysis of the pMSSM10 we also incorporate constraints on the measured Higgs signal rates as calculated with `HiggsSignals-1.3.1` [107, 108], which evaluates the χ^2 contribution of 77 channels from the Higgs boson searches at the LHC and the Tevatron (see [107, 108] for a complete list of references).

3.2.4 Dark Matter Relic Density

The cold dark matter density can be determined from anisotropies in the Cosmic Microwave Background, such as measured with high precision by the *Wilkinson Microwave Anisotropy Probe* (WMAP) satellite [109] and by the Planck satellite [110], in combination with other cosmological measurements. From these data the 6 parameters that constitute the ΛCDM can be extracted [3] and in particular $\Omega_{\rm CDM}h^2$. In our fits we use

$$\Omega_{\rm CDM}h^2 = 0.1186 \pm 0.0022_{\rm EXP} \pm 0.012_{\rm TH},$$

which can be found in Ref. [3] Table 5, the "*Planck*+lensing+WP+highL" column.[5] For the SUSY prediction we use `micrOMEGAs-3.2` [79]. Note that we assume a theoretical uncertainty of $\sim 10\%$ [33]. This theoretical uncertainty is much larger than the experimental uncertainty, reflecting the fact that the SUSY prediction for $\Omega_{\rm CDM}h^2$ is very sensitive to the MSSM spectrum. That is, the input parameters for a given model point may need tweaking to achieve the same $\Omega_{\rm CDM}h^2$ when using different spectrum and $\Omega_{\rm CDM}h^2$ calculators.

3.2.5 The Anomalous Dipole Moment of the Muon

To calculate the χ^2 contribution from a_μ we take the measured value [21] of $a_\mu^{\rm EXP} = (11,659,208.0\pm5.4_{\rm stat}\pm3.3_{\rm sys})\times10^{-10}$, whereas we use $a_\mu^{\rm SM} = (11,659,177.8\pm6.1_{\rm SM})\times10^{-10}$ for the SM calculation [92]. We also assume an uncertainty on the SUSY prediction of 2.0×10^{-10} [33] resulting in

$$a_\mu^{\rm EXP} - a_\mu^{\rm SM} = (30.2 \pm 5.4_{\rm stat} \pm 3.3_{\rm sys} \pm 6.1_{\rm SM} \pm 2.0_{\rm SUSY}) \times 10^{-10}.$$

[5] Lensing WP and highL are the other measurements that must be combined with the CMB data.

We calculate a_μ using `FeynHiggs` [106], which implements two-loop SUSY corrections to a_μ [111]. In the remainder of this thesis we will refer to a_μ as $(g-2)_\mu$.

3.2.6 Electroweak Precision Observables

The experiments at LEP and the SLC have established Z-pole observables, cf. section 2.5.5, to a very high precision and their measured values can be found in Table 8.4 in Ref. [18]. We use these values to constrain the Z-pole observables in our fit as listed in Table 3.3, with the exception of $\Delta\alpha^{(5)}_{\rm had}(M_Z)$, which we took from a table provided by the Gfitter Collaboration [19], cf. Ref. [20]. For the W mass we take the world average as reported in the Review of Particle Physics [17]

$$M_W = 80.385 \pm 0.015 \pm 0.010_{\rm SUSY},$$

where the theoretical uncertainty follows [33].

Observable	Constraint
$\Delta\alpha^{(5)}_{\rm had}(M_Z)$	0.02756 ± 0.00010
M_Z [GeV]	91.1875 ± 0.0021
Γ_Z [GeV]	$2.4952 \pm 0.0023 \pm 0.001_{\rm SUSY}$
$\sigma^0_{\rm had}$ [nb]	41.540 ± 0.037
R^0_ℓ	20.767 ± 0.025
$A^{0,\ell}_{\rm FB}$	0.01714 ± 0.00095
$\mathcal{A}_\ell(P_\tau)$	0.1465 ± 0.0032
$\mathcal{A}_\ell$(SLD)	0.1513 ± 0.0021
$R^0_{\rm b}$	0.21629 ± 0.00066
$R^0_{\rm c}$	0.1721 ± 0.0030
$A^{0,b}_{\rm FB}$	0.0992 ± 0.0016
$A^{0,c}_{\rm FB}$	0.0707 ± 0.0035
$\mathcal{A}_b$	0.923 ± 0.020
$\mathcal{A}_c$	0.670 ± 0.027
$\sin^2\theta^\ell_{\rm eff}(Q^{\rm had}_{\rm FB})$	0.2324 ± 0.0012

Table 3.3: *The Z-pole observables as listed in Table 8.4 in Ref. [18] (with the exception of $\Delta\alpha^{(5)}_{\rm had}(M_Z)$, which we took from [19], cf. Ref. [20]). In our fit we treat $\Delta\alpha^{(5)}_{\rm had}(M_Z)$ and M_Z as input parameters.*

We calculate M_W and the Z-pole observables using `FeynWZ` which is a private code by A.M. Weber based on [77] and [112]. This code takes $\Delta\alpha^{(5)}_{\rm had}(M_Z)$ and M_Z as input

parameters and we treat these as nuisance parameters in our fit, cf. Eq. 3.1.

3.2.7 Flavour Physics Observables

We take into account constraints on rare B decays, rare K decays, $B - \bar{B}$ mixing, and ϵ_K and their experimental values are listed in Table 3.4, cf. Table 1 in Ref. [44]. Note that for many of these observables we list the ratio with respect to the standard model prediction $O^{\mathrm{EXP/SM}}$, which are used to constrain the relative enhancement due to SUSY contributions $O^{\mathrm{SUSY/SM}}$.

Observable	Source	Constraint
$\mathrm{BR}(B_{s,d} \to \mu^+\mu^-)$	[13–15]	CMS & LHCb (unofficial) combination
$\mathrm{BR}^{\mathrm{EXP/SM}}_{B\to X_s\gamma}$	[12, 113, 114]	$1.089 \pm 0.070_{\mathrm{EXP}} \pm 0.080_{\mathrm{SM}} \pm 0.050_{\mathrm{SUSY}}$
$\mathrm{BR}^{\mathrm{EXP/SM}}_{B\to\tau\nu}$	[12, 16]	$1.39 \pm 0.28_{\mathrm{EXP}} \pm 0.13_{\mathrm{SM}}$
$\mathrm{BR}^{\mathrm{EXP/SM}}_{B\to X_s\ell\ell}$	[12]	0.99 ± 0.32
$\mathrm{BR}^{\mathrm{EXP/SM}}_{K\to\mu\nu}$	[11]	$1.008 \pm 0.014_{\mathrm{EXP+TH}}$
$\mathrm{BR}^{\mathrm{EXP/SM}}_{K\to\pi\nu\bar{\nu}}$	[115]	< 4.5
$\Delta M^{\mathrm{EXP/SM}}_{B_s}$	[116]	$0.97 \pm 0.20_{\mathrm{SM}}$
$\frac{\Delta M^{\mathrm{EXP/SM}}_{B_s}}{\Delta M^{\mathrm{EXP/SM}}_{B_d}}$	[116]	$0.86 \pm 0.14_{\mathrm{SM}}$
$\Delta\epsilon^{\mathrm{EXP/SM}}_K$	[117]	$1.14 \pm 0.10_{\mathrm{EXP+TH}}$

Table 3.4: *Experimental values of rare B decays, rare K decays, $B-\bar{B}$ mixing, and ϵ_K. Ratios with respect to the standard model prediction $O^{\mathrm{EXP/SM}}$ are used to constrain the relative enhancement due to SUSY contributions $O^{\mathrm{SUSY/SM}}$.*

For the constraint on $\mathrm{BR}(B_{s,d} \to \mu^+\mu^-)$ we use an implementation as detailed in Ref. [43], where a combined χ^2 contribution was constructed based on an unofficial combination of the CMS [14] and LHCb [13] results. For our fit of the pMSSM10 we

updated the value of the $B \to \tau\nu_\tau$ decay to the recent measurement by Belle [118]

$$\mathrm{BR}^{\mathrm{EXP/SM}}_{\mathrm{B}\to\tau\nu} = 1.12 \pm 0.27_{\mathrm{EXP}} \pm 0.1_{\mathrm{SM}}, \tag{3.6}$$

as well as the recent world average of the branching ratio for $B \to X_s\gamma$ in Ref. [119] and its ratio with the theoretical estimate in the SM in Ref. [120]

$$\mathrm{BR}^{\mathrm{EXP/SM}}_{\mathrm{B}\to\mathrm{X_s}\gamma} = 1.021 \pm 0.066_{\mathrm{EXP}} \pm 0.070_{\mathrm{SM}} \pm 0.050_{\mathrm{SUSY}}. \tag{3.7}$$

The SUSY predictions for flavour physics observables are calculated using `SuFla`, a private code by G. Isidori based on Refs. [96, 97] and references therein.

3.3 χ^2 Function Part II: Implementations of Non-Gaussian Constraints

In this section we describe the implementation of constraints on 1) squark and gluino production in the CMSSM, NUHM1, and NUHM2; 2) production of heavy neutral Higgs bosons decaying into taus; 3) spin-independent cross-section of neutralino-nucleus elastic scattering. Each of these constrains are presented in terms of 95% or 90% CL exclusion contours and therefore cannot be cast in a simple formula like Eq. 3.5. These constraints are referred to as non-Gaussian in Eq. 3.1.

3.3.1 Searches for Squarks and Gluinos in CMSSM, NUHM1, and NUHM2

The direct production of SUSY particles has been the topic of many searches by the ATLAS [25] and CMS [26] experiments at the LHC, which have so far yielded null results. Among these the hadronic searches for direct squark and gluino production using a jets $+ \not{E}_T$ signature, such as [121] ([122]) by ATLAS (CMS) using 20 fb^{-1} of $\sqrt{s} = 8$ TeV data, constrain most strongly the parameter spaces of the CMSSM, NUHM1, and NUHM2. That is, cross-sections for the production of strongly produced sparticles are generally larger than those of electroweakly produced sparticles, whereas their respective masses are related through unifying assumptions at the GUT scale.

ATLAS and CMS typically provide interpretations of their results as a 95% CL exclusion contour in the $(m_0, m_{1/2})$ plane for fixed values of A_0 and $\tan\beta$, although the limits are,

to a good approximation, independent of these parameters, cf. the discussion in Ref. [123]. In [42] this assertion was verified for the ATLAS jets $+\not{E}_T$ search at $\sqrt{s} = 7$ TeV with 5 fb^{-1} [124] and it was also verified that it holds for non-universal Higgs masses in the NUHM1 and NUHM2. For our implementation of the LHC searches for squarks and gluinos we use the interpretation of the jets $+\not{E}_T$ search by ATLAS [121] in terms of a 95% CL exclusion contour in the $(m_0, m_{1/2})$ plane.

Based on this contour a χ^2 contribution is assigned as first outlined in [38]. Given the dependence on two parameters $\chi^2 = 5.99$ is applied on the 95% CL contour. This contribution along the contour is extrapolated to other values of m_0 and $m_{1/2}$ along a line through the origin of the $(m_0, m_{1/2})$ plane according to the distance $\mathcal{M} \equiv \sqrt{m_0^2 + m_{1/2}^2}$ and the distance on the contour $\mathcal{M}_c$

$$\chi^2 = 5.99 \cdot \left(\frac{\mathcal{M}}{\mathcal{M}_c}\right)^{\alpha},$$

where α is set to 4, cf. the discussion in Ref. [38].

3.3.2 Searches for Heavy Higgs Bosons

The ATLAS (CMS) experiment has placed 95% CL exclusion limits on $\tan\beta$ as a function of the mass of the heavy neutral MSSM Higgs bosons based on searches for the $H/A \to \tau^+\tau^-$ decay with 20 (5/20) fb^{-1} of data at $\sqrt{s} = 8$ (7/8) TeV [125] ([126]). In our scans of the CMSSM, NUHM1, and NUHM2 we implemented the constraint based on the ATLAS search following the approach outlined in Ref. [40]: a χ^2 contribution of 5.99 is applied for values of M_A and $\tan\beta_{\rm c}(M_A)$ along the 95% CL exclusion contour. This contribution is assumed to scale quadratically with $\tan\beta$

$$\chi^2 = 5.99 \cdot \left(\frac{\tan\beta}{\tan\beta_{\rm c}(M_A)}\right)^2.$$

In our study of the pMSSM10 we refined our approach by replacing the approximate formula by a χ^2 evaluation based on the publicly available code `HiggsBounds-4.2.0` [127]. `HiggsBounds-4.2.0` calculates a χ^2 contribution on $H/A \to \tau^+\tau^-$ based on the CMS search.

3.3.3 Neutralino Scattering off Nuclei

For the constraints on neutralino scattering off nuclei we follow the approach that we first outlined in Ref. [43], which takes into account the experimental uncertainties on $\Sigma_{\pi N}$ and ς_0 in the theoretical calculation [84]. We use results from LUX [23], although XENON100 [22] has a similar sensitivity at large neutralino masses.

The LUX experiment provided a 90% CL limit contour in the $(M_{\rm WIMP}, \sigma_p^{\rm SI})$ plane, along which the expected number of signal events varies between 2.4 and 5.3 for different WIMP masses. This 90% CL was obtained using a profile likelihood test statistic designed to separate background- and signal-like interactions. In our approach we make the simplifying assumption that the 90% CL limit corresponds to the observation of one interaction $N_{\rm LUX} = 1$ (cf. Fig. 4 in Ref. [23] where one interaction is below solid red line). Assuming a Poisson distribution with zero background, the 90% CL interval for the mean of this distribution is given by $[0.11, 4.36]$ (cf. Table IV in Ref. [128]). Therefore we associate $N_{\rm contour} = 4.36$ to the excluded number of interactions on the contour and the number of interactions $N_{\rm SUSY}$ for other values of $\sigma_p^{\rm SI}$ is assumed to scale linearly. Taking into account the uncertainty on the spin-independent cross-section $\Delta\sigma_p^{\rm SI}({\rm SUSY})$ we constrain the neutralino-nucleus scattering using

$$\chi^2 = \begin{cases} \frac{4.61}{2.71} \cdot \frac{(N_{\rm SUSY} - N_{\rm LUX})^2}{\Delta N_{\rm LUX}^2 + \Delta N_{\rm SUSY}^2} & \text{if } N_{\rm SUSY} > 1 \\ 0 & \text{otherwise.} \end{cases}$$

Here $(\Delta)N_{\rm SUSY} = N_{\rm contour} \cdot (\Delta)\sigma_p^{\rm SI}({\rm SUSY})/\sigma_p^{\rm SI}({\rm contour})$ and $\Delta N_{\rm LUX} = (N_{\rm contour} - N_{\rm LUX})/\sigma_{90\%}$ ($\sigma_{90\%}^2 \approx 2.71$, which correspond to 90% CL of the χ^2 distribution with one degree of freedom). Since this constraint manifestly depends on $m_{\tilde{\chi}_1^0}$ and $\sigma_p^{\rm SI}$ we multiply by 4.61/2.71, where 4.61 corresponds to 90% CL of the χ^2 distribution with one degree of freedom.

We illustrate the effect of taking into account the theoretical uncertainty on the spin-independent cross-section in Fig. 3.1. For 1000 randomly selected points from our CMSSM sample we depict the χ^2 calculated whilst (without) taking into account $\Delta\sigma_p^{\rm SI}({\rm SUSY})$ in blue (red). We also display $\Delta\sigma_p^{\rm SI}({\rm SUSY})/\sigma_p^{\rm SI}({\rm contour})$ as a horizontal error bar for one of these points. This figure highlights that the uncertainties due to $\Sigma_{\pi N}$ and ς_0 are generally large and they significantly weaken the constraint.

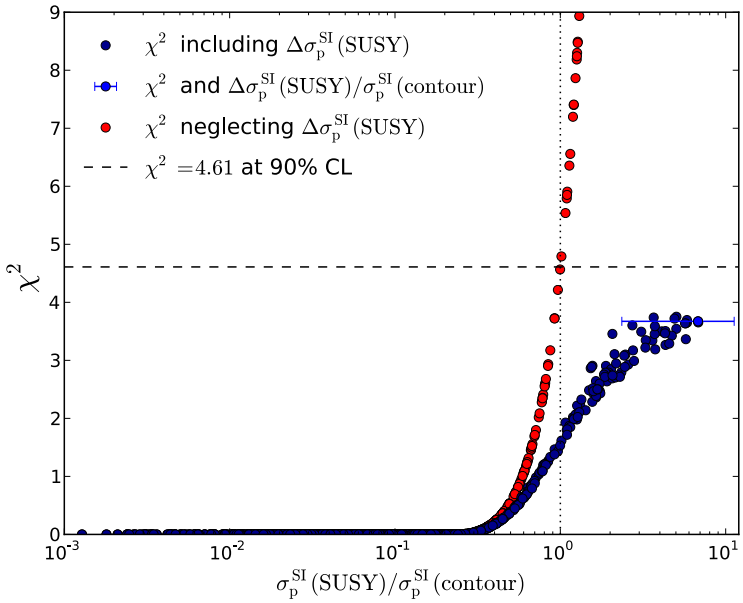

Figure 3.1: *Comparison of the constraint on the spin-independent cross-section with (blue points) and without (red points) taking into account the theoretical uncertainty* $\Delta\sigma_p^{\rm SI}$(SUSY). *For illustration* $\Delta\sigma_p^{\rm SI}$(SUSY)/$\sigma_p^{\rm SI}$(contour) *is depicted as a horizontal error bar for one point.*

3.4 χ^2 Function Part III: Implementation of Searches for SUSY Particles at LHC Run 1 in the pMSSM10

A central part of our analysis of the pMSSM10 is a comprehensive implementation of the searches for SUSY particles by ATLAS [25] and CMS [26] during LHC Run 1. Unlike the CMSSM, NUHM1, and NUHM2, there is *a priori* no straightforward parameterisation of a χ^2 contribution from these searches in the pMSSM10.

One of the greatest challenges is generalising the results from the experiments in a computationally economic way for every model point in the sampled parameter space. The method that comes closest to the "true" experimental constraint for a given model point is to "reinterpret" relevant searches by generating events, passing them through a detector simulation and an emulation of these searches. However, this approach usually takes at least a few minutes per model point using e.g. `PYTHIA 6` for the event generation and `Delphes 3` for the detector simulation. It would be computationally infeasible to apply

such an approach to all $\mathcal{O}(\times 10^9)$ model points in our fits.

However, there are guiding principles to approximate the constraints from the point-by-point reinterpretation. For a given mass the production cross-sections for strongly produced sparticles are much larger than for electroweakly produced sparticles. Accordingly, their respective mass ranges where LHC limits are applicable differ. We can therefore consider the limits for squarks and gluinos separately from electroweakinos and sleptons.

The mass limits on squarks and gluinos from individual searches still depend on the electroweakino and slepton masses, since they influence the possible decay chains. However, it was found in Ref. [129] that combining searches with sufficiently inclusive signatures with jets + X + $\not{E}_T$ yields mass limits that are, to a good approximation, universal. Following this approach we construct a 'universal' χ^2 function, which we refer to as $\chi^2(\text{LHC8}_{\text{col}})$ for squarks and gluino masses. We assess its validity and estimate quantitatively its associated uncertainties on the 68% and 95% CL lower limits in section 3.4.2.

The story is different for production of electroweakinos and sleptons where the limits do depend strongly on the mass hierarchy within the spectrum. However, this mass hierarchy simplifies because the squark and gluino masses must be larger to avoid strong constraints, thus leaving only the electroweakino and slepton masses and their hierarchy. We adopt an approach in which we take into account the decay modes of electroweakinos and sleptons and apply relevant limits from simplified model spectra (SMS) interpretations. The validation of this approach and estimation of the associated uncertainties is described in section 3.4.3.

An important caveat of the 'universal' limit approach is that in the region with compressed-stop spectra, where $m_{\tilde{t}_1} - m_{\tilde{\chi}_1^0} < m_t$ the sensitivity of searches does become strongly dependent on the details of the spectrum. Accordingly, we treat this case separately in an analogous way to the constraints on electroweakinos and sleptons as we describe in section 3.4.4.

3.4.1 Reinterpretation of Searches

Null-results from experimental searches for new physics are usually presented as 95% CL limits on parameters of a given signal model. These limits are established using the CL_s method, as is detailed in e.g. section 9 in Ref. [130]. The CL_s is calculated using the number of expected events from (SM) background, the number of observed events, and the simulated number of signal events, taking into account all the relevant systematic and statistical uncertainties. Estimating the number of expected background events and their

uncertainties is an essential part of the experimental effort and relies on the understanding of the detector response and all the systematic uncertainties. The predictions for the signal are obtained by generating signal events, which are then passed through a full detector simulation and analysed in the same way as the events from collision data. This yields a prediction for the number of signal events in each of the signal regions.

For the reinterpretation of the searches it is therefore justified to use the background estimation, the number of observed events, and the corresponding uncertainties that are provided by the experiments. Since signal events are expected to have more distinct signatures than the background events, such as large $\not{E}_T$, it is justified to use fast simulation tools to emulate the detector response. In the following we describe the software used for the event generation, detector simulation, implementation of searches and interpretation.

We note here that in order to translate the $\mathrm{CL_s}$ calculated for a generic spectrum in the MSSM into a χ^2 value, we interpret it as the p-value of the signal hypothesis assuming one degree of freedom. This translation could be improved and this may be considered in future work. However, it should not alter the results in this thesis beyond the uncertainties that arise from approximating the point-by-point reinterpretation.

Event Generation: `PYTHIA 6`

For production of SUSY particles in proton-proton collisions we generate events with `PYTHIA 6` [131]. `PYTHIA 6` generates the hard scattering process, performs the hadronisation and also calculates the production cross-section. The input can be conveniently parsed using the SUSY Les Houches Accord [132, 133] (SLHA) format, whereby it is possible (but not required) to provide decay tables of the SUSY particles.

CMS Searches: `Delphes` and `Scorpion`

For the reinterpretation of CMS searches we use the `Delphes` [134] fast detector simulation package and the `Scorpion` framework to emulate the analyses. `Scorpion` is a framework that was originally developed for the combination of various jets + X + $\not{E}_T$ CMS searches at $\sqrt{s} = 7$ TeV: the 0-lepton α_T [135], the 1-lepton L_p [136], the opposite-sign (OS) dilepton [137], and the same-sign (SS) dilepton [138]. The detector simulation was done using `Delphes 2`. The essential feature of the `Scorpion` framework is that it allows to combine searches to establish a combined $\mathrm{CL_s}$ value.[6] This combination is done by calculating the $\mathrm{CL_s}$ based on all the signal regions from each of the searches. If a search

[6] The $\mathrm{CL_s}$ calculation is done using the `LandS` package [139].

has defined overlapping signal regions, then only the signal region with the strongest expected limit is taken into account. Note that the searches have been chosen to have non-overlapping signatures guaranteeing no overlapping signal regions among different searches.

For the analysis of the pMSSM10 [60] we have substantially extended the `Scorpion` framework. First of all we moved to using `Delphes 3`, for practical reasons, and the tuning of the detector card is detailed in appendix A. Secondly we implemented the (then available) $\sqrt{s} = 8$ TeV and 20 fb^{-1} searches for jets $+ X + \not{E}_T$ as listed in Table 3.5. The validation is detailed in appendix A.

Searches	Reference	Signal Regions
Monojet	[140]	Strongest expected
0-lepton (M_{T2})	[130]	All
single-lepton ($M_{\mathrm{T2}}^{\mathrm{W}}$)	[141]	Strongest expected
SS-dilepton	[142]	All
OS-dilepton	[137]	All
$\geq$ 3-lepton	[143]	All

Table 3.5: *CMS searches implemented in the* `Scorpion` *framework that are used for this thesis.*

ATLAS Searches: `Atom`

For the recast of ATLAS we rely on `Atom` [144] (see e.g. [145, 146]), which is a framework based on `Rivet` [147]. `Atom` emulates the reported detector resolutions of ATLAS and CMS by mapping the truth level particles from the event generator to reconstructed objects, using analytic functions and numerical grids for parameters associated with momentum smearing and efficiencies of object reconstruction. A validation of the `Atom` code can be found in Ref. [148].

The implemented searches used for the analysis in this thesis and in Ref. [60] are listed in Table 3.6. The $\mathrm{CL_s}$ calculation is done in the same way as in `Scorpion`, namely using the `LandS` package and combining the signal regions from multiple searches. For each search the strongest expected signal region is used for the combination, since the searches defined overlapping signal regions. Since the 2-lepton searches have overlapping signatures, only the strongest expected signal region is taken from these two searches.

Searches	Reference
2-b-jets	[149]
1-lepton	[150, 151]
2-leptons (M_{T2})	[152]
2-leptons	[153]
3-leptons	[154]

Table 3.6: *ATLAS searches implemented in the* `Atom` *framework that are used in this thesis.*

3.4.2 Squarks and Gluinos

In the case of the pMSSM10 the implementation of the direct searches for squarks and gluinos is not as straightforward as in the CMSSM, NUHM1 and NUHM2. As we argued above, it would not be computationally possible to run a full reinterpretation for every individual model point of our sample. In order to establish a reasonable approximation we follow an approach outlined in Ref. [129] by constructing a 'universal' χ^2 function for squarks and gluinos, to which we refer as $\chi^2(\mathrm{LHC8_{col}})$, by combining inclusive CMS jets + X + $\not{E}_T$ searches.

In [129] it was found that combining the CMS results for the 0-lepton α_T [135], 1-lepton L_p [136], opposite-sign dilepton [137], and same-sign dilepton [138] searches at $\sqrt{s} = 7$ TeV with 5 fb^{-1} of data, it is possible to establish 'universal' lower limits on the gluino mass $m_{\tilde{g}}$ and the third-generation squark mass $m_{\tilde{q}3}$ depending on $m_{\tilde{\chi}_1^0}$ within the intrinsic sampling uncertainties. That is, these limits are independent of other model parameters, namely slepton and electroweakino masses. The idea behind this approach is that, although the other model parameters alter the possible decay chains, the combination of a sufficiently complete set of jets + X + $\not{E}_T$ searches should capture most of them.

In order to apply this approach to the pMSSM10 parameter space, we included also the first- and second-generation squark masses $m_{\tilde{q}}$ and updated to jets + X + $\not{E}_T$ searches at $\sqrt{s} = 8$ TeV with 20 fb^{-1} of data. Based on these searches we construct a χ^2 function that depends only on $m_{\tilde{\chi}_1^0}$, $m_{\tilde{g}}$, $m_{\tilde{q}}$, and the cross-section weighted average over the third-generation squark masses $m_{\tilde{q}3}$ that we refer to as $\chi^2(\mathrm{LHC8_{col}})$. One important caveat is that the universality of the mass limits does not hold in the case of compressed-stop spectra with $m_{\tilde{t}_1} - m_{\tilde{\chi}_1^0} < m_t$, where the stop decay into an on-shell top is kinematically forbidden and the limits do depend strongly on the stop decay modes. We treat these spectra separately as we detail in section 3.4.4 and ensure that the lighter stop does not contribute to the universal limit in this case by (effectively) setting its production

cross-section to zero in the calculation of $m_{\tilde{q}3}$.

We construct $\chi^2(\text{LHC8}_{\text{col}})$ as follows. We calculated $\chi^2(\text{LHC8}_{\text{col}})$ on a $1+3$ dimensional grid in $m_{\tilde{\chi}_1^0}$, $m_{\tilde{g}}$, $m_{\tilde{q}}$, and $m_{\tilde{q}3}$. The neutralino mass takes values $m_{\tilde{\chi}_1^0} = \{10,\ 110,\ \ldots,\ 610\}$ GeV. For each neutralino mass we defined a grid where $m_{\tilde{g}}$ and $m_{\tilde{q}}$ take values $\{m_{\tilde{\chi}_1^0}+40,\ m_{\tilde{\chi}_1^0}+140,\ \ldots,\ 1750,\ 2500,\ 5000\}$ GeV, whereas $m_{\tilde{q}3}$ takes values $\{m_{\tilde{\chi}_1^0}+80,\ m_{\tilde{\chi}_1^0}+180,\ \ldots,\ 1290,\ 2500,\ 5000\}$ GeV. Ellipses signify steps of 100 GeV so that the total number of points on this grid is 25,564. The spacing of the masses was chosen to have a fine granularity at low squark and gluino masses, whilst capturing relevant futures if one or more these masses becomes high. For each point on the grid we generated an SLHA file [132, 133] by setting the masses of the respective particles. Note in particular that all four third generation squark masses were set equal. We then calculated $\chi^2(\text{LHC8}_{\text{col}})$ for each point on the grid using `Scorpion`.

Fig. 3.2 displays 3- and 2-dimensional slices of the $1+3$-dimensional $\chi^2(\text{LHC8}_{\text{col}})$ grid where $m_{\tilde{\chi}_1^0} = 310$ GeV (top panel), $m_{\tilde{g}} = 2500$ GeV and $m_{\tilde{q}} = 2500$ GeV (bottom left panel), and $m_{\tilde{\chi}_1^0} = 310$ GeV and $m_{\tilde{q}} = 2500$ GeV (bottom right panel). The top panel illustrates the fine and coarse granularity at low and high masses of $m_{\tilde{g}}$, $m_{\tilde{q}}$, and $m_{\tilde{q}3}$ for a given value of $m_{\tilde{\chi}_1^0}$. The bottom left panel illustrates how the lowest $m_{\tilde{g}}$, $m_{\tilde{q}}$, and $m_{\tilde{q}3}$ masses on the grid depend on $m_{\tilde{\chi}_1^0}$, whereas the small but non-negligible dependence of $\chi^2(\text{LHC8}_{\text{col}})$ on large values of $m_{\tilde{g}}$ and $m_{\tilde{q}}$ is highlighted in the bottom right panel of Fig. 3.2.

Based on this grid we calculate $\chi^2(\text{LHC8}_{\text{col}})$ for a generic SUSY spectrum in two steps. The first step is to calculate the cross-section weighted average $m_{\tilde{q}3}$. This cross-section weighting is needed since the third generation squarks can have large splitting, whereas the χ^2 values on the grid were calculated assuming equal masses for the third-generation squark masses.[7] Based on the cross-section tables provided in Refs. [155, 156], one can verify that the stop/sbottom production cross-sections scale approximately as:

$$\sigma \propto \frac{1}{m^8}.$$

With this scaling the production cross-section corresponding to four different masses can

[7] Since the mass splitting between first and second generation squark masses is generally small in the pMSSM10, $m_{\tilde{q}}$ is simply the average of these masses.

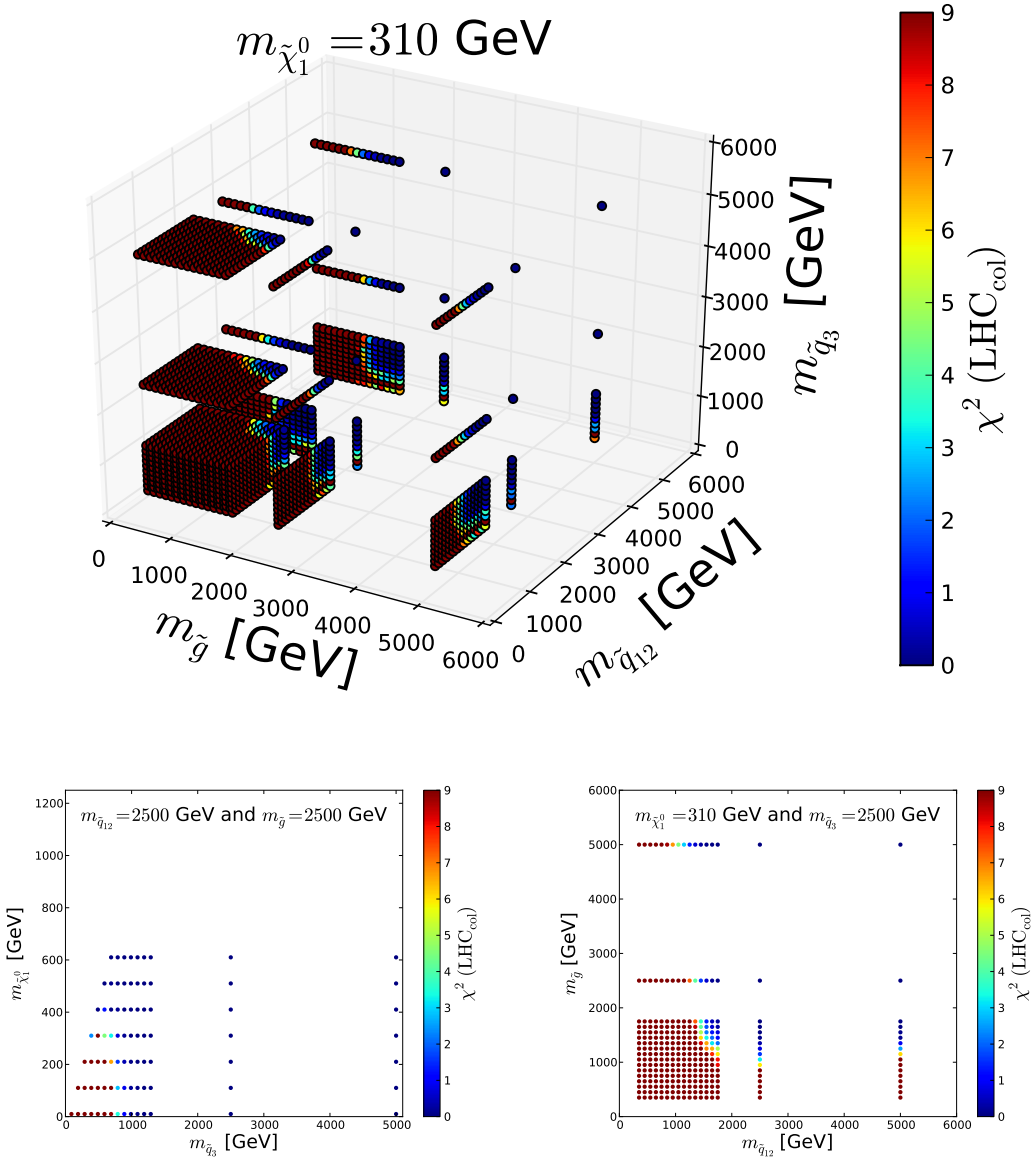

Figure 3.2: *Compilation of* 3- *and* 2-*dimensional slices of the* $1+3$-*dimensional* χ^2 *grid where* $m_{\tilde{\chi}_1^0} = 310$ GeV *(top),* $m_{\tilde{g}} = 2500$ GeV *and* $m_{\tilde{q}} = 2500$ GeV *(bottom left), and* $m_{\tilde{\chi}_1^0} = 310$ GeV *and* $m_{\tilde{q}3} = 2500$ GeV *(bottom right).*

be obtained from four equal masses if

$$\frac{4}{m_{\tilde{q}3}^8} \approx \sum_{i=1}^{4} \frac{1}{m_i^8},$$

which yields the equation for $m_{\tilde{q}3}$

$$m_{\tilde{q}3} := \left(\frac{1}{\sum_{i=4}^{4} \frac{1}{m_i^8}} \right)^{\frac{1}{8}} . \tag{3.8}$$

To ensure that $m_{\tilde{t}_1}$ does not contribute in the case of compressed-stop spectra it it is set to $m_{\tilde{t}_1} = 5$ TeV, thereby rendering its contribution negligible.

The second step is to obtain $\chi^2(\text{LHC8}_{\text{col}})$ by linear interpolation based on the (calculated) values of $m_{\tilde{\chi}_1^0}$, $m_{\tilde{g}}$, $m_{\tilde{q}}$, and $m_{\tilde{q}3}$. First an interpolation is done on the two 3-dimensional grids in $m_{\tilde{g}}$, $m_{\tilde{q}}$, $m_{\tilde{q}3}$ corresponding to the nearest values $m_{\tilde{\chi}_1^0\, i,i+1}$ on the grid: $m_{\tilde{\chi}_1^0\, i} \leq m_{\tilde{\chi}_1^0} < m_{\tilde{\chi}_1^0\, i+1}$. The two values $\chi^2(\text{LHC8}_{\text{col}})(m_{\tilde{\chi}_1^0\, i})$ and $\chi^2(\text{LHC8}_{\text{col}})(m_{\tilde{\chi}_1^0\, i+1})$ are then linearly interpolated according to $m_{\tilde{\chi}_1^0}$. If $m_{\tilde{\chi}_1^0}$ lies outside the grid then $\chi^2(\text{LHC8}_{\text{col}})$ is set to zero. If a value of $m_{\tilde{g}}$, $m_{\tilde{q}}$, or $m_{\tilde{q}3}$ lies outside the grid, then it is set to the closest value on the grid boundary.

In the following we validate the $\chi^2(\text{LHC8}_{\text{col}})$ and gauge quantitatively its uncertainty. We first compare $\chi^2(\text{LHC8}_{\text{col}})$ with $\chi^2(\texttt{Scorpion})$, i.e. the point-by-point reinterpretation, for 1000 model points that were randomly selected from our pMSSM10 sample requiring that $m_{\tilde{g}} < 1500$ GeV and/or $m_{\tilde{q}} < 1600$ GeV and/or $m_{\tilde{q}3} < 900$ GeV. The left panel of Fig. 3.3 displays the distribution of the differences between these two calculations and the RMS (root mean squared or standard deviation) of σ_{χ^2} on this distribution. In the right panel black points show $\chi^2(\text{LHC8}_{\text{col}})$ as a function of $\chi^2(\texttt{Scorpion})$ for these points, one (two) σ_{χ^2} bands are shown with dark (light) shading, and vertical and horizontal dashed lines indicate $\chi^2 = 3.84$, which corresponds to 95% CL_s. For the majority of points both methods either yield an exclusion greater than or smaller than 95% CL_s. Most of the remaining points differ by less than $2\sigma_{\chi^2}$.

It is *a priori* not clear whether $\sigma_{\chi^2} = 1.78$ is "good" or "bad". To address this question we assess quantitatively how this uncertainty on $\chi^2(\text{LHC8}_{\text{col}})$ propagates into the 68% and 95% CL contours in relevant mass planes. To this end we vary $\chi^2(\text{LHC8}_{\text{col}})$ up and down according to the σ_{χ^2} in the bins of $\chi^2(\text{LHC8}_{\text{col}}) < 1$, $\chi^2(\text{LHC8}_{\text{col}}) \geq 1$ and $\chi^2(\text{LHC8}_{\text{col}}) < 4$, and $\chi^2(\text{LHC8}_{\text{col}}) \geq 4$. Fig. 3.4 shows the results for the $(m_{\tilde{q}}, m_{\tilde{g}})$ (left panel) and the $(m_{\tilde{t}_1}, m_{\tilde{\chi}_1^0})$ (right panel) planes. Here $m_{\tilde{q}}$ is the average over the first- and second-generation right- and left-handed squark masses. The 95% (68%) CL contours are indicated with blue (red) lines for $\chi^2(\text{LHC8}_{\text{col}}) - \sigma_\chi^2$ (dotted), $\chi^2(\text{LHC8}_{\text{col}})$ (solid), and $\chi^2(\text{LHC8}_{\text{col}}) + \sigma_\chi^2$ (dashed-dotted). Empty and filled stars indicate their respective best-fit points (the latter two coincide). The $(m_{\tilde{q}}, m_{\tilde{g}})$ plane shows that the uncertainty

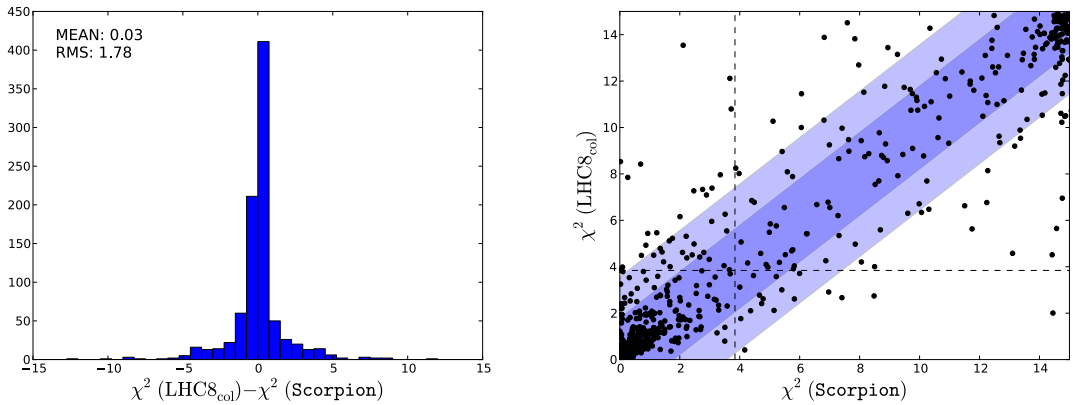

Figure 3.3: *Comparison of $\chi^2(LHC8_{col})$ with χ^2(**Scorpion**) for 1000 points that were randomly selected from our pMSSM10 sample. The left panel displays the distribution of the differences between the two calculations and the RMS on this distribution. In the right panel black points show $\chi^2(LHC8_{col})$ as a function of χ^2(**Scorpion**), blue bands indicate one and two times the RMS value that is quoted in the left panel, and dashed lines indicate $\chi^2 = 3.84$, which corresponds to 95% CL$_{\rm s}$.*

on $\chi^2(\text{LHC8}_{\text{col}})$ translates into an uncertainty on the mass lower limits of $m_{\tilde{q}}$ and $m_{\tilde{g}}$ of $\mathcal{O}(50$ GeV). The best-fit point changes location highlighting that there is no particular preference for $m_{\tilde{g}}$ or $m_{\tilde{q}}$ as we will see in chapter 5. The $(m_{\tilde{t}_1}, m_{\tilde{\chi}_1^0})$ plane shows nicely that the LHC8$_{\text{col}}$ constraint does not apply when $m_{\tilde{t}_1} - m_{\tilde{\chi}_1^0} < m_t$, although the LHC8$_{\text{EWK}}$ and LHC8$_{\text{stop}}$ constraints do apply as we discuss in section 3.4.4. The result of shifting $\chi^2(\text{LHC8}_{\text{col}})$ downwards is that a 68% CL region becomes available in this region, whereas only a few point are left for the nominal case. The compressed region also connects to the non-compressed region at 95% CL when $\chi^2(\text{LHC8}_{\text{col}})$ is shifted downwards. The 68% CL region for non-compressed spectra shows some small islands around $m_{\tilde{t}_1} \sim 800$ GeV when $\chi^2(\text{LHC8}_{\text{col}})$ is shifted downward. The upward shift has very little effect for both the 95% and 68% CL region.

3.4.3 Neutralinos, Charginos and Sleptons

As we showed above, the $\chi^2(\text{LHC8}_{\text{col}})$ function for gluinos and squarks is a good approximation for the "true" χ^2 that one would obtain from point-by-point reinterpretation. This highlights the relative universality of the mass limits irrespective of the decay chains. The situation is different for the production of $\tilde{\chi}_1^{\pm}$s, $\tilde{\chi}_2^0$s, and sleptons. For these sparticles the sensitivity of searches can depend strongly on the decay mode as can be seen

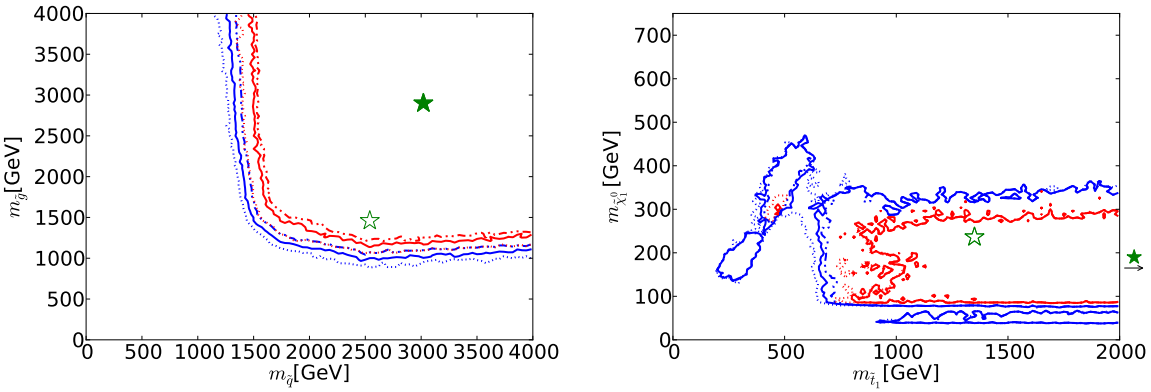

Figure 3.4: *The uncertainty associated with $\chi^2(LHC8_{col})$ in the $(m_{\tilde{q}}, m_{\tilde{g}})$ (left panel) and $(m_{\tilde{t}_1}, m_{\tilde{\chi}_1^0})$ (right panel) planes. The 95% (68%) CL contours are indicated with blue (red) lines for $\chi^2(LHC8_{col}) - \sigma^2_\chi$ (dotted), $\chi^2(LHC8_{col})$ (solid), and $\chi^2(LHC8_{col}) + \sigma^2_\chi$ (dashed-dotted). Empty and filled stars indicate their respective best-fit points (the latter two coincide).*

in Fig. 3.5 [157] where contours indicate the masses that are excluded at 95% CL by various ATLAS searches for leptons + $\not{E}_T$ [153, 154, 158] in various simplified model spectra (SMS) interpretations. For example, the associated $\tilde{\chi}_1^\pm \tilde{\chi}_2^0$ production at masses $m_{\tilde{\chi}_1^\pm} \simeq m_{\tilde{\chi}_2^0} \lesssim 700$ GeV and $m_{\tilde{\chi}_1^0} \lesssim 300$ GeV is excluded when they directly decay into on-shell selectrons or smuons (bordeaux red contour), whereas the decay via staus is only excluded for $m_{\tilde{\chi}_1^\pm} \simeq m_{\tilde{\chi}_2^0} \lesssim 400$ GeV and $m_{\tilde{\chi}_1^0} \lesssim 100$ GeV. Likewise the decay of $\tilde{\chi}_1^\pm \tilde{\chi}_2^0$ via WZ (green contour) is excluded at $m_{\tilde{\chi}_1^\pm} \simeq m_{\tilde{\chi}_2^0} \lesssim 400$ GeV for $m_{\tilde{\chi}_1^0} \lesssim 150$ GeV, whereas the decay via Wh is less constrained. Therefore we adopt an approach that does take into account information about the decay chains.

The aim of this approach is to approximate the "true" χ^2 that would be obtained from point-by-point reinterpretation using the ATLAS searches for $2l$+$\not{E}_T$ ($l = e, \mu$) [153] and $3L$+$\not{E}_T$ ($L = e, \mu, \tau$) [154] as implemented in `Atom`, cf. Table 3.6. In our procedure we constrain each decay mode according to the 95% CL exclusion contours from corresponding SMS interpretations. The use of simplified model spectra is justified by the observation that the mass hierarchy between the electroweakly produced sparticles is only dependent on their respective masses. That is, squarks and gluinos at similar masses are much more constrained due to their much larger production cross-section. The only exception is if the lightest stop is in the compressed region, a case that we treat separately as described in

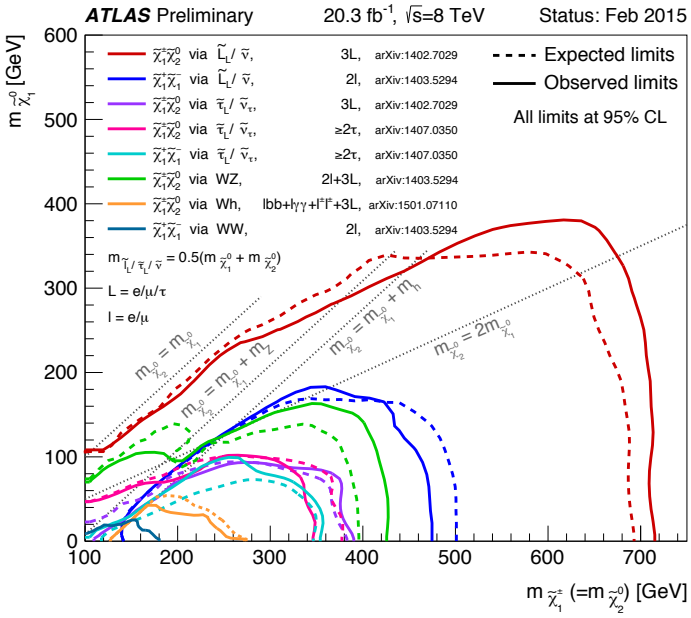

Figure 3.5: *ATLAS summary plot [157] of searches for neutralinos and charginos. Contours indicate the mass regions that are excluded at 95% CL by various ATLAS searches for leptons + $\not{E}_T$ [153, 154, 158] in various simplified model interpretations.*

section 3.4.4. For each decay mode a χ^2 contribution is calculated as

$$\chi^2_{\text{SMS}} = \min_{l,r} \left[15 \cdot B \cdot \frac{1}{e^{(d_{l,r}-\mu_{l,r})/\sigma_{l,r}} + 1} \right], \tag{3.9}$$

where

- the subscripts l, r indicate the 95% CL exclusion contour in the SMS interpretation to the left and right (in the horizontal direction, e.g. $m_{\tilde{\chi}_1^\pm} \simeq m_{\tilde{\chi}_2^0}$ or $m_{\tilde{\ell}}$) of the point on the contour with the largest value of $m_{\tilde{\chi}_1^0}$,
- B is the branching ratio of the decay mode, which is calculated using `SDECAY-1.3b` [159],
- d is the distance in GeV to the contour, and
- μ and σ control the fall-off of the χ^2 function in order to mimic the experimental uncertainty bands (and are in general functions of $m_{\tilde{\chi}_1^0}$).

We note that if one sets $\mu = -\sigma$, then $\chi^2_{\text{SMS}}(d = 0) \approx 4$, so that the exclusion on the contour corresponds approximately to the 95% CL_s. Finally, to avoid an unphysically slow

fall-off outside the 95% CL exclusion region we set $\sigma = 50$ GeV and adjust d accordingly if $\sigma > 50$ GeV and $d - \mu > \sigma$ (and hence $\chi^2_{\rm SMS} \lesssim 4$).

To illustrate the usage of Eq. 3.9 we depict in Fig. 3.6 the $\chi^2_{\rm SMS}/B$ function for the SMS interpretation of the ATLAS search for $3L + \not{E}_T$ ($L = e, \mu, \tau$) [154] that assumes associated $\tilde{\chi}_1^\pm \tilde{\chi}_2^0$ production with decays via selectrons, smuon and sneutrinos $\tilde{\ell}_L/\tilde{\nu}$ [154]. This $\chi^2_{\rm SMS}/B$ is used to constrain the $\tilde{\chi}_1^\pm \to \nu_\ell \tilde{\ell}_L(\ell\tilde{\nu}_\ell)/\tilde{\chi}_2^0 \to \ell\tilde{\ell}_L(\nu_\ell\tilde{\nu}_\ell)$ decay modes. In the left panel $\chi^2_{\rm SMS}/B$ is shown for a fixed value of $m_{\tilde{\chi}_1^0} = 300$ GeV where the green (blue) line corresponds to d_l, μ_l, σ_l (d_r, μ_r, σ_r), whereas vertical dashed lines indicate the position of the contour. Note that the χ^2 fall-off to the left is sharp and models the drop in acceptance of the search for small mass splittings $m_{\tilde{\ell}} - m_{\tilde{\chi}_1^0}$, whereas the fall-off is milder towards the right as to model the cross-section dependence. The right panel shows the same $\chi^2_{\rm SMS}/B$ (in colour) as a function of $m_{\tilde{\chi}_1^\pm} \simeq m_{\tilde{\chi}_2^0}$ and $m_{\tilde{\chi}_1^0}$, as well as the 95% CL exclusion contour [154] (blue line). Also note that we apply no constraint for $m_{\tilde{\chi}_1^0} \gtrsim 380$ GeV, the highest value on the 95% CL exclusion contour.

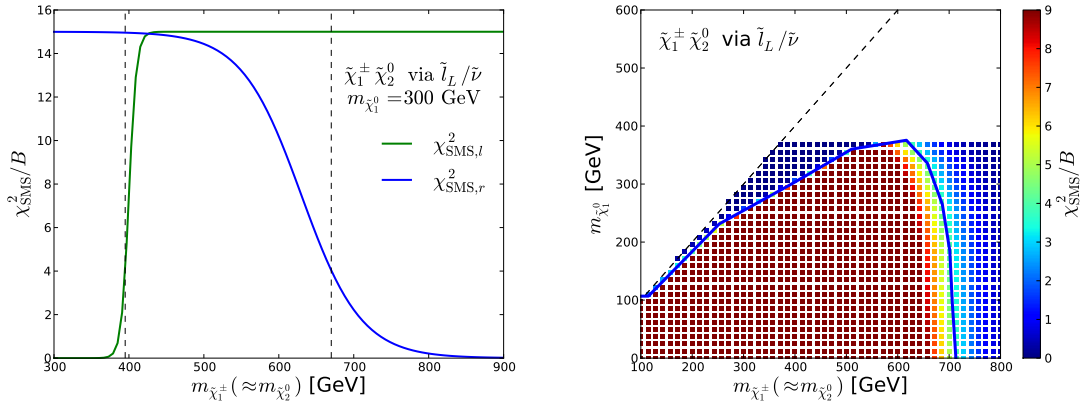

Figure 3.6: *Illustration of $\chi^2_{\rm SMS}/B$ as described in Eq. 3.9 for the SMS interpretation of associated $\tilde{\chi}_1^\pm \tilde{\chi}_2^0$ production decaying via $\tilde{\ell}_L/\tilde{\nu}$. The left panel shows $\chi^2_{\rm SMS}/B$ for a fixed value of $m_{\tilde{\chi}_1^0} = 300$ GeV and the green (blue) line corresponds to d_l, μ_l, σ_l, (d_r, μ_r, σ_r), whereas vertical dashed lines indicate the position of the contour. The right panel shows the same $\chi^2_{\rm SMS}/B$ (in colour) as a function of $m_{\tilde{\chi}_1^\pm} \simeq m_{\tilde{\chi}_2^0}$ and $m_{\tilde{\chi}_1^0}$, as well as the 95% CL exclusion contour [154] (blue line).*

Table 3.7 summarises the decay modes that we constrain, the respective SMS 95% CL exclusion contours that we use, as well as the associated values of $\mu_{l,r}$ and $\sigma_{l,r}$. In order to establish $\chi^2(\text{LHC8}_{\rm EWK})$, we tuned the $\mu_{l,r}$ and $\sigma_{l,r}$ parameters for each SMS interpretation in order to convincingly reproduce the point-by-point evaluation of $\chi^2(\texttt{Atom})$

for representative points from our sample. As we described above, the large value of $\sigma_r = 300$ GeV for the limit of $\tilde{\chi}_1^\pm \tilde{\chi}_2^0$ decaying via WZ is replaced with $\sigma_r = 50$ GeV (and d_r is adjusted accordingly) when $d_r - \mu_r > \sigma_r$ (and hence $\chi^2_{\rm SMS} \lesssim 4$). We have created our own 95% CL exclusion contour for the pair-production of selectrons and smuons. This is motivated by the enhanced production cross-section that is a result of nearly degenerate right- and left-handed sleptons in the pMSSM10. Also note that the (left-handed) sleptons may decay via $\tilde{\chi}_2^0$ or $\tilde{\chi}_1^\pm$. As we will see in chapter 5, $\tilde{\chi}_1^\pm$ coannihilation plays an important role in the pMSSM10 so that in many cases the chargino is almost degenerate with the LSP and the left-handed sleptons decay via $\tilde{\chi}_2^0$ and $\tilde{\chi}_1^\pm$. We denote the sum over the contributions as $\chi^2(\text{LHC8}_{\rm EWK})$.

Decay mode	SMS Contour	(μ_l, σ_l) [GeV]	(μ_r, σ_r) [GeV]
$\tilde{\chi}_1^\pm \to \nu_\ell \tilde{\ell}_L (\ell \tilde{\nu}_\ell)$ $\tilde{\chi}_2^0 \to \ell \tilde{\ell}_L (\nu_\ell \tilde{\nu}_\ell)$	$\tilde{\chi}_1^\pm \tilde{\chi}_2^0$ via $\tilde{\ell}/\tilde{\nu}_\ell$ Fig. 7(a) in Ref. [154]	(-5, 5)	(-40, 40)
$\tilde{\chi}_1^\pm \to W \tilde{\chi}_1^0$ $\tilde{\chi}_2^0 \to Z \tilde{\chi}_1^0$	$\tilde{\chi}_1^\pm \tilde{\chi}_2^0$ via WZ Fig. 7(b) in Ref. [153]	(-20, 20)	(-300, 300)
$\tilde{\ell}_R \to \ell \tilde{\chi}_1^0$ $\tilde{\ell}_L \to \ell \tilde{\chi}_{1,2}^0 (\nu_\ell \tilde{\chi}_1^\pm)$	Created using `Atom`	(-20, 10)	(-40, 30)

Table 3.7: *Decay modes and the 95% CL contours from SMS interpretations used to constrain them according to Eq. 3.9. For each contour the values for $\mu_{l,r}$ and $\sigma_{l,r}$ listed.*

We now compare $\chi^2(\text{LHC8}_{\rm EWK})$ with $\chi^2(\texttt{Atom})$. To get a good representation of decay chains we divided the $(m_{\tilde{\chi}_1^\pm} \simeq m_{\tilde{\chi}_2^0}, m_{\tilde{\chi}_1^0})$ in 100×100 bins and randomly selected one point in each bin. From the resulting points we randomly selected 1000 points to make the comparison. Fig. 3.7 displays the scatter plot for $\chi^2(\texttt{Atom})$ (top left) and $\chi^2(\text{LHC8}_{\rm EWK})$ (top right) in the $(m_{\tilde{\chi}_1^\pm} \simeq m_{\tilde{\chi}_2^0}, m_{\tilde{\chi}_1^0})$ plane, the distribution of the differences between $\chi^2(\texttt{Atom})$ and $\chi^2(\text{LHC8}_{\rm EWK})$ (bottom left), as well as $\chi^2(\text{LHC8}_{\rm EWK})$ as a function of $\chi^2(\texttt{Atom})$ (bottom right). The $\chi^2(\texttt{Atom})$ scatter plot highlights the strong dependence of the exclusion on the decay chain by featuring non-excluded points that are neighbouring excluded points, e.g. at $m_{\tilde{\chi}_1^\pm} \simeq m_{\tilde{\chi}_2^0} \sim 300$ GeV and $m_{\tilde{\chi}_1^0} \sim 50$ GeV. If we compare the scatter plots of $\chi^2(\texttt{Atom})$ with that of $\chi^2(\text{LHC8}_{\rm EWK})$ we see that most of these features are reproduced correctly by $\chi^2(\text{LHC8}_{\rm EWK})$. From the lower panels we see that the differences are centred around 0.62 and have an RMS of $\sigma_{\chi^2} = 2.31$.

We assess how σ_{χ^2} propagates into uncertainties on the 68% CL and 95% CL contours in the same way as for the $\text{LHC8}_{\rm col}$ constraint: we calculate σ_{χ^2} in bins of $\chi^2(\text{LHC8}_{\rm EWK})$

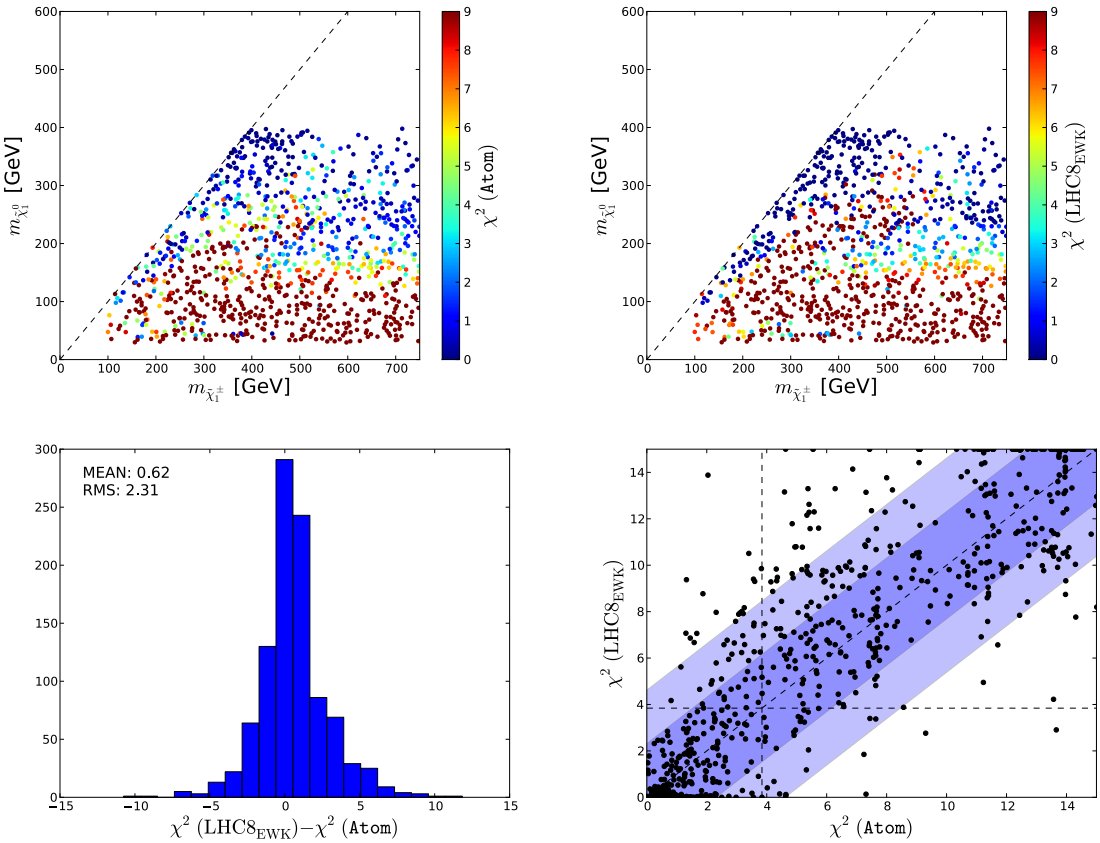

Figure 3.7: *Comparison between $\chi^2(LHC8_{EWK})$ and $\chi^2(\texttt{Atom})$ for 1000 semi-randomly selected points (see text). The four panels display the scatter plot for $\chi^2(\texttt{Atom})$ (top left) and $\chi^2(LHC8_{EWK})$ (top right) in the $(m_{\tilde{\chi}_2^0} \approx m_{\tilde{\chi}_1^\pm}, m_{\tilde{\chi}_1^0})$ plane, the distribution of the differences between $\chi^2(\texttt{Atom})$ and $\chi^2(LHC8_{EWK})$ (bottom left), as well as $\chi^2(LHC8_{EWK})$ as a function of $\chi^2(\texttt{Atom})$ (bottom right).*

and apply $\chi^2(\text{LHC8}_{\text{EWK}})$ to our sample shifted upwards and downwards by this binned σ_{χ^2}. The left [right] panel in Fig. 3.8 shows the 68% (95%) CL contours in red (blue) in the $(m_{\tilde{\chi}_1^\pm}, m_{\tilde{\chi}_1^0})$ $[(m_{\tilde{\mu}_R}, m_{\tilde{\chi}_1^0})]$ plane obtained by applying $\chi^2(\text{LHC8}_{\text{EWK}}) - \sigma_{\chi^2}$ (dotted), $\chi^2(\text{LHC8}_{\text{EWK}})$ (solid), and $\chi^2(\text{LHC8}_{\text{EWK}}) + \sigma_{\chi^2}$ (dashed-dotted). Filled and stars indicate their respective best-fit points (the first two coincide). We see that the contours in the $(m_{\tilde{\mu}_R}, m_{\tilde{\chi}_1^0})$ are stable and the up- and downward shifts translate into an uncertainty of ~ 50 GeV on the mass lower limits. In the $(m_{\tilde{\chi}_1^\pm}, m_{\tilde{\chi}_1^0})$ plane we see that the downward shift enlarges the 95% CL region between 400 GeV $\lesssim m_{\tilde{\chi}_1^\pm} \lesssim 750$ GeV and $m_{\tilde{\chi}_1^0} \lesssim 300$ GeV, and renders a low mass island at $m_{\tilde{\chi}_1^\pm} \lesssim 350$ GeV and $m_{\tilde{\chi}_1^0} \sim 50$ GeV preferred at the

68% CL. The upward shift has a small impact on the 95% CL contour. The 68% CL region located at small mass differences $m_{\tilde{\chi}_1^\pm} - m_{\tilde{\chi}_1^0}$ is stable under the up- and downward shift of $\chi^2(\text{LHC8}_{\text{EWK}})$.

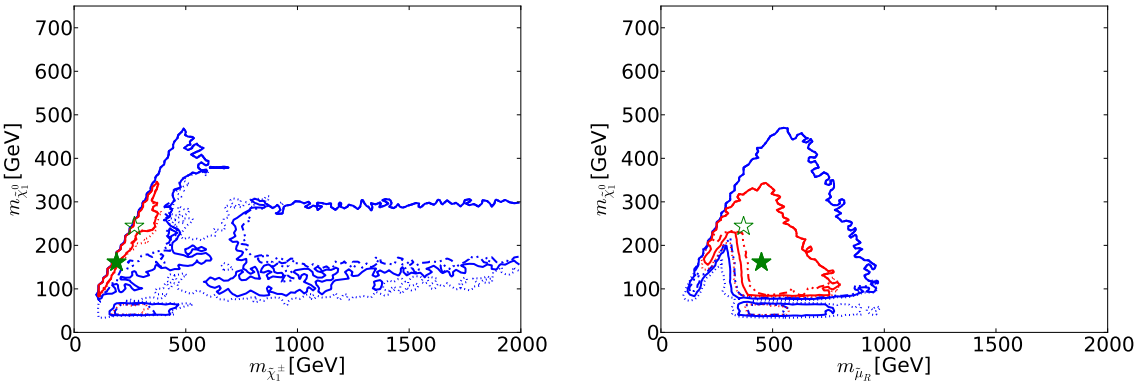

Figure 3.8: *The uncertainty associated with $\chi^2(LHC8_{EWK})$ in the $(m_{\tilde{\chi}_1^\pm}, m_{\tilde{\chi}_1^0})$ (left panel) and $(m_{\tilde{\mu}_R}, m_{\tilde{\chi}_1^0})$ (right panel) planes. The 95% (68%) CL contours are indicated with blue (red) lines for $\chi^2(LHC8_{EWK}) - \sigma_\chi^2$ (dotted), $\chi^2(LHC8_{EWK})$ (solid), and $\chi^2(LHC8_{EWK}) + \sigma_\chi^2$ (dashed-dotted). Filled and stars indicate their respective best-fit points (the first two coincide).*

3.4.4 Compressed-Stop Spectra

We now discuss the case of compressed-stop spectra for which $m_{\tilde{t}_1} - m_{\tilde{\chi}_1^0} < m_t$. Both ATLAS and CMS have placed special emphasis on this scenario, which is experimentally challenging and where the on-shell decay into the top quark is kinematically forbidden. To illustrate this we turn to the ATLAS summary plot in Fig. 3.9 [160], in which dashed lines indicate the separate kinematic regions: 1) $m_{\tilde{t}_1} - m_{\tilde{\chi}_1^0} < m_b + M_W$ where $\tilde{t}_1 \to c\tilde{\chi}_1^0$ and $\tilde{t}_1 \to bff'\tilde{\chi}_1^0$ are allowed; 2) $m_b + M_W < m_{\tilde{t}_1} - m_{\tilde{\chi}_1^0} < m_t$ where $\tilde{t}_1 \to bW\tilde{\chi}_1^0$ is allowed; 3) $m_{\tilde{t}_1} - m_{\tilde{\chi}_1^0} > m_t$ where the stop can decay into an on-shell top. Note that the latter region is covered by the LHC8_{col} constraint, cf. the bottom left panel of Fig. 3.2. On the other hand, the case where $m_{\tilde{t}_1} - m_{\tilde{\chi}_1^0} < m_t$ is explicitly taken out of the LHC8_{col} by assuming zero production cross-section for the cross-section averaged mass of the third-generation squarks. We treat this compressed-stop case separately, using an analogous approach to our treatment of the electroweakly produced sparticles.

As we will see in chapter 5, the fit has no particular preference for light stops, unlike light sleptons, which are preferred in order to fulfil $(g-2)_\mu$ and light charginos needed

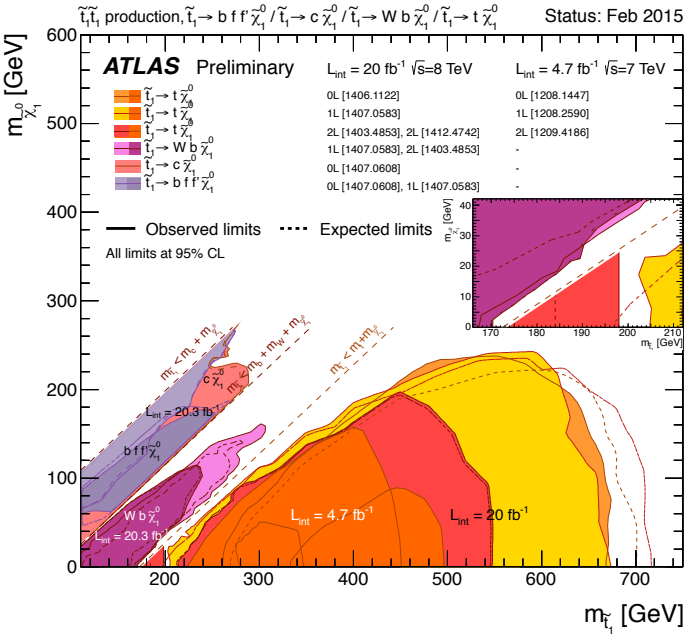

Figure 3.9: *ATLAS summary plot of stop searches [160].*

for $\tilde{\chi}_1^\pm$ coannihilation. In this sense the compressed-stop region is a more limited "corner" of the parameter space. In this "corner" the presence of the light stop introduces more possible mass hierarchies compared to the case of light sleptons and charginos only. To illustrate the interplay between the sparticles we display in Fig. 3.10 the dominant decay modes that have a branching ratio greater than 50% for 1000 points that were selected in the $(m_{\tilde{t}_1}, m_{\tilde{\chi}_1^0})$, analogously to the way we selected points for Fig. 3.7.

We see that for the majority of points the $\tilde{t}_1 \to b\tilde{\chi}_1^\pm$ decay mode (shown in yellow) dominates with this decay mode being allowed over the full kinematic range. For most of these points the $\tilde{\chi}_1^\pm$ and $\tilde{\chi}_2^0$ have a nearly degenerate mass with the lightest neutralino. We therefore apply the limit that was obtained by the ATLAS search for $2b$ + jets + $\not{E}_T$ [149] in the SMS interpretation of stop decaying via the chargino where $m_{\tilde{\chi}_1^\pm} - m_{\tilde{\chi}_1^0} = 5$ GeV is assumed. We found that it is appropriate to apply this limit for the model points with $m_{\tilde{\chi}_1^\pm} - m_{\tilde{\chi}_1^0} < 30$ GeV.

If $m_{\tilde{t}_1} - m_{\tilde{\chi}_1^0} > M_W + m_b$, the 3-body decay mode $\tilde{t}_1 \to bW\tilde{\chi}_1^0$ can dominate (shown as purple dots in Fig. 3.10). For this decay mode we implement the simplified model limit presented for $M_W + m_b < m_{\tilde{t}_1} - m_{\tilde{\chi}_1^0} < m_t$ in Fig. 15 of the ATLAS single-lepton analysis [151].

In the $m_{\tilde{t}_1} - m_{\tilde{\chi}_1^0} < M_W + m_b$ region, the decays $\tilde{t}_1 \to c\tilde{\chi}_1^0$ (red dots in Fig. 3.10) and

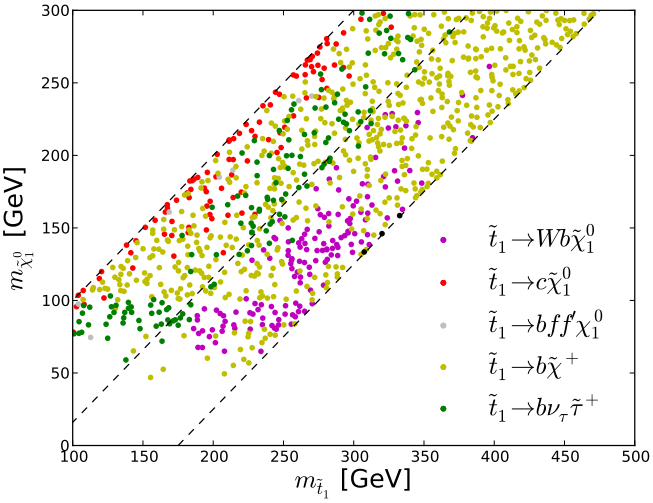

Figure 3.10: *Dominant decay chains for 1000 randomly selected points in the compressed-stop region.*

$\tilde{t}_1 \to bff'\tilde{\chi}_1^0$ (grey dots) can be the dominant stop decay modes. The $\tilde{t}_1 \to b\nu_\tau\tilde{\tau}_1$ mode (green dots in Fig. 3.10) may also dominate stop decay in this region, as well as in the $m_{\tilde{t}_1} - m_{\tilde{\chi}_1^0} \gtrsim M_W + m_b$ region. In this very compressed region we found that the most constraining (and implemented) search is the hadronic M_{T2} search by CMS [130]. Given our aim to approximate the point-by-point reinterpretation of ATLAS and CMS searches, and the absence of an interpretation for the $\tilde{t}_1 \to b\nu_\tau\tilde{\tau}_1$ mode, we derived our own SMS interpretations for the $\tilde{t}_1 \to c\tilde{\chi}_1^0$ and $\tilde{t}_1 \to b\nu_\tau\tilde{\tau}_1$ modes respectively, using this M_{T2} search. For the latter we assumed a mass splitting $m_{\tilde{\tau}_1} - m_{\tilde{\chi}_1^0} < 40$ GeV. We note in passing that the $\tilde{t}_1 \to bff'\tilde{\chi}_1^0$ turned out to have negligible impact on our study.

Table 3.8 summarises our implementation of the SMS limits, which are applied using Eq. 3.9, for the compressed-stop region. Note that this time $\mu_{l,r}$ and $\sigma_{l,r}$ depend on $m_{\tilde{\chi}_1^0}$ for the $\tilde{t}_1 \to b\tilde{\chi}_1^\pm$ and $\tilde{t}_1 \to bW\tilde{\chi}_1^0$ decay modes. In these cases multiple values of $\mu_{l,r}$ and $\sigma_{l,r}$ are given for different values of $m_{\tilde{\chi}_1^0}$. For intermediate values of $m_{\tilde{\chi}_1^0}$ the parameters are obtained by linear interpolation, whereas they are constant elsewhere. We denote the sum of these limits as $\chi^2(\mathrm{LHC8}_{\mathrm{stop}})$.

To tune and validate the implementation of the stop searches in Table 3.8 we calculated the "true" χ^2 using a hybrid between `Atom` and `Scorpion`. This hybrid was constructed to reflect that on the one hand the M_{T2} search of CMS (implemented in `Scorpion`) has the best sensitivity for the $\tilde{t}_1 \to c\tilde{\chi}_1^0$ and $\tilde{t}_1 \to b\nu_\tau\tilde{\tau}_1$ decay modes, whereas on the other

Decay	Contour	$m_{\tilde{\chi}_1^0}$ [GeV]	(μ_l, σ_l) [GeV]	(μ_r, σ_r) [GeV]	Condition/Remark
$\tilde{t}_1 \to b\tilde{\chi}_1^\pm$	Fig. 6(c) in Ref. [149]	210	(10, 20)	(-50, 50)	$m_{\tilde{\chi}_1^\pm} - m_{\tilde{\chi}_1^0} < 30$ GeV
		300	(-250, 200)	(-200, 200)	
$\tilde{t}_1 \to bW\tilde{\chi}_1^0$	Fig. 15 in Ref. [151]	100	(-20,50)	(-70, 50)	$M_W < m_{\tilde{t}_1} - m_{\tilde{\chi}_1^0} < m_t$
		150	(-50, 50)	(-100,50)	
$\tilde{t}_1 \to b\nu_\tau\tilde{\tau}_1$	Created using `Scorpion`	-	(-50, 50)	(-20, 50)	Based on [130], assuming $m_{\tilde{\tau}_1} - m_{\tilde{\chi}_1^0} \lesssim 40$ GeV
$\tilde{t}_1 \to c\tilde{\chi}_1^0$	Created using `Scorpion`	-	(-20, 20)	(-20, 20)	Based on [130]

Table 3.8: *Simplified model interpretations used to construct $\chi^2(LHC8_{stop})$. In some cases the values of $\mu_{l,r}$ and $\sigma_{l,r}$ depend on $m_{\tilde{\chi}_1^0}$. Whenever multiple values of these parameters are specified for different values of $m_{\tilde{\chi}_1^0}$, the parameters for intermediate values of $m_{\tilde{\chi}_1^0}$ are obtained by linear interpolation, and constant elsewhere.*

hand all the relevant searches for $\tilde{t}_1 \to b\tilde{\chi}_1^\pm$ and $\tilde{t}_1 \to bW\tilde{\chi}_1^0$, as well as the electroweakly produced sleptons and electroweakinos are available in `Atom`. Therefore we define

$$\chi^2(\texttt{Atom and Scorpion}) = \begin{cases} \max(\chi^2(\texttt{Atom}), \chi^2(\texttt{Scorpion})), \\ \qquad \text{if } \mathrm{BR}(\tilde{t}_1 \to c\tilde{\chi}_1^0) + \mathrm{BR}(\tilde{t}_1 \to b\nu_\tau\tilde{\tau}_1) > 50\% \\ \chi^2(\texttt{Atom}) \qquad \text{otherwise.} \end{cases} \tag{3.10}$$

In Fig. 3.11 we compare χ^2(`Atom` and `Scorpion`) (left panel) with $\chi^2(\mathrm{LHC8_{EWK}}) + \chi^2(\mathrm{LHC8_{stop}})$ (right) for the subset of points in Fig. 3.10 with $\chi^2(\mathrm{LHC8_{EWK}}) < 2$. We see that very good qualitative agreement is achieved between the two approaches despite the complexity of the spectra, with light stops, sleptons, and charginos and neutralinos. In Fig. 3.12 we compare the agreement of $\chi^2(\mathrm{LHC8_{EWK}}) + \chi^2(\mathrm{LHC8_{stop}})$ with the point-by-point evaluated χ^2(`Atom` and `Scorpion`) for all points in Fig. 3.10. The left panel shows the distribution of the differences, which are centred around 0.57 and have and RMS of $\sigma_{\chi^2} = 3.15$. In the right panel we display $\chi^2(\mathrm{LHC8_{EWK}}) + \chi^2(\mathrm{LHC8_{stop}})$ as a function of χ^2(`Atom` and `Scorpion`) and the 1 (2) σ_{χ^2} band is shaded dark (light) blue, whereas horizontal and vertical dashed lines indicate 95% $\mathrm{CL_s}$. The difference between $\chi^2(\mathrm{LHC8_{EWK}}) + \chi^2(\mathrm{LHC8_{stop}})$ and χ^2(`Atom` and `Scorpion`) are generally somewhat larger than in the case that only the $\chi^2(\mathrm{LHC8_{EWK}})$ constraint applies. This is expected, since the complexity of the spectra is increased.

Finally, we assess again quantitatively how the 68% and 95% CL regions would vary if we shifted $\chi^2(\mathrm{LHC8_{EWK}}) + \chi^2(\mathrm{LHC8_{stop}})$ up and down by σ_{χ^2} (in bins of $\chi^2(\mathrm{LHC8_{EWK}}) + \chi^2(\mathrm{LHC8_{stop}})$) as is shown in Fig. 3.13. The effect is that a larger island at $m_{\tilde{\chi}_1^0} \lesssim 220$ GeV

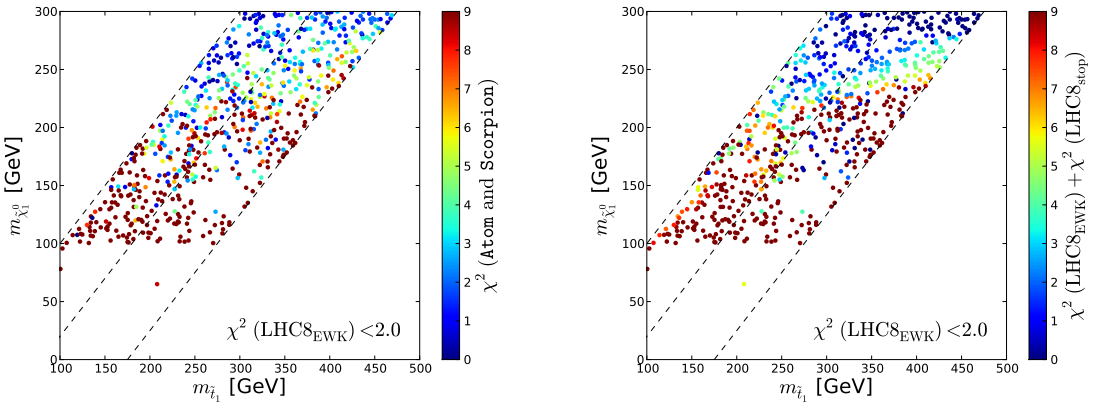

Figure 3.11: *Comparison between* χ^2(`Atom` *and* `Scorpion`) *(left panel) and* $\chi^2(LHC8_{stop}) + \chi^2(LHC8_{EWK})$ *(right panel) for the subset of points in Fig. 3.10 with* $\chi^2(LHC8_{EWK}) < 2$.

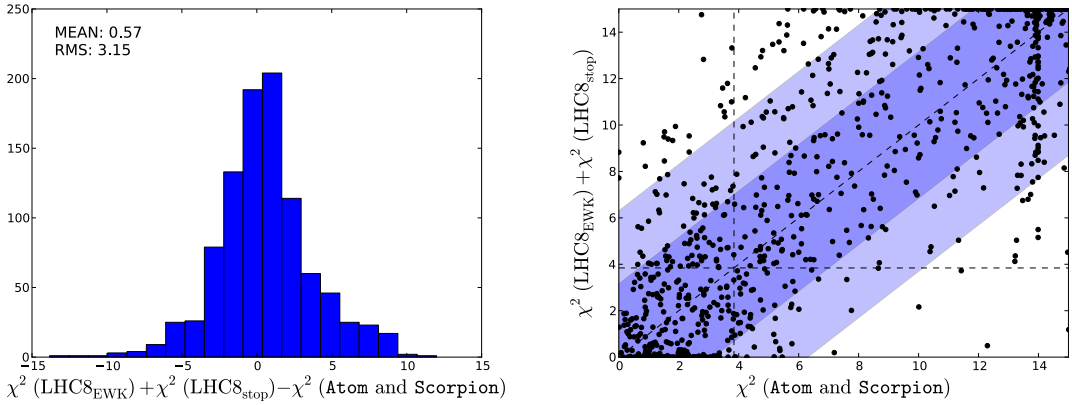

Figure 3.12: *Comparison between* χ^2(`Atom` *and* `Scorpion`) *and* $\chi^2(LHC8_{EWK}) + \chi^2(LHC8_{stop})$. *The left panel shows the differences, whereas the right panel shows* $\chi^2(LHC8_{EWK}) + \chi^2(LHC8_{stop})$ *as a function of* χ^2(`Atom` *and* `Scorpion`).

becomes available at the 95% CL in the case that we shift the $\chi^2(\text{LHC8}_{\text{EWK}})+\chi^2(\text{LHC8}_{\text{stop}})$ down with one σ_{χ^2}, which disappears when $\chi^2(\text{LHC8}_{\text{EWK}})+\chi^2(\text{LHC8}_{\text{stop}})$ is shifted upwards. The 95% CL regions at $m_{\tilde{\chi}_1^0} \gtrsim 250$ GeV on the other hand is more stable under the up- and downward shift.

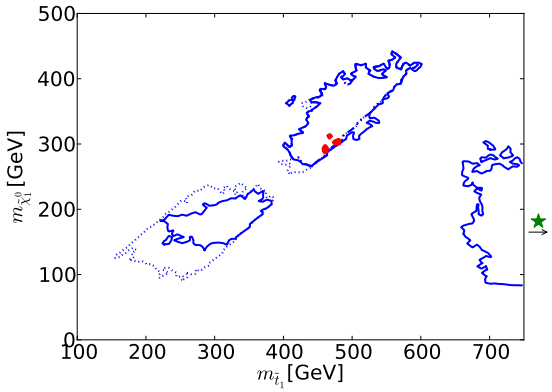

Figure 3.13: *The uncertainty associated with* $\chi^2(LHC8_{EWK}) + \chi^2(LHC8_{stop})$ *in the* $(m_{\tilde{t}_1}, m_{\tilde{\chi}_1^0})$ *plane. The 95% (68%) CL contours are indicated with blue (red) lines for* $\chi^2(LHC8_{EWK}) + \chi^2(LHC8_{stop}) - \sigma_\chi^2$ *(dotted),* $\chi^2(LHC8_{EWK}) + \chi^2(LHC8_{stop})$ *(solid), and* $\chi^2(LHC8_{EWK}) + \chi^2(LHC8_{stop}) + \sigma_\chi^2$ *(dashed-dotted). An arrow indicates the positions of the best-fit points, that all overlap.*

3.4.5 Summary

We now summarise how we implement the constraint coming from searches for SUSY particles at the LHC using the full Run 1 data set in the context of the pMSSM10. We argued that it is desirable to have a computationally economic alternative for point-by-point reinterpretation of $\mathcal{O}(10^9)$ model points with representative SUSY searches, such as implemented in `Scorpion` (cf. Table 3.5) and `Atom` (cf. Table 3.6).

In section 3.4.2 we discussed and validated how we parametrise the constraint on production of first-, second- and third-generation squarks and gluinos using $\chi^2(\text{LHC8}_{\text{col}})$. Following the approach outlined in Ref. [129] we constructed a universal χ^2 function that only depends on $m_{\tilde{\chi}_1^0}$, $m_{\tilde{g}}$, $m_{\tilde{q}_{12}}$, and $m_{\tilde{q}_3}$ (the production cross-section weighted average of third generation squark masses) and not on the decay modes in the spectrum. Such an approach yields an uncertainty of $\mathcal{O}(50$ GeV) on mass lower limits.

We also discussed and validated how we constrain the production of $\tilde{\chi}_1^\pm$, $\tilde{\chi}_2^0$ and slepton production using their respective decay chains in section 3.4.3. An appropriate χ^2 is assigned according to Eq. 3.9 and using the 95% CL exclusion contours and $\mu_{l,r}$ and $\sigma_{l,r}$ listed in Table 3.7. We refer to the sum of these χ^2 contributions as $\chi^2(\text{LHC8}_{\text{EWK}})$.

In the case of compressed-stop spectra, where $m_{\tilde{t}_1} - m_{\tilde{\chi}_1^0} < m_t$, the lighter stop is treated separately from the LHC8_{col} constraint by 1) calculating $m_{\tilde{q}_3}$ assuming negligible production cross-section for the lighter stop and 2) assigning a χ^2 to each decay mode

according to Eq. 3.9 using the 95% CL exclusion contours and $\mu_{l,r}$ and $\sigma_{l,r}$ listed in Table 3.8. We refer to the sum over the contributions in the latter step as $\chi^2(\text{LHC8}_{\text{stop}})$, which we detailed and validated in section 3.4.4.

We will refer to the collective of $\chi^2(\text{LHC8}_{\text{col}}) + \chi^2(\text{LHC8}_{\text{EWK}}) + \chi^2(\text{LHC8}_{\text{stop}})$ as the LHC8 constraints. These constraints serve as the approximation of the point-by-point reinterpretation using `Atom` and `Scorpion`, which implement a representative set of the searches at the LHC, cf. Tables 3.5 and 3.6.

3.5 Sampling Algorithm and Strategy

We now return to our aim of establishing confidence intervals for parameters and observables. As pointed out in section 3.1, confidence intervals (regions) can be defined according to the profile likelihood for the parameter(s) of interest θ as defined in Eq. 3.4. This defines the challenge to sufficiently sample the parameter space in regions where the "true" likelihood function lies within the required acceptance region, namely $\Delta\chi^2 < \Delta\chi^2(\alpha, n)$ (cf. Table 3.1). It is specifically desirable to sample the parameter space in all local maximum-likelihood regions. To this end we use the `MultiNest` algorithm [61–63] as implemented in the `MultiNest` $-$ `2.18` package. This algorithm was originally designed for Bayesian inference but was also shown to be an appropriate and computationally efficient tool for establishing profile likelihood functions [55]. In order to motivate our usage we give a brief overview of how the algorithm works.

The `MultiNest` algorithm keeps a list of N "active" parameter points in the n-dimensional unit cube. Unit cube parameters are transformed to "physical parameters" according to user-defined priors. The priors, e.g. flat, Gaussian, or soft flat (see below) define the scan ranges. The physical parameters are the inputs to the user-defined likelihood function.

The initial step of the algorithm is to uniformly sample N parameter points in the unit cube and evaluate the corresponding likelihood values. After the initial step the algorithm performs iterations in which the active point with the lowest likelihood is replaced with a point with higher likelihood. The procedure of finding a point with higher likelihood is based on so-called ellipsoidal nested sampling in which 1) ellipsoidal bounds are constructed (in the unit cube) based on clustering of the N active points, 2) one ellipsoid is randomly selected, 3) this ellipsoid is sampled until a point is found that has a higher likelihood than the lowest of the active points. The iterations continue until a stopping criterion is

reached, which can be controlled with the "tolerance".

The construction of the ellipsoids is at the heart of the `MultiNest` algorithm and is the main driver for its robustness and efficiency. Moreover, it was specifically designed to deal well with multiple local maxima, as well as elongated curving degeneracies. An important property of the `MultiNest` algorithm is that once a point with high likelihood makes it into the set of active N points, it forms a basin of attraction: one of the ellipsoidal bounds of step 1) will contain this point and therefore more points in its vicinity are sampled. This way even regions that have a small volume in the unit cube will be sampled eventually if at least one point from this region make it into the active points.

These properties lead to the way we configure the `MultiNest` algorithm for our fits of SUSY models. As shown in Ref. [55], reliable sampling of profile likelihood functions can be achieved by using a large number of active points, where e.g. $N = 20,000$ and a tolerance of 10^{-4} (as opposed to $N = 1,000$ and a tolerance of 0.5, which is suitable for Bayesian inference). However, with increasing N, the duration of the algorithm also increases. In order to avoid the longer duration, but extend the number of active points we use a different approach. We divide each scan range into segments. The "cross-product" of these segments then constitute boxes that span the full parameter space and we sample with `MultiNest` in every box with $N = 1000$. A scan is performed in every box. This way we have $n_{\text{boxes}} \cdot N$ active points. In order to avoid edge effects between two neighbouring parameter segments we introduce a smooth overlap by using "soft flat" priors. We define soft flat prior such that 80% is flat and lies within the nominal range of the segment, whereas 20% of the distribution lies outside the segment and is normally distributed as is shown if figure Fig. 3.14. We found that this approach is very efficient and enabled the exploration of 6- to 10-dimensional parameter spaces of the NUHM2 and pMSSM10 respectively.

3.5.1 Scan Ranges

To sample the parameter spaces of our supersymmetric models we need to define the ranges in which the input parameters are scanned. The chosen ranges of (soft SUSY breaking) mass parameters and trilinear couplings are generally motivated so as to cover the global χ^2 minimum whilst restricting the attention to mass scales that are relevant for the LHC. The range for $\tan\beta$ was chosen based on the requirement that Yukawa couplings y_t, y_b, y_τ remain perturbatively small, giving the approximate bounds $1.2 \lesssim \tan\beta \lesssim 65$ [68].

As pointed out in the previous section we partition the full parameter space into boxes

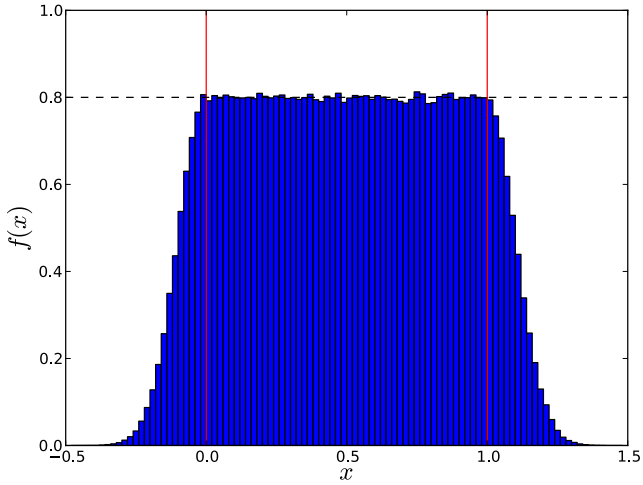

Figure 3.14: *Illustration of "soft flat" prior for which 80% is flat and lies within the nominal range of the segment ([0, 1] is displayed), whereas 20% of the distribution lies outside the nominal range and is normally distributed.*

defined by the cross-product of segmented parameters ranges. The ranges, the number of segments, and the resulting number of boxes that the we use in our scans of the CMSSM, NUHM1, NUHM2, and pMSSM10 are given in Table 3.9 to 3.12 respectively. Each of the resulting parameter segments is sampled using soft flat priors. Finally, we note that the nuisance SM parameters $m_t, \Delta\alpha^{(5)}_{\rm had}(M_Z), M_Z$ are sampled using Gaussian priors.

Parameter	Range	#Segments
m_0	(0, 6.7) TeV	5
$m_{1/2}$	(0, 4) TeV	3
A_0	(-5, 5) TeV	3
$\tan\beta$	(2 , 68)	3
#boxes		135

Table 3.9: *Sampling ranges and segment definitions in the CMSSM.*

3.6 The `MasterCode` Framework

The framework used to perform the global fits has been dubbed the `MasterCode` [34]. At the heart of the code are the three essential elements: 1) calculation of SUSY observables, 2)

Parameter	Range	#Segments
m_0	(-1.3, 4) TeV	4
m_H^2	(-50, 50) TeV^2	3
$m_{1/2}$	(0, 4) TeV	3
A_0	(-5, 5) TeV	2
$\tan\beta$	(2 , 68)	2
#boxes		144

Table 3.10: *Sampling ranges and segment definitions in the NUHM1.*

Parameter	Range	#Segments
m_0	(-1.3, 4) TeV	4
$m_{H_u}^2$	(-50, 50) TeV^2	3
$m_{H_d}^2$	(-50, 50) TeV^2	3
$m_{1/2}$	(0, 4) TeV	3
A_0	(-8, 8) TeV	1
$\tan\beta$	(2 , 68)	1
#boxes		108

Table 3.11: *Sampling ranges and segment definitions in the NUHM2.*

Parameter	Range	#Segments
M_1	(-1 , 1) TeV	2
M_2	(0 , 4) TeV	2
M_3	(-4 , 4) TeV	4
$m_{\tilde{q}}$	(0 , 4) TeV	2
$m_{\tilde{q}_3}$	(0 , 4) TeV	2
$m_{\tilde{\ell}}$	(0 , 2) TeV	1
M_A	(0 , 4) TeV	2
A	(-5 , 5) TeV	1
μ	(-5 , 5) TeV	1
$\tan\beta$	(1 , 60)	1
#boxes		128

Table 3.12: *Sampling ranges and segment definitions in the pMSSM10.*

calculation of the χ^2 as defined in Eq. 3.1 (or in fact any arbitrary function of observables) 3) the interface to an appropriate sampling algorithm. All three elements have been rewritten and extended to facilitate the analyses presented in Refs. [43, 44, 60] and in this

thesis. In previous sections of this chapter we have discussed in detail the calculation of the χ^2 function, as well as the `MultiNest` sampling algorithm. Therefore we conclude with a brief description of the calculation of SUSY observables.

The calculation of SUSY observables happens in three steps. First the full MSSM spectrum of masses, mixing matrices and couplings is calculated by `SOFTSUSY` [71], which runs RGEs for the CMSSM, NUHM1, NUHM2 or pMSSM10 input parameters.[8] The Higgs sector of this spectrum is then refined using calculations from `FeynHiggs`. The resulting spectrum serves as the input to the other codes that calculate observables as summarised in Table 3.13. Note that the constraints on Higgs signal-strengths, the $H/A \to \tau^+\tau^-$ decay and the calculation of decay tables have only been included in the analysis of the pMSSM10 [60].

Code	Reference	Observables
`SOFTSUSY-3.3.9`	[71]	SUSY spectrum
`FeynHiggs-2.10.0`	[75, 102–106, 111]	Higgs sector, $(g-2)_\mu$
`micrOMEGAs-3.2`	[79]	$\Omega_{\rm CDM}h^2$
`SSARD`	[84]	$\sigma_p^{\rm SI}$, $\Delta\sigma_p^{\rm SI}$
`SuFla`	[96, 97]	Flavour physics
`FeynWZ`	[77, 112]	M_W, Z-pole
`HiggsSignals-1.3.1`	[107, 108]	Constraints Higgs signal-strengths
`HiggsBounds-4.2.0`	[127]	Constraints $H/A \to \tau^+\tau^-$ decay
`SDECAY-1.3b`	[159]	Decay tables

Table 3.13: *Codes used to calculate SUSY observables in the* `MasterCode` *framework.*

3.7 Discussion

We pause here to compare our methodology with that of other groups that performed global fits of the CMSSM, NUHM1, and NUHM2 on the on hand, and pMSSMn models on the other hand, focussing on their latest results. The differences and similarities can be found in the statistical approach, the constraints that enter the likelihood function, and the sampling algorithm and strategy.

[8] Other models can easily be implemented.

3.7.1 The CMSSM, NUHM1, and NUHM2

In the following we compare the latest published results from `MasterCode` for the CMSSM and NUHM1 [43] (December 2013), and the NUHM2 [44] (August 2014) with Fittino [32] (April 2012), BayesFITS [48] (February 2013), and SuperBayes [56] (December 2012).

Statistical Interpretation

First we note that there is a difference in the statistical approach for establishing the unknown parameters of the model: frequentist or Bayesian. As described in section 3.1, a common frequentist approach for global fits is to establish confidence intervals and regions by providing profile likelihood functions. `MasterCode` and Fittino both followed this frequentist approach. The Bayesian approach is to provide credible intervals based on marginalised posterior probability distribution functions for a given prior, cf. section 38.4.1 in Ref. [17]. BayesFITS followed only the Bayesian approach, whereas SuperBayes provided both credible and confidence intervals and regions. We note that Bayesian credible intervals are subject to the choice of priors, whereas the frequentist confidence intervals are not.

Constraints

The constraints used by different groups are in general very similar. We compare them following the commonly used grouping into 'indirect constraints', 'cosmological and astrophysical constraints', and 'direct searches at collider experiments'. Note that our fits are the most up-to-date which is reflected in the publishing dates.

Indirect Constraints

All groups took into account electroweak precision observables, flavour physics observables, and $(g-2)_\mu$. However, there are differences between the particular choices. For example: all groups took into account M_W and $\sin\theta_{\text{eff}}$. `MasterCode` is the only group that took into account the other Z-pole observables listed in section 3.2.6. We will see that the χ^2 contribution of these Z-pole observables is indeed rather flat, which justifies that other groups have left them out.

For the flavour observables all groups considered the rare B meson decays $B_{s,d} \to \mu^+\mu^-$ $B \to X_s\gamma$ and $B \to \tau\nu_\tau$. Fittino and BayesFITS only took these into account. In addition, `MasterCode` took into account B mixing and K decays and mixing, whereas SuperBayes took into account D decays.

Finally, the $(g-2)_\mu$ constraint plays such a prominent role in global fits that BayesFITS and SuperBayes have also considered fits without this constraint applied.

Cosmological and Astrophysical Constraints

In the most recent publication of global fits of the CMSSM, NUHM1, and NUHM2 Fittino, `MasterCode`, BayesFITS, and SuperBayes all four used the relic density determined by WMAP [161, 162] or Planck [3], taking into account 10% theoretical uncertainty.

For the constraints from experiments for direct detection of dark matter scattering of nuclei the Fittino and SuperBayes groups incorporated the result from XENON100 [22], whereas `MasterCode` used the more recent LUX [23] result. All groups cautioned that the uncertainties on the $\sigma_p^{\rm SI}$ are generally large (due to hadronic and astrophysical uncertainties) and BayesFITS even omitted the constraint completely.

Fittino took into account constraints from indirect DM detection through the gamma-ray channel using results from Fermi-LAT [163] and H.E.S.S. [164]. These were found to have a negligible impact on their fit.

Direct Searches at Collider Experiments

The lower limits on sparticle masses established by LEP [80] were taken into account by all groups, except BayesFITS. However, it should be kept in mind that in the CMSSM, NUHM1, and NUHM2 the LHC limits [1, 2] have surpassed those of LEP.

To take into account limits from the direct searches for production of SUSY particles all four groups found that searches for jets $+\not{E}_T$ and 0-leptons are the most constraining. The following searches were used: Fittino: emulation of the ATLAS [165] and CMS [166] searches for jets $+\not{E}_T$ using 5 fb^{-1} of data at $\sqrt{s} = 7$ TeV; `MasterCode`: jets $+\not{E}_T$ search by ATLAS [121] with 20 fb^{-1} of data at $\sqrt{s} = 8$ TeV; BayesFITS: CMS search for jets $+\not{E}_T$ using the $\alpha_{\rm T}$ with 11.7 fb^{-1} at $\sqrt{s} = 8$ TeV [167]; and SuperBayes: ATLAS search for jets $+\not{E}_T$ [168] with 5.8 fb^{-1} at $\sqrt{s} = 8$ TeV. `MasterCode` has the most up-to-date results.

Finally, all groups took into account the measured mass of the lightest Higgs boson (although the Fittino results were obtained prior to the Higgs discovery) and exclusions of the Heavy Higgs bosons decaying into a pair of τs.

Sampling algorithm and strategy

To sample the parameter CMSSM, NUHM1, and NUHM2 spaces `MasterCode` BayesFITS, and SuperBayes used the `MultiNest` algorithm [61–63], although `MasterCode` has a unique

approach of partitioning the parameter space in boxes, cf. section 3.5. Fittino used the metropolis algorithm [64].

The sampled parameter ranges for m_0, $m_{1/2}$, and A_0, are up to tens of TeV in the Fittino and BayesFITS, whereas `MasterCode` and SuperBayes used up to the 5 TeV. As said above: profile likelihood functions minimise the χ^2 function for given parameters of interest. It is possible that larger parameter ranges minimise the profile likelihood functions further. However, larger parameter ranges do result in a courser granularity. Finally, BayesFITS and SuperBayes scanned with log priors in order to provide Bayesian interpretations with log priors. Since the frequentist interpretation is independent of the priors, the scanning with log priors only increases the granularity of the scan as low values of the parameters. The approach of scanning in boxes and the restricted parameter ranges results in a very fine granularity of our global fits.

3.7.2 pMSSM*n*

We now compare the differences in methodology used for our pMSSM10 analysis (April 2015) to that of other groups that analysed pMSSMn models taking into account constraints from searches for direct production of sparticles, namely a pMSSM9 by BayesFITS [57] (June 2013) and a pMSSM15 by SuperBayes [59] (May 2014).

Models

The assumptions described in section 2.4 lead to a pMSSM with 19 parameters. In order to study its properties `MasterCode`, BayesFITS, and SuperBayes made some further simplifications in order to reduce the dimensionality of the parameter space.

In particular, the independent parameters in the pMSSM9 considered by BayesFITS are (using the same notation as in section 2.4)

$$M_2, \quad M_3, \quad m_{\tilde{Q}}, \quad m_{\tilde{L}}, \quad A_u, \quad A_\tau, \quad M_A, \quad \mu, \quad \tan\beta, \tag{3.11}$$

where the remaining parameters are set to

$$M_1 = 0.5 \cdot M_2, \qquad m_{\tilde{Q}} = m_{\tilde{t}} = m_{\tilde{b}}, \qquad m_{\tilde{L}} = m_{\tilde{\tau}},$$
$$m_{\tilde{q}} = m_{\tilde{u}} = m_{\tilde{d}} = 2.5 \text{ TeV}, \qquad A_b = -0.5 \text{ TeV}, \qquad m_{\tilde{\ell}} = m_{\tilde{e}} = m_{\tilde{\mu}} = M_1 + 50 \text{ GeV}.$$

The most important difference with our pMSSM10 is that M_1 is not a free parameter and that the smuon and selectron masses are related to M_1.

The pMSSM15 considered by SuperBayes has the following fixed relations

$$m_{\tilde{q}} = m_{\tilde{u}} = m_{\tilde{d}}, \qquad A_0 \equiv A_b(M_{\rm GUT}) = A_\tau(M_{\rm GUT}), \qquad m_{\tilde{\ell}} = m_{\tilde{e}}. \tag{3.12}$$

This model has most notably more freedom in the third generation squark and slepton sector.

Statistical Interpretation

Despite their collaboration names both BayesFITS and SuperBayes interpreted their results by providing frequentist confidence intervals, for the reason that the the large dimensionality of the parameter spaces introduces "severe prior-dependent volume effects" [59]. This allows to directly compare the results.

Constraints

For all three groups the constraints used in the fits of the pMSSMn are again very similar to those of the CMSSM, NUHM1, and NUHM2.

BayesFITS used the experimental constraints on M_h, $\Omega_{\rm CDM}h^2$, B-physics observables, M_W, $\sin^2\theta_{\rm eff}$, $(g-2)_\mu$, XENON100 [22], and the CMS search for jets $+\not{E}_T$ using the $\alpha_{\rm T}$ variable with 11.7 fb^{-1} of data taken at $\sqrt{s} = 8$ TeV [167] and the CMS search for jets + $3\ell + \not{E}_T$ with 9.2 fb^{-1} of data at $\sqrt{s} = 8$ TeV [169]. We discuss the implementation of the CMS searches in more detail below.

SuperBayes used not only the usual electroweak precision observables M_W, $\sin^2\theta_{\rm eff}$, but also Γ_Z, $\sigma^0_{\rm had}$, R^0_ℓ, R^0_b, R^0_c, $\mathcal{A}_\ell$, $\mathcal{A}_b$, $\mathcal{A}_c$, $A^{0,\ell}_{\rm FB}$, $A^{0,b}_{\rm FB}$, $A^{0,c}_{\rm FB}$. They also used the usual constraints from B and D physics observables, $\Omega_{\rm CDM}h^2$, XENON100 [22], and the Higgs mass. In addition SuperBayes used constraints on the decay rates of the Higgs boson, and on direct production of sparticles based on the ATLAS searches for jets and 0 leptons [124] and 3 leptons [170] both with 4.7 fb^{-1} of data at $\sqrt{s} = 7$ TeV. SuperBayes also considered the possibility that the lightest neutralino does not account for the full relic density, however keeping the upper bound. Therefore, annihilation processes are still required to fulfil this constraint. For the constraint from XENON100 [22] SuperBayes took both SI and SD scattering into account and the expected rate was assumed to scale with relic density in the case it was below the experimental value.

Both BayesFITS and SuperBayes provided profile likelihoods with and without taking into account the constraint on $(g-2)_\mu$. They also both took into account the LEP lower limits on masses [80]. We would like to point out here that both BayesFITS and SuperBayes used the mass lower limit derived that assumes GUT relations between M_1 and M_2. This is a valid assumption for BayesFITS, but not for SuperBayes.

Searches for Direct Production of Sparticles

To constrain the searches for direct production of sparticles at the LHC, BayesFITS implemented and validated simulation based point-by-point the CMS searches for jets + $\not{E}_T$ using the α_{T} variable with 11.7 fb^{-1} of data taken at $\sqrt{s} = 8$ TeV [167] and for jets + $3\ell + \not{E}_T$ with 9.2 fb^{-1} of data at $\sqrt{s} = 8$ TeV [169]. They claim that they calculated the χ^2 contribution point-by-point for the "sensitive" parameter points (1% of the 1.8×10^6 points sampled). The 3 leptons + jets + $\not{E}_T$ search was found to be more sensitive: 4×10^5 points out of 1.8×10^6. Since point-by-point reinterpretation would be computationally prohibitive, they only did this for a subset of 40,000 model points. We would like to point out though that the sensitivity might be "artificially high" due to the fixed relations $M_1 = 0.5 \cdot M_2$ and $m_{\tilde{\ell}} = m_{\tilde{e}} = m_{\tilde{\mu}} = M_1 + 50$ GeV: if the LSP is Bino-like, then $\tilde{\chi}_1^\pm$ and $\tilde{\chi}_2^0$ are Wino-like and have a mass of $m_{\tilde{\chi}_1^\pm} \simeq m_{\tilde{\chi}_2^0} \sim 2 \cdot m_{\tilde{\chi}_1^0}$, so that they decay via on-shell electrons and smuons. This is the most sensitive channel for the 3 leptons search. In our analysis of the pMSSM10 we allow for more different hierarchies between $\tilde{\chi}_1^\pm/\tilde{\chi}_2^0$ and sleptons and managed to treat constrain them appropriately.

The SuperBayes group is indeed able to perform point-by-point reinterpretation the ATLAS searches for jets and 0 leptons [124] and 3 leptons [170] both with 4.7 fb^{-1} of data at $\sqrt{s} = 7$ TeV. However, they did not attempt to include the corresponding constraint in the likelihood function used to produce the profile likelihood functions. Rather, they provide the χ^2 value for the parameter points corresponding to the profile likelihood functions obtained without the constraints on direct production.

We conclude that our implementation of searches for direct production of sparticles at ATLAS and CMS is much more comprehensive and complete than that of BayesFITS and SuperBayes.

Chapter 4

The CMSSM, NUHM1, and NUHM2 after LHC Run 1

In this chapter we present the results of our global fits of the CMSSM, NUHM1 and NUHM2 to experimental data available after Run 1 of the LHC. These fits take into account constraints from cosmology, electroweak precision observables, flavour observables, Higgs physics, and searches for direct production of SUSY particles at the LHC with 20 fb^{-1} of data at $\sqrt{s} = 8$ TeV. The implementations of these constraints have been detailed in sections 3.2 to 3.4. We sampled the parameter spaces of the CMSSM, NUHM1, and NUHM2 with 6.8×10^6, 1.6×10^7, and 4.0×10^7 model points respectively, within the ranges defined in section 3.5.1.

The fulfilment of the dark matter relic density constraint plays a vital role in our global fits of the CMSSM, the NUHM1, and the NUHM2. As we will see below, the various regions in their parameter spaces can be conveniently characterised by the annihilation mechanisms that underlie this fulfilment: the stau coannihilation, A/H funnel, hybrid, $\tilde{\chi}_1^\pm$ coannihilation, stop coannihilation, and focus point mechanisms, cf. section 2.5.2. We developed a colour scheme to indicate their location as we describe in section 4.1.

The rest of this chapter is structured as follows. In section 4.2 we discuss in detail our results for the CMSSM. We first identify the 68% and 95% CL regions in the parameter space and how they are characterised by the DM mechanisms. Then, we assess how the χ^2 function and the contributions from individual constraints vary throughout the parameter space for each of these DM mechanisms. We then turn to predictions for physical observables, where we discuss in particular the mass predictions for different DM mechanisms.

We discuss the results for the NUHM1 and NUHM2 in section 4.3, highlighting the differences between the three models. We follow the same structure as section 4.2: first discussing the parameters, then some overall features of the total χ^2 function as well as individual constraints, followed by physical observables. Throughout this discussion we comment extensively on the mechanisms that underlie the fulfilment of the relic density constraint, as well as the contributions from other constraints.

4.1 Characterisation of DM Mechanisms in the CMSSM, NUHM1, and NUHM2

To facilitate DM mechanism characterisation, we constructed metrics that tend to zero for the respective DM mechanisms. They express relevant features of the mass spectrum as well as the Bino, and Higgsino composition of the LSP (the latter being only considered when necessary). The metrics, their required values, and colour coding are given by:

$$\begin{aligned}
\text{stau coannihilation (pink)}: &\quad \left(\frac{m_{\tilde{\tau}_1}}{m_{\tilde{\chi}_1^0}} - 1\right) + (1 - \mathbf{N}_{11}^2) < 0.15, \\
\text{A/H funnel (blue)}: &\quad \left|\frac{M_A}{m_{\tilde{\chi}_1^0}} - 2\right| + (1 - \mathbf{N}_{11}^2) < 0.7, \\
\tilde{\chi}_1^{\pm} \text{ coannihilation (green)}: &\quad \left(\frac{m_{\tilde{\chi}_1^{\pm}}}{m_{\tilde{\chi}_1^0}} - 1\right) + (1 - \mathbf{N}_{13}^2 - \mathbf{N}_{14}^2) < 0.75, \\
\text{stop coannihilation (grey)}: &\quad \frac{m_{\tilde{t}_1}}{m_{\tilde{\chi}_1^0}} - 1 < 0.2, \\
\text{focus point (cyan)}: &\quad \frac{\mu}{m_{\tilde{\chi}_1^0}} - 1 < 0.3, \\
\text{slepton coannihilation (yellow)}: &\quad \frac{m_{\tilde{\nu}_\ell}}{m_{\tilde{\chi}_1^0}} - 1 < 0.05.
\end{aligned} \tag{4.1}$$

The first three metrics consist of two terms, the second of which specifies the Bino and Higgsino content of the LSP using the elements of the neutralino mixing matrix $\mathbf{N}_{11}$, and $\mathbf{N}_{13}$ and $\mathbf{N}_{14}$ (cf. Eq. 2.8), respectively. The metrics and the required values are empirical and work well within the CMSSM, NUHM1, and NUHM2. We verified extensively that points fulfilling these metrics indeed correspond to the indicated DM mechanisms.

In the case of coannihilation with a particle "X" Eq. 4.1 explicitly requires the mass of particle "X" to be close to that of the LSP. For the A/H funnel mechanism the Heavy

Higgs bosons are required to be near resonance.

For $\tilde{\chi}_1^\pm$ coannihilation we require that the neutralino has a large Higgsino composition. The observation that in our scans of the CMSSM, NUHM1, and NUHM2 the $\tilde{\chi}_1^\pm$ coannihilation only manifests itself for a Higgsino-like neutralino can be understood from the relations between gaugino masses in GUT models $M_1 : M_2 : M_3 \approx 1 : 2 : 6$ (cf. Eq. 2.5). By consequence, μ needs to be lowered to be below or similar to M_1 in order to achieve near degeneracy between the $\tilde{\chi}_1^0$, $\tilde{\chi}_2^0$ and $\tilde{\chi}_1^\pm$. As we commented in section 2.5.2, the $\tilde{\chi}_1^\pm$ coannihilation is very efficient in the case that the neutralino is Higgsino like, so it dominates over other processes. In the NUHM1 and NUHM2 we will see cases where the stau is nearly degenerate and the heavy Higgs is near resonance, but where indeed the $\tilde{\chi}_1^\pm$ coannihilation mechanism dominates. To distinguish these cases we added requirements on the Bino and Higgsino composition to the metrics describing the stau coannihilation, A/H funnel, and $\tilde{\chi}_1^\pm$ coannihilation mechanisms.

The focus point region usually refers to the region where the RGEs have "focussing" properties [82] and μ is low for high values of m_0 [68]. Therefore we require μ to be near the neutralino mass. As argued above, $\tilde{\chi}_1^\pm$ coannihilation may occur for low values of μ. To distinguish the mechanisms that are specific to the focus point region we therefore add the requirement that the $\tilde{\chi}_1^\pm$ coannihilation requirement is not fulfilled.

Finally, the colours mix whenever multiple metrics are fulfilled. In practice this only happens in the hybrid region, where staus annihilate through the Higgs funnel, which is indicated with purple (cf. section 2.5.2).

4.2 The CMSSM

Before we proceed we briefly recapitulate some of the terminology that facilitates the discussion of the results. Following a frequentist approach we provide 68% and 95% CL intervals and regions for parameters and physical observables. We recall from section 3.1 that these are defined as the intervals (regions) where the one- (two-) dimensional profile likelihood functions, cf. Eq. 3.4, take values $\Delta\chi^2 \leq 1$ and $\Delta\chi^2 \leq 4$ ($\Delta\chi^2 \leq 2.30$ and $\Delta\chi^2 \leq 5.99$), respectively.[1] The $\Delta\chi^2$ is the difference with respect to the global χ^2 minimum to which we refer as the "best-fit point". The χ^2 function is defined in Eq. 3.1, and individual contributions have been specified in sections 3.2 and 3.3. We extensively

[1] Although strictly speaking these $\Delta\chi^2$ values correspond to 68.3% and 95.4% (68.3% and 95%) CL respectively, cf. Table 3.1. These $\Delta\chi^2$ values have been used consistently by the `MasterCode` Collaboration [171].

refer to such contributions as "the constraint on/from observable X", or "the X constraint".

4.2.1 Parameters

We first turn to the parameter planes of the CMSSM in Fig. 4.1. Here from left to right and top to bottom the $(m_0, m_{1/2})$, $(m_0, \tan\beta)$, (m_0, A_0), $(\tan\beta, m_{1/2})$, $(A_0, m_{1/2})$, and $(A_0, \tan\beta)$ planes are displayed. The red and blue lines indicate the 68% and 95% CL contours respectively, whereas the green stars indicate location of the best-fit point. Coloured shadings indicate the regions that correspond to stau coannihilation (pink), A/H funnel (blue), hybrid (purple), $\tilde{\chi}_1^\pm$ coannihilation (green) and focus point (cyan) mechanism.

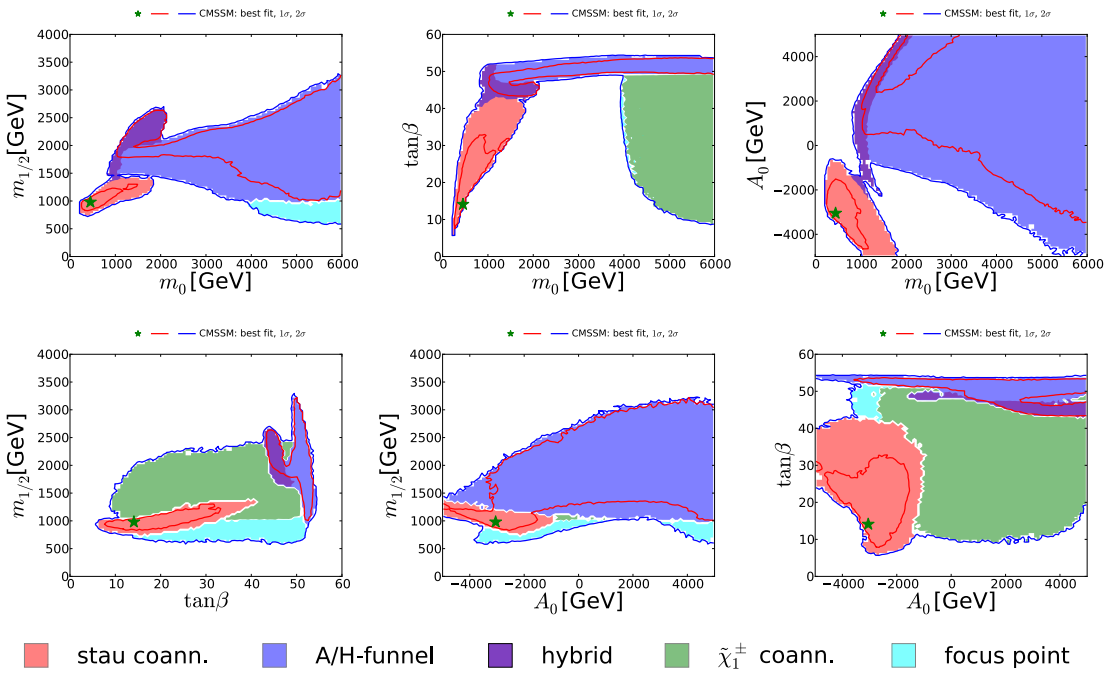

Figure 4.1: *A compilation of parameter planes in the CMSSM, with shading according to the dominant mechanisms for fulfilling the dark matter density following Eq. 4.1. In each plane, red and blue lines indicate the 68% and 95% CL contours, respectively. Green stars denote the best-fit point. Coloured shadings to indicate the regions that correspond to the stau coannihilation (pink), A/H funnel (blue), hybrid (purple), $\tilde{\chi}_1^\pm$ coannihilation (green) and focus point (cyan) mechanism.*

The stau coannihilation region (pink shaded) is located at low values of $200 \lesssim m_0 \lesssim$

2000 GeV and $750 \lesssim m_{1/2} \lesssim 1500$ GeV. The values of $\tan\beta$ increase with m_0 as can be seen from the $(m_0, \tan\beta)$ plane, whereas from the (m_0, A_0) plane we see that A_0 is negative and decreases with increasing m_0. Note that the allowed values of the A_0 parameter tend to go outside its scan range for $1000 \lesssim m_0 \lesssim 2000$ GeV.

This highlights a feature of our fits that should be kept in mind when interpreting the results. Some of the 68% and 95% CL regions in the parameter space extend beyond the ranges that were scanned in our fits. Consequently, some of the features in the profile likelihoods functions can be attributed to the limitation in the scanned parameter ranges.

We now turn to the A/H funnel (blue shaded) region. In the $(m_0, m_{1/2})$ plane we see that this mechanism comes into play for $m_0 \gtrsim 1000$ GeV and the allowed range for $m_{1/2}$ increases with m_0. Here we see another instance of 68% and 95% CL contours that do not close within a sampled range, namely of m_0. The value of $\tan\beta$ is between ~ 47 and ~ 55. The (m_0, A_0) plane indicates that the lower bound on negative A_0 decreases with increasing m_0, whereas the $(A_0, m_{1/2})$ plane indicates that the lower bound on A_0 increases with increasing $m_{1/2}$. Here we see again that the 68% and 95% contours do not close within the sampled ranges of A_0.

The hybrid region (purple shaded) appears for values of $1000 \lesssim m_0 \lesssim 2000$ GeV $m_{1/2} \gtrsim 1500$ GeV. This region is located between $42 \lesssim \tan\beta \lesssim 53$ and at the lower bound of m_0 for given positive A_0, as can be seen from the (m_0, A_0) plane. Note that this region is disjoint from the stau coannihilation-only region. There is a small region where the colour indicating the hybrid region "leaks" into the stau coannihilation region, which is located at the boundary of these disjoint regions, cf. the (m_0, A_0) plane at $m_0 \sim 1000$ GeV and $A_0 \sim -1500$ GeV. This is an artefact of the metrics defined in Eq. 4.1.

We indicate the focus point mechanism with cyan shading. This region has high values of $m_0 \gtrsim 4000$ GeV, whereas $m_{1/2} \lesssim 1000$ GeV. Note that in the various planes, it is mainly the $m_{1/2}$ parameter that separates the focus point from the A/H funnel region and $\tilde{\chi}_1^\pm$ coannihilation region. In both regions μ approaches M_1, but only for $m_{1/2} \gtrsim 1000$ GeV the chargino mass is sufficiently close to the LSP mass. Note that in the $(m_0, m_{1/2})$ plane the A/H funnel mechanism is preferred over the $\tilde{\chi}_1^\pm$ coannihilation and focus point mechanisms, so that the latter two are not visible in this plane. However due to the strong dependence of the A/H funnel mechanism on $\tan\beta$, the $\tilde{\chi}_1^\pm$ coannihilation region is indeed visible in parameter planes that do depend on $\tan\beta$.

For reference, the m_0, $m_{1/2}$, A_0 and $\tan\beta$ parameters, as well as the total χ^2, the number of degrees of freedom d.o.f., and the corresponding χ^2-probability are given for the best-fit points of each of the DM mechanisms, in Table 4.1. They were obtained by minimising

the total χ^2 function while restricting points to fulfil the respective requirements on the DM metrics as describes in Eq. 4.1. Note that the χ^2 values for the stau coannihilation mechanism, the A/H funnel mechanism have almost identical $\chi^2 \sim 35$, whereas the hybrid mechanism is only 0.8 higher. The $\tilde{\chi}_1^\pm$ coannihilation mechanism and focus point mechanism have $\Delta\chi^2 \sim 3$ with respect to the overall minimum. We also see again that the stau coannihilation mechanism best-fit point is located at low masses of m_0 and $m_{1/2}$ a negative A_0 and low $\tan\beta$. The A/H funnel mechanism, $\tilde{\chi}_1^\pm$ coannihilation mechanism, and focus point mechanism have $m_0 \gtrsim 5600$ GeV, which is close to the end of the sampled range.

	Stau Coann.	H/A Funnel	Hybrid	Chargino Coann.	Focus Point
m_0 [GeV]	430	5650	1750	5990	5950
$m_{1/2}$ [GeV]	970	2100	2470	2220	2030
A_0 [GeV]	-3020	780	4300	2820	4300
$\tan\beta$	14.0	51.0	45.0	43.0	51.0
χ^2	35.0	35.1	35.8	38.2	38.1
d.o.f.	24	24	24	24	24
χ^2-probability	6.8%	6.7%	5.7%	3.3%	3.4%

Table 4.1: *The m_0, $m_{1,2}$, A_0 and $\tan\beta$ parameters, as well as the total χ^2, the number of degrees of freedom d.o.f., and the corresponding χ^2-probability for the CMSSM best-fit points when restricting the fit to fulfil the respective requirements for the DM mechanisms, as defined in Eq. 4.1.*

In summary, we see that the DM mechanisms conveniently characterise different regions in the preferred parameters in the CMSSM. In particular, the stau coannihilation and the A/H funnel give almost equally good fits, the hybrid region is also favoured in 68% CL regions, whereas the $\tilde{\chi}_1^\pm$ coannihilationand focus point mechanisms are only available in the 95% CL regions.

4.2.2 The χ^2 Function

In this section we discuss how the individual constraints contribute to the total χ^2 function, which we refer to as "χ^2 breakdown". To facilitate this discussion we consider for each of the DM mechanisms the best-fit point, as well as model points along restricted profile likelihood functions for m_0 and $m_{1/2}$. These restricted profile likelihood functions for m_0

and $m_{1/2}$ were obtained as usual, cf. section 3.1, but with the restriction that model points need to to fulfil the requirements defined in Eq. 4.1.

In Fig. 4.2 we display the χ^2 breakdown of the best-fit point, and restricted profile likelihood functions of m_0 and $m_{1/2}$ for the stau coannihilation mechanism. The ordering of the (groups of) constraints and the colours used are specified in the legend. There is an almost flat contribution from the sum over constraints on flavour observables (excluding $\mathrm{BR}(B \to X_s\gamma)$ and $\mathrm{BR}(B_{s,d} \to \mu^+\mu^-)$), depicted in dark slate grey. For these observables the individual constraints are also almost constant. We will see below that this is not true for all of the parameter space, which justifies their use in the fit. The sum of the contributions from the Z-pole observables constraints, depicted by dark slate blue, is also rather flat. However, in particular the contributions from the $A_{\mathrm{FB}}^{0,b}$ and $\mathcal{A}_\ell(\mathrm{SLD})$ constraints generally vary throughout the parameter space, although their contributions go in opposite directions. Next, we note that the $(g-2)_\mu$ constraint (in teal) generally has a large contribution, ranging from 7.5 at $m_{1/2} \sim 720$ GeV to 10.1 at high m_0 and $m_{1/2}$. On top of these relatively flat constraints, we see that the χ^2 function is more significantly shaped by the constraints from jets $+\not{E}_T$ (grey), $\mathrm{BR}(B \to X_s\gamma)$ (blue), $\mathrm{BR}(B_{s,d} \to \mu^+\mu^-)$ (green), and M_W (magenta). At low values of m_0 and $m_{1/2}$ the jets $+\not{E}_T$ constraint gives the major contribution, whereas the contributions from the $\mathrm{BR}(B \to X_s\gamma)$, $\mathrm{BR}(B_{s,d} \to \mu^+\mu^-)$ and M_W constraints increase with increasing m_0 and $m_{1/2}$.

Fig. 4.3 displays the breakdowns of the total χ^2 in individual contributions for points that fulfil the A/H funnel metric. Along the restricted profile likelihood function for m_0, the summed contributions of the flavour observables (excluding $\mathrm{BR}(B \to X_s\gamma)$ and $\mathrm{BR}(B_{s,d} \to \mu^+\mu^-)$) (dark slate grey) as well as the Z-pole observables (dark slate blue) are again mostly flat, whereas the contribution from the $(g-2)_\mu$ constraint (teal) increases with increasing m_0. On the other hand, in the $m_{1/2}$ case we see a modest dependence on $m_{1/2}$ of the contributions from the constraint on flavour observables (excluding $\mathrm{BR}(B \to X_s\gamma)$ and $\mathrm{BR}(B_{s,d} \to \mu^+\mu^-)$), justifying their use in our fit. Towards lower m_0, the contributions from the constraints on M_h (cyan), and $\mathrm{BR}(B_{s,d} \to \mu^+\mu^-)$ (green) become sizable, whereas for high m_0 the M_W (magenta) constraint yields ~ 1.4.

The χ^2 breakdowns for the hybrid, focus point, and $\tilde{\chi}_1^\pm$ coannihilation mechanisms can be found in the appendix B, in Figs. B.1 to B.3. We note that the χ^2 function in hybrid region is similar to the A/H funnel region for values of 1000 GeV $\lesssim m_0 \lesssim$ 2000 GeV. For the focus point and $\tilde{\chi}_1^\pm$ coannihilation mechanisms it is mainly the LUX [23] constraint (red) that disfavours this region. Accordingly, μ is low and takes similar values to M_1, so that the LSP is an admixture of Bino and Higgsino, which in turn results in a large σ_p^{SI} cf.

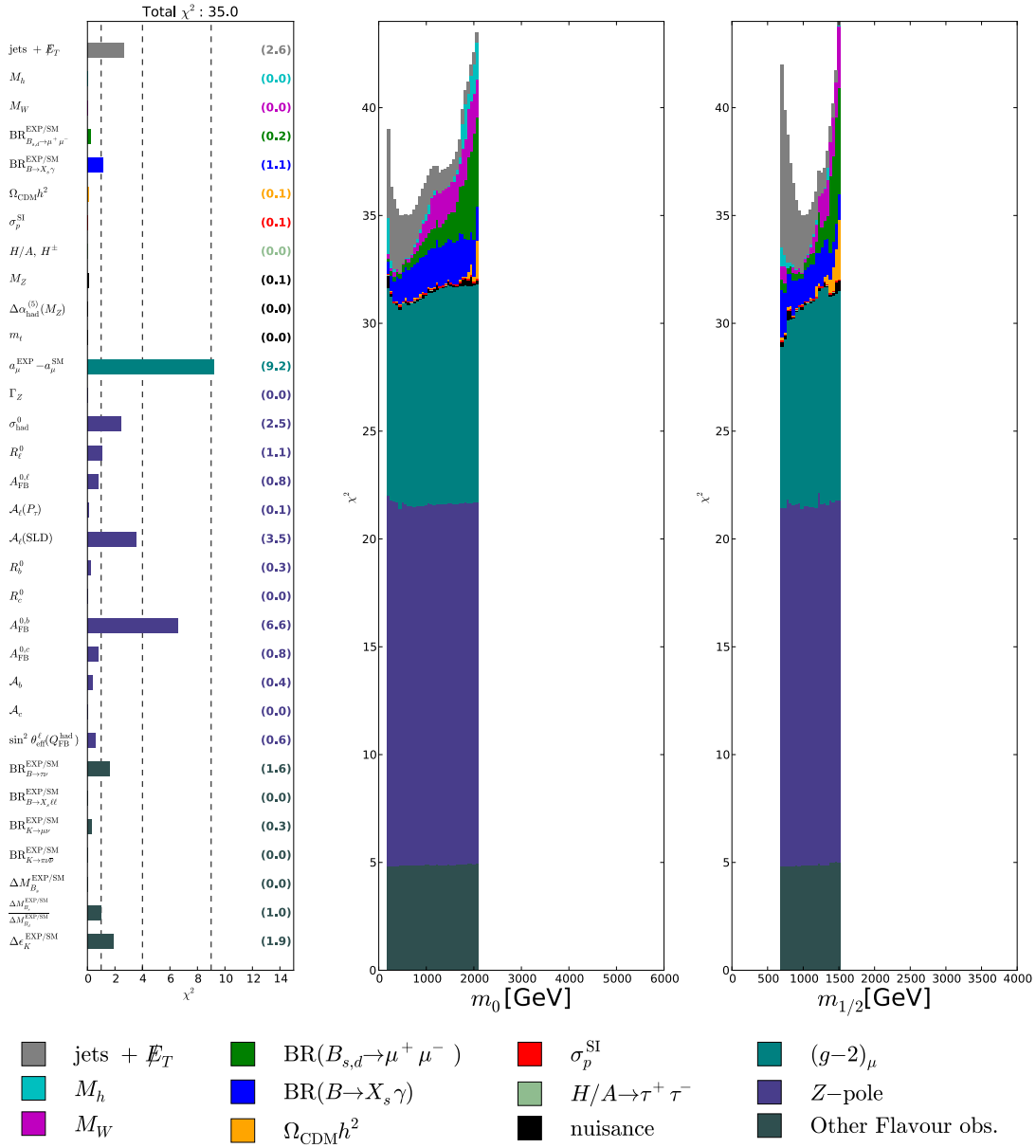

Figure 4.2: *Breakdown of the total χ^2 in individual contributions for points in the CMSSM fulfilling the **stau coannihilation metric**, as defined in Eq. 4.1. The panels show the breakdowns for the best-fit point (left), and along the restricted profile likelihood functions of m_0 (middle) and $m_{1/2}$ (right). The ordering of the (groups of) constraints and the colours used are specified in the legend.*

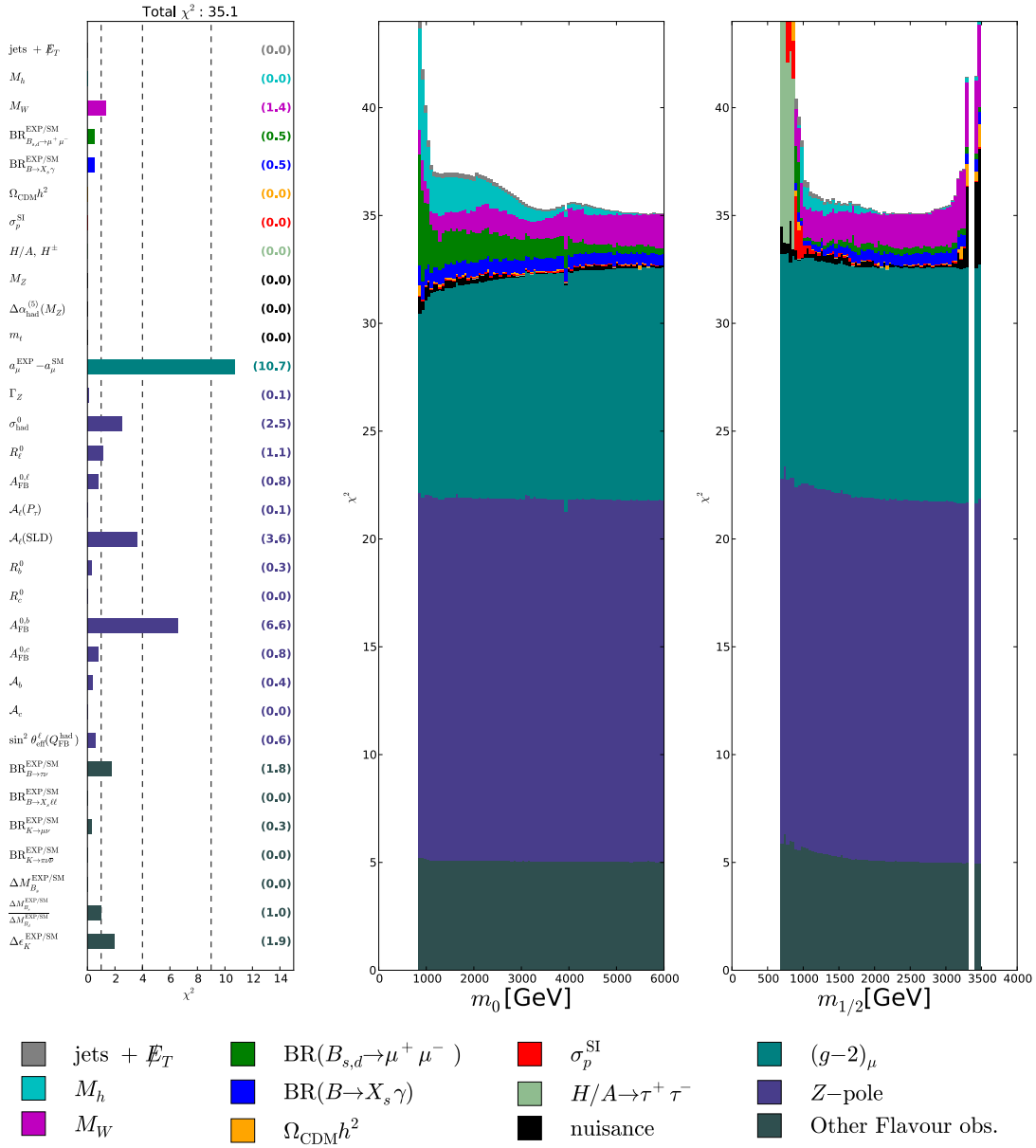

Figure 4.3: *Breakdown of the total χ^2 in individual contributions for points in the CMSSM fulfilling the* ***A/H funnel metric****, as defined in Eq. 4.1. The panels show the breakdowns for the best-fit point (left), and along the restricted profile likelihood functions of m_0 (middle) and $m_{1/2}$ (right). The ordering of the (groups of) constraints and the colours used are specified in the legend.*

section 2.5.3. We further note that for the $\tilde{\chi}_1^\pm$ coannihilation and focus point mechanisms $m_0 \lesssim 5000$ GeV is increasingly disfavoured by the M_h constraint (cyan) with decreasing m_0.

4.2.3 Predictions for Physical Observables

Masses

We now examine the spectra that correspond to these different DM mechanisms. We first consider the spectra for the best-fit points. From left to right and top to bottom Fig. 4.4 shows the mass spectra for the stau coannihilation, A/H funnel, hybrid, focus point, and $\tilde{\chi}_1^\pm$ coannihilation mechanisms, respectively. In Table 4.2 the values are given for a selection of these masses. Note that Fig. 4.4 and Table 4.2 nicely illustrate the typical mass configurations for the DM mechanism: a nearly degenerate $\tilde{\tau}_1$ and $\tilde{\chi}_1^0$ mass in the stau coannihilation and hybrid case; H/A masses that are $\sim 2 \cdot m_{\tilde{\chi}_1^0}$ in the A/H funnel and hybrid case; a nearly degenerate $\tilde{\chi}_1^\pm$ mass in the $\tilde{\chi}_1^\pm$ coannihilation case; high sfermion masses in the focus point case. The best-fit spectra show that only the masses in the CMSSM stau coannihilation region are within reach for LHC Run 2. All the other scenarios have multi-TeV sfermions and a neutralino mass of $m_{\tilde{\chi}_1^0} \gtrsim 900$ GeV. This statement holds more generally as we will see in the following.

[GeV]	Stau Coann.	H/A Funnel	Hybrid	Chargino Coann.	Focus Point
$m_{\tilde{g}}$	2130	4620	5110	4870	4480
$m_{\tilde{q}_R}$	1900	6680	4670	7070	6870
$m_{\tilde{t}_1}$	970	4700	3880	5000	4760
$m_{\tilde{b}_1}$	1580	5230	4310	5750	5320
$m_{\tilde{\ell}_R}$	560	5690	1970	6040	5990
$m_{\tilde{\tau}_1}$	410	4080	1090	4900	4220
$m_{\tilde{\chi}_1^0}$	410	940	1090	930	890
$m_{\tilde{\chi}_1^\pm}$	790	1130	2020	940	940
M_A	1910	2070	2200	3780	2180

Table 4.2: *Masses for the CMSSM best-fit points for the stau coannihilation, A/H funnel, hybrid, focus point, and $\tilde{\chi}_1^\pm$ coannihilation mechanisms.*

In Fig. 4.5 we display profile likelihood functions for $m_{\tilde{g}}$, $m_{\tilde{q}_R}$, $m_{\tilde{t}_1}$, $m_{\tilde{b}_1}$, $m_{\tilde{\ell}_R}$, $m_{\tilde{\tau}_1}$, $m_{\tilde{\chi}_1^0}$, $m_{\tilde{\chi}_1^0}$, $m_{\tilde{\chi}_1^\pm}$, and M_A from left to right and from top to bottom. The dashed lines

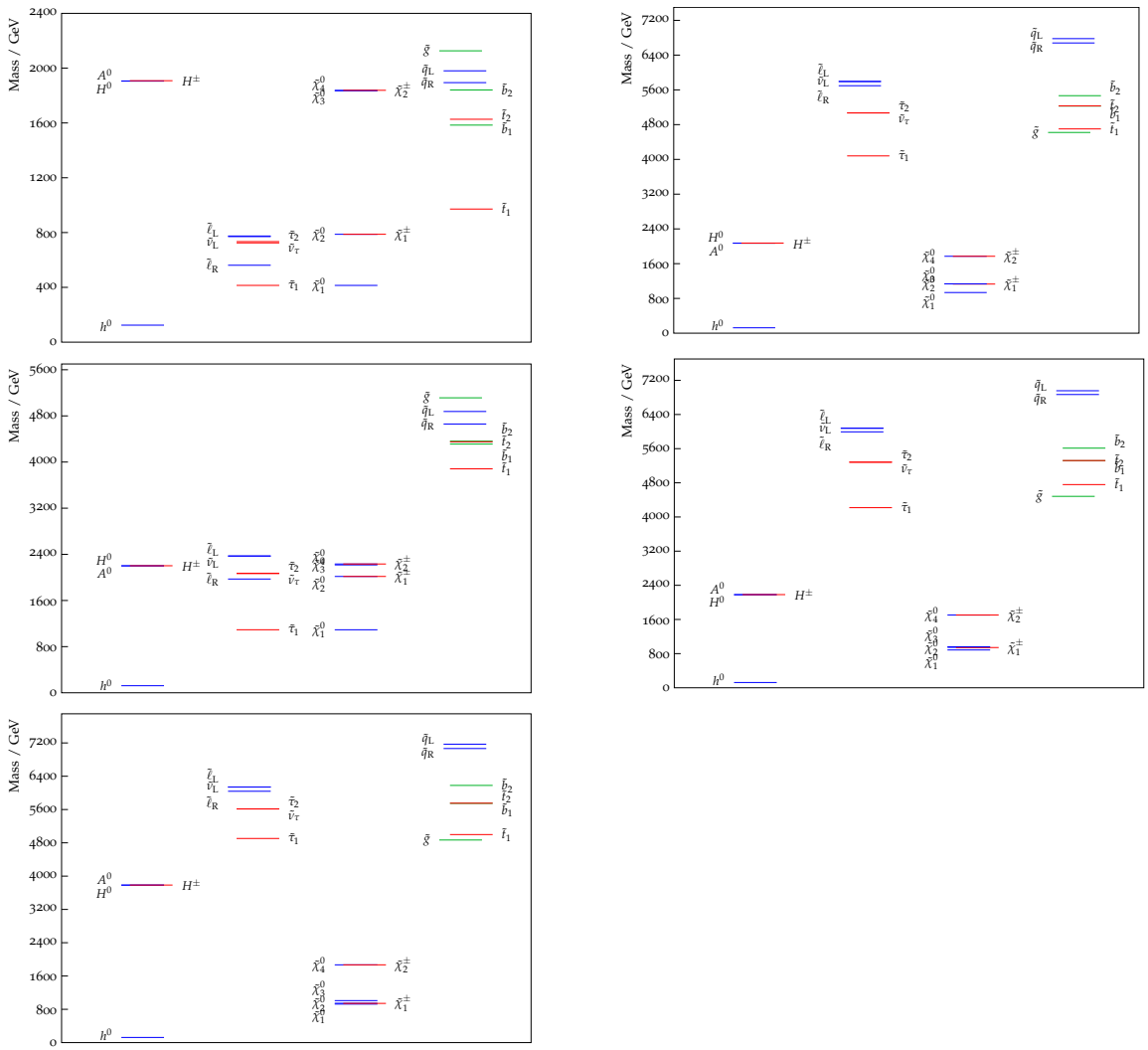

Figure 4.4: *Mass spectra in the CMSSM of the best-fit points for the stau coannihilation (upper left panel), A/H funnel (upper right panel), hybrid (middle left panel), focus point (middle right panel), and $\tilde{\chi}_1^\pm$ coannihilation (lower left panel) mechanisms.*

show the profile likelihood for the full sample, whereas the other lines are the profile likelihood functions when we require the points to fulfil the metrics corresponding to stau coannihilation (red), A/H funnel (blue), hybrid (purple), $\tilde{\chi}_1^\pm$ coannihilation (green), and the focus point (cyan), as defined in Eq. 4.1. We now discuss the mass confidence intervals for each of the DM mechanisms.

Stau coannihilation region (red): this region gives narrow 95% confidence intervals for at low masses for all sparticles. In fact, the overall 95% CL lower limit on all masses

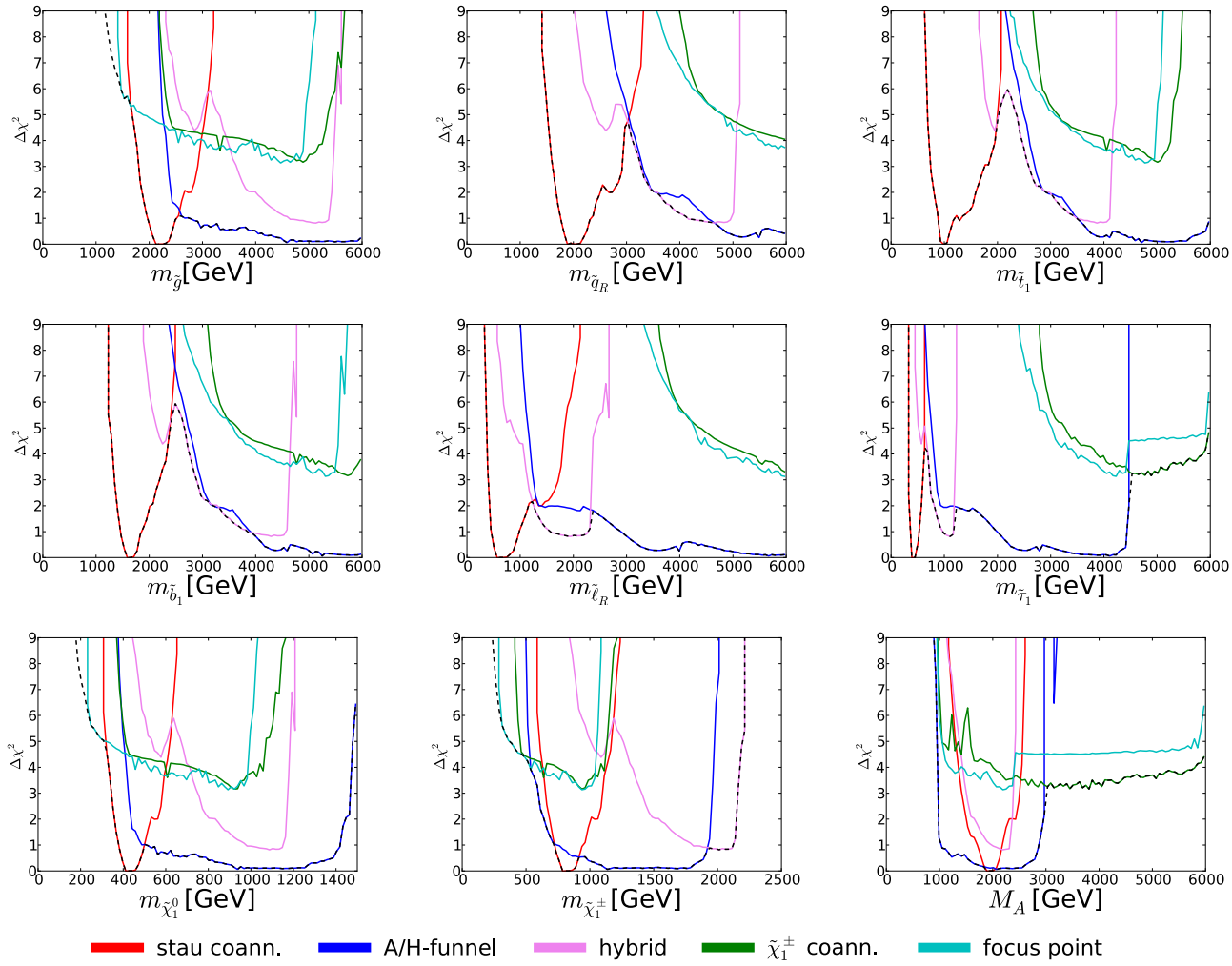

Figure 4.5: *Mass predictions in the CMSSM for the full sample (black dashed line) and for the points fulfilling the criteria in Eq. 4.1 for the stau coannihilation (red), the A/H funnel (blue), the hybrid (purple), the $\tilde{\chi}_1^\pm$ coannihilation (green) and the focus point (cyan) mechanism. All lines correspond to $\Delta\chi^2$ with respect to the overall minimum.*

correspond to the stau coannihilation region, except for $m_{\tilde{\chi}_1^\pm}$ and M_A. The χ^2 minimum is well separated from the other mechanisms for e.g. $m_{\tilde{q}_R}$, $m_{\tilde{t}_1}$, $m_{\tilde{b}_1}$, and $m_{\tilde{\tau}_1}$ where $\Delta\chi^2 > 4$ before another the hybrid mechanism takes over. As we mentioned in section 4.2.2 the lower bound on the masses in the stau coannihilation region is mainly driven by the jets $+\not{E}_T$ constraint, whereas the upper limit on the masses is driven by the constraints on $\mathrm{BR}(B \to X_s\gamma)$, $\mathrm{BR}(B_{s,d} \to \mu^+\mu^-)$, and M_W.

***A/H* Funnel region (blue):** the χ^2 minimum in this region has $\Delta\chi^2 \sim 0.1$ with

respect to the global minimum. We see that in the displayed ranges there is only a lower bound on most of the masses, the exceptions being $m_{\tilde{\tau}_1}$, $m_{\tilde{\chi}_1^0}$, $m_{\tilde{\chi}_1^\pm}$ and M_A. Their values of m_0 and $m_{1/2}$ correspond to the end of the sampled range. Since the LSP is Bino-like in the A/H funnel region, the $\tilde{\chi}_1^0$, $\tilde{g}$ masses and M_A are related by $m_{1/2}$ and the relation $M_A \sim 2 \cdot m_{\tilde{\chi}_1^0}$. Therefore the χ^2 function for these masses follow follows that of $m_{1/2}$, cf. the right panel in Fig. 4.3, where we see that the lower bound is mainly driven by the $H/A \to \tau^+\tau^-$constraint. The lower bound on the sfermion masses is mainly due to the $B_{s,d} \to \mu^+\mu^-$ and M_h constraints, be it somewhat compensated for by better agreement with $(g-2)_\mu$, cf. the middle panel in Fig. 4.3.

Hybrid region (purple): the hybrid region is very similar to the A/H funnel region, except that the allowed range in m_0 and $m_{1/2}$ is bounded from above at 2000 GeV and 2500 GeV respectively. For example: comparing two points that minimise the χ^2 function at $m_{\tilde{g}} \sim 5000$ GeV, corresponding to the A/H funnel and the hybrid mechanisms respectively, we see that the m_0 parameter equals 5850 GeV and 1800 GeV respectively. For these two points the largest difference in constraints is the M_h constraint: 0.0 and 0.9 respectively. Note that there appears a local minimum at e.g. $m_{\tilde{g}} \sim 2850$ GeV. These are actually stau coannihilation only points, despite their colouring. This reflects the leakage, that we already mentioned in section 4.2.1.

$\tilde{\chi}_1^\pm$ coannihilation (green) and focus point (cyan) regions: we observe again that the χ^2 minimum has an offset compared to e.g. the A/H funnel region, which originates from the LUX [23] upper limit on σ_p^{SI}. The lower bound on sfermion masses is driven by the M_h constraint, cf. the m_0 profile likelihood in Fig. B.2. The profile likelihood functions of $m_{\tilde{\chi}_1^0}$, $m_{\tilde{\chi}_1^\pm}$, and $m_{\tilde{g}}$ exhibit the same behaviour as the that of $m_{1/2}$ in the right panel of Fig. B.2. There is no longer an upper bound on M_A, whereas the lower bound is again driven by $H/A \to \tau^+\tau^-$. Finally, we note that the focus point region (cyan lines) looks overall very similar to the chargino coannihilation region.

M_h and the $(M_A, \tan\beta)$ Plane

The left panel in Fig. 4.6 shows the profile likelihood function for M_h in blue and the individual χ^2 contribution from the constraint on M_h in red. It is interesting to note that the fit has difficulty to get $M_h > 126.0$: the $\Delta\chi^2$ values exceed the constraint value. This is mainly due to the top mass (nuisance parameter), which takes values above the nominal value. For lower values of M_h the profile likelihood function simply follows the constraint value.

In Fig. 4.6 we display the $(M_A, \tan\beta)$ plane, where the contours, star and coloured shading within the contours have the same significations as in Fig. 4.5. We also display a magenta line that indicates the $H/A \to \tau^+\tau^-$ 95% CL exclusion from ATLAS [125], which is used to constrain $\tan\beta$ as a function of M_A, as described in section 3.3.2. Fig. 4.6 shows that the $H/A \to \tau^+\tau^-$ constraint is sensitive to the A/H funnel region, whereas the other regions are untouched. M_A is restricted to be between ~ 1000 GeV and ~ 3000 GeV for the stau coannihilation, A/H funnel, and hybrid regions. In the $\tilde{\chi}_1^\pm$ coannihilation and focus point regions, M_A is not longer related to the neutralino mass and can take higher values.

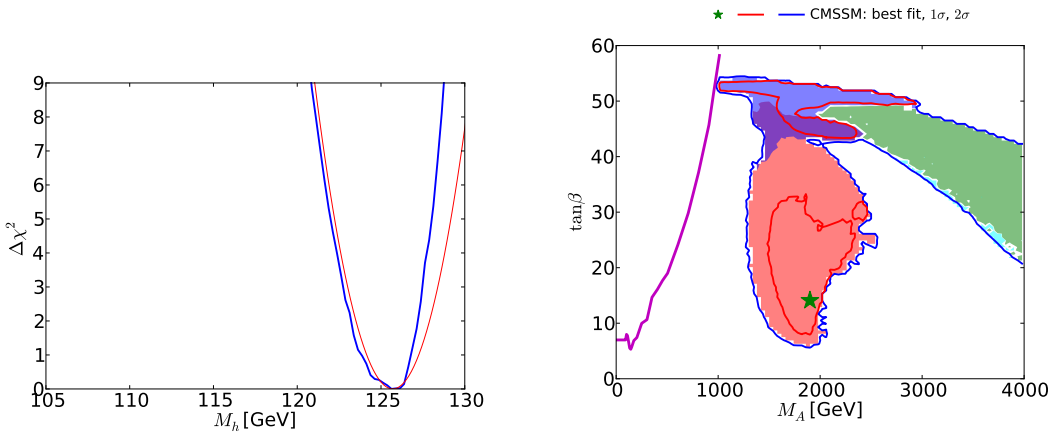

Figure 4.6: *Prediction for the light and heavier $\mathcal{CP}$-odd Higgs boson masses. In the left panel the profile likelihood function for M_h is depicted in blue, whereas the individual χ^2 contribution from the constraint on M_h is shown in red. The red and blue contours, the green star and the shading in the right panel have the same signification as in Fig. 4.1. The magenta line indicates the 95% CL exclusion by ATLAS [125].*

$(g-2)_\mu$ and $B_{s,d} \to \mu^+\mu^-$

We recall from section 4.2.2 that the $(g-2)_\mu$ constraint generally yields a contribution of $\gtrsim 9.0$. Fig. 4.7 left illustrates that the CMSSM cannot accommodate the measured value of $(g-2)_\mu$. The constraints from jets $+\not{E}_T$ and M_h are the main drivers of this tension. On the one hand $(g-2)_\mu$ requires smuon (and chargino masses) to be $\mathcal{O}(100$ GeV), on the other hand the jets $+\not{E}_T$ and M_h constraints push the gluino and first-, second- and third-generation squark masses to high values. The tension arises from the relations between the masses of smuons and strongly interacting sparticles as a result of the unification of

sfermion and gaugino mass parameters at the GUT scale.

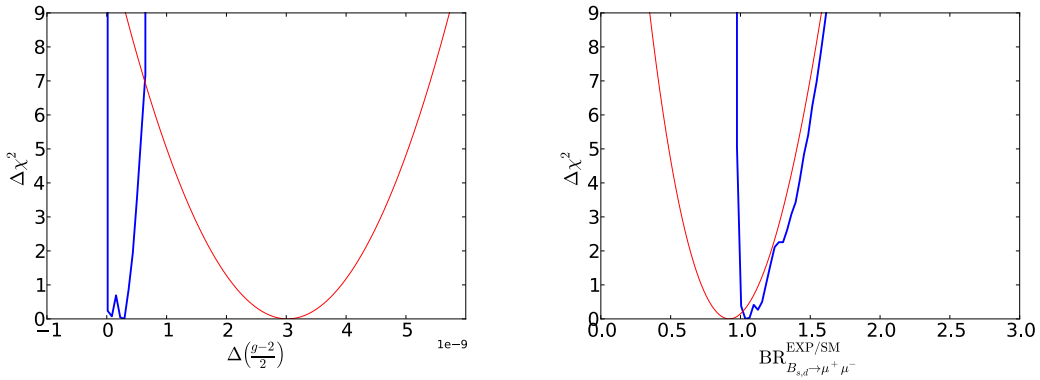

Figure 4.7: *The profile likelihood functions (blue) for the SUSY contribution to* $(g-2)_\mu$ *(left panel) and for* $\mathrm{BR}^{\mathrm{EXP/SM}}_{B_{s,d}\to\mu^+\mu^-}$ *(right panel). In both panels, the red line shows the individual* χ^2 *contribution of the corresponding constraints.*

In contrast to the $(g-2)_\mu$ constraint, our fit of the CMSSM has no difficulty to accommodate the constraint on $\mathrm{BR}^{\mathrm{EXP/SM}}_{B_{s,d}\to\mu^+\mu^-}$ as can be seen in Fig. 4.7 right, where for $\mathrm{BR}^{\mathrm{EXP/SM}}_{B_{s,d}\to\mu^+\mu^-} > 1.0$ the profile likelihood function closely follows the value of the constraint. Note however, that the CMSSM does not allow for values for $\mathrm{BR}^{\mathrm{EXP/SM}}_{B_{s,d}\to\mu^+\mu^-}$ below 1.0.

Direct Detection of Dark Matter

We now turn to our predictions for the σ_p^{SI} as a function of the neutralino mass in Fig. 4.8. In this figure we display the regions that are excluded by LUX [23] and XENON100 [22] with shaded green, whereas the region where the background from neutrinos dominates is shaded yellow [172], i.e. below the "neutrino floor" (dashed orange line). The blue and red contours, the green star and the colours have the same significations as in Fig. 4.4. The first thing to note is that the stau coannihilation region has very low values of $\sigma_p^{\mathrm{SI}} \sim 10^{-47}\mathrm{cm}^2$. Whereas the stau coannihilation region should be partially within reach of the LHC Run 2, it will be hard to probe with direct detection experiments. The contrary is true for the A/H funnel $\tilde{\chi}_1^\pm$ coannihilation and focus point regions: in the A/H funnel region the spin-independent cross-section is $10^{-46} \lesssim \sigma_p^{\mathrm{SI}} \lesssim 10^{-44}\mathrm{cm}^2$, whereas in the $\tilde{\chi}_1^\pm$ coannihilation and focus point regions $\sigma_p^{\mathrm{SI}} \gtrsim 10^{-44}\mathrm{cm}^2$, which is already constrained by the constraint on σ_p^{SI} from LUX [23]. In these regions the masses are typically higher, which renders it impossible to find them at the LHC. This highlights the complementarity of direct searches for dark matter at the LHC and direct detection experiments.

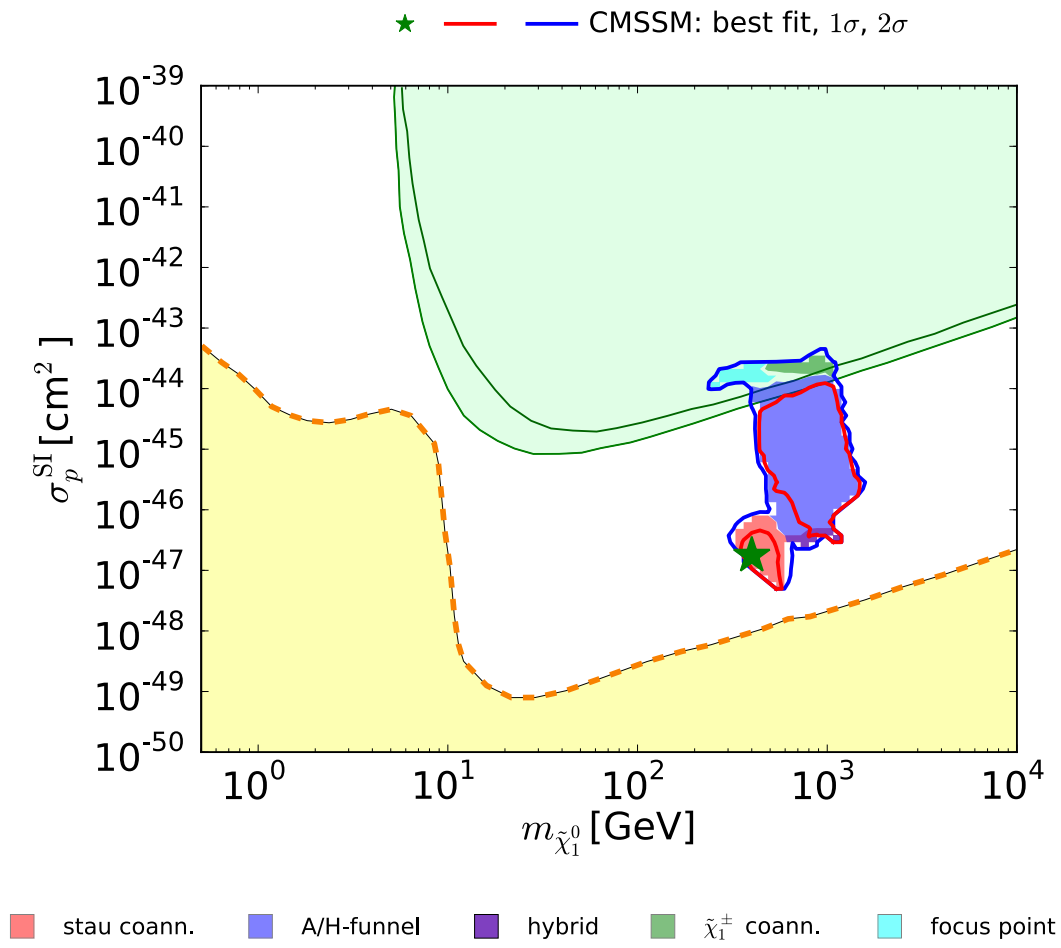

Figure 4.8: *The $(m_{\tilde{\chi}_1^0}, \sigma_p^{\rm SI})$ plane in the CMSSM. The red and blue contours, the green star and the coloured shading inside the contour have the same significations as in Fig. 4.1. Also shown are the 90% CL upper limits from LUX [23] and XENON100 [22] (green lines) and the region where the background from neutrinos dominates (yellow shaded) [172].*

4.3 The NUHM1 and the NUHM2

In this section we discuss the effect of lifting the degeneracy of the $m_{H_u}^2$ and $m_{H_d}^2$ with m_0^2 at the GUT scale. In the NUHM1 these parameters are set equal (denoted as m_H^2), whereas in the NUHM2 they are allowed to vary independently. Note that in this section the profile likelihood functions for the NUHM1 were obtained including the CMSSM sample, and the profile likelihood functions for the NUHM2 were obtained including the NUHM1 and

CMSSM samples. This was done to ensure that $\chi^2|_{\text{NUHM2}} \leq \chi^2|_{\text{NUHM1}} \leq \chi^2|_{\text{CMSSM}}$. The exceptions are the planes involving $m^2_{H_{u,d}}$, to avoid degeneracy lines.

In the NUHM1 and NUHM2 negative value of m_0^2 at the GUT scale can yield non-tachyonic sfermion masses at the electroweak scale. In principle negative values of m_0^2 could raise cosmological issues, but this does not necessarily lead to an unacceptable evolution of the Universe [173], cf. Ref. [44] for more discussion on negative m_0^2. We incorporate negative values of m_0^2 by defining $m_0 = \text{sign}(m_0^2)\sqrt{|m_0^2|}$.

4.3.1 Parameters

In this section we highlight some of the differences between the CMSSM, NUHM1, and NUHM2 by considering the m_0, $m^2_{H_u}$ and $m^2_{H_d}$ parameters. Figures corresponding to other parameter dependencies can be found in appendix B, Fig. B.4 to B.7. First we consider the $(m_0, m_{1/2})$ plane in Fig. 4.9. In the top left panel we overlaid the 68% (95%) CL contours using red (blue) lines for the NUHM2 (solid), NUHM1 (dashed) and CMSSM (dotted). The top right, bottom left and bottom right panels show the individual plots for the CMSSM, NUHM1, and NUHM2 respectively, and the contours, green stars and coloured shading have the same significations as in Fig. 4.1. Furthermore, a magenta line indicates the 95% CL exclusion contour from the ATLAS jets $+\not{E}_T$ search [121] used to constrain m_0 and $m_{1/2}$ as described in section 3.3.1.

The first observation is that in the NUHM1 and NUHM2 the $\tilde{\chi}_1^\pm$ coannihilation mechanism becomes available at values for $m_{1/2} \gtrsim 2000$ GeV, because of the additional freedom in $m^2_{H_{u,d}}$: points in this region take values $m^2_{H_{u,d}} > m_0^2$. This feature is highlighted in planes that show $m^2_{H_{u,d}}$ as a function of m_0 in Fig. 4.10, where we display (m_0, m_H^2) plane of the NUHM1 in the top left panel, and the $(m_0, m^2_{H_u})$, $(m_0, m^2_{H_d})$, and $(m^2_{H_u}, m^2_{H_d})$ planes of the NUHM2 in the top right, bottom left and bottom right panels, respectively. To guide the eye dashed black lines indicate where $m^2_{H_{u,d}} = m_0^2$ in the NUHM1 and NUHM2 or where $m^2_{H_u} = m^2_{H_d}$ in the NUHM2. Hence the CMSSM should be recovered along this line in the (m_0, m_H^2) in the NUHM1, whereas the NUHM1 should be recovered along the this line in the $(m^2_{H_u}, m^2_{H_d})$ plane in the NUHM2. Comparing the location of the $\tilde{\chi}_1^\pm$ coannihilation region (green shaded) in the (m_0, m_H^2) plane of the NUHM1 with the $(m_0, m^2_{H_u})$ and $(m_0, m^2_{H_d})$ planes of the NUHM2, we see that in the (m_0, m_H^2) plane of the NUHM1 the $\tilde{\chi}_1^\pm$ coannihilation regions is very similar to that in the $(m_0, m^2_{H_u})$ plane in the NUHM2, whereas it differs from the $(m_0, m^2_{H_d})$ plane. The appearance of the $\tilde{\chi}_1^\pm$ coannihilation region can also be interpreted as the freedom to choose μ or (and) M_A in the NUHM1

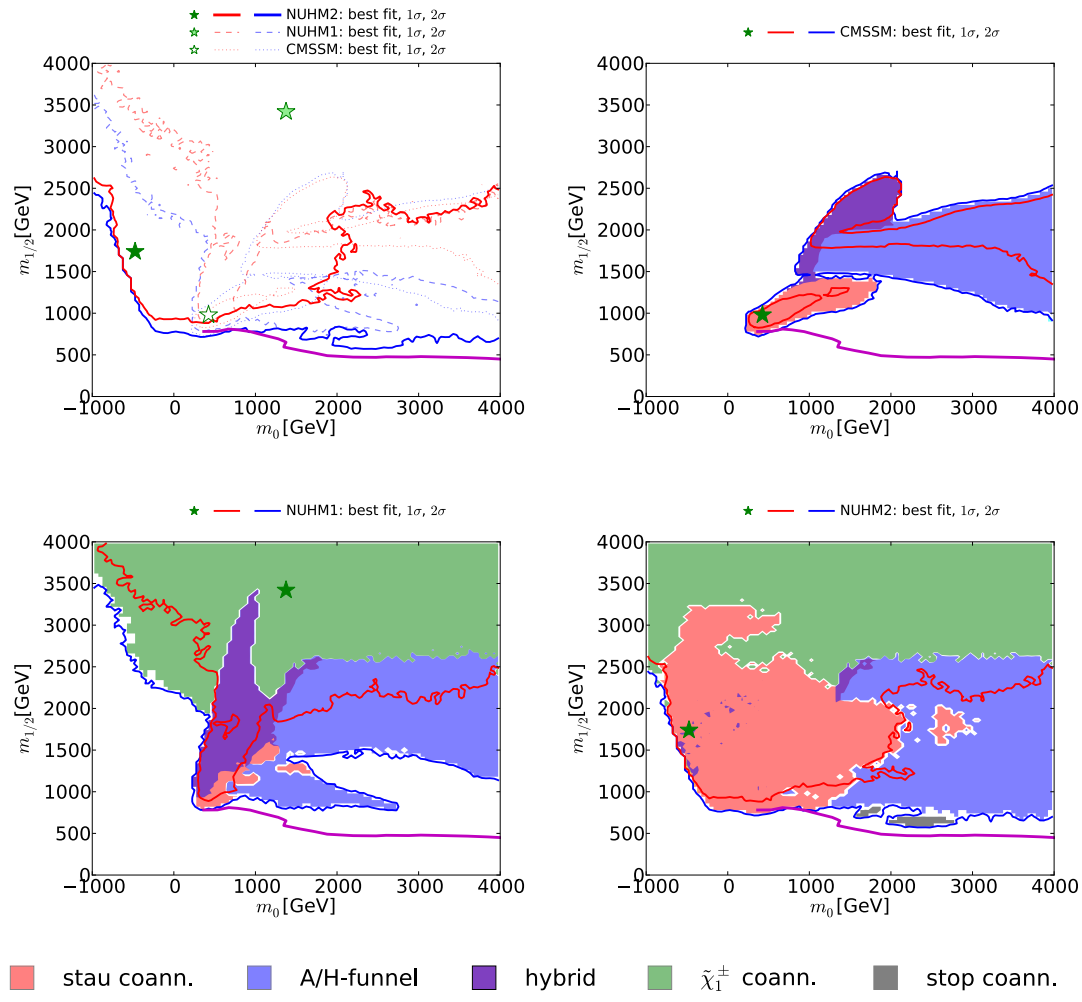

Figure 4.9: *The $(m_0, m_{1/2})$ in the CMSSM, NUHM1, and NUHM2. The top left panel displays the 68% (95%) CL contours using red (blue) lines for the NUHM2 (solid), NUHM1 (dashed) and CMSSM (dotted). Their respective best-fit points are shown in using filled, light green-filled and empty stars. The top right, bottom left and bottom right panels show the individual plots for the CMSSM, NUHM1, and NUHM2 respectively, and the contours, green stars and coloured shading have the same significations as in Fig. 4.1. Furthermore, a magenta line indicates the 95% CL exclusion contour from the* jets $+ \not{E}_T$ *search [121].*

(NUHM2), cf. section 2.3. In the $\tilde{\chi}_1^\pm$ coannihilation region we find that $\mu \sim 1000$ GeV, whereas $M_1 \gtrsim \mu + 250$ GeV. This results in nearly mass degenerate Higgsino-like $\tilde{\chi}_1^0$, $\tilde{\chi}_2^0$, and $\tilde{\chi}_1^\pm$, so that $\tilde{\chi}_1^\pm$ coannihilation is indeed the dominant DM mechanism. We also note that values of m_0^2 are allowed to be negative in the $\tilde{\chi}_1^\pm$ coannihilation region in both the

NUHM1 and the NUHM2.

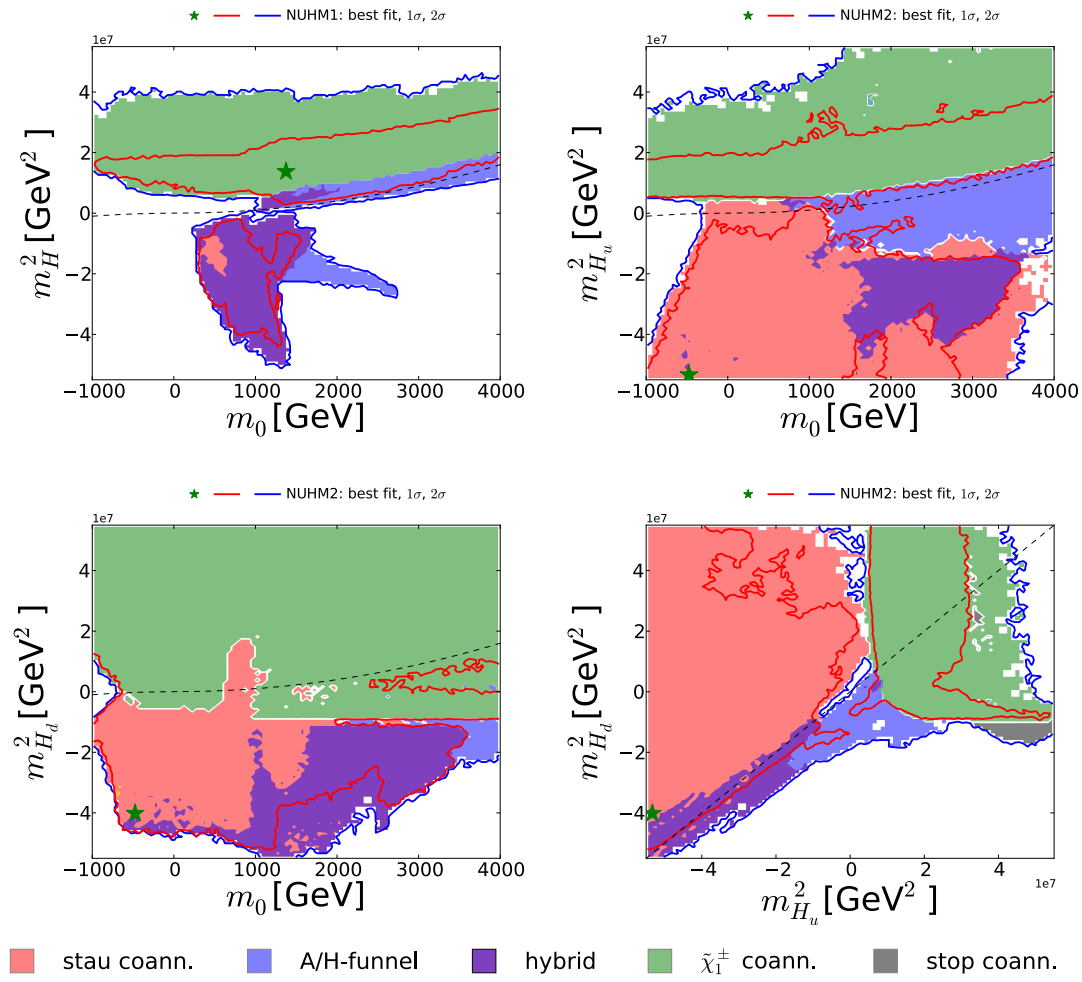

Figure 4.10: *Comparison between $m_{H_u}^2$, $m_{H_d}^2$, and m_0 in the NUHM1 and NUHM2. The top left panel shows the (m_0, m_H^2) plane of the NUHM1, and the top right, bottom left and bottom right panels show the $(m_0, m_{H_u}^2)$, $(m_0, m_{H_d}^2)$, and $(m_{H_u}^2, m_{H_d}^2)$ planes, respectively. The contours, green stars and coloured shading have the same significations as in Fig. 4.1. To guide the eye dashed black lines indicate where $m_{H_{u,d}}^2 = m_0^2$ in the NUHM1 and NUHM2 or where $m_{H_u}^2 = m_{H_d}^2$ in the NUHM2.*

Turning back to Fig. 4.9 we observe that in the NUHM1 the hybrid mechanism is preferred over stau coannihilation at low values of m_0 and $m_{1/2}$, whereas in the NUHM2 stau coannihilation is the preferred mechanism for DM annihilation for these low masses. This effect can also be understood if we look at Fig. 4.10. From the (m_0, m_H^2) plane in the

NUHM1 (top left) we see that the negative values of $m^2_{H_{u,d}}$ allows for the hybrid mechanism to occur at low masses of m_0 and $m_{1/2}$. In the NUHM2, we see the same preference along the degeneracy line of $m^2_{H_u} = m^2_{H_d}$ in the $(m^2_{H_u}, m^2_{H_d})$ plane (bottom right). On the other hand, stau coannihilation becomes the preferred mechanism for $m^2_{H_u} < m^2_{H_d}$ and it can also be achieved at negative values of m^2_0.

Next, we consider the A/H funnel region. We first note the we retrieve the CMSSM-like region in the $(m_0, m_{1/2})$ plane of the NUHM1, located at $m_0 \gtrsim 1500$ GeV and $m_{1/2} \gtrsim 1500$ GeV. Indeed, these points lie along the degeneracy line where $m^2_H = m^2_0$ in the (m_0, m^2_H) plane. Note however that in the NUHM1 an additional region becomes available at $m_{1/2} \lesssim 1500$ GeV and $m_0 \lesssim 3000$ GeV. The (m_0, m^2_H) plane in Fig. 4.1 reveals that this region is located at negative m^2_H: roughly -2×10^{10} GeV^2. In the $(m_0, m_{1/2})$ plane of NUHM2 we see that this region extends further. The $(m^2_{H_u}, m^2_{H_d})$ of the NUHM2 shows that $m^2_{H_d}$ is predominantly negative, whereas $m^2_{H_u}$ takes both positive and negative values.

We now turn to Table 4.3, which lists the parameters of the best-fit points in the CMSSM, NUHM1 and NUHM2 for the stau coannihilation/hybrid, A/H funnel, and $\tilde{\chi}^{\pm}_1$ coannihilation, as well as their total χ^2, the number of degrees of freedom (d.o.f.) and the corresponding χ^2-probability. Note that the global χ^2 minimum in the NUHM1 corresponds to $\tilde{\chi}^{\pm}_1$ coannihilation and in the NUHM2 it corresponds to stau coannihilation although the latter is almost negligibly favoured over $\tilde{\chi}^{\pm}_1$ coannihilation. Also note that the best-fit point of the A/H funnel region of the NUHM1 is located at negative m^2_H, whereas in the NUHM2 $m^2_{H_u} \sim m^2_{H_d} > m^2_0$.

4.3.2 The χ^2 Functions

In this section we highlight some differences between the χ^2 function of the CMSSM, NUHM1, and NUHM2. We restrict our attention to the DM mechanisms that minimise the overall χ^2 function in the NUHM1 and NUHM2: the stau coannihilation, hybrid, and $\tilde{\chi}^{\pm}_1$ coannihilation mechanisms.

The variation of the χ^2 function in the parameter space for the different DM mechanisms is well reflected in the $m_{1/2}$ profile likelihood functions. In Fig. 4.11 we compare the breakdown of the total χ^2 into individual contributions along the $m_{1/2}$ profile likelihood function for points satisfying the stau coannihilation metric in the CMSSM (left) and NUHM2 (right), and points satisfying the hybrid metric in the NUHM1 (middle). The ordering of the (groups of) constraints and the colours used are specified in the legend.

Parameter	CMSSM			NUHM1			NUHM2		
	$\tilde{\tau}_1$ Coann.	H/A funnel	$\tilde{\chi}_1^\pm$ Coann.	Hybrid	H/A Funnel	$\tilde{\chi}_1^\pm$ Coann.	$\tilde{\tau}_1$ Coann.	H/A Funnel	$\tilde{\chi}_1^\pm$ Coann.
m_0 [GeV]	430	5650	5990	470	470	1380	-470	1940	720
$m_{H_u}^2$ [GeV^2]	m_0^2	m_0^2	m_0^2	-2.54×10^7	-1.90×10^7	1.33×10^7	-5.10×10^7	9.65×10^6	7.98×10^6
$m_{H_d}^2$ [GeV^2]	m_0^2	m_0^2	m_0^2	$m_{H_u}^2$	$m_{H_u}^2$	$m_{H_u}^2$	-4.11×10^7	8.13×10^6	4.57×10^7
$m_{1/2}$ [GeV]	970	2100	2220	1270	1070	3420	1700	2620	2820
A_0 [GeV]	-3020	780	2820	-5700	-4950	3140	-4890	900	1580
$\tan\beta$	14.0	51.0	43.0	11.0	10.0	39.0	20.0	42.0	29.0
χ^2	35.0	35.1	38.2	33.2	33.8	32.7	32.6	33.8	32.6
d.o.f.	24	24	24	23	23	23	22	22	22
χ^2-probability	6.8%	6.7%	3.3%	7.8%	6.8%	8.6%	6.9%	5.1%	6.8%

Table 4.3: *The m_0, $m_{H_u}^2$, $m_{H_u}^2$, A_0, and $\tan\beta$ parameters, as well as the total χ^2, the d.o.f., and the associated χ^2-probability for the CMSSM, NUHM1, and NUHM2 best-fit points that fulfil stau coannihilation (or hybrid), A/H funnel, $\tilde{\chi}_1^\pm$ coannihilation metrics.*

It is interesting to see that our fit of the CMSSM cannot fulfil the $\Omega_{\rm CDM}h^2$ (orange) and BR($B_{s,d} \to \mu^+\mu^-$) constraints (green) for $m_{1/2} \gtrsim 1250$ GeV, whereas our fit of the NUHM1 has a smaller χ^2 contribution from the BR($B_{s,d} \to \mu^+\mu^-$) constraint and the contribution is negligible in the NUHM2. As we saw in section 2.5.6, the SUSY contribution to BR($B_{s,d} \to \mu^+\mu^-$) can be sizable at low values of M_A and large values of $\tan\beta$. Inspecting three representative points from each model at $m_{1/2} \sim 1500$ GeV we see that $\tan\beta \sim 44$ in the CMSSM, $\tan\beta \sim 16$ for the NUHM1 and $\tan\beta \sim 21$ in the NUHM2. Comparing the NUHM1 and NUHM2 points, we see that their parameters are very similar, except for m_0 being smaller in the NUHM2, where the contribution from the $(g-2)_\mu$ constraint is smaller, and $m_{H_u}^2$ being smaller than $m_{H_d}^2$ so that M_A moves upwards. This exemplifies the effect of the additional freedom in $m_{H_{u,d}}^2$ in the NUHM1 and NUHM2: M_A and $\tan\beta$ are less constrained so that BR($B_{s,d} \to \mu^+\mu^-$) can be fulfilled. We finally note that comparing the local minimum at $m_{1/2} \sim 1000$ GeV in the CMSSM and the NUHM1, it is mainly the BR($B \to X_s\gamma$) (blue) constraint that differs.

We now turn to Fig. 4.12 where we display the analogous χ^2 breakdown for model points along the $m_{1/2}$ profile likelihood functions restricted to points fulfilling the $\tilde{\chi}_1^\pm$ coannihilation mechanism in the CMSSM (left), NUHM1 (middle), and NUHM2 (right). This figure illustrates once more that our fit of the CMSSM cannot accommodate $\tilde{\chi}_1^\pm$ coannihilation at sufficiently low $\sigma_p^{\rm SI}$, whereas this does become possible in the NUHM1 and NUHM2 at $m_{1/2} \gtrsim 2500$ GeV. In the NUHM1 and NUHM2 μ can be significantly lower than M_1 at these high values of $m_{1/2}$ yielding an almost purely Higgsino like LSP.

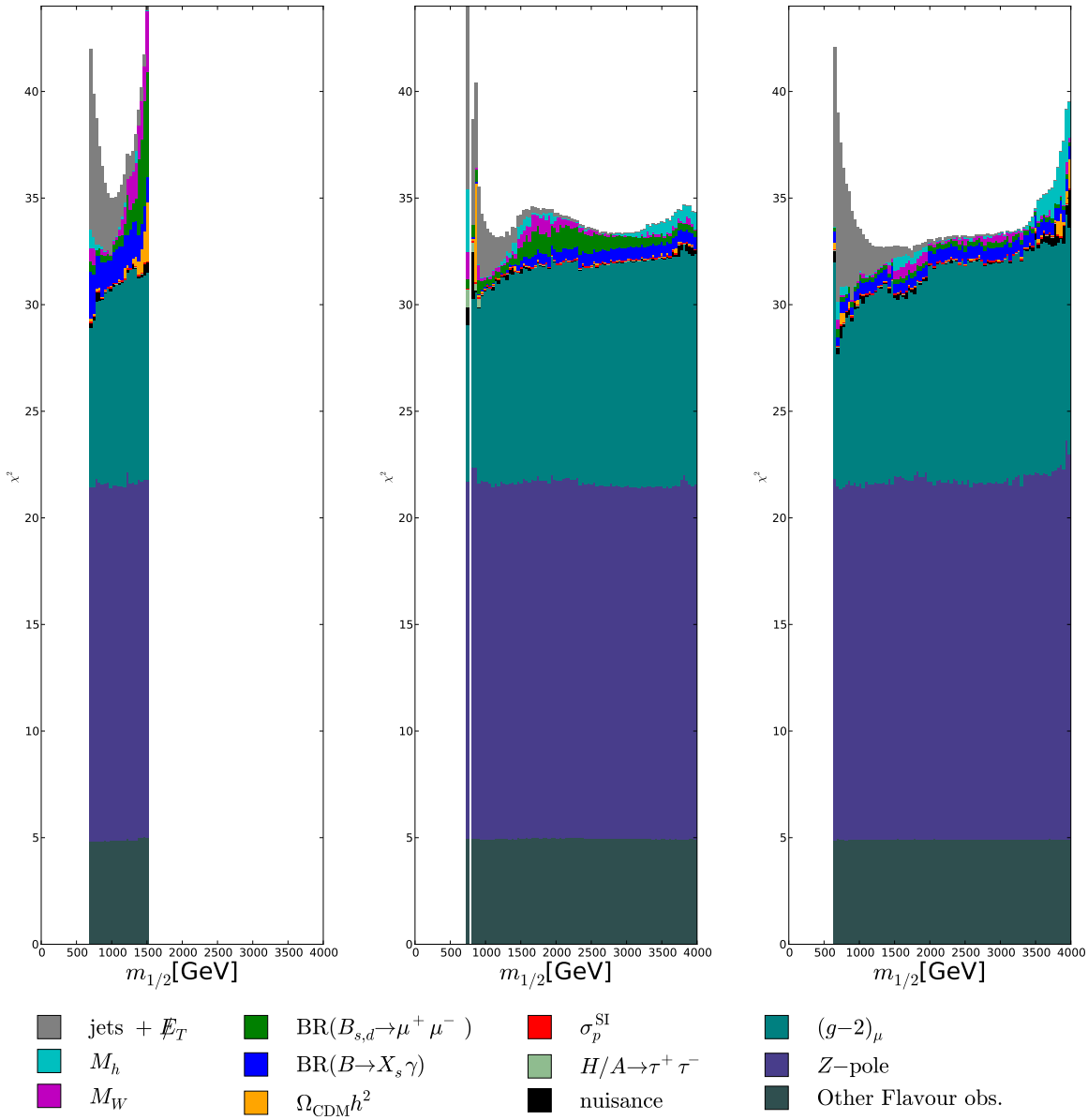

Figure 4.11: *Breakdown in individual contributions of the total χ^2 function for model points along the profile likelihood function of $m_{1/2}$ for points satisfying the* ***stau coannihilation metric*** *in the CMSSM (left) and the NUHM2 (right), and for points satisfying the* ***hybrid metric*** *in the NUHM1 (middle). The ordering of the (groups of) constraints and the colours used are specified in the legend.*

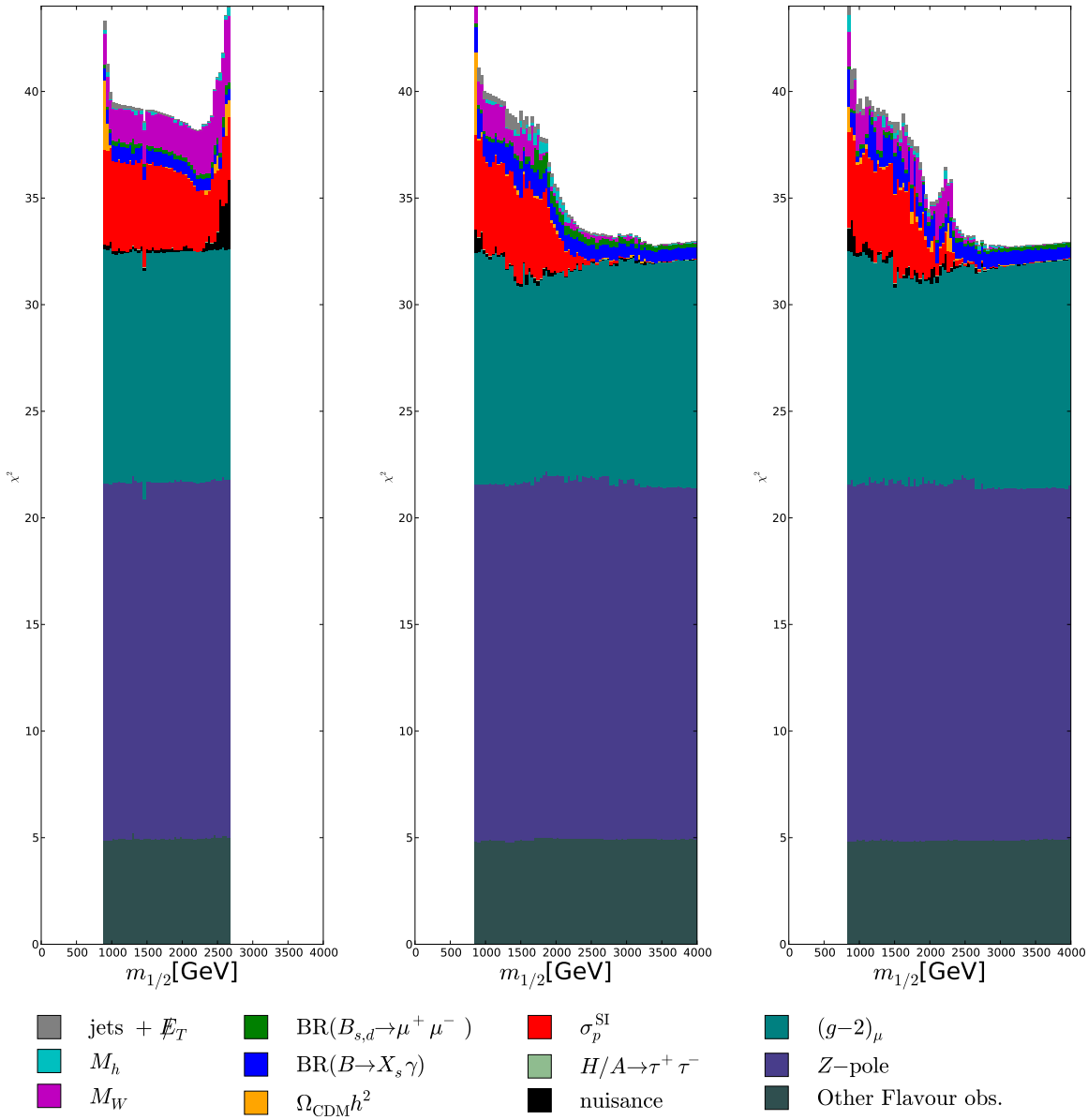

Figure 4.12: *Breakdown in individual contributions of the total χ^2 function for model points along the profile likelihood function of $m_{1/2}$ for points fulfilling the of the* $\tilde{\chi}_1^\pm$ ***coannihilation metric*** *in the CMSSM (left), the NUHM1 (middle) and the NUHM2 (right). The ordering of the (groups of) constraints and the colours used are specified in the legend.*

4.3.3 Predictions for Physical Observables

Masses

In Fig. 4.13 we compare the mass predictions of the CMSSM (dotted line), NUHM1 (dashed line), and NUHM2 (solid line). In these line styles we display the profile likelihood functions for $m_{\tilde{g}}$, $m_{\tilde{q}_R}$, $m_{\tilde{t}_1}$, $m_{\tilde{b}_1}$, $m_{\tilde{\ell}_R}$, $m_{\tilde{\tau}_1}$, $m_{\tilde{\chi}_1^0}$, $m_{\tilde{\chi}_1^\pm}$, and M_A from the left to right and from top to bottom.

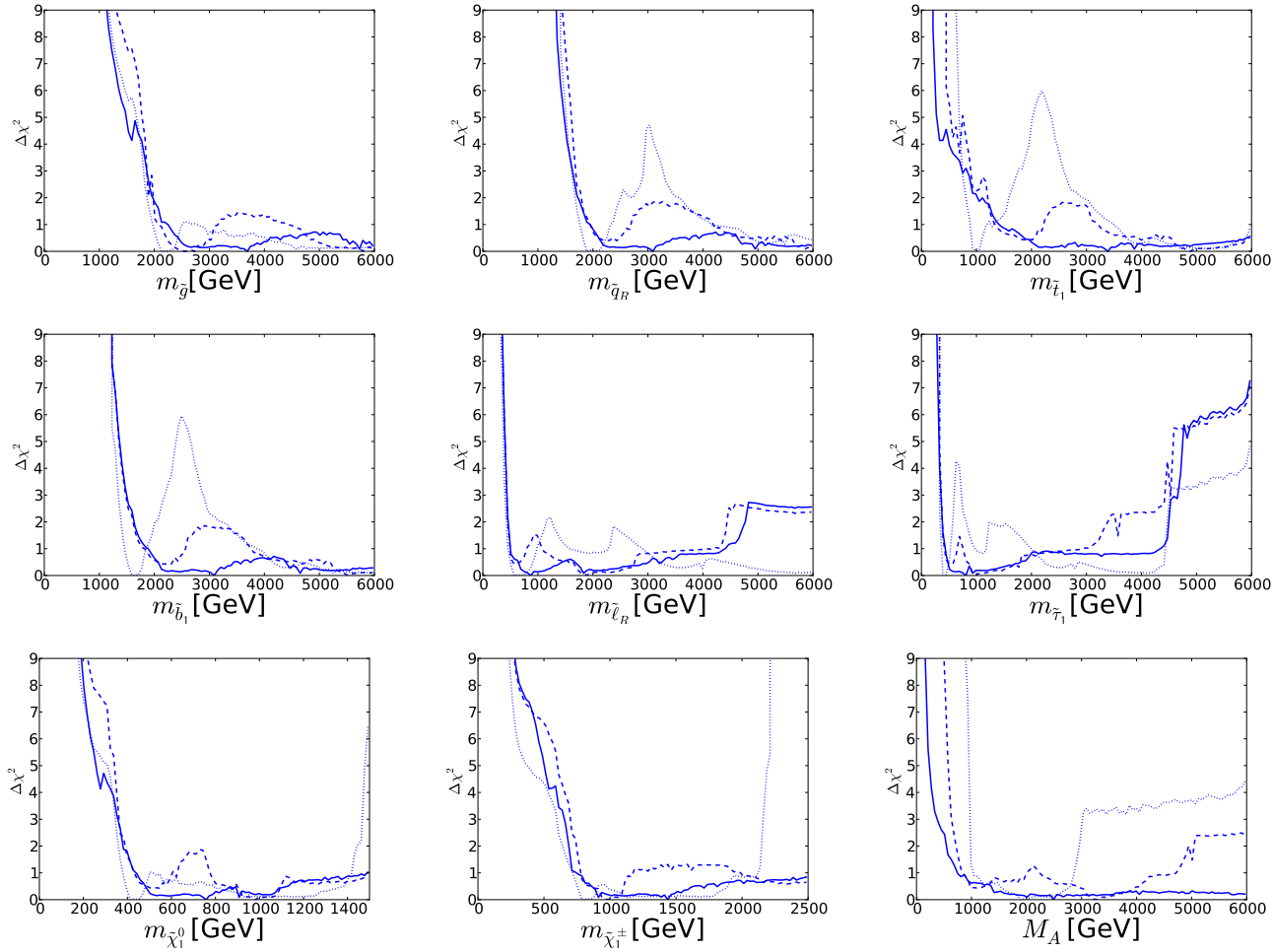

Figure 4.13: *Profile likelihood functions for a selection of sparticle masses in the CMSSM (dotted), the NUHM1 (dashed), and NUHM2 (solid).*

Starting with $m_{\tilde{g}}$, we see that the three models give very similar predictions. The 95% CL lower bound is located at ~ 1750 GeV. This lower bound is mainly driven by the jets $+ \not{E}_T$ constraint via $m_{1/2}$. For values of $m_{\tilde{g}} \lesssim 1700$ GeV the contribution from this

constraint is lowered by moving to high values of m_0, resulting in a larger contribution from $(g-2)_\mu$. There is no upper bound visible in the displayed range.

The profile likelihood function for the average over the first two generations right-handed squarks $m_{\tilde{q}_R}$ reveals again the very separated stau coannihilation region in the CMSSM at $m_{\tilde{q}_R} \sim 2000$ GeV, as opposed to the NUHM1 and NUHM2, where the hybrid and stau coannihilation regions are less constrained from above by the $B_{s,d} \to \mu^+\mu^-$ and $B \to X_s\gamma$ constraints. Nonetheless, the lower bound on $m_{\tilde{q}_R}$ at 95% CL is very similar in the three models, namely $m_{\tilde{q}_R} \gtrsim 1650$ GeV.

The profile likelihood functions for $m_{\tilde{t}_1}$ and $m_{\tilde{b}_1}$ show very similar features as that of the $m_{\tilde{q}_R}$, although the low mass features differ somewhat for the stop mass. The CMSSM has a clear local minimum, which is also the global minimum, at $m_{\tilde{t}_1} \sim 1000$ GeV and $m_{\tilde{b}_1} \sim 1600$ GeV. In the NUHM1 (NUHM2) there is a small downward tick at $m_{\tilde{t}_1} \sim 570$ (330) GeV, corresponding to the stop coannihilation region.

The lower bounds on the right-handed slepton ($\sim$ 400 GeV) and stau masses ($\sim$ 330 GeV) are again very similar for the three models. Note that for masses $m_{\tilde{\ell}_R,\tilde{\tau}_1} \gtrsim$ 4500 GeV the NUHM1 and NUHM2 profile likelihood functions only contain CMSSM points. This is because in our fit of the CMSSM, the m_0 parameter is sampled up to 6 TeV as opposed to 4 TeV in the NUHM1 and NUHM2. One could envisage that the profile likelihood functions of the NUHM1 and NUHM2 would minimise further if m_0 was scanned in a larger range.

We now turn to the profile likelihood functions of the lightest neutralino and chargino masses. We note that at low masses the profile likelihood function for $m_{\tilde{\chi}_1^0}$ follows that of $m_{\tilde{\tau}_1}$ for the three models, because these points fulfil $\Omega_{\rm CDM}h^2$ by the stau coannihilation and hybrid mechanisms. In the NUHM1 and NUHM2 there is also an interval where $m_{\tilde{\chi}_1^0}$ follows $m_{\tilde{\chi}_1^\pm}$ for points of the $\tilde{\chi}_1^\pm$ coannihilation region.

Finally, we turn to the profile likelihood function for M_A. We see that the lower bound is quite different in the three different models. This is due to the $\tan\beta$ dependence of the $H/A \to \tau^+\tau^-$ constraint, cf. the discussion of the $(M_A, \tan\beta)$ plane below. In the CMSSM masses $\gtrsim$ 3000 GeV are somewhat disfavoured and correspond to the focus point and $\tilde{\chi}_1^\pm$ coannihilation regions, which receive a sizable χ^2 contribution from $\sigma_p^{\rm SI}$. In the NUHM1 and NUHM2 these values are also in the $\tilde{\chi}_1^\pm$ coannihilation region and are respectively less constrained by M_W.

For reference we provide a table with masses of the best-fit points in the CMSSM, NUHM1 and NUHM2 for the stau coannihilation/hybrid, A/H funnel, and $\tilde{\chi}_1^\pm$ coannihilation in Table 4.4.

	CMSSM			NUHM1			NUHM2		
	$\tilde{\tau}_1$	H/A	$\tilde{\chi}_1^\pm$	Hybrid	H/A	$\tilde{\chi}_1^\pm$	$\tilde{\tau}_1$	H/A	$\tilde{\chi}_1^\pm$
[GeV]	Coann.	Funnel	Coann.		Funnel	Coann.	Coann.	Funnel	Coann.
$m_{\tilde{g}}$	2130	4620	4870	2750	2350	6890	3670	5400	5740
$m_{\tilde{q}_R}$	1900	6680	7070	2410	2080	6010	3080	4970	4920
$m_{\tilde{t}_1}$	970	4700	5000	2030	1740	4860	3420	3910	3860
$m_{\tilde{b}_1}$	1580	5230	5750	2330	2010	5560	3060	4480	4620
$m_{\tilde{\ell}_R}$	560	5690	6040	660	610	1870	880	2150	1850
$m_{\tilde{\tau}_1}$	410	4080	4900	560	540	1000	780	1580	920
$m_{\tilde{\chi}_1^0}$	410	940	930	550	460	980	760	1160	910
$m_{\tilde{\chi}_1^\pm}$	790	1130	940	1050	880	980	1430	1430	920
M_A	1910	2070	3780	1090	930	3250	2470	2450	6500

Table 4.4: *Masses for the CMSSM, NUHM1, and NUHM2 best-fit points that fulfil stau coannihilation (or hybrid), A/H funnel, $\tilde{\chi}_1^\pm$ coannihilation metrics.*

M_h, $(g-2)_\mu$, and $\mathrm{BR}_{B_{s,d}\to\mu^+\mu^-}^{\mathrm{EXP/SM}}$

In Fig. 4.14 we show the one-dimensional profile likelihood functions for the lightest Higgs mass (left panel), $(g-2)_\mu$ (middle panel), and $\mathrm{BR}_{B_{s,d}\to\mu^+\mu^-}^{\mathrm{EXP/SM}}$ (right panel) for the CMSSM (dotted blue), the NUHM1 (dashed blue), and the NUHM2 (solid blue). Red lines indicate the individual contribution from their corresponding constraints.

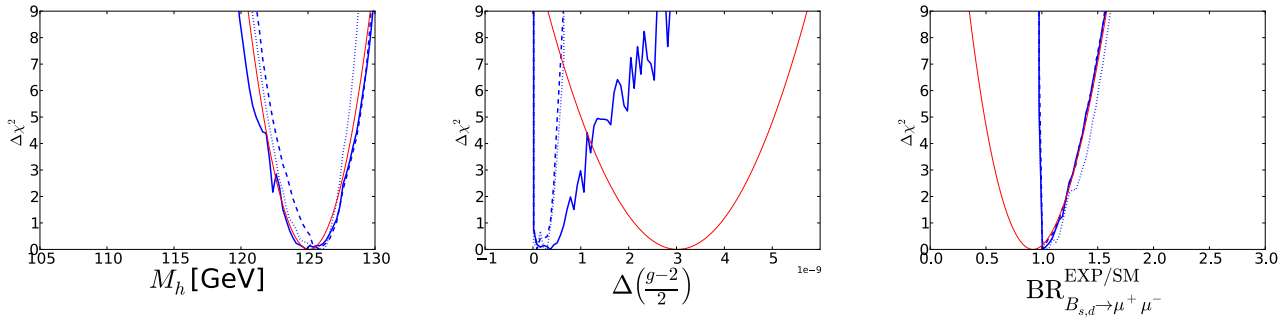

Figure 4.14: *Profile likelihood functions for M_h, $(g-2)_\mu$, and $\mathrm{BR}_{B_{s,d}\to\mu^+\mu^-}^{\mathrm{EXP/SM}}$ in the CMSSM (dotted blue), the NUHM1 (dashed blue), and NUHM2 (solid blue). The value of the χ^2 contributions of the corresponding constraints is depicted in red.*

In the left panel see that the profile likelihood functions for the Higgs mass closely follow the χ^2 contribution of the constraint. Only the profile likelihood function of the NUHM2 is lower for values lower than $M_h < 125.7$. This is due to a decreasing contribution

from the $(g-2)_\mu$ constraint with decreasing M_h where points correspond to the slepton coannihilation region. This effect is also visible in the profile likelihood function for $(g-2)_\mu$ in the middle panel. It illustrates that the SUSY contributions to $(g-2)_\mu$ can even take values as high as the measured value, however, at the expense of not fulfilling the M_h constraint. Our fits of the CMSSM and NUHM1, on the other hand, can not accommodate the $(g-2)_\mu$ constraint in the same way. Their profile likelihood functions highlight the tension between the jets $+ \not{E}_T$ and M_h constraints on the one hand and the $(g-2)_\mu$ constraint on the other hand.

The profile likelihood function for $\mathrm{BR}^{\mathrm{EXP/SM}}_{B_{s,d}\to\mu^+\mu^-}$ follows closely the experimental constraint, indicating that sum over the other constraints is rather constant. However, we recall that $\mathrm{BR}^{\mathrm{EXP/SM}}_{B_{s,d}\to\mu^+\mu^-}$ plays an important role in shaping the parameter space, cf. section 4.2.2.

$(M_A, \tan\beta)$ Plane

In Fig. 4.15 we display the $(M_A, \tan\beta)$ planes of the CMSSM, NUHM1 and NUHM2. In the top left panel their 68% (95%) CL contours are overlaid with red (blue) dotted, dashed and solid lines, respectively. The locations of the best-fit point points are indicated with empty, light green filled and solid green filled green stars, respectively. In top right, bottom left, and bottom right panels we display the coloured planes (using the same significations as in Fig. 4.1) for the CMSSM, NUHM1, and NUHM2 respectively. To guide the eye, the 95% CL exclusion contour from the $H/A \to \tau^+\tau^-$ search at ATLAS [125] is indicated with a magenta line in of the each panels.

Fig. 4.15 illustrates nicely the effective additional freedom in M_A or (and) μ in the NUHM1 (NUHM2). We first compare the hybrid and A/H funnel regions in the CMSSM and NUHM1. In the CMSSM, the condition that $m_{\tilde{\chi}_1^0} \sim 0.5 M_A$ is only fulfilled for larger values of $42 \lesssim \tan\beta \lesssim 55$ whereas in the NUHM1 $\tan\beta$ can take any value between ~ 5 and ~ 60. This can be attributed to the effective freedom in the NUHM1 to choose M_A. Note, however, that the hybrid and A/H funnel regions in the CMSSM and NUHM1 still favour $M_A \lesssim 3000$ GeV. At larger values of M_A the $\tilde{\chi}_1^\pm$ coannihilation mechanism is preferred and we see again that the allowed ranges for $\tan\beta$ in the NUHM1 are larger than in the CMSSM. This can be attributed to the effective freedom in μ in the NUHM1, whilst being restricted to the M_A values of the CMSSM. In the NUHM2 these restrictions are lifted and the hybrid, A/H funnel, $\tilde{\chi}_1^\pm$ coannihilation mechanisms are preferred throughout the $(M_A, \tan\beta)$ plane. The same considerations apply to regions where the stau coannihilation mechanism is preferred.

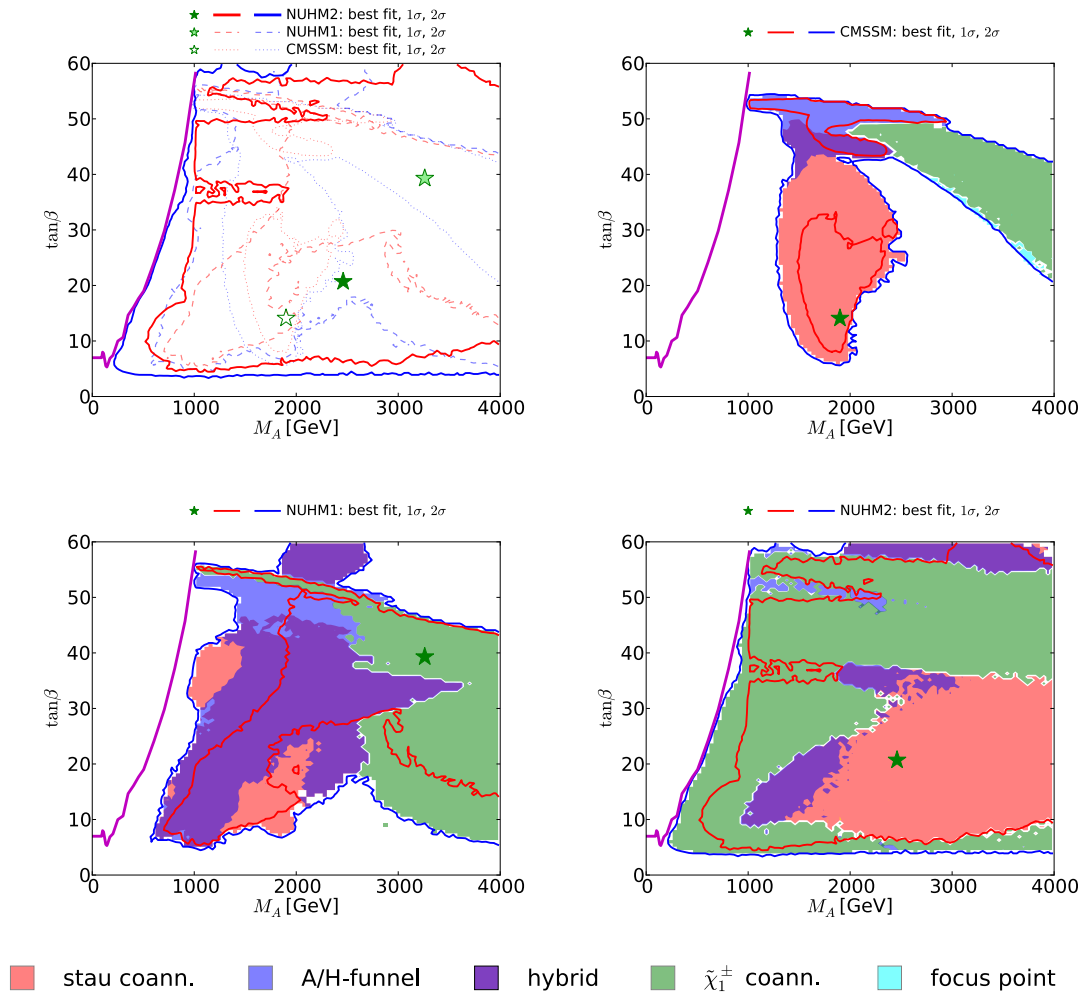

Figure 4.15: *The $(M_A, \tan\beta)$ plane in the CMSSM, NUHM1, and NUHM2. In the top left panel their 68% (95%) CL contours are overlaid with red (blue) dotted, dashed and solid lines, respectively. The position of the best-fit points are indicated with empty, light green filled and solid green filled green stars, respectively. The top right, bottom left, and bottom right panels display the coloured planes (using the same significations as in Fig. 4.1) for the CMSSM, NUHM1, and NUHM2, respectively. To guide the eye, the 95% CL exclusion contour from the $H/A \to \tau^+\tau^-$ search at ATLAS [125] is indicated with a magenta line in of the each panels.*

Direct Detection of Dark Matter

Finally, we turn to the $(m_{\tilde{\chi}_1^0}, \sigma_p^{\rm SI})$ planes for the CMSSM, NUHM1, and NUHM2 in Fig. 4.16. The disposition of the planes and the significations of the contours, stars and coloured shading is analogous to that of Fig. 4.15, with the addition that the green shaded

region is excluded at 90% CL by LUX [23] and XENON100 [22], whereas the dashed orange lines indicate the neutrino floor below which backgrounds from neutrinos are expected to dominate over a dark matter signal (yellow shaded) [172]. We see that with the additional degrees of freedom in $m^2_{H_{u,d}}$ the NUHM1 and NUHM2 reach to cross-sections below the neutrino floor. For these models we see again that the $\tilde{\chi}^{\pm}_1$ coannihilation region should be in reach for future direct detection experiment, even though the corresponding sparticle masses would be far beyond the reach of the LHC with 300 fb^{-1} or even 3000 fb^{-1}. The stau coannihilation and hybrid regions, on the other hand, have very low cross-sections.

4.4 Interlude

In this chapter we discussed the results of our global fits of the CMSSM, NUHM1, and NUHM2, paying particular attention to the characterisation of the regions in the parameter space according to the mechanisms that underlie fulfilment of the relic density constraint. We found that the allowed parameters in 68% and 95% CL regions often extend beyond the sampled ranges, reflecting that the χ^2 function varies only modestly throughout the parameter space. We considered the contributions of individual constraints and found that in particular the individual constraint from $(g-2)_\mu$ has rather large contribution between ~ 7.5 and ~ 10.2: a good fulfilment of the $(g-2)_\mu$ constraint is in tension with the constraints arising from M_h and searches for jets $+ \not{E}_T$ at the LHC. This tension can be understood from the implicit lower bound on smuon masses, which are related to squark and gluino masses via the unified m_0 and $m_{1/2}$ parameters at the GUT scale, as well as the preference for heavy stop masses to obtain the measured value of M_h. These considerations motivate to also consider phenomenological models where no assumptions are made about the extrapolation of model soft SUSY breaking parameters at the GUT scale and this is the topic of the next chapter.

4.5 Discussion

We now discuss the similarities and differences between our fit of the CMSSM and the NUHM1 [43] (December 2013) and of the NUHM2 [44] (August 2014) with Fittino [32] (April 2012), BayesFITS [48] (February 2013), and SuperBayes [56] (December 2012). In general, our results of the are similar to those of other groups, although our sampling of the NUHM1 and NUHM2 seems more complete. Our results are also the most up-to-date.

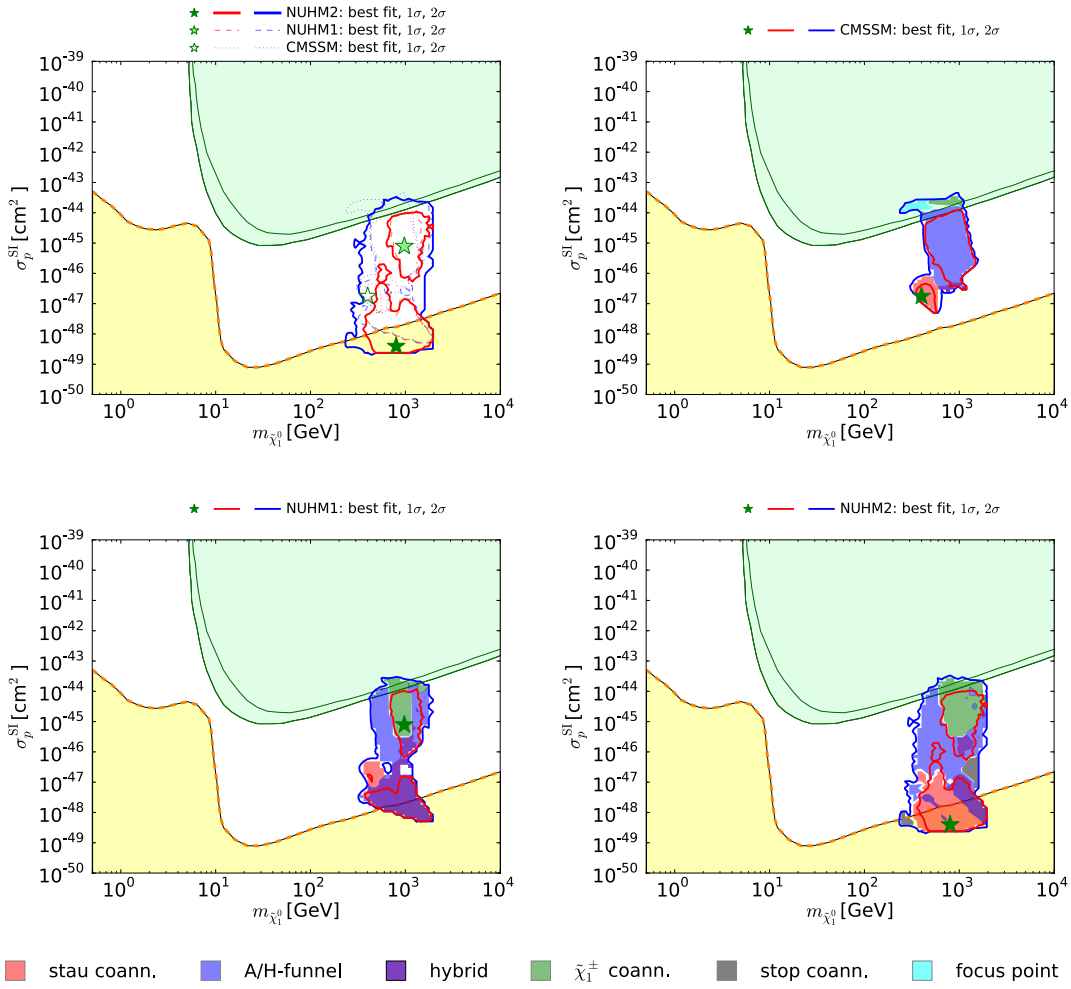

Figure 4.16: *The $(m_{\tilde{\chi}_1^0}, \sigma_p^{\rm SI})$ plane in the CMSSM, NUHM1, and NUHM2. The disposition of the planes and the significations of the contours, stars and coloured shading is analogous to that of Fig. 4.15, with the addition that the green shaded region is excluded at 90% CL by LUX [23] and XENON100 [22], whereas the dashed orange lines indicate the neutrino floor below which backgrounds from neutrinos are expected to dominate over dark matter signal (yellow shaded) [172].*

One of the important features in this thesis is the visual identification of the dominant DM annihilation mechanisms. Other groups identify and discuss these mechanisms as well, but it is not displayed so explicitly.

We turn to the $(m_0, m_{1/2})$ plane of the CMSSM in Fig. 7(a) of Ref. [32], which shows the Fittino fit assuming an (at that time tentative) measurement of the Higgs mass at

$M_h = 126$ GeV. We see that the stau coannihilation region at low values of m_0 and $m_{1/2}$ is very similar to that of our fit, cf. Fig. 4.1, although the separation between the stau coannihilation region and A/H funnel is less well defined. This can be understood from the $B_{s,d} \to \mu^+\mu^-$ constraint that became more stringent with the first evidence reported in November 2012 by LHCb [174]. The A/H funnel region, on the other hand, does not extend to large values of m_0. One explanation is that the current constraints are more stringent than those in April 2012 so that the current 95% CL regions were more disfavoured at that time. Another possibility is that their sampling algorithm missed this region. Fittinos $(A_0, \tan\beta)$ plane in Fig. 7(b) of Ref. [32] looks similar to ours in Fig. 4.1. In Fittinos $(m_0, m_{1/2})$ plane of the NUHM1, displayed in Fig. 12(a), the 68% CL region appears to be in the stau coannihilation region. The A/H funnel region also seems to appear at the 95% CL. However, the $\tilde{\chi}_1^\pm$ coannihilation region seems to be missing or is at least incomplete. This could be due to the earlier status of the constraints, but it might well be that the Metropolis algorithm did not properly sample this annihilation region.

Fig. 4(a) in Ref. [48] displays the $(m_0, m_{1/2})$ plane of BayesFITS. It reveals that there is a focus point region (where chargino coannihilation is possibly the dominant mechanism) preferred at $m_0 \gtrsim 6$ TeV, i.e. beyond our scanned range. This region did not show up in our fits because it is disfavoured by constraints on $\sigma_p^{\rm SI}$, as can be seen in section 4.8, which BayesFITS did not include. On the other hand, it is mentioned in Ref. [48] that at very high values of m_0 the LSP becomes almost purely Higgsino, which would yield low values of $\sigma_p^{\rm SI}$. It would be interesting to extend the scan ranges of m_0 and $m_{1/2}$ for our fit of the CMSSM, although this is beyond the scope of this thesis. We do not discuss the BayesFITS results of the NUHM, since there is no comparable Bayesian or frequentist analysis of this model in Ref. [48].

Fig. 1 in Ref. [56] show the 68%, 95%, and 99% credible regions results for flat priors (top row) and for log priors (middle row), and the 68%, 95%, and 99% CL intervals (bottom row) in the $(m_{1/2}, m_0)$ (left), $(\tan\beta, A_0)$ (middle), and $(m_{\tilde{\chi}_1^0}, \sigma_p^{\rm SI})$ (right) planes for SuperBayes. Fig. 4 displays the results when the $(g-2)_\mu$ constraint is dropped, where the panels have the same disposition as in Fig. 1. It is interesting to note that with flat priors, the A/H funnel region is preferred, with log priors both the A/H funnel and stau coannihilation region is preferred, whereas in the profile likelihood functions the stau coannihilation region is preferred. The latter also reveals that the $(g-2)_\mu$ constraint strongly favours the stau coannihilation region, more so than in our fit. This could be a result of the implementation of the of the null results from searches for jets + $\not{E}_T$: SuperBayes imposed the 95% CL exclusion contour as a rigid cut instead of modelling the

parameter dependence. Indeed, when the $(g-2)_\mu$ constraint is dropped, as shown in Fig. 4, the profile likelihood function is more similar to ours. In the profile likelihood function in the $(m_0, m_{1/2})$ plane (Fig. 4 bottom left) it is apparent that SuperBayes also finds the hybrid region. Finally, we turn that SuperBayes' results for the NUHM2, which are displayed in Fig. 6 in Ref. [56]. It is interesting to note that SuperBayes only seems to find the $\tilde{\chi}_1^\pm$ coannihilation region. Ironically, this is quite the opposite of the findings of Fittino. Our results of the NUHM2, on the other hand, include the stau coannihilation, A/H funnel, hybrid, $\tilde{\chi}_1^\pm$ coannihilation, and even the stop coannihilation region. A possible explanation is found in Table. 7 in Ref. [56], where it seems that the $(g-2)_\mu$ constraint is fulfilled at their best fit point, even very high values of $m_0 = 1500$ GeV and $m_{1/2} = 3800$ GeV, which seems suspicious. Another possibility is that our sampling is more complete thanks to the sampling in boxes.

Chapter 5

The pMSSM10 after LHC Run 1

This chapter contains results that have been published in Ref. [60]. The results for the CMSSM, NUHM1, and NUHM2 shown in this chapter were obtained with updated constraints for the Higgs mass [24], BR($B \to \tau\nu_\tau$) [118], and BR($B \to X_s\gamma$) [119, 120] compared to the analysis in section 4. As outlined in section 3.4 the implementation of constraints based on searches for direct production of SUSY particles at the LHC with 20 fb^{-1} of data at 8 TeV is a central part of this analysis. We refer to the sum of the LHC8$_{\rm col}$, LHC8$_{\rm EWK}$, and LHC8$_{\rm stop}$ constraints as "the LHC8 constraints" and throughout this chapter we facilitate the discussion by comparing the results of the full fit, including the LHC8 constraints, with a fit where these constraints are dropped.

5.1 Parameters and χ^2 Function

We defined the pMSSM10 by setting at the input scale M_{SUSY} the soft SUSY breaking

- gaugino mass parameters M_1, M_2, M_3,
- unified scalar mass parameters for left- and right-handed first- and second-generation squarks $m_{\tilde{q}_{12}}$,
- unified scalar mass parameters for left- and right-handed third-generation squarks $m_{\tilde{q}_3}$,
- unified scalar mass parameters for left- and right-handed first-, second-, and third-generation sleptons $m_{\tilde{\ell}}$,
- unified scalar trilinear couplings A,

as well as

- the pseudo-scalar mass M_A,
- the Higgsino mass parameter μ,

along with the ratio of vacuum expectation values $\tan\beta$. Given the large number of free parameters and the fact that they are closely related to physical masses of sparticles, we restrict the discussion in this section to the interplay between the most important constraints and highlight the parameters that turn out to be most sensitive to these constraints.

One of the most striking features of our fit of the pMSSM10 is that it is possible to fulfil the $(g-2)_\mu$ constraint whilst respecting the constraints from sparticle searches at the LHC. As we mentioned in section 2.5.4, sizable SUSY contributions, and therefore good fulfilment of the $(g-2)_\mu$ constraint, can be achieved by having smuon masses of $\mathcal{O}(100$ GeV). Light chargino masses can contribute, but are not required [93].

Given the importance of the $(g-2)_\mu$ constraint we first turn to Fig. 5.1. In the left panel we display the one-dimensional likelihood function for the SUSY contribution to $(g-2)_\mu$ in the pMSSM10 (solid black line) and compare it to those in the CMSSM (dotted blue), NUHM1 (dashed blue), and NUHM2 (solid blue). A red line shows the χ^2 contribution from the $(g-2)_\mu$ constraint. It is immediately obvious that the tension between the $(g-2)_\mu$ constraint and constraints on lightest Higgs mass and direct searches for SUSY particles, present in the CMSSM, NUHM1, and NUHM2, is not present in the pMSSM10. This is the result of the smuon mass being no longer related to the strongly interacting sparticles via GUT scale relations. However, we do note that SUSY contributions larger than the experimental value have a $\Delta\chi^2$ larger than the contribution from the $(g-2)_\mu$ constraint alone. This is the result of constraints on smuon and selectron production.

To illustrate this, we compare in the right panel of Fig. 5.1 the total χ^2 functions of the pMSSM10 with all constraints applied (solid line), and with the $\chi^2(\mathrm{LHC8_{EWK}})$ set to zero (dashed line). We see that SUSY contributions larger than the measured value are indeed more favoured in the latter case. On the other hand, we also see that the minimum decreases from 83.2 to 82.6, i.e. by only 0.6 units, which confirms the statement that the tension between the $(g-2)_\mu$ constraint and direct SUSY searches is resolved in the pMSSM10.

Another very important feature is that in the 68% CL region, it is the $\tilde{\chi}_1^\pm$ coannihilation annihilation mechanism that governs the fulfilment of the relic density constraint. By

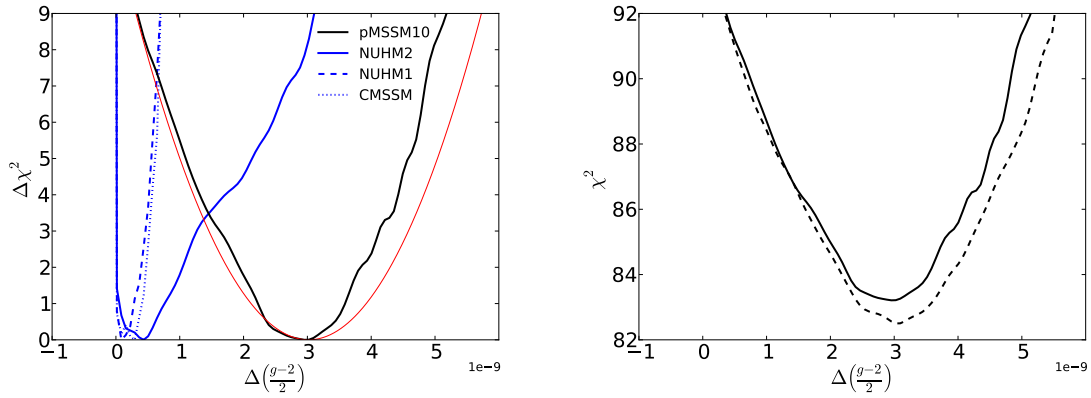

Figure 5.1: *One-dimensional profile likelihood functions for the SUSY contribution to* $(g-2)_\mu$*. The left panel displays likelihood functions in the pMSSM10 (solid black), CMSSM (dotted blue), NUHM1 (dashed blue), and NUHM2 (solid blue), whereas a red line shows the* χ^2 *contribution from the* $(g-2)_\mu$ *constraint. In the right panel the total* χ^2 *functions are shown in the pMSSM10 with all constraints applied (solid line), and with* $\chi^2(LHC8_{EWK})$ *set to zero (dashed line).*

consequence the mass splitting between $m_{\tilde{\chi}_1^\pm} \simeq m_{\tilde{\chi}_2^0}$ and the LSP is small, and correspondingly $M_1 \simeq M_2$.[1] With this configuration $\tilde{\chi}_1^0$ has mainly a Bino composition, $\tilde{\chi}_1^\pm$ and $\tilde{\chi}_2^0$ mainly a Wino composition, and $\tilde{\chi}_3^0/\tilde{\chi}_4^0/\tilde{\chi}_2^\pm$ a Higgsino composition.

To see the interplay between the $(g-2)_\mu$, LHC8 and relic density constraints we turn to Fig. 5.2, where we display the $(m_{\tilde{\mu}_R}, m_{\tilde{\chi}_1^0})$ (left panel) and $(m_{\tilde{\chi}_1^\pm}, m_{\tilde{\chi}_1^0})$ planes (right panel). The red and blue solid (dashed) lines indicate the 68% and 95% CL contours in the case that the LHC8 constraints are (not) applied, and the location of the best-fit point is indicated with a filled (empty) green star. In the $(m_{\tilde{\mu}_R}, m_{\tilde{\chi}_1^0})$ plane we see that the lightest neutralino is constrained to be $m_{\tilde{\chi}_1^0} \lesssim 360$ GeV ($m_{\tilde{\chi}_1^0} \lesssim 470$ GeV), whereas the right-handed smuon is constrained to take values of $m_{\tilde{\mu}_R} \lesssim 800$ GeV ($m_{\tilde{\mu}_R} \lesssim 950$ GeV) at the 68% (95%) CL, when the LHC8 constraints are applied. These well defined ranges for $m_{\tilde{\chi}_1^0}$ and $m_{\tilde{\mu}_R}$, and indeed all sleptons, is the result of good fulfilment of the $(g-2)_\mu$ constraint.

The effect of the LHC8 constraints (most notably the search for direct production of sleptons, cf. Table 3.7) is to disfavour a wedge at low masses, although leaving a strip where the mass splitting $m_{\tilde{\mu}_R} - m_{\tilde{\chi}_1^0}$ is small. Note that in this strip values of $m_{\tilde{\chi}_1^0} \lesssim 150$ GeV are only allowed at 95% CL, where the stau t-channel exchange governs the fulfilment of the dark matter relic density constraint. Consequently $\tilde{\chi}_1^\pm$ coannihilation needs to

[1] $M_1 \simeq M_2$ at the low scale results in $M_1 \simeq 2 \cdot M_2$ at GUT scale.

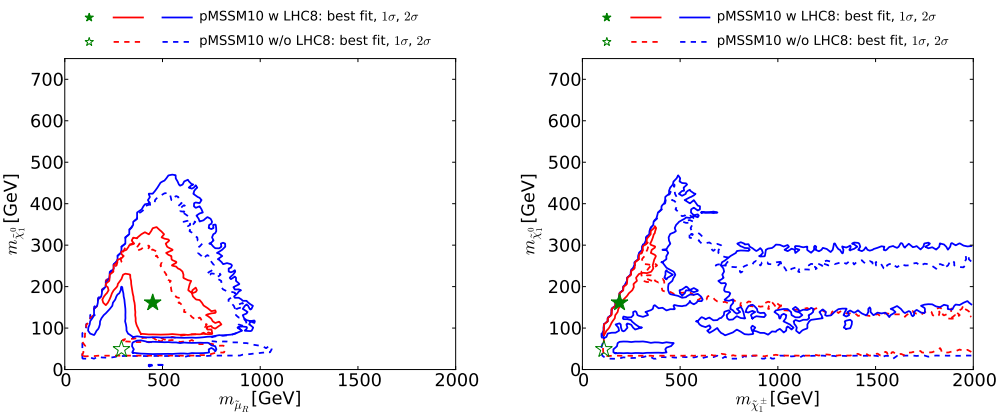

Figure 5.2: *The $(m_{\tilde{\mu}_R}, m_{\tilde{\chi}_1^0})$ (left panel) and $(m_{\tilde{\chi}_1^\pm}, m_{\tilde{\chi}_1^0})$ (right panel) parameter planes in the pMSSM10. The red and blue solid (dashed) lines indicate the 68% and 95% CL contours in the case that the LHC8 constraints are (not) applied, and the location of the best-fit point is indicated with a filled (empty) star.*

be avoided and the chargino masses are pushed to higher masses of ~ 700 GeV, which are only allowed at the 95% CL. Also visible in the $(m_{\tilde{\mu}_R}, m_{\tilde{\chi}_1^0})$ plane is the "gap" at $m_{\tilde{\chi}_1^0} \sim 70$ GeV and $m_{\tilde{\mu}_R} \gtrsim 300$ GeV both with and without the LHC8 constraints applied. The region above (below) this gap corresponds to the $\tilde{\chi}_1^\pm$ coannihilation (Z-funnel and h-funnel) mechanism(s). After the LHC8 constraints are applied, the region below the gap is only allowed at the 95% CL as a result of the constraints on the simplified model decay of $\tilde{\chi}_1^\pm \tilde{\chi}_2^0$ via WZ, cf. Table 3.7.

We now turn to the $(m_{\tilde{\chi}_1^\pm}, m_{\tilde{\chi}_1^0})$ plane in the right panel of Fig. 5.2, and we first consider the situation without the LHC8 constraints (dashed lines and empty star). Unlike the smuon mass, which is bounded from above by the $(g-2)_\mu$ constraint, there is no visible bound on the chargino mass. Indeed the 68% CL contour reaches to $m_{\tilde{\chi}_1^\pm} > 2000$ GeV, and the 68% CL upper bound on $m_{\tilde{\chi}_1^0}$ decreases from $m_{\tilde{\chi}_1^0} \lesssim 300$ GeV at $m_{\tilde{\chi}_1^\pm} \sim 300$ GeV to $m_{\tilde{\chi}_1^0} \lesssim 150$ GeV for $m_{\tilde{\chi}_1^\pm} \gtrsim 1000$ GeV. The relic density is brought in the allowed cosmological range by 1) $\tilde{\chi}_1^\pm$ coannihilation in the diagonal regions, 2) by stau coannihilation for $m_{\tilde{\chi}_1^0} \gtrsim 150$ GeV and 3) by stau t-channel exchange for $m_{\tilde{\chi}_1^0} \lesssim 150$ GeV. The latter region corresponds to the bulk of the 68% CL for off-diagonal chargino masses. Here the lighter stau mass is typically $m_{\tilde{\tau}_1} \sim 100$ GeV, which is near the lower bound from LEP, whereas the other slepton masses are around $m_{\tilde{\ell}} \sim 200$ GeV. For this reason the stau t-channel exchange is implicitly disfavoured by the constraints on direct slepton production, cf. Table 3.7, as can be seen from the solid line in the right panel of Fig. 5.2. The stau

coannihilation region remains allowed at 95% CL. We are left with the $\tilde{\chi}_1^\pm$ coannihilation region at 68% CL. Finally, we note that after applying the LHC8 constraints there is a region between $m_{\tilde{\chi}_1^\pm} \sim 500$ GeV and 750 GeV that is disfavoured by the constraint on associated production of $\tilde{\chi}_1^\pm \tilde{\chi}_2^0$ decaying via sleptons [154], cf. Fig. 3.5.

We would like to emphasize that the removal of the t-channel stau exchange region is an artefact of the slepton mass universality assumed in the pMSSM10. It is envisaged that allowing the stau mass to vary independently could result in t-channel selectron and smuon exchange. This way the 68% CL region in the $(m_{\tilde{\chi}_1^\pm}, m_{\tilde{\chi}_1^0})$ would be recovered in the regions where $m_{\tilde{\chi}_1^\pm} \gtrsim 750$ GeV, where there is no constraint from associated production of $\tilde{\chi}_1^\pm \tilde{\chi}_2^0$ decaying via sleptons [154], cf. Fig. 3.5. Such models are beyond the scope of this thesis.

Other planes where we can see the interplay between the $(g-2)_\mu$, relic density, and LHC8 constraints and the imposed relation between the sleptons masses is in the $(M_A, \tan\beta)$ and $(m_{\tilde{\mu}_R}, \tan\beta)$ parameter planes, as shown in Fig. 5.3, where the contours and stars have the same significations as in Fig. 5.2. In the $(M_A, \tan\beta)$ plane (left panel) we note that for values of $M_A \lesssim 2000$ GeV the preferred values of $\tan\beta$ are restricted to $25 \lesssim \tan\beta \lesssim 45$ at 68% CL when the LHC8 constraints are applied, whereas the lower limit is $\tan\beta \gtrsim 3$ when the LHC8 constraints are not applied. We find that when we consider model points in the nominal 68% CL at $\tan\beta \sim 35$ and $M_A \sim 1500$ GeV, lowering $\tan\beta$ yields a χ^2 contribution from the $(g-2)_\mu$ constraint of ~ 2.0, which is enough to place is outside the 68% CL region. As can be seen from the $(m_{\tilde{\mu}_R}, \tan\beta)$ plane, the low $\tan\beta$ regions correspond to low values of $m_{\tilde{\mu}_R}$, which are constrained by the searches for slepton production, cf. Table 3.7.

We now turn to the Table 5.1, where we compare the χ^2 contributions of various (groups of) constraints for the pMSSM10, CMSSM, NUHM1 and NUHM2 best-fit points. Note that for the GUT models we use the updated constraints on $\mathrm{BR}(B \to \tau\nu_\tau)$ [118], $\mathrm{BR}(B \to X_s\gamma)$ [119, 120], and M_h [24]. For each (group of) constraint(s) the number of degrees of freedom (d.o.f.) is indicated. As in Ref. [60], these are defined as the constraints that contribute significantly to the fit. Note that the collective of LHC8 constraints is counted as one degree of freedom, which is consistent with the $\mathrm{CL_s}$ to χ^2 conversion for point-by-point reinterpretation. The bottom rows list the number of parameters and nuisance parameters, the total χ^2/d.o.f. and the corresponding χ^2 probability. For the pMSSM10 best-fit point we also provide the χ^2 contribution corresponding to the Higgs signal strengths evaluated by `HiggsSignals`. We see that the largest improvement in the total χ^2 can be attributed to the $(g-2)_\mu$ constraint, whereas other constraints generally

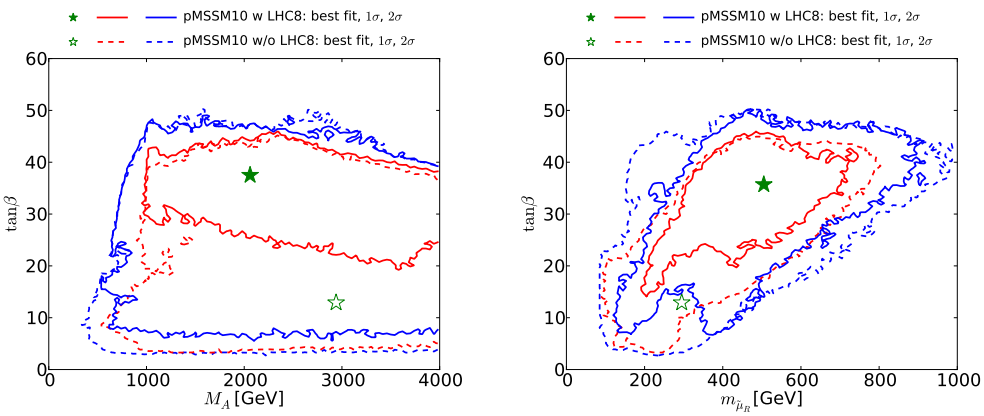

Figure 5.3: *The $(m_{\tilde{\mu}_R}, m_{\tilde{\chi}_1^0})$ (left panel) and $(m_{\tilde{\chi}_1^\pm}, m_{\tilde{\chi}_1^0})$ (right panel) parameter planes in the pMSSM10. The red and blue solid (dashed) lines indicate the 68% and 95% CL contours in the case that the LHC8 constraints are (not) applied, and the location of the best-fit point is indicated with a filled (empty) star.*

yield comparable or small contributions.

For completeness we provide the breakdown of the total χ^2 function into its contributions from individual constraints in Fig. 5.4. The panels show the breakdowns for the best-fit point (left), and along the profile likelihood functions of $m_{\tilde{\mu}_R}$ (middle) and $m_{\tilde{\chi}_1^\pm}$ (right). The ordering of the (groups of) constraints and the colours used are specified in the legend. Fig. 5.4 confirms that the $(g-2)_\mu$ constraint (teal) is the most important constraint for both the $m_{\tilde{\mu}_R}$ and $m_{\tilde{\chi}_1^\pm}$ profile likelihood functions, whereas for $m_{\tilde{\chi}_1^\pm}$ the LHC8_{EWK} constraints (light green) also play an important role. Note that the lower bound on $m_{\tilde{\chi}_1^\pm}$ is given by the LEP constraint [80] (yellow).

5.2 Physical Observables

5.2.1 Physical Masses

Mass Planes

We first discuss the physical masses our fit of the pMSSM10, starting with some of the strongly interacting sparticles. In Fig. 5.5 we display from top left to bottom right the gluino, first- and second-generation squark, the lighter stop, and the lighter sbottom masses each versus the lightest neutralino mass. The contours and stars have the same significations as in Fig. 5.2, with the additional remark that arrows indicate the location

Constraint	(d.o.f.)	pMSSM10	CMSSM	NUHM1	NUHM2
LHC8	(1)	0.2	-	-	-
Jets+$\not{E}_T$	(1)	-	2.0	0.0	0.5
M_h	(1)	0.0	0.1	0.1	0.4
M_W	(1)	0.0	0.0	0.0	0.4
BR($B_{s,d} \to \mu^+\mu^-$)	(1)	0.2	0.5	0.3	0.4
BR($B \to X_s\gamma$)	(1)	0.1	0.5	0.0	0.0
BR($B \to \tau\nu_\tau$)	(1)	0.2	0.2	0.2	0.2
Other Flavour Obs.	(5)	3.3	3.2	3.3	3.3
$\Omega_{\rm CDM}h^2$	(1)	0.1	0.0	0.0	0.0
$\sigma_p^{\rm SI}$	(1)	0.0	0.0	0.0	0.0
$H/A \to \tau^+\tau^-$	(1)	0.0	0.0	0.0	0.0
Nuisance	(3)	0.0	0.1	0.0	0.1
$(g-2)_\mu$	(1)	0.0	9.3	10.6	8.4
Z Pole	(13)	16.3	16.8	16.5	16.7
Parameters		10 + 3	4 + 3	5 + 3	6 + 3
χ^2/d.o.f.		20.5/18	32.8/24	31.1/23	30.3/22
χ^2 Probability		0.31	0.11	0.12	0.11
χ^2(HS)	(77)	62.8	-	-	-

Table 5.1: *Table comparing the best-fit point of the pMSSM10 to those of the CMSSM, NUHM1, and NUHM2. The χ^2 contribution of (groups of) constraints and the corresponding number of degrees of freedom (d.o.f.) are listed in the first part of the table. The bottom rows list the number of (nuisance) parameters, the total χ^2/d.o.f and the corresponding χ^2 probability, as well as the χ^2 contribution from the Higgs signal rates as evaluated by* `HiggsSignals`*. The latter is omitted in the comparison between the pMSSM10, CMSSM, NUHM1 and NUHM2.*

of the best-fit point whenever it is beyond the displayed mass range.

Turning to the $(m_{\tilde{g}}, m_{\tilde{\chi}_1^0})$ plane (top left), the immediate visual impression is that the LHC8 constraints (most notably LHC8$_{\rm col}$) result in a lower bound on $m_{\tilde{g}} \gtrsim 1000(1250)$ GeV at the 95% (68%) CL. We see again that the LHC8 constraints remove the t-channel stau exchange region at low values of $m_{\tilde{\chi}_1^0} \lesssim 80$ GeV, so that only the h- and Z-funnel regions are allowed at the 95% CL. We see a similar impact of the LHC8 constraints in the $(m_{\tilde{q}}, m_{\tilde{\chi}_1^0})$ plane (top right), where this time the 95% (68%) CL lower bound are given by $m_{\tilde{q}} \gtrsim 1250(1500)$ GeV.

The picture is somewhat more complicated for the lighter stop and sbottom masses, in particular the compressed-stop region where $m_{\tilde{t}_1} - m_{\tilde{\chi}_1^0} < m_t$. We recall that by construction the LHC8$_{\rm col}$ constraint does not apply to the lighter stop in the compressed region where $m_{\tilde{t}_1} - m_{\tilde{\chi}_1^0} < m_t$, since in this region the limits depend strongly on the decay modes. Instead, the possible decay modes in this region are constrained by the LHC8$_{\rm stop}$

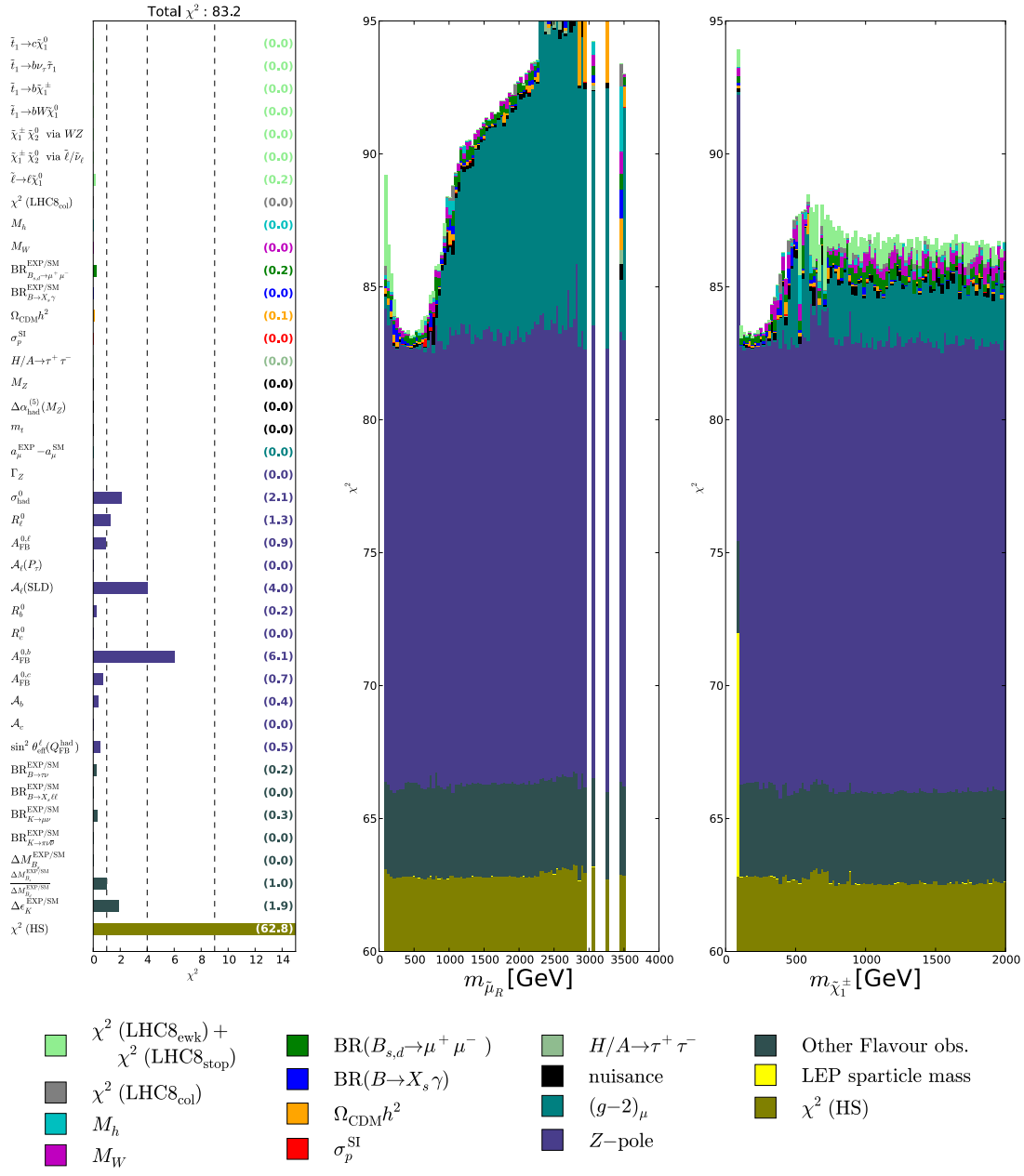

Figure 5.4: *Breakdown of the total χ^2 in individual contributions for points in the pMSSM10. The panels show the breakdowns for the best-fit point (left), and along the profile likelihood functions of $m_{\tilde{\mu}_R}$ (middle) and $m_{\tilde{\chi}_1^\pm}$ (right). The ordering of the (groups of) constraints and the colours used are specified in the legend.*

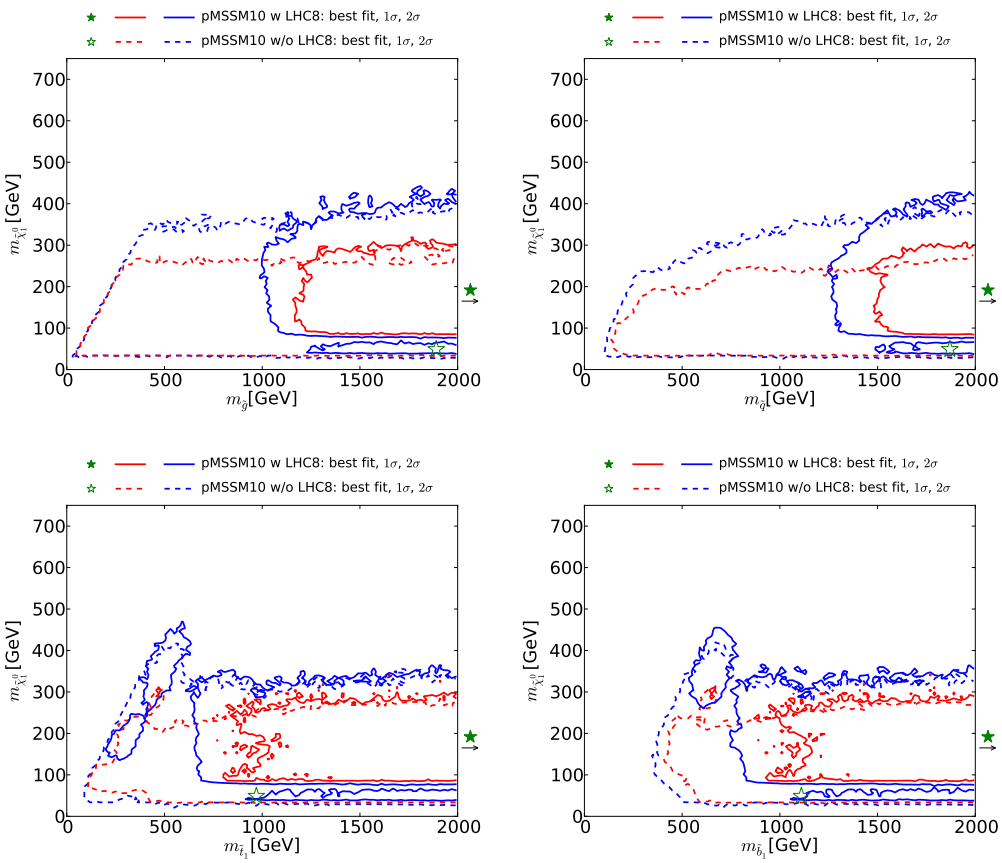

Figure 5.5: *Physical mass planes for the coloured sparticles. Displayed are (from top left to bottom right) the gluino, first- and second-generation squark, the lighter stop, and the lighter sbottom masses each versus the lightest neutralino mass. The contours and stars have the same significations as in Fig. 5.2, with the additional remark that arrows indicate the location of the best-fit point whenever in is beyond the displayed mass range.*

constraint.

Let us first consider the $(m_{\tilde{t}_1}, m_{\tilde{\chi}_1^0})$ plane in bottom left panel of Fig. 5.5. When the LHC8 constraints are not applied, we see that there are three blobs in the compressed region that are available at the 68% CL. The first, located at $m_{\tilde{\chi}_1^0} \sim 100$ GeV corresponds to the t-channel stau exchange and is disfavoured by the constraint on slepton pair production, and the stop decaying into $bW\tilde{\chi}_1^0$, as well as the chargino decay via sleptons. The second is located at $m_{\tilde{\chi}_1^0} \sim 200$ GeV and corresponds to the $\tilde{\chi}_1^\pm$ coannihilation region. After applying the LHC8 constraints, this region is only allowed at 95% CL as a result of the higher smuon masses and the constraints on the stop decaying into $b\tilde{\chi}_1^\pm$ or $b\nu_\tau\tilde{\tau}_1$. We recall

that the uncertainties on the LHC8$_{\text{stop}}$ and LHC8$_{\text{EWK}}$ constraints are large in this region and a (hypothetical) point-by-point reinterpretation could alter the 95% as we assessed in Fig. 3.13. The third (smaller) blob is located at $m_{\tilde{\chi}_1^0} \sim 270$ GeV, also corresponds to the $\tilde{\chi}_1^\pm$ coannihilation region. Even when the LHC8 constraints are applied, this region still has a few points that are allowed at the 68% CL and this region is relatively robust against uncertainties on the LHC8$_{\text{stop}}$ and LHC8$_{\text{EWK}}$ constraints. Shifting our attention to the non-compressed region, we see that the LHC8 constraints effectively put a lower bound of $m_{\tilde{t}_1} \gtrsim 700(900)$ GeV at the 95% (68%) CL.

The $(m_{\tilde{b}_1}, m_{\tilde{\chi}_1^0})$ plane is displayed in the bottom right panel of Fig. 5.5. We see that the features discussed in for the lighter stop are repeated for the lighter sbottom. As expected, the LHC8$_{\text{col}}$ constraint places similar lower bounds on the sbottom masses.

Next we consider the $(m_{\tilde{\tau}_1}, m_{\tilde{\chi}_1^0})$ plane in Fig. 5.6. As expected, this plane looks very similar to the $(m_{\tilde{\mu}_R}, m_{\tilde{\chi}_1^0})$ plane. We note, however, that the constraint on slepton production only results in a low-mass wedge being disfavoured to 95% CL, in contrast to the smuon case where this wedge was removed.

We now consider the $(m_{\tilde{\chi}_3^0}, m_{\tilde{\chi}_1^0})$ plane in the right panel of Fig. 5.6. Before applying the LHC8 constraints the 68% CL region reaches to values of $m_{\tilde{\chi}_3^0} \gtrsim 1000$ GeV where the relic density constraint is fulfilled by stau coannihilation, whereas the LHC8 constraints disfavour this region to be only available at the 95% CL. After applying the LHC8 constraints, the 68% CL region at $m_{\tilde{\chi}_3^0} - m_{\tilde{\chi}_1^0} \gtrsim 200$ GeV correspond again to the chargino coannihilation mechanism. Here the LSP has mainly a Bino composition, $\tilde{\chi}_2^0/\tilde{\chi}_1^\pm$ a Wino composition, and thus the $\tilde{\chi}_3^0$ has mainly a Higgsino composition and its mass is closely related to the μ parameter. On the other hand, we also see a region where the mass splitting $m_{\tilde{\chi}_3^0} - m_{\tilde{\chi}_1^0}$ tends to zero. Here μ approaches M_1 whereas M_2 takes larger values. Correspondingly all electroweakinos are rather mixed, e.g. the LSP has a non-negligible Higgsino component, $\tilde{\chi}_2^0$ is an admixture of Wino and Higgsino, $\tilde{\chi}_3^0$ is mostly Higgsino although it has some non-negligible Bino component, and $\tilde{\chi}_4^0$ has a larger Wino component. The spin-independent cross-section is correspondingly large, although it is below the upper limits set by LUX [23] and XENON100 [22]. The mechanism responsible for bringing the relic density in the allowed cosmological range is t-channel stop exchange and to a lesser extend by t-channel chargino exchange.

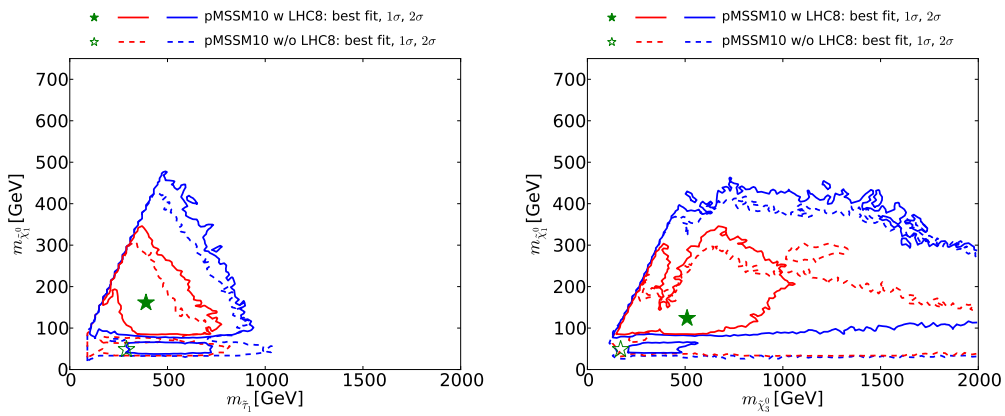

Figure 5.6: *Physical mass planes for the lighter stau (left) and $\tilde{\chi}_3^0$ (right) masses versus the lightest neutralino mass. The contours and stars have the same significations as in Fig. 5.2.*

Mass Spectra

In the previous section we discussed in depth the interplay of the LHC8, $(g-2)_\mu$, and relic density constraints and the effect in various mass planes. We will now focus on general features of the mass spectrum and highlight some specific examples that we recommend as benchmark points for future searches at the LHC, cf. Ref. [60].

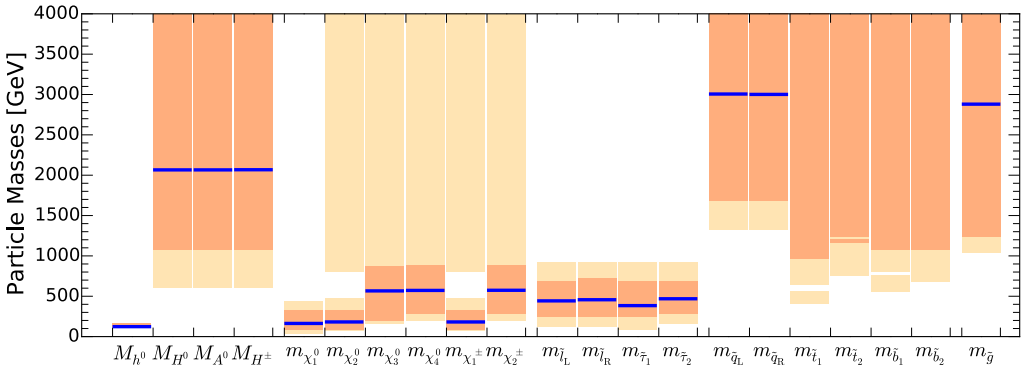

Figure 5.7: *Summary of sparticle mass predictions in the pMSSM10. The lighter and darker peach bars indicate the 95% and 68% CL intervals, whereas the blue horizontal lines indicate the locations of the masses of the best-fit point (some of which are beyond the displayed range).*

A summary of all sparticle masses is given in Fig. 5.7. In this figure lighter and darker peach bars indicate the 95% and 68% CL intervals, respectively, and blue horizontal lines indicate the locations of the masses of the best-fit point (some of which are outside the displayed range). Starting from the left, we see that the lightest Higgs boson simply takes

its measured value, whereas the heavier Higgs bosons are relatively unconstrained, with lower bounds $\gtrsim 600(1000)$ GeV at the 95% (68%) CL. The picture looks different for the electroweakinos where there is an overall preference for light masses ($\lesssim 500(1000)$) at the 68% CL. However, all electroweakino masses (except for the LSP mass) are essentially only bounded from below at the 95% CL. To reduce the verbosity in the discussion below, we note that overall the LSP has mainly a Bino composition, the $\tilde{\chi}_1^\pm$ and $\tilde{\chi}_2^0$ a Wino composition and the $\tilde{\chi}_2^\pm$, $\tilde{\chi}_3^0$, and $\tilde{\chi}_4^0$ a Higgsino composition. We therefore refer to these mass eigenstates as the Bino (or LSP), Winos and Higgsinos, although strictly speaking they have some residual mixing with the other gauge eigenstates.

The right- and left-handed first-, second-, as well as third-generation sleptons have well defined preferred mass ranges below 1000 GeV at the 95% CL. Next, the first- and second-generation right- and left-handed squark masses by construction have a very similar preferred range and are only bounded from below. The 68% CL interval for lighter and heavier stop and sbottom masses is also only bounded from below. However, we note that the lighter stop and sbottom masses have a separated region with low masses that are allowed at 95% CL (which corresponds to the compressed-stop region). The gluino mass is also relatively undetermined and is only bounded from below.

In the following we discuss the individual spectra and the decay chains of the best-fit point and a number of benchmark model points that feature sparticle masses that should be within reach for LHC Run 2. The benchmark points were selected as to minimise the χ^2 function at specific points in the planes of Fig. 5.5:

Low $m_{\tilde{t}_1}$ one of the 68% CL points in the compressed-stop region,

Low $m_{\tilde{q}}$ $m_{\tilde{q}} \sim 1530$ GeV and $m_{\tilde{\chi}_1^0} \sim 200$ GeV,

Low $m_{\tilde{g}}$ $m_{\tilde{g}} \sim 1290$ GeV and $m_{\tilde{\chi}_1^0} \sim 180$ GeV, and

Low All a point within the 68% CL region subject to the requirement that all sparticle masses are below 2 TeV.

Their corresponding parameters are listed in Table 5.2, whereas the decay tables for the $\tilde{\chi}_2^0$, the $\tilde{\chi}_1^\pm$, the left- and right-handed smuon, gluino, left- and right-handed sup, and lighter stop are listed in Table 5.3. The full SLHA [132, 133] files can be found at the `MasterCode` website [171].

Parameter	Best-Fit	Low $m_{\tilde{t}_1}$	Low $m_{\tilde{q}}$	Low $m_{\tilde{g}}$	Low All
M_1	170 GeV	300 GeV	210 GeV	190 GeV	-120 GeV
M_2	170 GeV	310 GeV	220 GeV	200 GeV	160 GeV
M_3	2600 GeV	1660 GeV	3730 GeV	-1070 GeV	1700 GeV
$m_{\tilde{q}_{12}}$	2880 GeV	3700 GeV	1530 GeV	2430 GeV	1790 GeV
$m_{\tilde{q}_3}$	4360 GeV	720 GeV	1840 GeV	3780 GeV	1300 GeV
$m_{\tilde{\ell}}$	440 GeV	390 GeV	430 GeV	410 GeV	740 GeV
M_A	2070 GeV	3540 GeV	2810 GeV	2990 GeV	1350 GeV
A	790 GeV	1790 GeV	2510 GeV	3000 GeV	1863 GeV
μ	550 GeV	1350 GeV	640 GeV	530 GeV	190 GeV
$\tan\beta$	37.6	37.3	40.8	33.9	35.4
χ^2/d.o.f.	20.5/18	22.2/18	22.0/18	22.3/18	22.2/18
χ^2 probability	0.31	0.22	0.23	0.22	0.22

Table 5.2: *Parameters of the best-fit point and benchmark points selected to lie in the compressed-stop region (Low $m_{\tilde{t}_1}$), to have low first- and second-generation squark (Low $m_{\tilde{q}}$) or gluino masses (Low $m_{\tilde{g}}$), and to have all masses low (Low All).*

Best-Fit Point

We first consider the best-fit point, the spectrum of which is displayed in Fig. 5.8. The branching ratios of each of the decay modes, cf. Table 5.3, are indicated with accordingly grey shaded dashed lines. We first note that the best-fit point has nearly degenerate LSP and Wino masses, namely $m_{\tilde{\chi}_1^0} \sim 160$ GeV and $m_{\tilde{\chi}_1^\pm} \simeq m_{\tilde{\chi}_2^0} \sim 180$ GeV and correspondingly $M_1 \simeq M_2$ as can be seen in Table 5.2. Consequently they decay via off-shell bosons into $f\bar{f}^{(\prime)}\tilde{\chi}_1^0$ or $\gamma\tilde{\chi}_1^0$. Another consequence is that the decay chains of the left-handed smuon and sup, as well as the gluino evolve via $\tilde{\chi}_1^\pm\tilde{\chi}_2^0$.

The slepton masses are close to each other e.g. $m_{\tilde{\ell}_L} \sim 440$ GeV, $m_{\tilde{\ell}_R} \sim 460$ GeV, $m_{\tilde{\tau}_1} \sim 380$ GeV and $m_{\tilde{\tau}_2} \sim 470$ GeV. The Higgsinos have masses of 570 GeV and their masses are indeed close to $\mu \sim 550$ GeV. The heavy Higgs bosons have an almost equal mass of ~ 2070 GeV.

The first- and second-generation squark masses (~ 3000 GeV) are slightly above the gluino mass (~ 2880 GeV). Accordingly, the left-handed squarks decay mainly into $q'\tilde{\chi}_1^\pm/q\tilde{\chi}_2^0$, whereas right-handed squarks decay mainly into the corresponding quark and the LSP. The gluino decays via off-shell squarks $q\bar{q}'\tilde{\chi}_1^\pm/q\bar{q}\tilde{\chi}_2^0$. The third-generation squark masses have a relatively high masses of ~ 4380 GeV. Correspondingly, the lighter stop decays via the heavier (Higgsino-like) chargino and neutralinos as well as via the gluino.

Decay mode	Best-Fit	Low $m_{\tilde{t}_1}$	Low $m_{\tilde{q}}$	Low $m_{\tilde{g}}$	Low All
$\tilde{\chi}_2^0 \to f\bar{f}\tilde{\chi}_1^0$	80	100	89	86	100
$\tilde{\chi}_2^0 \to \gamma\tilde{\chi}_1^0$	20	-	11	14	-
$\tilde{\chi}_1^\pm \to f\bar{f}'\tilde{\chi}_1^0$	100	-	100	100	100
$\tilde{\chi}_1^\pm \to \nu_\tau\tilde{\tau}_1$	-	100	-	-	-
$\tilde{\mu}_L \to \mu\tilde{\chi}_1^0$	7	14	7	6	11
$\tilde{\mu}_L \to \nu_\mu\tilde{\chi}_1^\pm/\mu\tilde{\chi}_2^0$	93	86	93	94	50
$\tilde{\mu}_L \to \nu_\mu\tilde{\chi}_2^\pm/\mu\tilde{\chi}_{3,4}^0$	-	-	-	-	39
$\tilde{\mu}_R \to \mu\tilde{\chi}_1^0$	98	100	99	98	90
$\tilde{\mu}_R \to \mu\tilde{\chi}_2^0$	2	-	1	2	-
$\tilde{\mu}_R \to \mu\tilde{\chi}_{3,4}^0$	-	-	-	-	10
$\tilde{g} \to q\bar{q}$	-	-	71	-	-
$\tilde{g} \to q_3\tilde{q}_3$	-	100	29	-	100
$\tilde{g} \to q\bar{q}\tilde{\chi}_1^0$	10	-	-	11	-
$\tilde{g} \to q\bar{q}'\tilde{\chi}_1^\pm/q\bar{q}\tilde{\chi}_2^0$	74	-	-	77	-
$\tilde{g} \to q_3\bar{q}_3'\tilde{\chi}_1^\pm/q_3\bar{q}_3\tilde{\chi}_2^0$	3	-	-	5	-
$\tilde{g} \to q\bar{q}'\tilde{\chi}_2^\pm/q\bar{q}\tilde{\chi}_{3,4}^0$	2	-	-	2	-
$\tilde{g} \to q_3\bar{q}_3'\tilde{\chi}_2^\pm/q_3\bar{q}_3\tilde{\chi}_{3,4}^0$	10	-	-	5	-
$\tilde{u}_L \to u\tilde{\chi}_1^0$	-	-	-	-	1
$\tilde{u}_L \to d\tilde{\chi}_1^\pm/u\tilde{\chi}_2^0$	95	23	99	23	66
$\tilde{u}_L \to d\tilde{\chi}_2^\pm/u\tilde{\chi}_{3,4}^0$	1	-	1	-	29
$\tilde{u}_L \to u\tilde{g}$	4	77	-	77	4
$\tilde{u}_R \to u\tilde{\chi}_1^0$	80	5	99	5	74
$\tilde{u}_R \to u\tilde{\chi}_2^0$	2	-	1	-	-
$\tilde{u}_R \to u\tilde{\chi}_{3,4}^0$	-	-	-	-	10
$\tilde{u}_R \to u\tilde{g}$	18	95	-	95	16
$\tilde{t}_1 \to t\tilde{\chi}_1^0$	5	1	5	2	7
$\tilde{t}_1 \to b\tilde{\chi}_1^\pm$	-	99	13	3	4
$\tilde{t}_1 \to t\tilde{\chi}_2^0$	-	-	6	1	3
$\tilde{t}_1 \to b\tilde{\chi}_2^\pm/t\tilde{\chi}_{3,4}^0$	53	-	76	29	86
$\tilde{t}_1 \to t\tilde{g}$	42	-	-	65	-

Table 5.3: *Decay tables of various sparticles for the best-fit point and benchmark points selected to lie in the compressed-stop region (Low $m_{\tilde{t}_1}$), to have low first- and second-generation squark (Low $m_{\tilde{q}}$) or gluino masses (Low $m_{\tilde{g}}$), and to have all masses low (Low All). Branching ratios are given as percentages.*

Low $m_{\tilde{t}_1}$

We now turn to the benchmark point that was selected to have a low stop mass and its spectrum is displayed in the top left panel of Fig. 5.9. For this point the stop mass is given

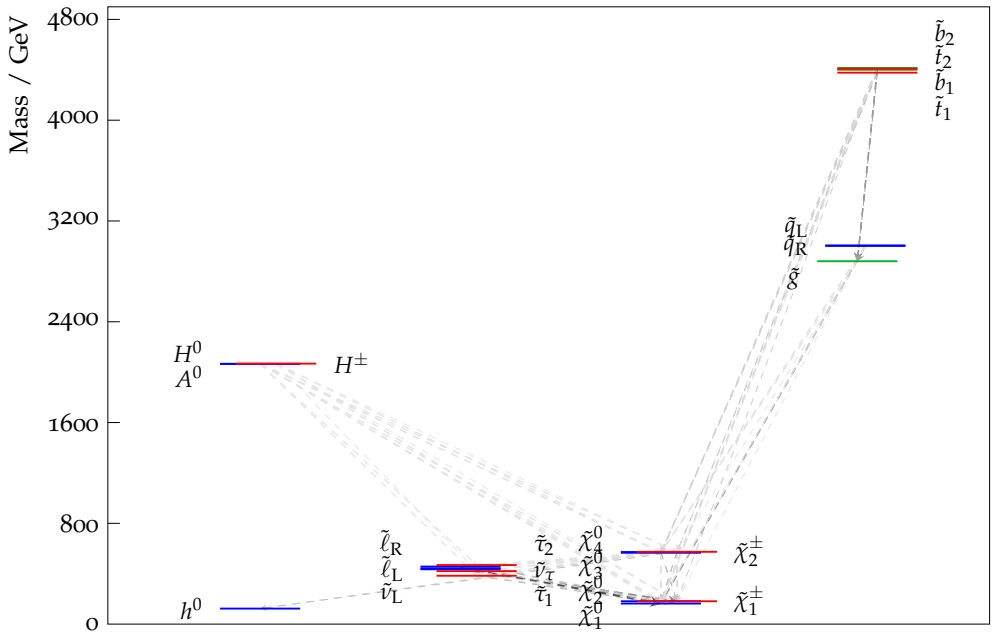

Figure 5.8: *Mass spectrum of the pMSSM10 best-fit point. The branching ratios of different decay modes are indicated using grey shading.*

by 478 GeV and the LSP mass by 304. As can be seen from Table 5.3, the stop decays mainly into $b\tilde{\chi}_1^\pm$. For this spectrum the slepton masses have a relatively large splitting and the stau mass is just below the $m_{\tilde{\chi}_1^\pm} \simeq m_{\tilde{\chi}_2^0} \sim 330$. As a result $\tilde{\chi}_1^\pm$ decays via the stau, whereas $\tilde{\chi}_2^0$ decays mainly into an off-shell stau and neutrino. The left-handed smuon has a mass of ~ 410 GeV and decays mainly via $\tilde{\chi}_1^\pm$ or $\tilde{\chi}_2^0$, whereas the right-handed smuon decays 100% into $\mu\tilde{\chi}_1^0$. The Higgsinos have masses of ~ 1350 GeV, whereas the heavy Higgs bosons have masses of around 3540 GeV.

The first- and second generation squarks have relatively high masses of approximately 3730 GeV they decay mainly into gluinos, which have a mass of ~ 1770. The gluinos decay with similar branching ratios to each of the third generation squarks, with a mild preference for the lighter stops and sbottoms.

Low $m_{\tilde{q}}$

In the top right panel of Fig. 5.9 we display the benchmark point at values of the first- and second-generation squark masses that should be accessible during the LHC Run 2. The overall impression is that the electroweakino, and slepton sectors are very comparable to those of the best-fit point: $m_{\tilde{\chi}_1^\pm} \simeq m_{\tilde{\chi}_2^0}$ close to the LSP mass, followed by slepton masses

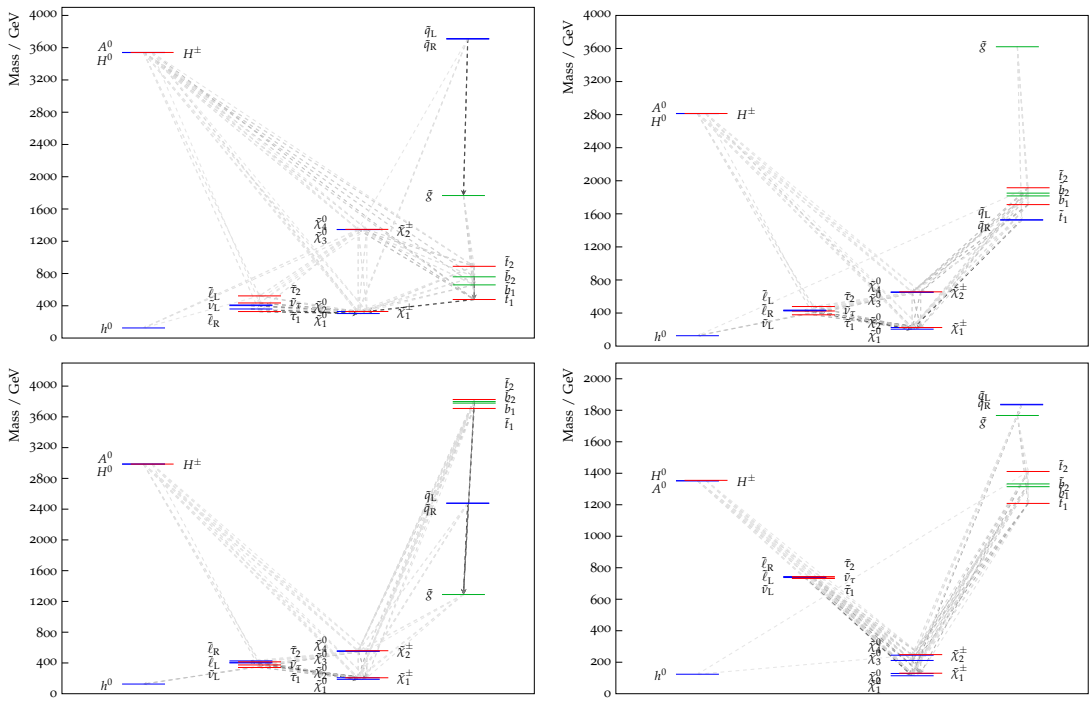

Figure 5.9: *Mass spectrum of four benchmark points defined in the text. From top left to bottom right we display the "Low $m_{\tilde{t}_1}$", "Low $m_{\tilde{q}}$", "Low $m_{\tilde{g}}$", and "Low All" points. The branching ratios of different decay modes are indicated using grey shading.*

with small splitting, and the masses of the Higgsinos well below 1 TeV.

In the coloured sector we see that this time the first- and second generation squarks have the lowest masses of around 1520 GeV. Because of the compressed Winos the left-handed squarks decay with a branching ratio of almost 100% to via $\tilde{\chi}_1^\pm \tilde{\chi}_2^0$, whereas right-handed squarks decay almost 100% into $q\tilde{\chi}_1^0$. The third generation squarks are have somewhat higher masses ($m_{\tilde{t}_1} \sim 1710$ GeV, $m_{\tilde{b}_1} (\simeq m_{\tilde{b}_2}) \sim 1820$ GeV, and $m_{\tilde{t}_2} \sim 1920$ GeV) and they decay mainly into Higgsinos accompanied by top and bottom quarks. The gluino has a high mass of ~ 3620 GeV and decays mainly into first- and second-generation squark (with a branching ratio of 71%), although it decays with 29% branching ratio into third-generation squarks.

Low $m_{\tilde{g}}$

We now consider the third benchmark point at a relatively low gluino mass of ~ 1290 GeV, the spectrum and decay chains are depicted in the bottom left panel of Fig. 5.9. The

slepton and electroweakino sectors show again nearly degenerate Bino and Winos (at ~ 200 GeV), nearly degenerate sleptons (at ~ 400 GeV), and nearly degenerate Higgsinos (at 660 GeV).

The gluino decays mainly via off-shell first and second generation squarks, which again evolves mainly via Winos. The first- and second generation squarks have masses around 2670 GeV and they mainly decay into gluinos and the left-handed squarks also decay into Winos. The third-generation squarks decay mainly into gluinos and with a smaller branching ratio into Higgsinos.

Low All

Finally, we discuss a spectrum that has masses below 2 TeV for all sparticles. We begin with noting that all electroweakinos have relatively small masses of $\lesssim 250$ GeV and, correspondingly, their composition is somewhat more mixed than for the other benchmark points. The slepton masses are nearly degenerate at a mass of approximately 740 GeV. We see from Table 5.3 that the left-handed smuon decays into all electroweakinos, whereas right-handed smuons decay mainly to the LSP.

We see that the third generation squark have masses $m_{\tilde{t}_1} \sim 1210$, $m_{\tilde{b}_1} \sim 1310$, $m_{\tilde{b}_2} \sim 1330$ GeV, and $m_{\tilde{t}_2} \sim 1411$ GeV and they mainly decay via Higgsinos. The gluino has a mass of ~ 1770 and decays into third generation squarks. The first- and second-generation right(left)-handed squarks have a mass of approximately 1830 GeV and they decay mainly (into a Bino) via Winos, but also via Higgsinos. The third generation squark masses decay mainly via Higgsinos.

Summary

We have discussed in detail the mass spectra and corresponding decay modes for our best-fit point as well as four benchmark points. Their parameters, total χ^2/d.o.f and the corresponding χ^2 probabilities are listed in Table 5.2, and the decay tables for some representative sparticles are listed in Table 5.3. Common features are the mainly Bino composition of $\tilde{\chi}_1^0$, a Wino composition of the $\tilde{\chi}_1^\pm/\tilde{\chi}_2^0$ and Higgsino composition of $\tilde{\chi}_2^\pm/\tilde{\chi}_3^0/\tilde{\chi}_4^0$. For all spectra the Winos have masses very close to the Bino and their masses are approximately $m_{\tilde{\chi}_1^\pm} \simeq m_{\tilde{\chi}_2^0} \sim m_{\tilde{\chi}_1^0} + 20$ GeV. The slepton masses are generally close, due to their common soft SUSY breaking parameter at M_{SUSY}, and $m_{\tilde{\tau}_1}$ is the lowest as a result of the larger splitting with respect to other sleptons. In all (except for the "Low All") spectra the Higgsino masses are above the slepton masses so that the left-handed sleptons decay mainly via the Winos, and right-handed sleptons decay directly into $\ell\tilde{\chi}_1^0$. The decay

modes of the coloured sparticles depend on their mass hierarchy. For example: when the gluino mass is below all squark masses, as is the case for the best-fit and "Low $m_{\tilde{g}}$" point, it decays via off-shell squarks. On the other hand, when the gluino mass exceeds those of squark masses, it decays into the kinematically available squarks. The decay of left(right)-handed first- and second-generation evolves via the gluino, if kinematically favoured, or via Winos (into a Bino) and to a lesser degree via Higgsinos. The third generation squarks on the other hand preferably decay via Higgsinos as a result of the interaction vertices that scale with the Yukawa coupling.

Comparison with the CMSSM, NUHM1, and NUHM2

To complete the discussion of the physical masses in the pMSSM10, we make a brief comparison between some mass predictions of coloured and non-coloured sparticles in the pMSSM10 with predictions in the CMSSM, NUHM1, and NUHM2.

In Fig. 5.10 we display (from the top left to bottom right) the one-dimensional profile likelihood functions for $m_{\tilde{g}}$, $m_{\tilde{q}}$, $m_{\tilde{t}_1}$, $m_{\tilde{b}_1}$in the pMSSM10 (solid black), NUHM2 (solid blue), NUHM1 (dashed blue) and CMSSM (dotted blue). The top left panel indicates that significantly lower gluino masses are allowed in the pMSSM10 than in the CMSSM, NUHM1, and NUHM2: $m_{\tilde{g}} \gtrsim 1000(1250)$ GeV at the 95% (68%) CL compared to $m_{\tilde{g}} \gtrsim 1750(2000)$ GeV in the other models. On the other hand, the gluino mass is not bounded from above (at least within the displayed range) for any of the models. The lower bound on the first- and second-generation squark masses (in the top right panel of Fig. 5.10) is very similar in the four models, though slightly lower in the pMSSM10. In the bottom left panel we see that the lower bounds for the lighter stop mass are remarkably similar in the four models: in the CMSSM, the 95% CL lower bound coincides with that of non-compressed spectra in the pMSSM10, whereas in the NUHM1 and NUHM2 lower masses are allowed that correspond to the stop coannihilation mechanism (and thus to compressed-stop spectra) and their 95% CL lower bounds agree well with those in the pMSSM10. The local minimum in the pMSSM10 profile likelihood at $m_{\tilde{t}_1} \simeq 480$ GeV corresponds precisely to the "Low $m_{\tilde{t}_1}$" benchmark point discussed above. The lower bound on the sbottom masses on the other hand is significantly lower in the pMSSM10 as a result of the difference in the unifying assumptions of the models.

We turn to Fig. 5.11 (the colours and line styles have the same signification as in Fig. 5.10) where we compare the mass predictions for $m_{\tilde{\chi}_1^0}$, $m_{\tilde{\chi}_1^\pm}$, $m_{\tilde{\tau}_1}$, $m_{\tilde{\mu}_R}$. As we discussed above, the $(g-2)_\mu$ constraint can be fulfilled by having low smuon masses (which constrains

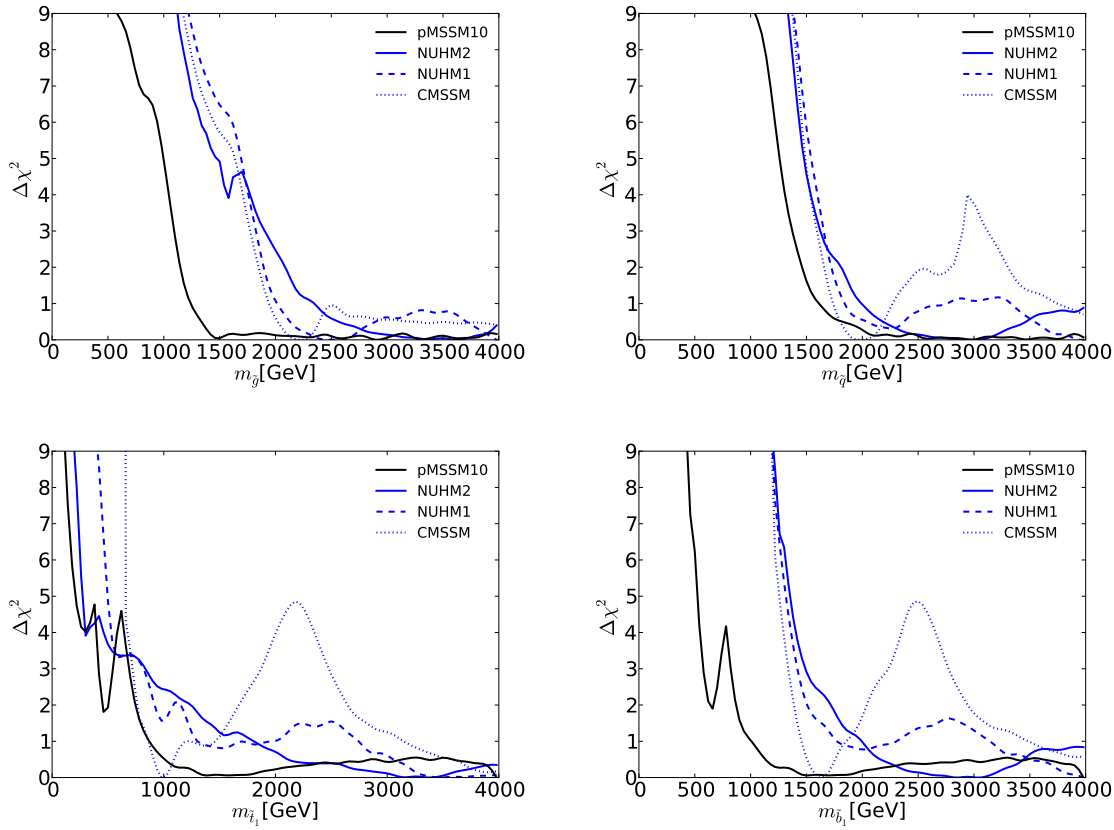

Figure 5.10: *Comparison of predictions for masses of coloured sparticles in the pMSSM10 (solid black), CMSSM (dotted blue), NUHM1 (dashed blue), and NUHM2 (solid blue). The panels display (from the top left to bottom right) the one-dimensional profile likelihood functions for* $m_{\tilde{g}}$, $m_{\tilde{q}}$, $m_{\tilde{t}_1}$, $m_{\tilde{b}_1}$.

the LSP mass and in the pMSSM10 also the stau masses) and to a lesser degree on the chargino mass. Since in the CMSSM, NUHM1, and NUHM2, the smuon mass is related to the coloured sector via m_0 and $m_{1/2}$, the $(g-2)_\mu$ constraint cannot be fulfilled in these models and therefore the predictions in the pMSSM10 differ significantly from those in the CMSSM, NUHM1, and NUHM2.

Finally, we discuss the masses the light and have Higgs bosons as displayed in the left and right panel of Fig. 5.12, respectively. As before, we compare the pMSSM10 to the CMSSM, NUHM1, and NUHM2 respectively indicated with black solid, and blue dotted, dashed and solid lines. For the lightest Higgs mass we show in red the χ^2 contribution from the constraint from the experimental value smeared by a theoretical uncertainty

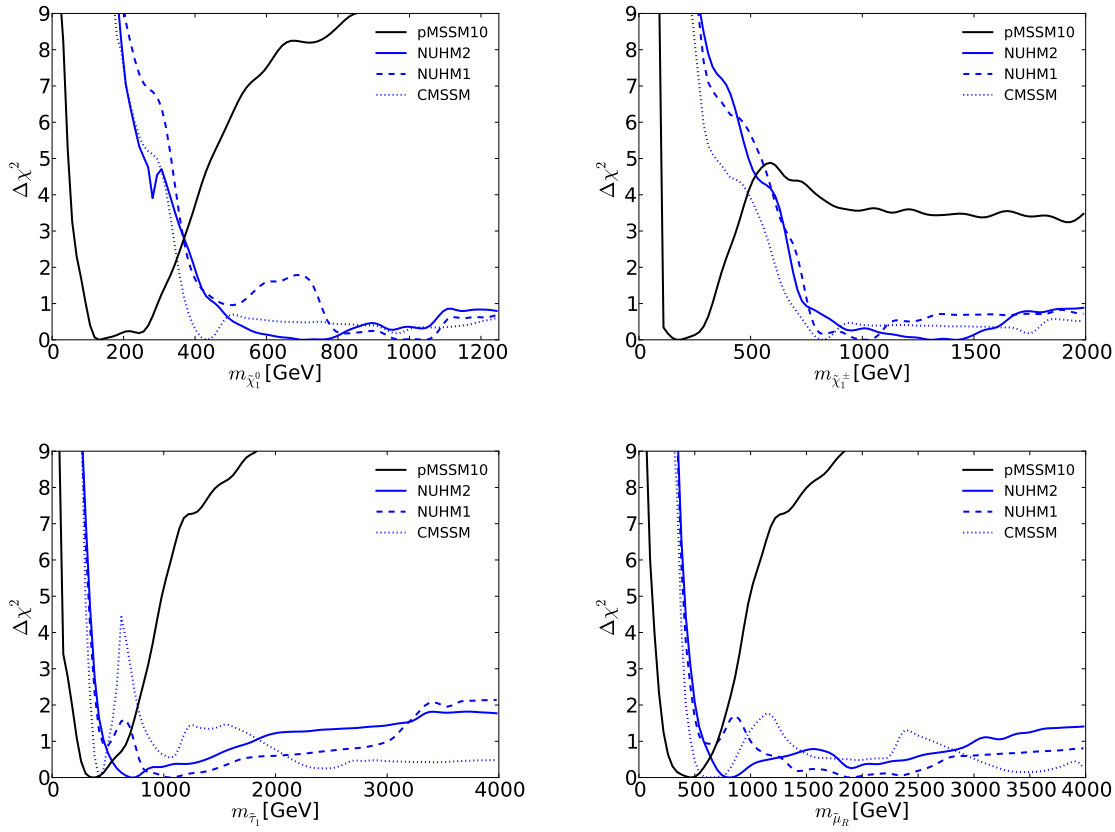

Figure 5.11: *Comparison of predictions for masses of electroweak sparticles in the pMSSM10 (solid black), CMSSM (dotted blue), NUHM1 (dashed blue), and NUHM2 (solid blue). The panels display (from the top left to bottom right) the one-dimensional profile likelihood functions for* $m_{\tilde{\chi}_1^0}$, $m_{\tilde{\chi}_1^\pm}$, $m_{\tilde{\tau}_1}$, $m_{\tilde{\mu}_R}$.

of 1.5 GeV and we note that the predictions in the pMSSM10 are very similar to this constraint.

As we saw before, the heavy Higgs is essentially unconstrained from above and only constrained from below by a $\tan\beta$ dependent lower limit. In the pMSSM10 we saw in section 5.1 that an interplay between slepton mass universality at $M_{\rm SUSY}$, constraints on slepton pair production, and the fulfilment of the relic density constraint by the $\tilde{\chi}_1^\pm$ coannihilation mechanism result in a low values of M_A and $\tan\beta$ to be disfavoured. By consequence the lower limit on M_A is higher in the pMSSM10 than in the NUHM2, and comparable to (lower than) the lower bound in the NUHM1 (CMSSM), cf. Fig. 4.15.

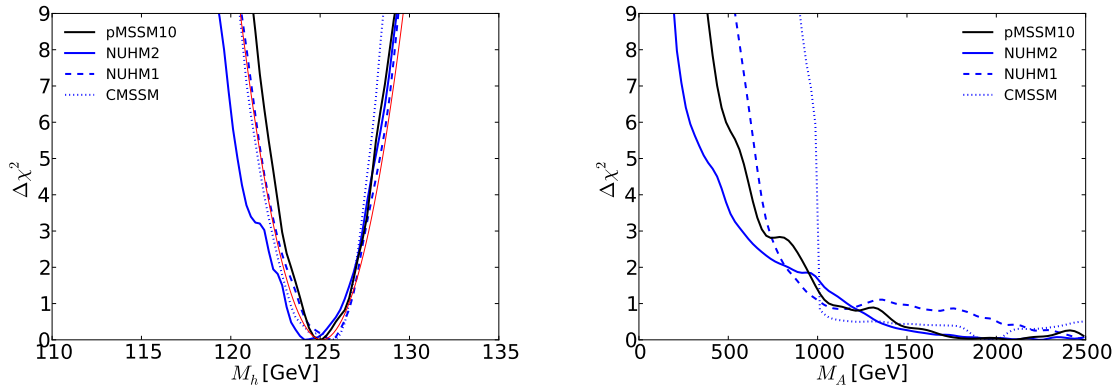

Figure 5.12: *Comparison of predictions for the masses of the light (left panel) and heavy Higgs bosons (right panel) in the pMSSM10, CMSSM, NUHM1, and NUHM2. The χ^2 contribution from the M_h constraint is depicted as a red line.*

5.2.2 $B_{s,d} \to \mu^+\mu^-$ Decay

Next, we turn to the one-dimensional profile likelihood function for $\mathrm{BR}^{\mathrm{EXP/SM}}_{B_{s,d}\to\mu^+\mu^-}$ in the pMSSM10 and compare it to those in the CMSSM, NUHM1, and NUHM2 in Fig. 5.13. It is interesting to note that in the pMSSM10 it is possible to have a suppression of this decay compared to the SM prediction, whereas this is not the case in the CMSSM, NUHM1, and NUHM2. It also appears that the overall $\Delta\chi^2$ function in the pMSSM10 has higher values than the χ^2 contribution from the experimental constraint (the red line), indicating that other constraints also disfavour other values of $B_{s,d} \to \mu^+\mu^-$.

5.2.3 Direct Detection of Dark Matter

We consider the prospects for direct detection of dark matter in underground experiments. In Fig. 5.14 we display the two-dimensional profile likelihood for the spin-independent cross-section off the proton σ_p^{SI} as a function of the LSP mass. The red and blue solid (dashed) lines show the 68% and 95% CL contours in case that the LHC8 constraints are (not) applied. The green shaded region indicates the 90% CL upper limits on σ_p^{SI} as a function of $m_{\tilde{\chi}_1^0}$ as established by LUX [23] and XENON100 [22]. The yellow shading indicates the region below the neutrino floor (orange dashed line), where WIMP elastic scattering off nuclei would be indistinguishable from the elastic scattering of neutrinos off nuclei [172]. A magenta line indicates the future sensitivity of the LZ experiment [175].

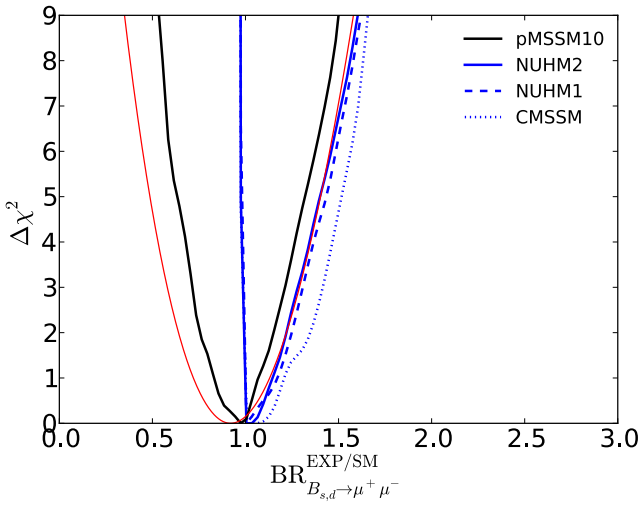

Figure 5.13: *One-dimensional profile likelihood function for the rare $B_{s,d} \to \mu^+\mu^-$ decay in the pMSSM10, CMSSM, NUHM1, and NUHM2. The χ^2 contribution from the $B_{s,d} \to \mu^+\mu^-$ constraint is depicted as a red line.*

We see again that the LHC8 constraints remove the region where t-channel stau exchange brings the relic density into the cosmologically allowed range, namely at LSP masses $m_{\tilde{\chi}_1^0} \lesssim 80$ GeV. On the log scale it is more visible that the Z- and h-funnel are the remaining mechanisms that allow to fulfil (at the 95% CL) the relic density constraint. Another interesting observation is that the spin-independent cross-section can take values below the neutrino floor, and this is allowed at the 68% CL when the LHC8 constraints are not applied. However, when the LHC8 constraints are applied, the 68% CL region favours spin-independent cross-sections that would be within reach for the future LZ experiment. This highlights the complementarity between direct detection experiments and sparticle searches at the LHC.

We note that values of the σ_p^{SI} are allowed below the neutrino floor at the 95% CL, even when the LHC8 constraints are applied. This is due to cancellations between different contributions to the spin-independent cross-section matrix element. One might wonder whether the spin-independent cross-section off the proton could be very different from that off the neutron. We address this question in Fig. 5.15 where we display the scatter plot of the spin-independent elastic scattering cross-section off the proton (horizontal axis) and off the neutron (vertical axis) for model points sampled in the $(m_{\tilde{\chi}_1^0}, \sigma_p^{\mathrm{SI}})$ plane. The colours indicate whether the σ_p^{SI} and/or σ_n^{SI} are above or below the neutrino floor. A diagonal

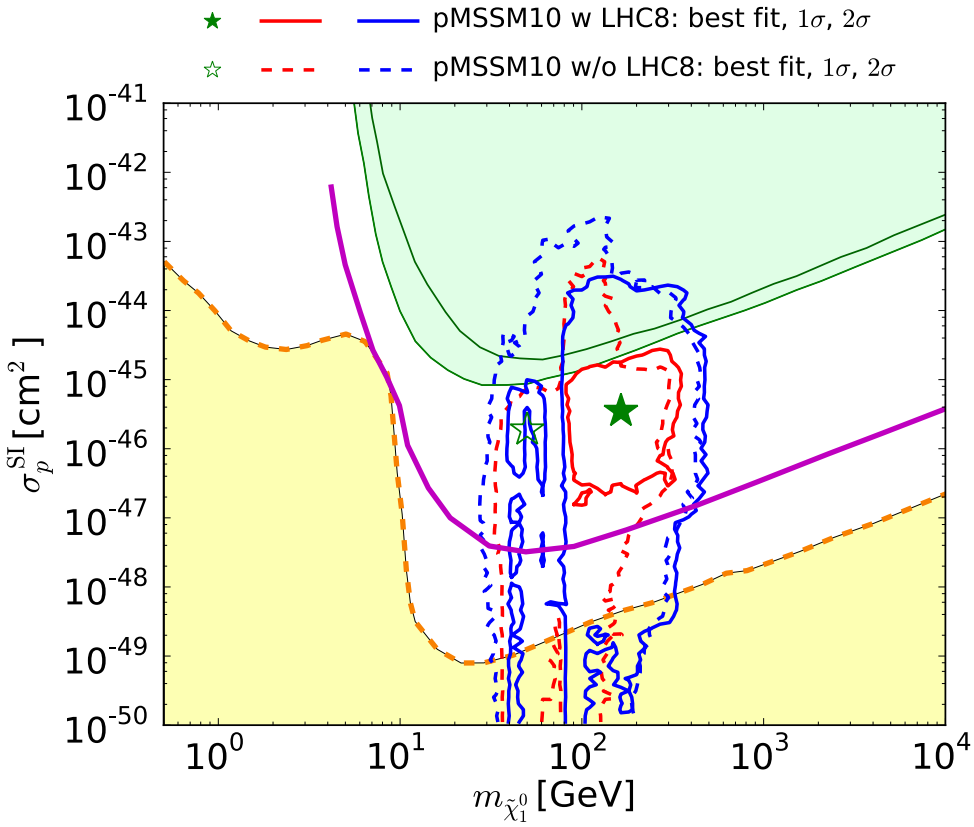

Figure 5.14: *The 68% and 95% CL contours in the $(m_{\tilde{\chi}_1^0}, \sigma_p^{\rm SI})$ plane compared to 90% CL upper limits on $\sigma_p^{\rm SI}$ from LUX [23] and XENON100 [22], future sensitivity of the LZ experiment [175], and the neutrino floor [172]. The red and blue solid (dashed) lines show the 68% and 95% CL contours in case that the LHC8 constraints are (not) applied. The green shaded region indicates the 90% CL upper limits on $\sigma_p^{\rm SI}$ as a function of $m_{\tilde{\chi}_1^0}$ by LUX and XENON100. The yellow shaded region indicates the region below the neutrino floor (orange dashed line). A magenta line indicates the future sensitivity of the LZ experiment.*

dashed line indicates where $\sigma_p^{\rm SI}$ and $\sigma_n^{\rm SI}$ are equal. We see that the majority of points have either both $\sigma_p^{\rm SI}$ and $\sigma_n^{\rm SI}$ above the neutrino floor (black) or both $\sigma_p^{\rm SI}$ and $\sigma_n^{\rm SI}$ below the neutrino floor (red). There are only a few points where $\sigma_p^{\rm SI}$ is above and $\sigma_n^{\rm SI}$ is below the neutrino floor (blue) or visa versa (green). We conclude that there is no 'no-loose' theorem in the pMSSM10 for the direct detection of dark matter scattering.

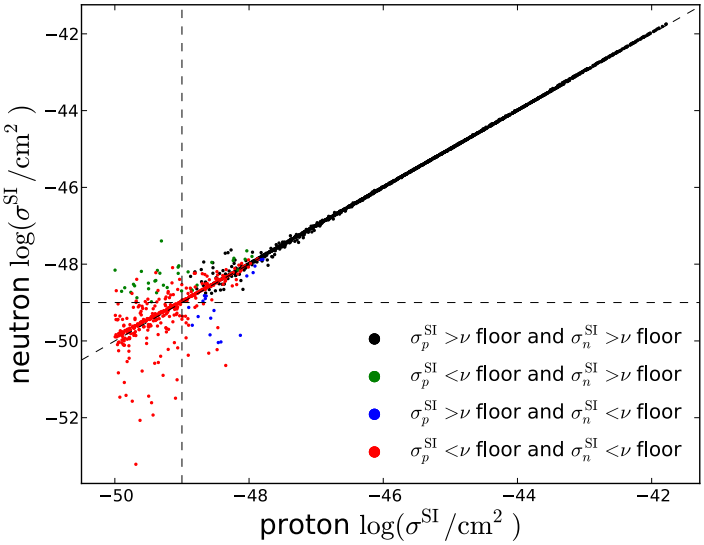

Figure 5.15: *Scatter plot of the spin-independent elastic scattering cross-section off the proton (horizontal axis) and off the neutron (vertical axis) for model points sampled in the* $(m_{\tilde{\chi}_1^0}, \sigma_p^{\rm SI})$ *plane. The colours indicate whether the* $\sigma_p^{\rm SI}$ *and/or* $\sigma_n^{\rm SI}$ *are above or below the neutrino floor. A diagonal dashed line indicates where* $\sigma_p^{\rm SI}$ *and* $\sigma_n^{\rm SI}$ *are equal.*

5.3 Extrapolation to High Scales

In the pMSSM10 we set soft SUSY breaking parameters at an input scale $M_{SUSY} \equiv \sqrt{m_{\tilde{t}_1} m_{\tilde{t}_2}}$, not making any assumptions or imposing any restrictions on how these may extrapolate to the GUT scale (M_{GUT}) using the renormalisation-group equations (RGEs). However, one might still be curious what the properties are of the soft SUSY breaking parameters when they are extrapolated to high energy scales. We first turn to Fig. 5.16, where we show the extrapolation of the soft SUSY breaking parameters to high energies for the best-fit point of the pMSSM10. Here the black, darker grey, and lighter grey lines correspond to M_1, M_2, and M_3 respectively. The other lines correspond to $\text{sign}(m_0^2) \cdot \sqrt{|m_0^2|}$ where m_0^2 refers to scalar mass-squared parameters of the right- and left-handed sleptons (red), right- and left-handed first- and second-generation squarks (blue), and right- and left-handed third-generation squarks (green). In the pMSSM10 these parameters are set to unify at $M_{\rm SUSY}$ to masses $m_{\tilde{\ell}}$, $m_{\tilde{q}_{12}}$, and $m_{\tilde{q}_3}$, respectively. We first observe that the right-handed selectron and smuon mass squared parameters (the lower red line) become negative, i.e. they become tachyonic. Particles that become tachyonic may raise cosmological issues, but they do not necessarily lead to an unacceptable evolution of the Universe [173]. The

next thing to note is that $M_1 \simeq M_2$ at M_{SUSY} results in $M_1 \simeq 2 \cdot M_2$ at M_{GUT}, whereas $M_3(M_{GUT})$ is far from $M_1(M_{GUT})$ or $M_2(M_{GUT})$. The scalar mass parameters are also non-universal.

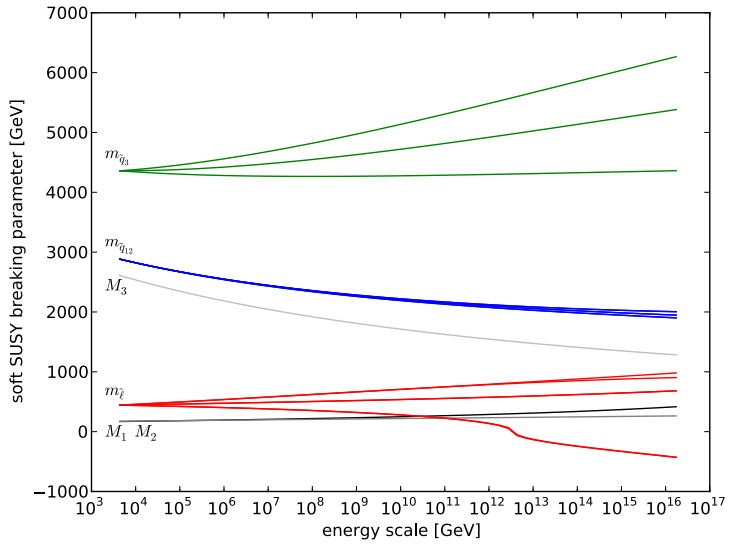

Figure 5.16: *Illustration of the extrapolation to higher energies of the pMSSM10 soft SUSY breaking parameters, using* SOFTSUSY *[71], based on the best-fit point. The black, darker grey, and lighter grey lines indicate M_1, M_2, and M_3 respectively. Other lines correspond to sign$(m_0^2)\cdot\sqrt{|m_0^2|}$ where m_0^2 refers to scalar mass-squared parameters of the right- and left-handed sleptons (red), right- and left-handed first- and second-generation squarks (blue), and right- and left-handed third-generation squarks (green). In the pMSSM10 the latter parameters are set to unify at $M_{\rm SUSY}$ to the input parameters $m_{\tilde{\ell}}$, $m_{\tilde{q}_{12}}$, and $m_{\tilde{q}_3}$, respectively.*

In the remainder of this section we restrict our attention to model points that have no tachyonic sfermions at the GUT scale. We emphasize that this cut significantly reduces the number of model points, and one may anticipate that some parts of the profile likelihood functions shown here would minimise further in a dedicated scan. Nonetheless, we expect that most of the features discussed in this section would also be present in such a dedicated scan. Encouragingly, the overall χ^2 minimum increases by only 0.2 from 83.2 to 83.4.

In Fig. 5.17 we display (from top left to bottom right) the $(m_{\tilde{q}}, m_{\tilde{g}})$, $(m_{\tilde{t}_1}, m_{\tilde{\chi}_1^0})$, $(m_{\tilde{\chi}_1^\pm}, m_{\tilde{\chi}_1^0})$ and $(m_{\tilde{\mu}_R}, m_{\tilde{\chi}_1^0})$ planes. This time the solid (dashed) red and blue lines indicate 68% and 95% CL regions respectively when the anti-tachyon cut is (not) applied.[2] In the $(m_{\tilde{q}}, m_{\tilde{g}})$ plane (top left) we can clearly see that requiring positive sfermion mass-squared

[2]Hence these dashed lines correspond to the solid lines in previous figures.

parameters m_0^2 removes model points above a diagonal line. Above this line the negative renormalisation by M_3 drives the squark m_0^2 negative at M_{GUT} [60]. The $(m_{\tilde{t}_1}, m_{\tilde{\chi}_1^0})$ plane (top right) reveals that after the anti-tachyon cut 800 GeV $\lesssim m_{\tilde{t}_1} \lesssim$ 2000 GeV are only allowed at the 95% CL, with the exception of a small strip of $\tilde{\chi}_1^0$ masses below $\sim$ 150 GeV, and the compressed region is completely removed. For some model points at $m_{\tilde{t}_1} \sim 900$ GeV and $m_{\tilde{\chi}_1^0} \sim 200$ GeV, the right-handed sbottom mass-squared parameter as well as the right-handed first- and second-generation slepton mass-squared parameters become negative. In the $(m_{\tilde{\chi}_1^\pm}, m_{\tilde{\chi}_1^0})$ plane we see that the anti-tachyon cut leaves the $\tilde{\chi}_1^\pm$ coannihilation region as well as h- and Z-funnel regions unharmed, but it completely removes the stau coannihilation region. By consequence, values of $m_{\tilde{\chi}_1^\pm} \gtrsim 500$ GeV are disfavoured. This removal can be mainly attributed to the right-handed selectron and smuon mass-squared parameters. The same effect is visible in the $(m_{\tilde{\mu}_R}, m_{\tilde{\chi}_1^0})$ plane, where all points near the diagonal are removed.

Another topic that we discuss in the section is the departure of the soft SUSY breaking parameters from universality at the GUT scale. To this end we consider "non-universality measures" for gauginos and sfermions defined as the root-mean-squared of the difference of gaugino and sfermion mass parameters with their respective averages:

$$\sigma_{M,m} \equiv \sqrt{\sum_i^N (m_i - \bar{m})^2 / N} \tag{5.1}$$

where m_i are the gaugino mass parameters and square roots of the (positive) sfermion mass-squared parameters at the GUT scale and $\bar{m}$ is denotes their respective averages. By construction the non-universality measures σ_M and σ_m vanish when exact unification is achieved for the gaugino and sfermion mass parameters. In Fig. 5.18 we show the two-dimensional profile likelihood for (σ_m, σ_M). We can see that in the 95% and 68% CL regions there is no preference for universality of sfermion masses. This is to be expected, given the preference for small smuon masses imposed by the $(g-2)_\mu$ constraint, the lower bound on first- and second-generation squarks, and the tachyon-cut imposed preference for heavy stop masses.

The non-universality measure for gauginos σ_M on the other hand does tend to zero at the 95% CL. These point have $M_1 : M_2 : M_3 \simeq 1 : 2 : 6$ at M_{SUSY}, have a small but non-negligible Higgsino component and the relic density constraint is fulfilled by t-channel stop exchange. They do however have spin-independent cross-sections larger than the upper limits by LUX [23] and XENON100 [22] and only the uncertainty on σ_p^{SI} (due

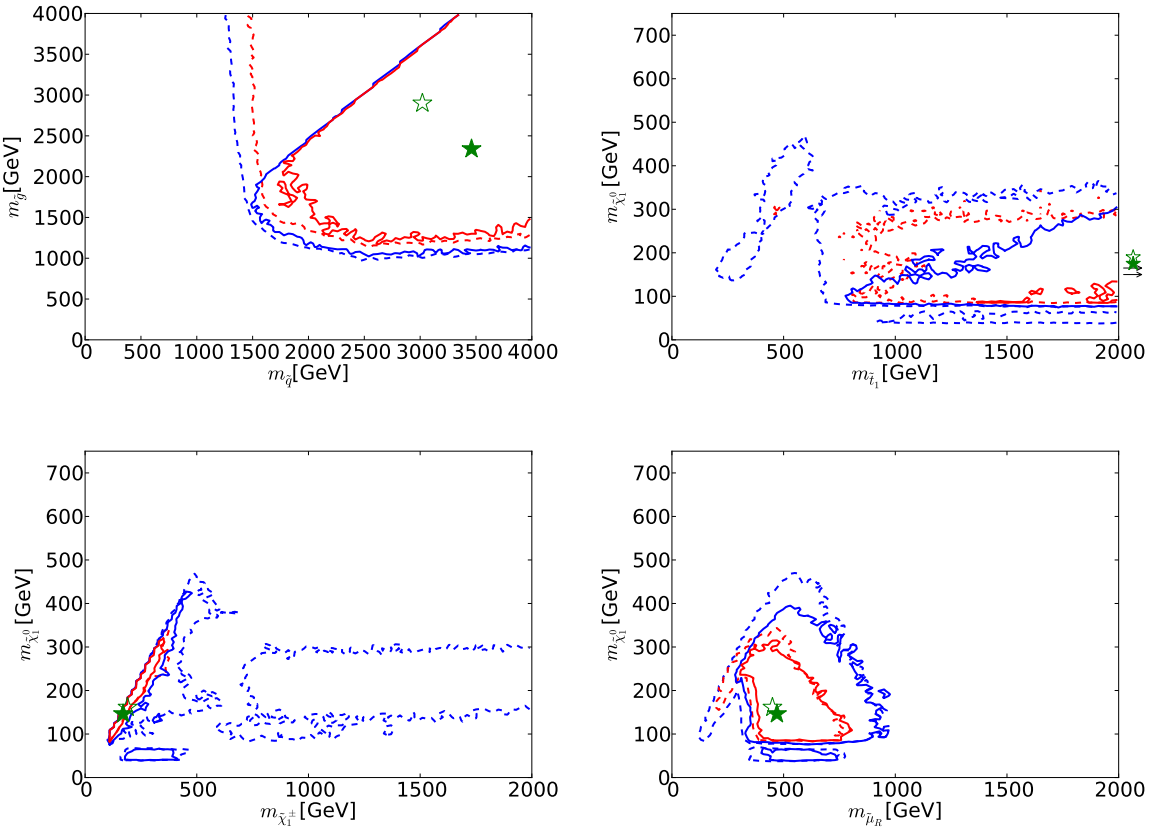

Figure 5.17: *Illustration of the impact of the anti-tachyon cut on sfermions. From top left to bottom right the* $(m_{\tilde{q}}, m_{\tilde{g}})$, $(m_{\tilde{t}_1}, m_{\tilde{\chi}_1^0})$, $(m_{\tilde{\chi}_1^\pm}, m_{\tilde{\chi}_1^0})$ *and* $(m_{\tilde{\mu}_R}, m_{\tilde{\chi}_1^0})$ *planes are displayed where the solid (dashed) red and blue lines indicate 68% and 95% CL regions respectively when the anti-tachyon cut is (not) applied.*

to hadronic uncertainties) renders these point accessible. The 68% CL region shows a larger degree of non-universality. This can be explained by the fulfilment of the relic density constraint by the $\tilde{\chi}_1^\pm$ coannihilation mechanism, so that $|M_1| \simeq |M_2|$ and they are generally low to fulfil the $(g-2)_\mu$ constraint, together with the lower bound from the LHC8 constraints on gluino masses and possible sign differences between M_1, M_2 and M_3.

In conclusion, the $\tilde{\chi}_1^\pm$ coannihilation region and Z- and h-funnel regions would survive if one required that sfermions may not be tachyonic at higher energy scales and such a requirement would barely alter the global χ^2 minimum. We reiterate that tachyonic sfermions do not necessarily yield an unacceptable evolution of the Universe [173]. We also considered the degree of non-universality if one extrapolates the soft SUSY parameters of

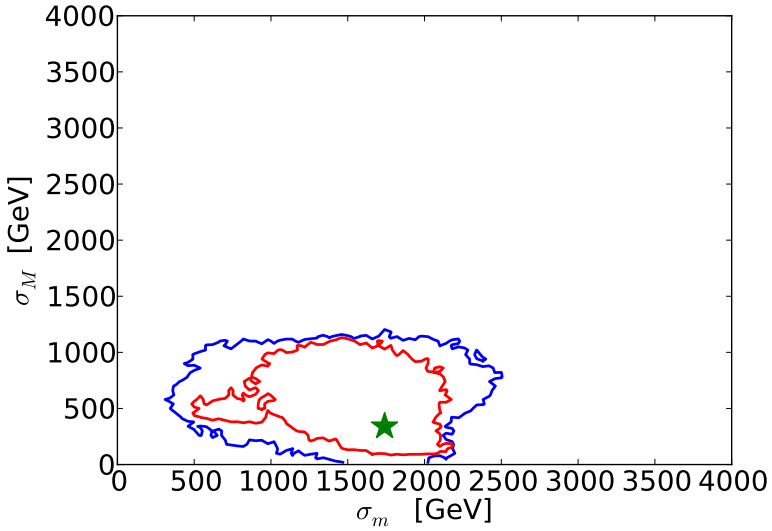

Figure 5.18: *Two-dimensional profile likelihood function indicating the degree of non-universality of the gaugino and sfermion soft SUSY mass parameters at the GUT scale.*

the pMSSM10 to the GUT scale. Here we saw that scalar universality is quite strongly violated, whereas gaugino universality is mainly violated by the splitting between the gluino mass, the fulfilment of the relic density constraint by the $\tilde{\chi}_1^{\pm}$ coannihilation mechanism, and possible sign differences between M_1, M_2 and M_3.

5.4 Prospects for Sparticle Detection in Future LHC Runs

At the time of the completion of this thesis the LHC has started Run 2. During Run 2 data will be taken at a centre-of-mass energy of $\sqrt{s} = 13$ TeV and it is expected that the ATLAS and CMS experiments will have collected an integrated luminosity of 300 fb^{-1} by the early 2020s. There are also plans for a subsequent upgrade of the LHC so that it can run at higher luminosities and ultimately collect 3000 fb^{-1} of integrated luminosity. In this section we discuss some prospects for direct searches for sparticles by ATLAS and CMS during these future runs of the LHC based on our fit of the pMSSM10. We adopt projections of sensitivities for future runs of the LHC based on simulation studies by ATLAS [176–179] as well as extrapolations of current limits as reported in Ref. [60].

In first year(s) of data Run 2 the ATLAS and CMS searches will benefit from the increase in the centre-of-mass energy from 8 to 13 TeV. With just a few fb^{-1} of data the LHC searches should be able to probe gluino masses and squark masses of ~ 1500 GeV, cf. Fig. 3a and 3b in Ref. [178], which are within the 68% CL region as can be seen from the top panels in Fig. 5.5. For the third-generation quarks (bottom panels in Fig. 5.5) we note that besides masses of $m_{\tilde{t}_1} \sim 800$ GeV and $m_{\tilde{b}_1} \sim 900$ GeV at the 68% CL, there are also masses of 200 GeV $\lesssim m_{\tilde{t}_1} \lesssim 600$ GeV and $m_{\tilde{b}_1} \sim 600$ GeV available in the compressed-stop region (as well as a few model points at the 68% CL). These regions may also be partly accessible in the first years of Run 2, cf. Fig. 9a in Ref. [178].

We now turn to more long-term prospects for Run 2 and beyond. We first consider a simulation study by the ATLAS Collaboration, which explored the discovery and exclusion reach for a generic $\not{E}_T$ search with 300 and 3000 fb^{-1} of data at $\sqrt{s} = 14$ TeV, as is shown in Fig. 13 in Ref. [179]. In Fig. 5.19 we depict our 68% and 95% CL contours with red and blue lines respectively and the location of the best-fit point as a green star, to be compared with the 5σ-discovery (95% CL$_\mathrm{s}$-exclusion) contour with 300 fb^{-1} of data with a solid (dashed) magenta line. We can see that a large part of the parameter space 68% CL region and notably the best-fit point will be probed already during LHC Run 2.

In Figs. 5.20 and 5.21 we revisit some of the previously displayed sparticle mass planes by carefully assessing the decay modes within the 95% CL region and comparing these to projected sensitivities in future runs of the LHC. In each panel the model points within the 95% CL region are shaded according to the "dominant" decay mode, by which we mean the decay mode that has a branching ratio exceeding 50%, using colours as indicated in the legend. Model points for which all of these branching ratios less are than 50% are shaded grey. As before, the red and blue lines indicate the 68% and 95% CL contours, whereas green stars indicate the location of the best-fit point.

We compare these detailed maps of decay modes to sensitivity projections of searches at future runs of the LHC, which we adopted from simulation studies by ATLAS [176, 177] as well as extrapolations of current limits as reported in Ref. [60]. The projections for searches with 300 (3000) fb^{-1} of data at $\sqrt{s} = 14$ TeV are indicated with solid (dashed) lines with colours matching the relevant dominant decay mode. The extrapolation of current 95% CL limit contours in Ref. [60] was done as follows. Given a 95% CL exclusion contour in a SMS plane $(m_X, m_{\tilde{\chi}_1^0})$, the current 95% CL limits on $m_{\tilde{\chi}_1^0}$ and m_X were first rescaled using the `Collider Reach` tool [180], assuming that the current search performance is maintained. Then the current 95% CL exclusion contour was extrapolated assuming the same shape as the current limit, reflecting a similar experimental acceptance. We summarise the

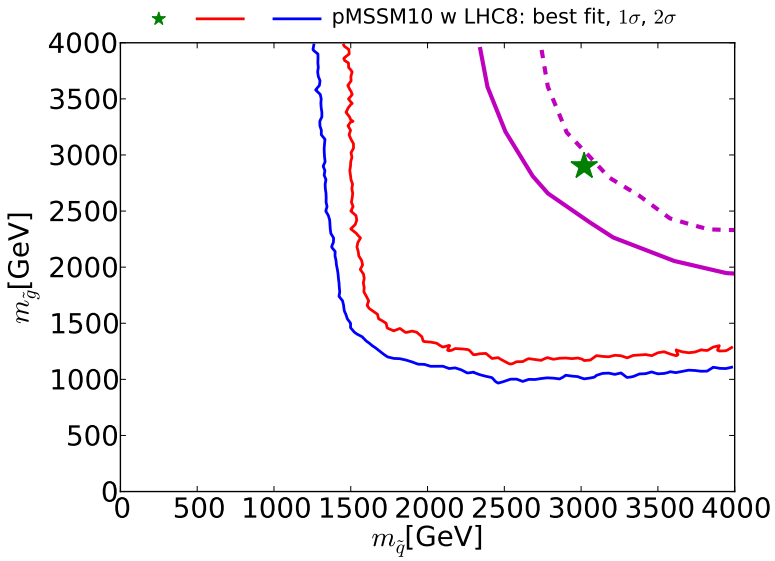

Figure 5.19: *The 68% and 95% CL contours in the $(m_{\tilde{q}}, m_{\tilde{g}})$ plane to be compared with the 5σ-discovery (95% $\mathrm{CL_s}$-exclusion) reaches for searches for first- and second-generation squarks and gluinos in Run 2 [179] indicated with solid (dashed) magenta lines. The 68% and 95% CL contours are indicated with red and blue lines respectively and the location of the best-fit point with a green star.*

projections shown in Figs. 5.20 and 5.21 in Table 5.4.

A recurring theme is that in the 68% CL the $\tilde{\chi}_1^\pm$ coannihilation mechanism brings the relic density in the cosmologically acceptable range. Therefore most model points have a spectrum with a small mass gap $m_{\tilde{\chi}_1^\pm} \simeq m_{\tilde{\chi}_2^0} \sim m_{\tilde{\chi}_1^0} + 20$ GeV, where the $\tilde{\chi}_1^0$ and $\tilde{\chi}_1^\pm/\tilde{\chi}_2^0$ have mainly a Bino and Wino composition respectively (and $\tilde{\chi}_2^\pm/\tilde{\chi}_3^0/\tilde{\chi}_4^0$ mainly Higgsino). By consequence, many of the decay chains in the 68% CL evolve via the Winos $\tilde{\chi}_1^\pm/\tilde{\chi}_2^0$. This scenario is consistently indicated with pale blue shading.

We first turn to top left panel of Fig. 5.20 were we display the dominant decay modes in the $(m_{\tilde{t}_1}, m_{\tilde{\chi}_1^0})$ plane. Thin black dashed lines indicate where mass splittings $m_{\tilde{t}_1} - m_{\tilde{\chi}_1^0} = 0, M_W + m_b, m_t$ and projections for 300 fb^{-1} of data at $\sqrt{s} = 14$ TeV, as detailed in Table 5.4, are shown using solid lines. We note that for the majority of model points in the compressed region the stop mainly decays into $b\tilde{\chi}_1^\pm$ as the result of the small mass splitting between the $\tilde{\chi}_1^\pm/\tilde{\chi}_2^0$ and the $\tilde{\chi}_1^0$. Since no simulation studies by ATLAS or CMS are available for the corresponding SMS model $\tilde{t}_1 \to b\tilde{\chi}_1^\pm$, we adopt the projection made in Ref. [60] (cf. Table 5.4), which is shown as a pale blue line. We see that such a search would significantly probe the 95% CL region with compressed-stop spectra. There

Figure	SMS model	Colour	Study	Source
5.20 top left	$\tilde{t}_1 \to t\tilde{\chi}_1^0$	black	ATLAS simulation	Fig. 5 [176]
	$\tilde{t}_1 \to b\tilde{\chi}_1^\pm$	pale blue	extrapolation	Fig. 6c [149]
5.20 top right	$\tilde{\chi}_1^\pm\tilde{\chi}_2^0$ via Wh	orange	ATLAS simulation	Fig. 4 [177]
	$\tilde{\chi}_1^\pm\tilde{\chi}_2^0$ via WZ	yellow	ATLAS simulation	Fig. 5a [177]
	$\tilde{\chi}_1^\pm\tilde{\chi}_2^0$ via $\tilde{\tau}_1/\tilde{\nu}_\tau$	light purple	extrapolation	Fig. 6c [149]
5.20 bottom left	$\tilde{\mu}_R \to \mu\tilde{\chi}_1^0$	pale blue	extrapolation	Fig. 8a [153]
5.20 bottom right	$\tilde{\mu}_L \to \mu\tilde{\chi}_1^0$	pale blue	extrapolation	Fig. 8b [153]
5.21 left	$\tilde{g} \to q\bar{q}\tilde{\chi}_1^0$	pale blue	ATLAS simulation	Fig. 9a [177]
5.21 right	$\tilde{q} \to q\tilde{\chi}_1^0$	pale blue	ATLAS simulation	Fig. 9c [177]

Table 5.4: *Overview of projected sensitivities of LHC SUSY searches with 300 (3000) fb^{-1} of data at $\sqrt{s} = 14$ TeV that are shown in Figs. 5.20 and 5.21 with solid (dashed) lines. For each projection the SMS model, the corresponding line colour in Figs. 5.20 and 5.21, and the study in which these projections were obtained are listed. We adopt the extrapolations made in Ref. [60] using the* `Collider Reach` *tool [180] as explained in the text. References indicate the contours that were used for these extrapolations.*

is also a small island located at $m_{\tilde{t}_1} \sim 300$ GeV and $m_{\tilde{\chi}_1^0} \sim 200$ GeV where for some model points the stop decay via the off-shell charginos dominates. For many model points at stop masses larger than ~ 700 GeV the stop decay via Higgsinos dominates.

We now turn to the top right panel of Fig. 5.20 where the model points are coloured according to the dominant decay modes of $\tilde{\chi}_1^\pm$ and $\tilde{\chi}_2^0$, thin black lines indicate mass gaps $(m_{\tilde{\chi}_1^\pm} \simeq m_{\tilde{\chi}_2^0}) - m_{\tilde{\chi}_1^0}$ of $\{0 \text{ GeV}, M_Z, M_h\}$, and projections are shown as detailed in Table 5.4. We see that in the 68% CL region the $\tilde{\chi}_1^\pm$ and $\tilde{\chi}_2^0$ mainly decay via off-shell bosons since it is located at small mass differences $m_{\tilde{\chi}_1^\pm} - m_{\tilde{\chi}_1^0} \lesssim 40$ GeV. Sensitivity of Monojet-like searches that directly target such compressed electroweakino spectra have been explored in Ref. [181] and it was found that they could exclude $m_{\tilde{\chi}_1^\pm} \lesssim 200$ GeV for a small mass gap $m_{\tilde{\chi}_1^\pm} - m_{\tilde{\chi}_1^0} \lesssim 20$ GeV with 300 fb^{-1} of data, assuming optimistic systematic uncertainties. This could exclude the best-fit point it. However, we would like to stress that the sensitivity of these searches strongly depends on the mass gap. The decay via staus is also available at 68% CL in a small region where $m_{\tilde{\chi}_1^\pm} \sim 300$ GeV and $m_{\tilde{\chi}_1^0} \sim 250$ GeV. The latter decay mode is also dominant at 95% CL region for points at $\tilde{\chi}_1^0$ masses between ~ 100 GeV and ~ 450 GeV and mass splittings up to $m_{\tilde{\chi}_1^\pm} - m_{\tilde{\chi}_1^0} \lesssim 400$ GeV. In the region where 150 GeV $\lesssim m_{\tilde{\chi}_1^0} \lesssim 300$ GeV and $m_{\tilde{\chi}_1^\pm} \gtrsim 750$ GeV (which corresponds to stau coannihilation) the dominant decay is via left-handed selectrons and smuons, although there are also model points where the decay via staus dominates. Finally, we see a small

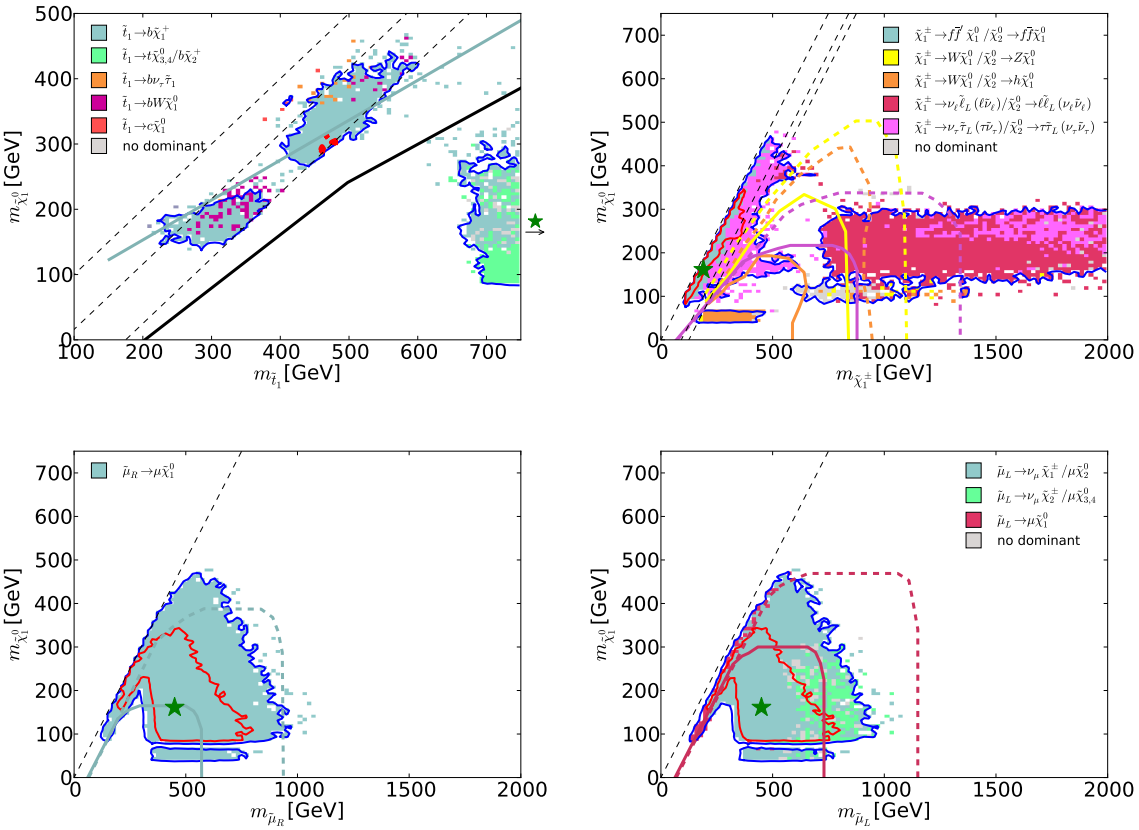

Figure 5.20: *The mass planes (from top left to bottom right) of $m_{\tilde{t}_1}$, $m_{\tilde{\chi}_1^\pm}$, $m_{\tilde{\mu}_L}$, and $m_{\tilde{\mu}_R}$ versus the LSP mass, where each point within the 95% CL region is shaded according to the decay mode that has a branching ratio of $> 50\%$ as detailed in the legends, or grey if no branching ratio exceeds 50%. In each panel blue and red lines indicate the 68% and 95% CL contours respectively, whereas a green star indicates the location of the best-fit point (if the best-fit point lies outside the displayed range, its location is indicated with an arrow). Thin dashed lines indicate the respective mass splittings with $m_{\tilde{\chi}_1^0}$ of $\{0\ GeV,\ M_W + m_b,\ m_t\}$ (top left), $\{0\ GeV,\ M_Z,\ M_h\}$ (top right), 0 GeV (bottom left) and 0 GeV (bottom right). We also display in each panel solid and dashed lines that indicate the projected 95% CL exclusion reaches with respectively 300 and 3000 fb^{-1} of data as detailed in Table 5.4.*

island at $m_{\tilde{\chi}_1^0} \sim 45, 62.5$ GeV and $m_{\tilde{\chi}_1^\pm} \lesssim 450$ that corresponds to the Z- and h-funnels. In this region the $\tilde{\chi}_2^0$ decay to $h\tilde{\chi}_1^0$ dominates and one could envisage that it is well within reach of 3-lepton $+ \not{E}_T$ searches, for which the projected sensitivity [177] for associated $\tilde{\chi}_1^\pm \tilde{\chi}_2^0$ production with decays via Wh is depicted with orange lines.

We now turn to the $(m_{\tilde{\mu}_R}, m_{\tilde{\chi}_1^0})$ and the $(m_{\tilde{\mu}_L}, m_{\tilde{\chi}_1^0})$ planes in the bottom panels of Fig. 5.20. The $(m_{\tilde{\mu}_R}, m_{\tilde{\chi}_1^0})$ plane reveals that the dominant decay chain is into $\mu\tilde{\chi}_1^0$, which

actually has branching ratios exceeding 90% in most of the 95% CL region. We see that the best-fit point would already be in reach for a dilepton search for right-handed sleptons after 300 fb^{-1} of data, whereas a large fraction of the 68% CL region is within reach with the 3000 fb^{-1}, with the important caveat that the strip along the diagonal is untouched. The picture seems somewhat different in the $(m_{\tilde{\mu}_L}, m_{\tilde{\chi}_1^0})$ plane where the decay to $\mu\tilde{\chi}_1^0$ is indicated with bordeaux red shading and only appears when mass differences $m_{\tilde{\mu}_L} - m_{\tilde{\chi}_1^0}$ are small. In the rest of the 68% CL region, the left-handed smuon decays via Winos, although at larger $m_{\tilde{\mu}_L}$ masses the decay in to Higgsinos becomes dominant. Note that the projected sensitivities that are displayed with pale blue lines were extrapolated based on the $\tilde{\mu}_L \to \mu\tilde{\chi}_1^0$ SMS interpretation in Ref. [153]. However, given the small mass gap between the Winos and the Bino, the search should have similar sensitivity to the $\tilde{\mu}_L \to \mu\tilde{\chi}_2^0$ decay.

We now turn to the $(m_{\tilde{g}}, m_{\tilde{\chi}_1^0})$ plane in the left panel of Fig. 5.21. We see that going from lower gluino masses ~ 1000 GeV to higher masses $m_{\tilde{g}} \sim 4000$ GeV, the dominant decay modes shift from off-shell decays via squarks to on-shell decays into squarks. The off-shell decay via first- and second-generation squarks is mainly into Winos, whereas the gluino decay via off-shell third-generation squarks is via both Winos and Higgsinos. The projected sensitivity of jets $+ \not{E}_T$ searches, even though it was derived for the $\tilde{g} \to q\bar{q}\tilde{\chi}_1^0$ decay, should be indicative for the $\tilde{g} \to q\bar{q}'\tilde{\chi}_1^\pm / \tilde{g} \to q\bar{q}\tilde{\chi}_2^0$ due to the small mass gap between the Winos and the Bino. We see that such searches would cover a large fraction of the displayed 95% and 68% CL regions.

We finally turn to the projection in the $(m_{\tilde{q}}, m_{\tilde{\chi}_1^0})$ plane displayed in the right panel of Fig. 5.21. For most of the 95% CL region the squark decay via Winos dominates, although decay via gluinos becomes available for larger squark masses. With a solid (dashed) line we indicate the projection by the ATLAS Collaboration [177] of the sensitivity of jets + $\not{E}_T$ searches for the squark pair production with the decay mode $\tilde{q} \to q\tilde{\chi}_1^0$ with 300 (3000) fb^{-1} of 14 TeV data. Given the small mass splitting between $m_{\tilde{\chi}_1^\pm} \simeq m_{\tilde{\chi}_2^0}$ and $m_{\tilde{\chi}_1^0}$ this projection should be indicative for the reach at the future runs of the LHC.

5.5 Prospects for Sparticle Detection at a Future e^+e^- Collider

We now discuss some prospects for a possible future e^+e^- collider. Fig. 5.22 displays the one-dimensional profile likelihood functions for the lowest particle pair- and associated

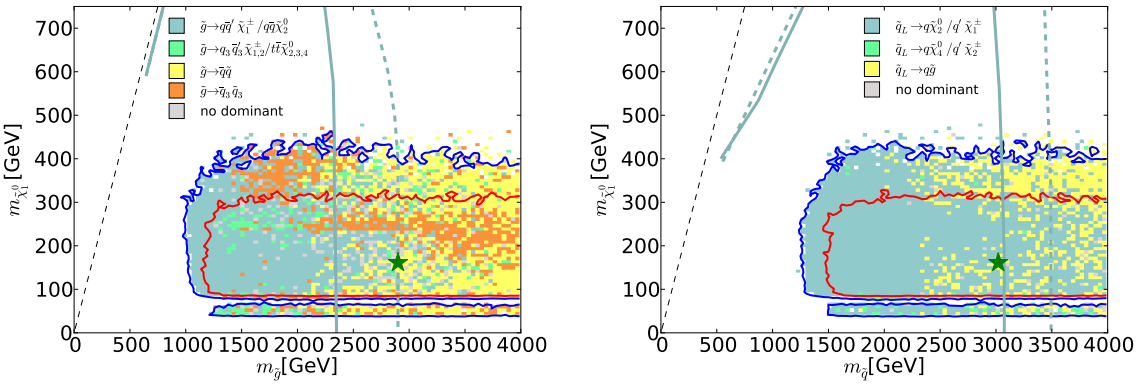

Figure 5.21: *The $(m_{\tilde{g}}, m_{\tilde{\chi}_1^0})$ and $(m_{\tilde{q}}, m_{\tilde{\chi}_1^0})$ mass planes in which each point within the 95% CL region is shaded according to the decay mode that has a branching ratio of $> 50\%$ as detailed in the legends, or grey if no branching ratio exceeds 50%. In each panel blue and red lines indicate the 68% and 95% CL contours respective, whereas a green star indicates the location of the best-fit point. Thin dashed lines indicate where $m_{\tilde{g}} = m_{\tilde{\chi}_1^0}$ (left) and $m_{\tilde{q}} = m_{\tilde{\chi}_1^0}$ (right). We also display in each panel solid and dashed lines that indicate the projected 95% CL exclusion reaches with respectively 300 and 3000 fb^{-1} of data as detailed in Table 5.4.*

electroweakino production thresholds in e^+e^- annihilation in the pMSSM10 (solid black), CMSSM (dotted blue), NUHM1 (dashed blue) and NUHM2 (solid blue). For the pair- and associated production of $\tilde{\chi}_1^0\tilde{\chi}_1^0$ (upper left), $\tilde{\chi}_1^0\tilde{\chi}_2^0$ (upper right) and $\tilde{\chi}_1^\pm\tilde{\chi}_1^\mp$ (lower right) production, we see that the largest parts of the 68% CL intervals in the pMSSM10 lie within reach of an e^+e^- collider with centre-of-mass energy of 500 GeV and the threshold locations that would be within reach of a 1000 GeV collider are favoured at $\Delta\chi^2 \leq 3$, although there is no upper limit at 95% CL. For the associated $\tilde{\chi}_1^0\tilde{\chi}_3^0$ production (lower left) the 68% CL interval lies between threshold centre-of-mass energies of ~ 300 GeV and ~ 1100 GeV and there is again no upper limit at the 95% CL. In all cases, the expected threshold locations in the pMSSM10 are at considerably lower centre-of-mass energies than the CMSSM, NUHM1, and NUHM2.

5.6 Discussion

In the following we compare our results of the pMSSM10 with those of the pMSSM9 by BayesFITS [57] and of the pMSSM15 by SuperBayes [59] highlighting some representative

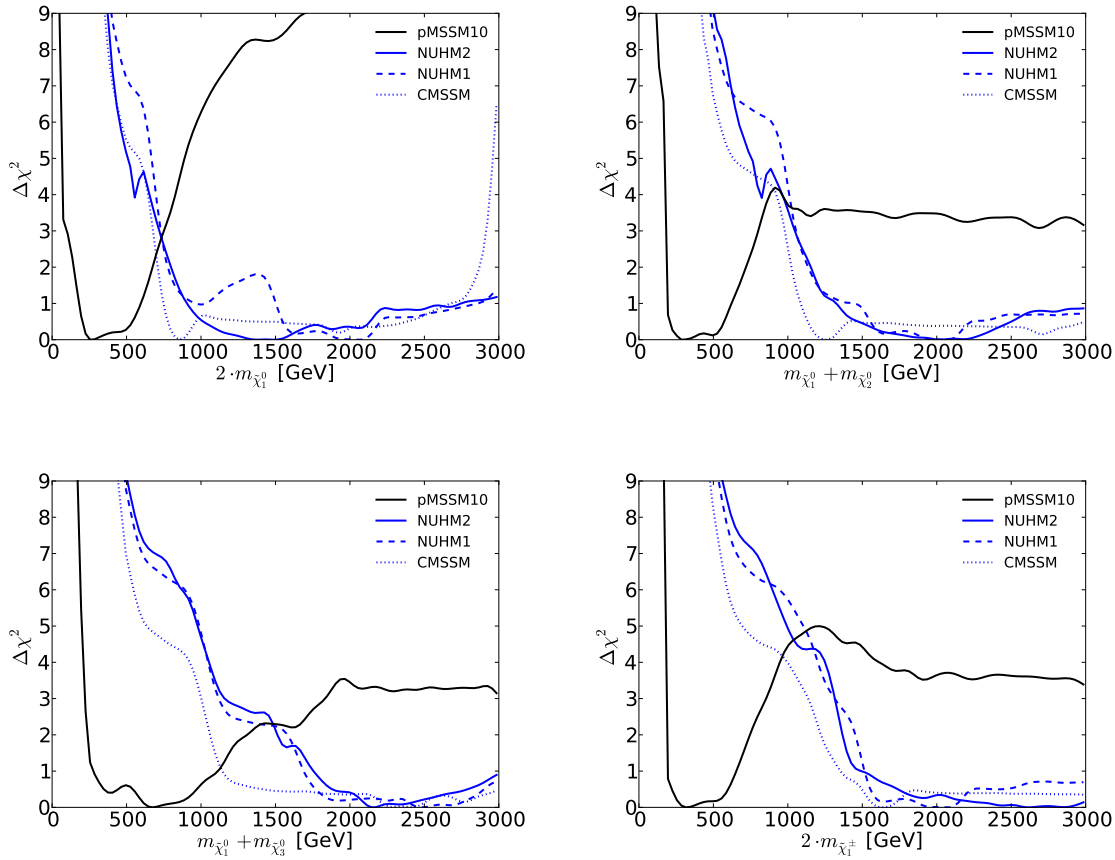

Figure 5.22: *The one-dimensional profile likelihood functions for thresholds for (from top left to bottom right) pair- and associated* $\tilde{\chi}_1^0\tilde{\chi}_1^0$, $\tilde{\chi}_1^0\tilde{\chi}_2^0$, $\tilde{\chi}_1^0\tilde{\chi}_3^0$, *and* $\tilde{\chi}_1^\pm\tilde{\chi}_1^\mp$ *production in* e^+e^- *annihilation.*

figures in these references.

In Fig. 5 of Ref. [57] the (M_1, μ) plane is shown in the pMSSM9, followed by a discussion of the DM annihilation processes in the early universe. They also find the h-funnel region where the LSP is mainly Bino-like and $m_{\tilde{\chi}_1^0} \sim 62.5$ GeV, the slepton t-channel exchange region (bulk) for $m_{\tilde{\chi}_1^0} \lesssim 100 - 150$ GeV, and the slepton coannihilation region for $100 - 150$ GeV $\lesssim m_{\tilde{\chi}_1^0} \lesssim 300$ GeV, as well as a region where the LSP is an admixture of the Bino and Higgsino. However, the pMSSM9 as defined by BayesFITS does not allow for the $\tilde{\chi}_1^\pm$ coannihilation region where $M_1 \simeq M_2$. Also, the "basic" results of BayesFITS do not include the $(g-2)_\mu$ constraint, so that large values of $m_{\tilde{\chi}_1^0}$ are not disfavoured. On the other hand, they find that the "basic" constraint together with the $(g-2)_\mu$ constraint and the 3-lepton search only leave a very small region that is allowed at the 95% CL. The relation of $M_1 = 0.5 \cdot M_2$ and $m_{\tilde{\mu}} = M_1 + 50$ GeV cause the $\tilde{\chi}_1^\pm/\tilde{\chi}_2^0$

to decay into on-shell selectrons and smuons, a decay to which the 3-lepton search is very sensitive, and $(g-2)_\mu$ to be only fulfilled for small values of M_1 (and hence $m_{\tilde{\mu}}$) disfavouring the bulk and slepton-coannihilation regions. Therefore, the $\tilde{\chi}_1^\pm$ coannihilation region in the pMSSM10 gives a better fit to all constraints than the pMSSM9 considered in [57]. We conclude that the pMSSM10 is more comprehensive than the pMSSM9 as defined by BayesFITS and that our implementation of the LHC constraints is more complete.

Finally, we consider Fig. 10 in Ref. [59], where from left to right the $(m_{\tilde{g}}, m_{\tilde{q}})$, $(m_{\tilde{\chi}_1^\pm}, m_{\tilde{\chi}_1^0})$, and $(m_{\tilde{\chi}_1^0}, \sigma_p^{\mathrm{SI}})$ planes are displayed for profile likelihood functions with (top row) and without (bottom row) the $(g-2)_\mu$ constraint taken into account. For each point in the planes the colour coding indicates the level of exclusion by the ATLAS searches for jets and 0 leptons [124] and 3 leptons [170] both with 4.7 fb^{-1} of data at $\sqrt{s} = 7$ TeV. We would like to emphasize that this information only provides an indication of the impact of searches for direct production of sparticles, in contrast to the full implementation of these searches as we did in our fits. Consider for example the $(m_{\tilde{g}}, m_{\tilde{q}})$ plane in the top left panel of Fig. 10 in Ref. [59], where we see that almost all points are excluded a level of 1σ or higher. Comparing this to Fig. 5.19, we see that beyond the LHC limits on squark and gluino masses the full plane is allowed at the 68% CL. We conclude that the pMSSM15 fit by the SuperBayes Collaboration would benefit from also adopting a complete implementation of the LHC constraints.

Chapter 6

Conclusions

In this thesis we assessed the status of global fits of the CMSSM, NUHM1, NUHM2, and pMSSM10 taking into account experimental constraints available after Run 1 of the LHC. These global fits included experimental constraints from flavour physics observables [11–16], electroweak precision observables [17–20], the anomalous magnetic dipole moment of the muon [21], direct detection of dark matter [22, 23], the relic density of dark matter [3], properties of the Higgs boson [24], and direct searches for production of SUSY particles during LHC Run 1 [25, 26].

Novel aspects in this thesis are the in depth mapping of the annihilation processes that underlie the fulfilment of the cosmological constraint on the dark matter relic density $\Omega_{\rm CDM}h^2$ for the CMSSM, NUHM1, and NUHM2, using the metrics defined in Eq. 4.1. This thesis also features the first global fit of a pMSSMn (a reduced version of the general 19 parameter pMSSM [10]) with a comprehensive treatment of searches for SUSY particles at the LHC with the full Run 1 data set of 20 fb^{-1} at $\sqrt{s} = 8$ TeV.

One of the recurring themes in all global fits is the (non-) fulfilment of the constraint that comes from the anomalous magnetic dipole moment of the muon $(g-2)_\mu$, which is experimentally found to be enhanced [21] with respect to the SM prediction [92]. It is well known that low smuon masses are required to satisfy this constraint [93]. In the CMSSM, NUHM1, and NUHM2 the constraints from direct SUSY searches for squarks and gluinos at the LHC [121] and the mass of the Higgs boson [24] cannot be reconciled with such small smuon masses. Consequently, there is no preference for low mass SUSY spectra in these three models compared to high mass spectra. In the pMSSM10 the slepton (and electroweakino) masses are no longer related to the squark and gluino masses, so that the $(g-2)_\mu$ constraint can be fulfilled. This constrains sleptons and electroweakinos to have

low masses, whereas strongly produced sparticles are relatively unconstrained. Comparing the contributions from (groups) of constraints in Table 5.1, we saw that the contribution of the $(g-2)_\mu$ constraint significantly reduces in the pMSSM10. This table also allowed to compare the total χ^2/d.o.f., namely 32.8/24 (CMSSM), 31.1/23 (NUHM1), 30.3/22 (NUHM2), 20.5/18 (pMSSM10), and the respective associated χ^2 probabilities are 11%, 12%, 11%, and 31%.

6.1 The CMSSM, NUHM1, and NUHM2

As said, for the CMSSM we discussed in detail the regions in parameter space that correspond to the annihilation mechanisms responsible for bringing the dark matter relic density $\Omega_{\rm CDM}h^2$ into the allowed cosmological range, in particular highlighting corresponding predictions for sparticle masses. The relevant "DM mechanisms" in the CMSSM are stau coannihilation, A/H funnel, $\tilde{\chi}_1^\pm$ coannihilation, and focus point, as well as a "hybrid" between the stau coannihilation and A/H funnel mechanisms for which staus annihilate through on-shell heavy Higgs bosons.

The stau coannihilation region is located at $200 \lesssim m_0 \lesssim 2000$ GeV and $750 \leq m_{1/2} \leq 1500$ GeV, and has well defined mass predictions: they are bounded from below by the searches for squarks and gluinos [121, 122] and bounded from above by the combined constraint from CMS [14] and LHCb [13] on BR($B_{s,d} \to \mu^+\mu^-$), as well as the $\Omega_{\rm CDM}h^2$ constraint. In fact, the stau coannihilation region in the CMSSM is the only region that will be significantly probed in future runs of the LHC, as can be seen from the red lines in Fig. 4.5. On the other hand, the prospects for direct detection are less promising. Although the stau coannihilation region has spin-independent cross-section above the "neutrino floor", even LZ [175] will only be partially sensitive to the preferred values in the $(m_{\tilde{\chi}_1^0}, \sigma_p^{\rm SI})$ plane.

The A/H funnel and hybrid regions generally have larger lower bounds on the sparticle masses than the stau coannihilation region, although in the hybrid region both m_0 and $m_{1/2}$ are bounded from above: $m_0 \lesssim 2000$ GeV and $m_0 \lesssim 2500$ GeV. At large values of m_0, the A/H funnel region yields an almost equally good fit as in the stau coannihilation region. The corresponding masses are far beyond the reach of the LHC. On the positive note, future experiments for direct detection of dark matter should have access to a large fraction of the viable parameter space.

The focus point region as well as the $\tilde{\chi}_1^\pm$ coannihilation region occur for values of

$m_0 \gtrsim 4000$ GeV. Here μ approaches M_1 so that the LSP obtains a significant Higgsino composition. Consequently, $\sigma_p^{\rm SI}$ is sizable and is inside the region excluded at 90% CL by LUX [23] and XENON100 [22].

In the NUHM1 and NUHM2 $m_{H_u}^2$ and $m_{H_d}^2$ can vary independently, although they are set equal in the NUHM1. This additional freedom is equivalent to the freedom to choose M_A or (and) μ. One of the consequences is that μ may take values similar to or below M_1 when $m_{1/2} \gtrsim 2000$ GeV for any value of m_0. In this case the LSP is mainly Higgsino-like, as well as $\tilde{\chi}_2^0$ and $\tilde{\chi}_1^\pm$ and their masses are similar so that the $\Omega_{\rm CDM}h^2$ constraint is fulfilled by $\tilde{\chi}_1^\pm$ coannihilation. In contrast to the CMSSM, the values of $\sigma_p^{\rm SI}$ are below the 90% CL upper limit by LUX [23] and XENON100 [22].

We also saw that in the NUHM1 negative values of m_H^2 facilitate the hybrid mechanism and, compared to the CMSSM, allow larger values of $m_{1/2}$ at low values of m_0. In the NUHM2 the stau coannihilation region is generally favoured as a result of the lifted degeneracy between $m_{H_u}^2$ and $m_{H_d}^2$. This region even extends to negative values of m_0^2.

We also studied the differences in the χ^2 function between the three models. For example, in the NUHM1 we found that the constraints from BR($B_{s,d} \to \mu^+\mu^-$) can be accommodated more easily at large $m_{1/2}$ in the case of the hybrid mechanism, whereas in the NUHM2 it can be completely accommodated as seen in Fig. 4.11.

For the mass predictions this translates in rather (almost) flat profile likelihood functions for the NUHM1 (NUHM2), as compared to the CMSSM, which has a distinct minimum at low masses corresponding to the stau coannihilation region. Even though the NUHM1 and NUHM2 have more free parameters, the mass lower limits are very similar to those in the CMSSM. Finally, we saw that the additional freedom in $m_{H_u}^2$ and $m_{H_d}^2$ make available a region at the 68% CL with values of $\sigma_p^{\rm SI}$ below the neutrino floor.

6.2 The pMSSM10

In the second part of this thesis we considered results for the pMSSM10, which we defined by specifying M_A, μ, and soft SUSY breaking gaugino mass parameters M_1, M_2, M_3, unified first- and second-generation squark mass parameters $m_{\tilde{q}_{12}}$, unified third-generation squark mass parameters $m_{\tilde{q}_3}$, unified first-, second- and third-generation slepton mass parameters $m_{\tilde{\ell}}$, and unified trilinear couplings A, at an input scale $M_{SUSY} = \sqrt{m_{\tilde{t}_1} \cdot m_{\tilde{t}_2}}$, as well as the ratio of Higgs vacuum expectation values $\tan\beta$.

One of the main challenges was to establish an appropriate treatment of SUSY searches

at the LHC with 20 fb^{-1} of data at $\sqrt{s} = 8$ TeV, with the particular aim to approximate point-by-point reinterpretation. In the pMSSM10 it is no longer true that generic jets $+ \not{E}_T$ searches for squarks and gluinos implicitly constrain slepton and electroweakino masses, and therefore the full spectrum of sparticle masses needs to be taken into account. However, the mass scales to which the LHC searches have sensitivity are very different for strongly and electroweakly produced sparticles. This, and the observation that the mass limits for squarks and gluinos are relatively insensitive to the further details of the spectrum when sufficiently inclusive searches are combined [129], lead to define a universal χ^2 function only based on $m_{\tilde{\chi}_1^0}$, $m_{\tilde{g}}$, $m_{\tilde{q}_{12}}$, and $m_{\tilde{q}_3}$ (the production cross-section weighted average over the third generation squark masses) that we refer to as $\chi^2(\text{LHC8}_{\text{col}})$.

The sensitivity of searches for sleptons and electroweakinos depends more strongly on the hierarchy between masses, although masses where the LHC searches have sensitivity are generally smaller than for strongly produced sparticles. Hence, to constrain the masses of sleptons and electroweakinos we took into account the decay modes of individual sparticles, applying limits from simplified model interpretations according to corresponding branching ratios. We also treat the case of compressed stops $m_{\tilde{t}_1} - m_{\tilde{\chi}_1^0} < m_t$ in this way, whilst assuring that it does not contribute to $\chi^2(\text{LHC8}_{\text{col}})$. We refer to constraints the constraints on slepton and electroweakino production as $\chi^2(\text{LHC8}_{\text{EWK}})$, and to the constraints on the compressed stop as $\chi^2(\text{LHC8}_{\text{stop}})$.

We extensively validated the LHC8 constraints by making comparisons with point-by-point reinterpretations of representative model points from our sample. Thereby we established quantitatively how the corresponding uncertainty propagates into uncertainties on the 68% and 95% CL contours in the relevant mass planes. We found that our results are sufficiently robust against the uncertainties arising from the LHC8 constrains.

One of the most defining features of our pMSSM10 scan is the fulfilment of the $(g-2)_\mu$ constraint. This fulfilment is achieved by low smuon masses $m_{\tilde{\mu}} \lesssim 1000$ GeV (and therefore low selectron and stau masses). Due to an interplay between the LHC8 constraint on smuon and selectron pair production, the $\Omega_{\text{CDM}}h^2$ constraint and the $(g-2)_\mu$ constraint, it turns out that $\tilde{\chi}_1^\pm$ coannihilation is the DM mechanism throughout the 68% CL region. This is achieved by having $M_1 \simeq M_2$ at the M_{SUSY} scale, so that the LSP is Bino-like, and $\tilde{\chi}_2^0$ and $\tilde{\chi}_1^\pm$ are Wino-like. In models where M_1 and M_2 unify at the GUT scale, this would be hard if not impossible. Without the LHC8 constraints applied the stau coannihilation and t-channel stau exchange mechanisms are also allowed in 68% CL regions, but the constraints on smuon and selectron pair production remove the t-channel stau exchange region and disfavours the stau coannihilation region to be only allowed in 95% CL regions.

A consequence of the latter is that $\tilde{\chi}_1^\pm$ and $\tilde{\chi}_2^0$ masses are preferred to be $\lesssim 500$ GeV at 68% CL, whereas masses $\gtrsim 800$ GeV are allowed at 95% CL, as can be seen in Fig. 5.7. Similarly, the masses of $\tilde{\chi}_3^0$, $\tilde{\chi}_4^0$, and $\tilde{\chi}_2^\pm$, which are mainly Higgsino-like, are preferred to be $\lesssim 900$ GeV, although there is no upper limit in the sampled range. On the other hand, the masses of squarks and gluinos are poorly determined above the lower limits from the LHC8$_{\rm col}$ constraint ($m_{\tilde{q}} \gtrsim 1400$ GeV and $m_{\tilde{g}} \gtrsim 1000$ GeV at 95% CL). The lighter stop (sbottom) mass has a local minimum at the 95% CL at low masses 390 (530) GeV $\lesssim m_{\tilde{t}_1} \lesssim 570$ (760) GeV and is allowed for values larger then ~ 670 (820) GeV. The heavy Higgs sector is essentially only bounded from below by the constraint from the CMS $H/A \to \tau^+\tau^-$ search [126], with the caveat that $25 \lesssim \tan\beta \lesssim 45$ is preferred at 68% CL at low value of M_A. Comparing the pMSSM10 to the CMSSM, NUHM1, and NUHM2, we find that the mass lower limits on first- and second-generation and top squarks are very similar, whereas the lower limits on gluino and sbottom masses are significantly lower in the pMSSM10. The mass lower limits for sleptons and electroweakinos differ substantially from those of the CMSSM, NUHM1, and NUHM2 due to the fulfilment of the $(g-2)_\mu$ constraint. The corresponding threshold energies for the pair- and associated-production of electroweakinos is therefore much lower and may well be in reach of an e^+e^- collider with centre-of-mass energy of 1000 GeV or even 500 GeV.

We identified four benchmark model points which minimise the χ^2 function for "Low $m_{\tilde{t}_1}$" ($m_{\tilde{t}_1} = 478$ GeV, $m_{\tilde{\chi}_1^0} = 304$ GeV), "Low $m_{\tilde{q}}$" ($m_{\tilde{q}} = 1520$ GeV, $m_{\tilde{\chi}_1^0} = 205$ GeV), "Low $m_{\tilde{g}}$" ($m_{\tilde{g}} = 1290$ GeV, $m_{\tilde{\chi}_1^0} = 190$ GeV), and a model point within the 68% CL region with all masses in reach for future Runs of the LHC "Low All". All these point have $m_{\tilde{\chi}_2^0} \simeq m_{\tilde{\chi}_1^\pm} \sim m_{\tilde{\chi}_1^0} + 20$ GeV so that $\tilde{\chi}_2^0$ and $\tilde{\chi}_1^\pm$ decay via off-shell bosons, and they have mainly a Wino composition. Another result is that the left-handed sleptons, which have masses below Higgsino-like $\tilde{\chi}_3^0$, $\tilde{\chi}_4^0$, $\tilde{\chi}_2^\pm$ for all except the "Low all" model point, decay via $\tilde{\chi}_1^\pm$ or $\tilde{\chi}_2^0$, whereas right-handed sleptons decay directly into $\tilde{\chi}_1^0$. The analogous is true for left- and right-handed first- and second-generation squarks, although they may also decay via the gluino if it is kinematically favoured. The third generation squarks tend to decay more via the Higgsino-like $\tilde{\chi}_3^0$, $\tilde{\chi}_4^0$, $\tilde{\chi}_2^\pm$. Gluinos decay directly into any generation squark if it is kinematically allowed, of via off-shell squark decays into $\tilde{\chi}_1^\pm$ or $\tilde{\chi}_2^0$. These benchmark points illustrate that masses of $\tilde{\chi}_2^0$ and $\tilde{\chi}_1^\pm$ close to that of the LSP is one of the outcomes of our global fit and that this impacts the decay chains of other sparticles. We therefore advocate that ATLAS and CMS should consider adding interpretations of their results in simplified model spectra with $\tilde{\chi}_2^0$ and $\tilde{\chi}_1^\pm$ interleaved and close in mass to the LSP.

We also considered the prospects for direct detection of dark matter in underground

experiments. The $\tilde{\chi}_1^\pm$ coannihilation region corresponds to values of $\sigma_p^{\rm SI}$ that should be well within the reach of LZ [175]. Interestingly, the results in the $(m_{\tilde{\chi}_1^0}, \sigma_p^{\rm SI})$ plane without the LHC8 constraints applied show that the 68% CL region extends to very low values of $\sigma_p^{\rm SI}$ reaching far below the neutrino floor. The LHC8 constraints render such values only available at the 95% CL, highlighting the complementarity between direct searches at colliders and underground facilities.

Another topic that we discussed is the extrapolation of the soft SUSY breaking mass parameters to energies close to the GUT scale. We considered in particular the impact of an "anti-tachyon" cut, i.e requiring that no sfermion mass-squared parameter become negative as the result of the RG running, cautioning that tachyonic particles at higher energies do not necessarily yield an unacceptable evolution of the Universe [173]. We found that an anti-tachyon cut removes model points above a diagonal line in the $(m_{\tilde{q}}, m_{\tilde{g}})$ plane, as well as model points that correspond to the stau coannihilation region. It would also favour large stop masses of $\sim$ 4000 GeV. However, the 68% CL region in the $(m_{\tilde{\chi}_1^\pm}, m_{\tilde{\chi}_1^0})$ plane remains almost untouched and χ^2 value for the best-fit point only increases with 0.2. We also considered predictions for "non-universality measures" for gauginos and sfermions that would tend to zero if exact unification of their respective soft SUSY breaking parameters was achieved. We found that the universality of the soft SUSY breaking sfermion mass-squared parameters at the GUT scale is disfavoured. This is expected from the requirement of small smuon masses in order to fulfil the $(g-2)_\mu$ constraint, which could not be achieved in e.g. the CMSSM, NUHM1 and NUHM2, and the evolution of the RGEs for unified mass parameters at the M_{SUSY} scale. Model points where gauginos mass parameters unify are only available at the 95% CL and correspond to the region excluded at 90% CL by LUX [23] and XENON100 [22]. The universality for gaugino masses is not available at in the 68% CL region, given the relation $M_1 \simeq M_2$ at the M_{SUSY} scale, the lower bound on gluino masses and hence M_3, and the relative possible negative values of M_1 and M_3.

Finally, we provided detailed maps of the predicted decay modes in a selection of mass planes. We saw again that many decay chains evolve via $\tilde{\chi}_1^\pm$ and $\tilde{\chi}_2^0$ as a result of the $\tilde{\chi}_1^\pm$ coannihilation mechanism that underlies the fulfilment of the relic density constraint. We compared these to projections of sensitivities of future searches at the LHC with 300 and 3000 fb^{-1} at $\sqrt{s} = 14$ TeV, which we adopted from simulation studies by ATLAS [176,177] and extrapolation of current results derived in Ref. [60]. The collective of searches at future Runs of the LHC should significantly probe our global fit of the pMSSM10. We await with interest the verdict of future searches during the LHC Run 2 and beyond.

Appendix A

Validation of Delphes and Scorpion

A.1 Tuning the Delphes 3 Detector Card

The Delphes 3 framework [134] is designed to emulate the detector response and object reconstruction for an arbitrary detector, with a particular emphasis on the ATLAS and CMS detectors. The detector response is modelled by propagating the long-lived truth-level particles through the tracker detector (embedded in the magnetic field), the electromagnetic and hadronic calorimeters, and the muon identification system, and applying energy and momentum smearing. Physics objects, such as electrons, muons, photons, jets are then reconstructed, emulating b and τ tagging as well as isolation algorithms and their efficiencies. This procedure is specified in the `detector card`. To match the reconstruction of the SUSY analyses listed in Table 3.5 we adjusted the default CMS detector card provided in Delphes release 3.1.2.

In particular, we adopted the efficiency formula for b-tagging as presented in the same-sign (SS) dilepton search at CMS [142], as well as isolation criteria for electrons, muons, and taus. We also adjusted the EfficiencyFormulas in the MuonEfficiency and ElectronEfficiency modules to reproduce the lepton selection efficiencies, including the effects of reconstruction, identification, and isolation presented in Ref. [142]. In Fig. A.1 the selection efficiencies for muons (red) and electrons (blue) obtained with Scorpion (left panel) are compared with those obtained in Ref. [142] (right panel). The parametrisation of the selection efficiency [142] is indicated as a black line in both panels. We see that the lepton selection efficiency obtained in Scorpion matches well with that of CMS. Finally, we set the EfficiencyFormula in the TauTagging module to 0.6, based on the efficiency for the loose dβ algorithm presented in Ref. [182].

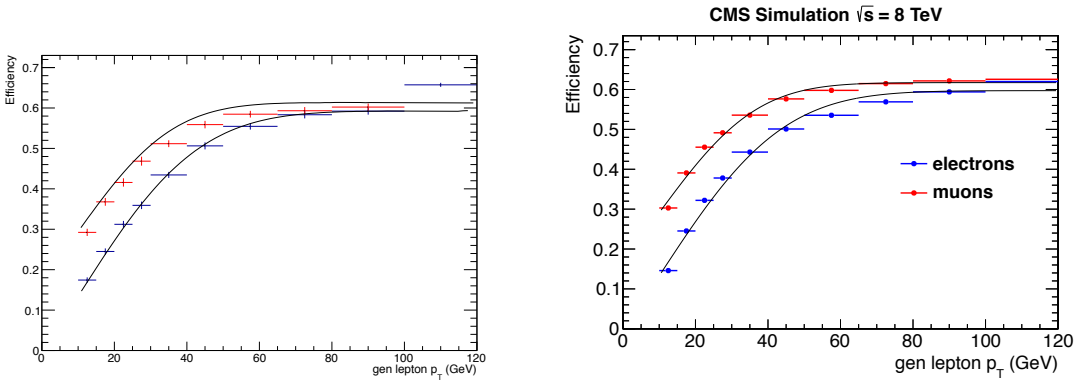

Figure A.1: *Comparison between the muon (red) and electron (blue) selection efficiencies, including the effects of reconstruction, identification, and isolation, obtained in* `Scorpion` *(left panel) and CMS [142] (right panel). Black lines indicate the parametrisation presented in Ref. [142].*

A.2 Validation of CMS Searches

We extensively validated the implementations of the CMS searches in `Scorpion` that are listed in Table 3.5. Part of this validation is reproducing the 95% CL exclusion limits that CMS provided in various SMS interpretations as displayed in Fig. A.2 and A.3. Here red lines indicate the observed 95% CL exclusion limits from CMS, and the black lines show those obtained with `Scorpion`. Black dots indicate the locations in the plane for which the point-by-point reinterpretation was performed. For these validations we used production cross-sections provided in Ref. [183], which have been calculated at next-to-leading order (NLO) in the strong coupling constant and includes, where possible, the resummation of soft gluon emission at the next-to-leading logarithmic (NLL) accuracy, except for the opposite-sign (OS) dilepton search for which we assumed a K-factor of 2. The Monojet analysis was validated and used in Ref. [184].

We first note that excellent agreement is obtained for the SS dilepton search [142], displayed in the top panels of Fig. A.3. This reflects the fact that the `Delphes` detector card was tuned to match the detector response and reconstruction reported by this search. The limits for the 0-lepton M_{T2} search obtained with `Scorpion` reach somewhat further than those of CMS [130], although we note that the uncertainties in e.g. the $pp \to \tilde{t}_1\tilde{t}_1,\ \tilde{t}_1 \to t\tilde{\chi}_1^0$ interpretation are of $\mathcal{O}(100\ \mathrm{GeV})$ at the 2σ experimental uncertainty and the `Scorpion` limit is compatible with the expected limit obtained by CMS, cf. Fig. 12c [130]. The 1-lepton $M_{\mathrm{T2}}^{\mathrm{W}}$ search [141] (bottom panels of Fig. A.2), the OS dilepton search [137] (middle

panel of Fig. A.3), and the ≥3-lepton search [142] (bottom panels of Fig. A.3) also show good agreement within the experimental uncertainties. This validates the implementation of the CMS searches in `Scorpion`.

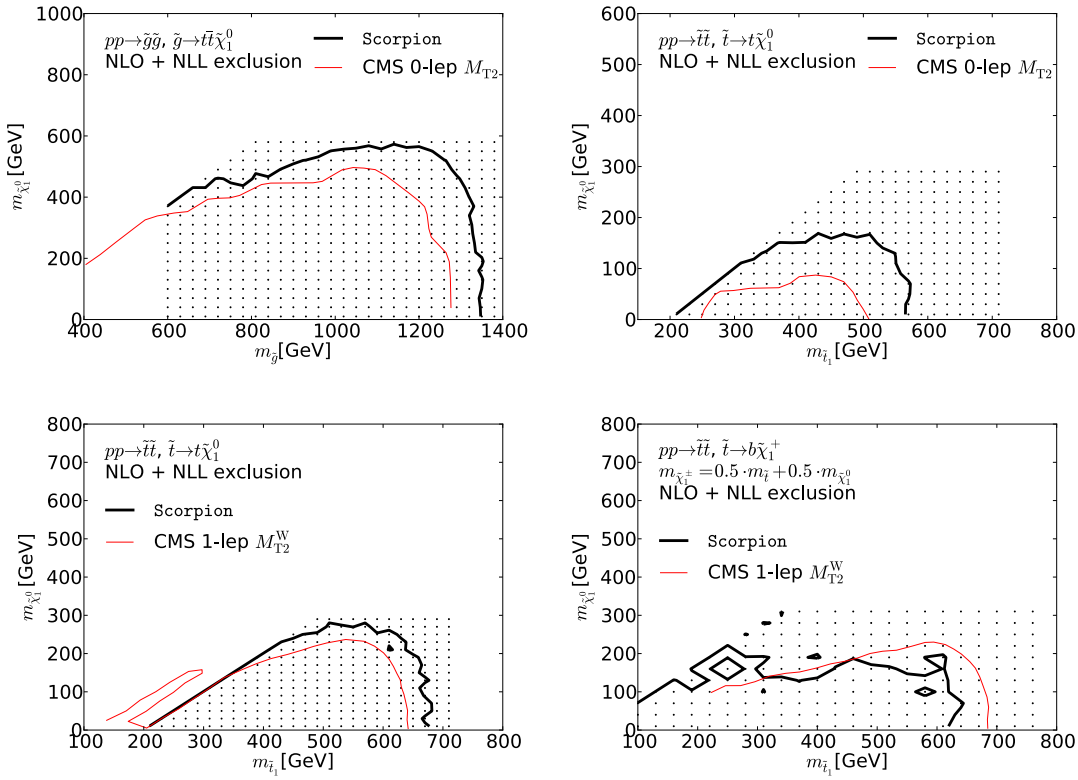

Figure A.2: *Comparison of the observed 95% CL exclusion contour in SMS interpretations obtained with* ***Scorpion*** *(black lines) with those obtained by CMS (red lines) for the 0-lepton M_{T2} search [130] (top panels) and the 1-lepton M_{T2}^W search (bottom panels). The SMS models are specified in the legends.*

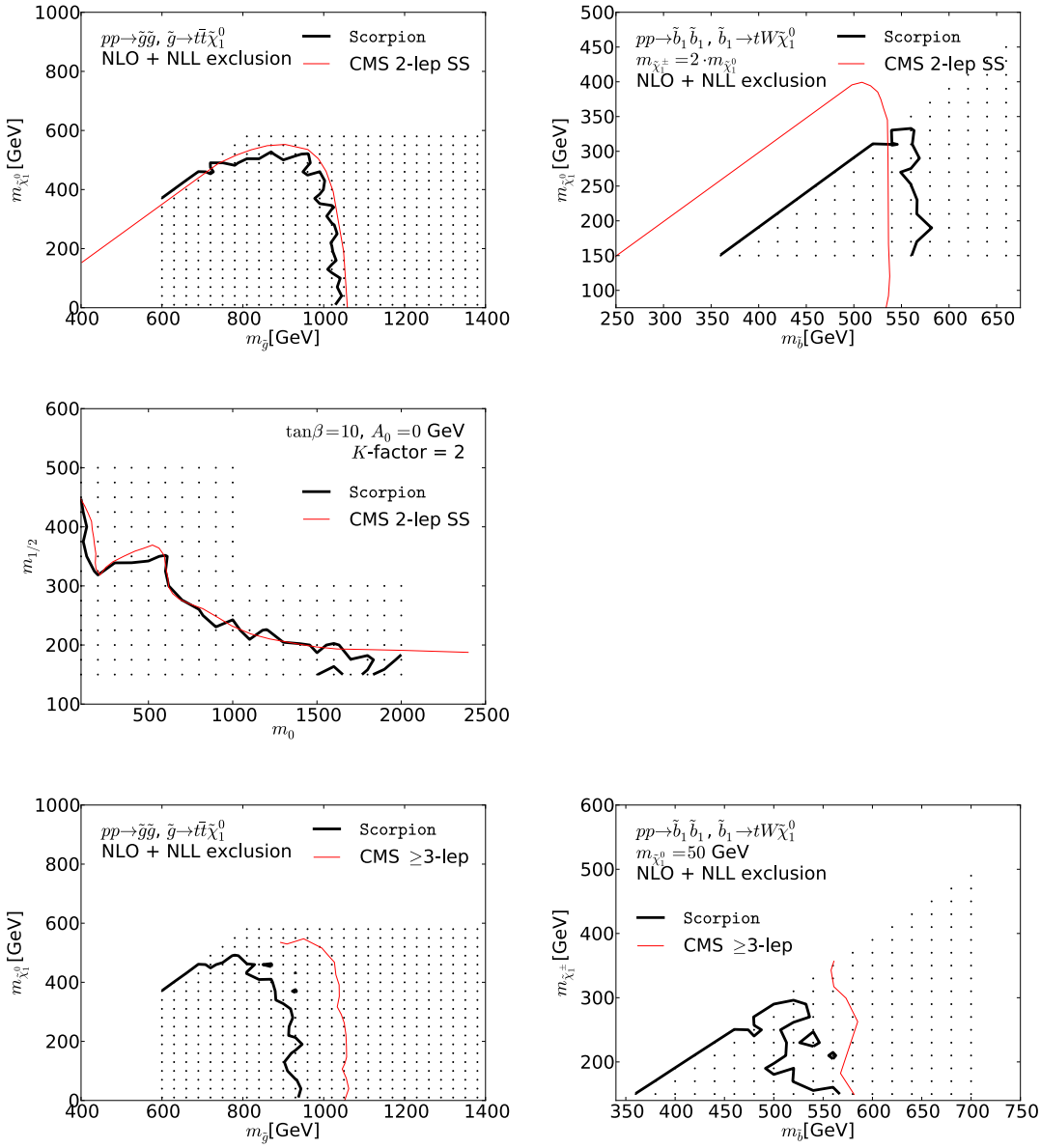

Figure A.3: *Comparison of the observed 95% CL exclusion contour in SMS interpretations obtained with* **Scorpion** *(black lines) with those obtained by CMS (red lines) for the same-sign (SS) dilepton search [142] (top panels), the opposite-sign (OS) dilepton search [137] (middle panel), and the $\geq$3-lepton search [142] (bottom panels). The SMS models are specified in the legends.*

Appendix B

Additional Figures for the CMSSM, NUHM1, and NUHM2

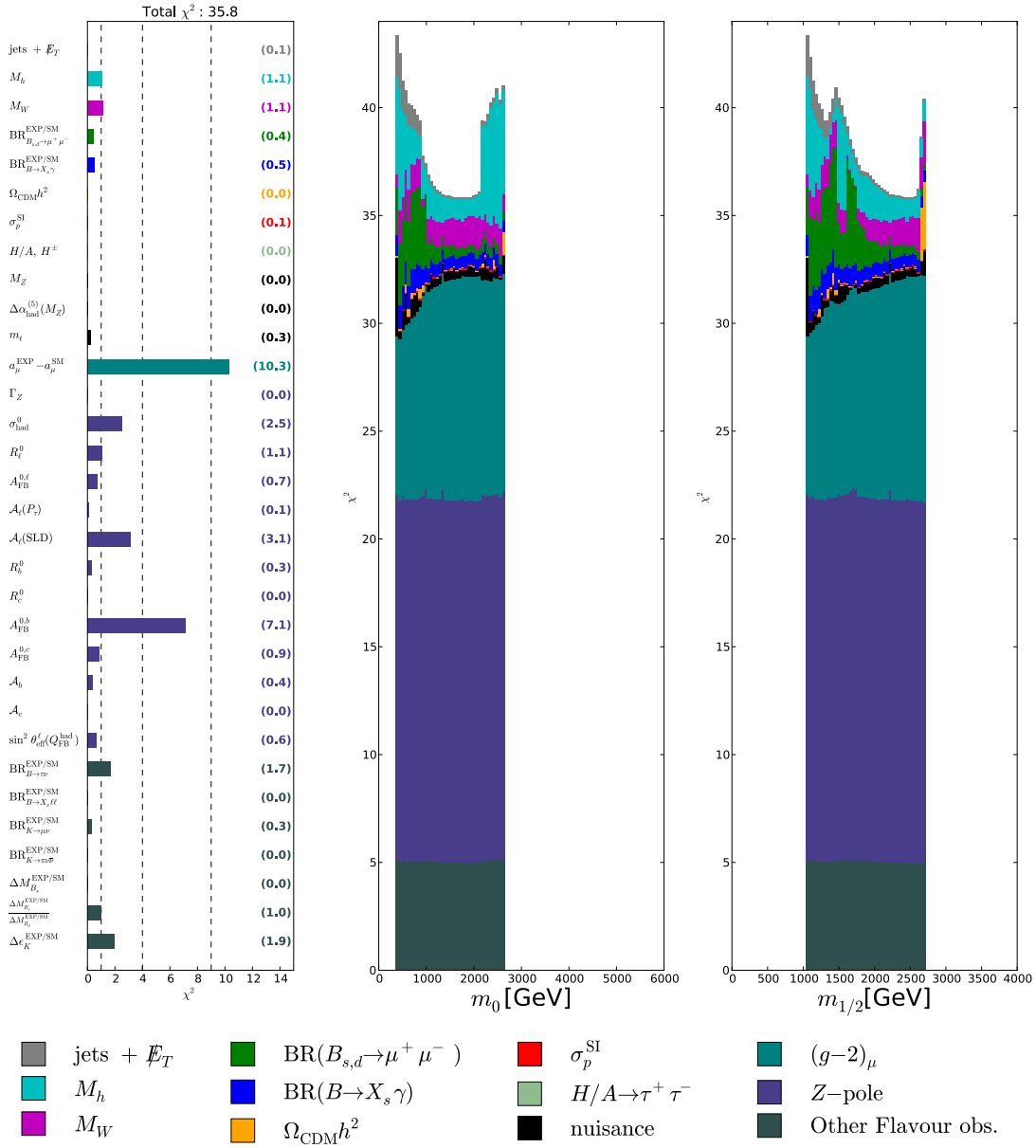

Figure B.1: *Breakdown of the total χ^2 in individual contributions for points in the CMSSM fulfilling the* ***hybrid metric****, as defined in Eq. 4.1. The panels show the breakdowns for the best-fit point (left), and along the restricted profile likelihood functions of m_0 (middle) and $m_{1/2}$ (right). The ordering of the (groups of) constraints and the colours used are specified in the legend.*

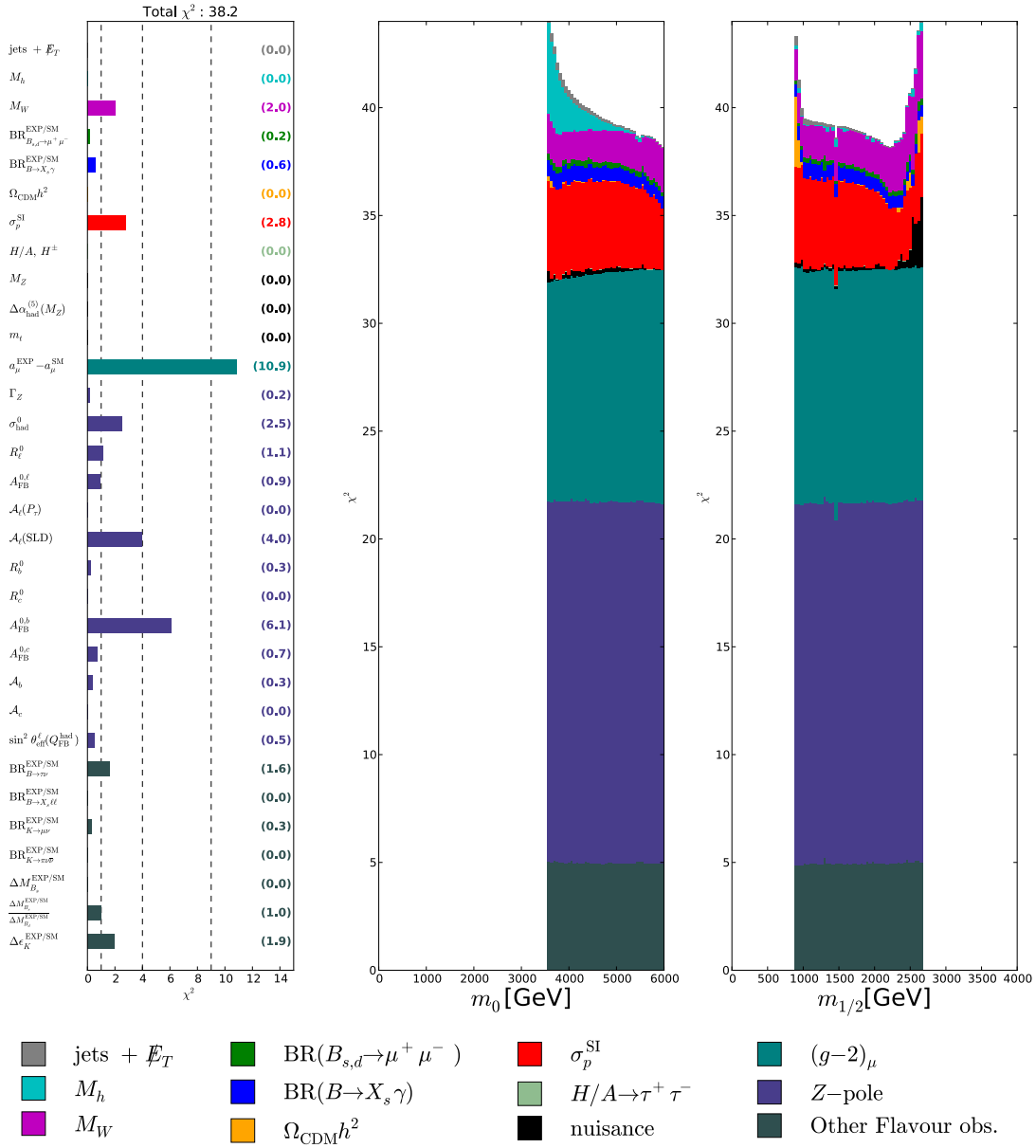

Figure B.2: *Breakdown of the total χ^2 in individual contributions for points in the CMSSM fulfilling the* $\tilde{\chi}_1^\pm$ ***coannihilation metric****, as defined in Eq. 4.1. The panels show the breakdowns for the best-fit point (left), and along the restricted profile likelihood functions of m_0 (middle) and $m_{1/2}$ (right). The ordering of the (groups of) constraints and the colours used are specified in the legend.*

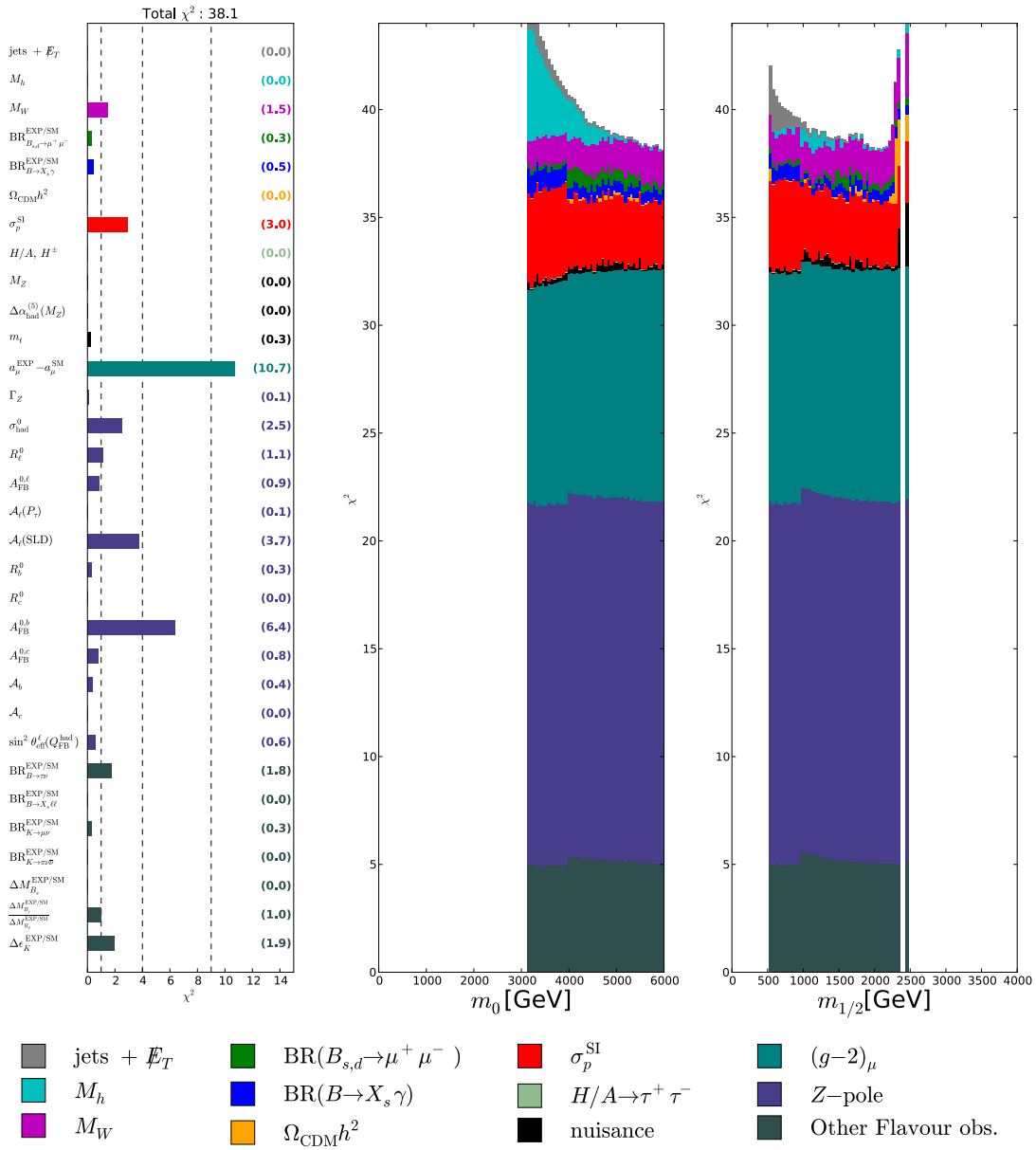

Figure B.3: *Breakdown of the total χ^2 in individual contributions for points in the CMSSM fulfilling the* ***focus point metric****, as defined in Eq. 4.1. The panels show the breakdowns for the best-fit point (left), and along the restricted profile likelihood functions of m_0 (middle) and $m_{1/2}$ (right). The ordering of the (groups of) constraints and the colours used are specified in the legend.*

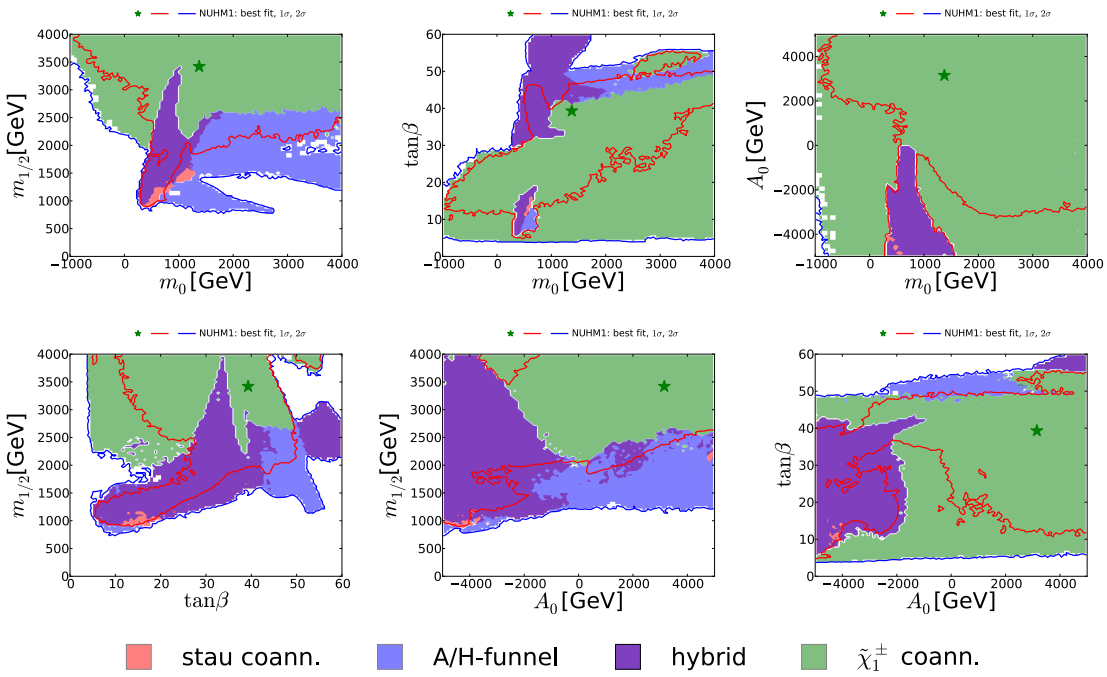

Figure B.4: *A compilation of parameter planes in the NUHM1* ***not depending*** *on $m^2_{H_u}$ and/or $m^2_{H_d}$, with shading according to the dominant mechanisms for fixing the dark matter density following Eq. 4.1. In each plane, red and blue lines indicate the 68% and 95% CL contours, respectively. Green stars denote the best-fit point. The stau coannihilation region is shaded pink, the A/H funnel region is shaded blue, the hybrid region is shaded purple, the $\tilde{\chi}_1^{\pm}$ coannihilation region is shaded green.*

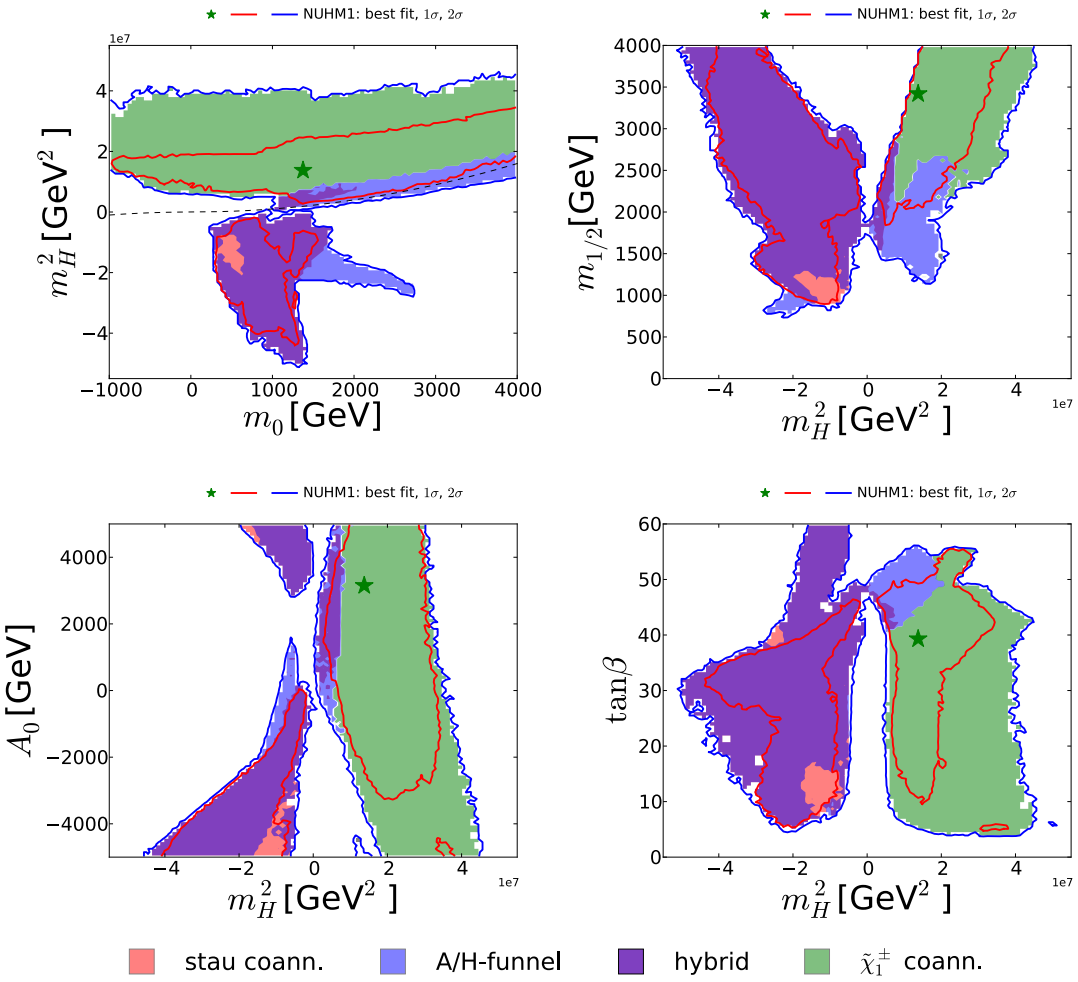

Figure B.5: *A compilation of parameter planes in the NUHM1* ***depending*** *on $m_{H_u}^2$ and/or $m_{H_d}^2$, with shading according to the dominant mechanisms for fixing the dark matter density following Eq. 4.1. In each plane, red and blue lines indicate the 68% and 95% CL contours, respectively. Green stars denote the best-fit point. The stau coannihilation region is shaded pink, the A/H funnel region is shaded blue, the hybrid region is shaded purple, the $\tilde{\chi}_1^{\pm}$ coannihilation region is shaded green.*

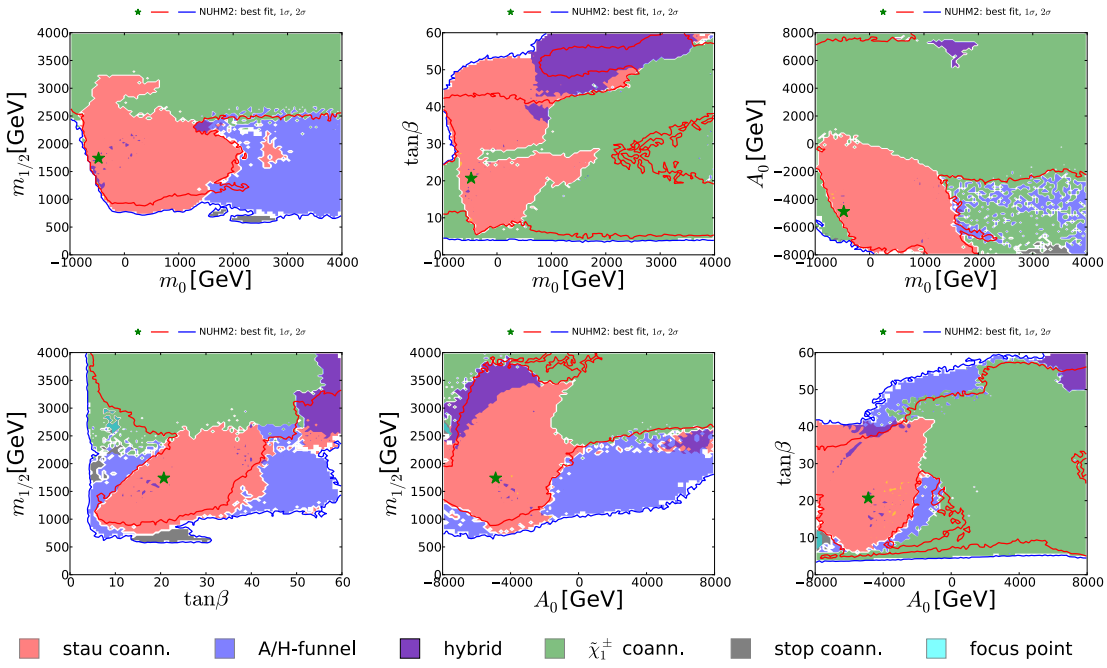

Figure B.6: *A compilation of parameter planes in the NUHM2* ***not depending*** *on $m^2_{H_u}$ and/or $m^2_{H_d}$, with shading according to the dominant mechanisms for fixing the dark matter density following Eq. 4.1. In each plane, red and blue lines indicate the 68% and 95% CL contours, respectively. Green stars denote the best-fit point. The stau coannihilation region is shaded pink, the A/H funnel region is shaded blue, the hybrid region is shaded purple, the $\tilde{\chi}_1^{\pm}$ coannihilation region is shaded green, and the slepton coannihilation region is shaded yellow.*

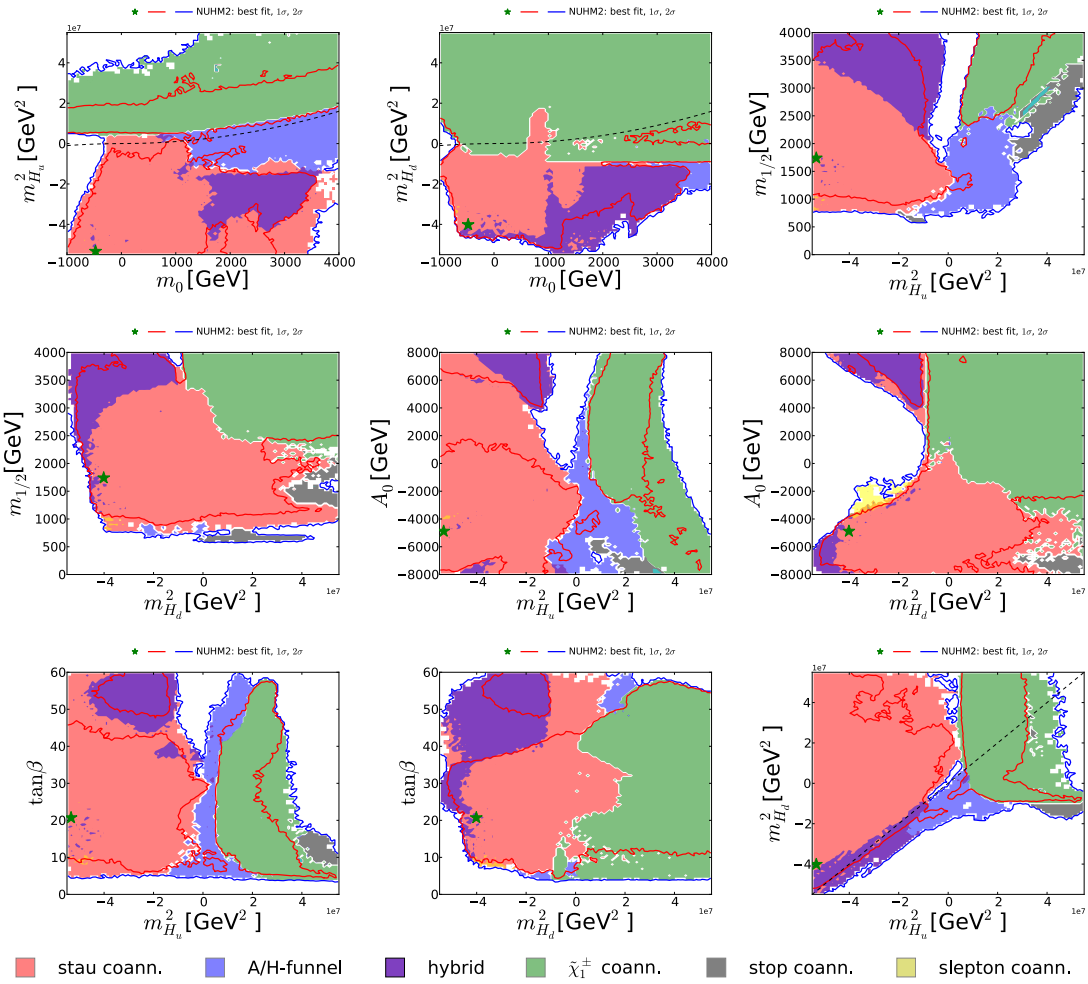

Figure B.7: *A compilation of parameter in the NUHM2* ***depending*** *on $m^2_{H_u}$ and/or $m^2_{H_d}$, with shading according to the dominant mechanisms for fixing the dark matter density following Eq. 4.1. In each plane, red and blue lines indicate the 68% and 95% CL contours, respectively. Green stars denote the best-fit point. The stau coannihilation region is shaded pink, the A/H funnel region is shaded blue, the hybrid region is shaded purple, the $\tilde{\chi}_1^{\pm}$ coannihilation region is shaded green, and the slepton coannihilation region is shaded yellow.*

Bibliography

[1] ATLAS, G. Aad *et al.*, *Observation of a new particle in the search for the Standard Model Higgs boson with the ATLAS detector at the LHC*, Phys. Lett. **B716** (2012) 1, arXiv:1207.7214.

[2] CMS, S. Chatrchyan *et al.*, *Observation of a new boson at a mass of 125 GeV with the CMS experiment at the LHC*, Phys. Lett. **B716** (2012) 30, arXiv:1207.7235.

[3] Planck, P. A. R. Ade *et al.*, *Planck 2013 results. XVI. Cosmological parameters*, Astron. Astrophys. **571** (2014) A16, arXiv:1303.5076.

[4] J. L. Feng, *Naturalness and the Status of Supersymmetry*, Ann. Rev. Nucl. Part. Sci. **63** (2013) 351, arXiv:1302.6587.

[5] H. P. Nilles, *Supersymmetry, Supergravity and Particle Physics*, Phys. Rept. **110** (1984) 1.

[6] H. E. Haber and G. L. Kane, *The Search for Supersymmetry: Probing Physics Beyond the Standard Model*, Phys. Rept. **117** (1985) 75.

[7] J. R. Ellis, S. Kelley, and D. V. Nanopoulos, *Probing the desert using gauge coupling unification*, Phys. Lett. **B260** (1991) 131.

[8] G. L. Kane, C. F. Kolda, L. Roszkowski, and J. D. Wells, *Study of constrained minimal supersymmetry*, Phys. Rev. **D49** (1994) 6173, arXiv:hep-ph/9312272.

[9] J. R. Ellis, K. A. Olive, and Y. Santoso, *The MSSM parameter space with nonuniversal Higgs masses*, Phys. Lett. **B539** (2002) 107, arXiv:hep-ph/0204192.

[10] MSSM Working Group, A. Djouadi *et al.*, *The Minimal supersymmetric standard model: Group summary report*, arXiv:hep-ph/9901246.

[11] FlaviaNet Working Group on Kaon Decays, M. Antonelli *et al.*, *Precision tests of the Standard Model with leptonic and semileptonic kaon decays*, arXiv:0801.1817.

[12] Heavy Flavor Averaging Group, Y. Amhis *et al.*, *Averages of B-Hadron, C-Hadron, and tau-lepton properties as of early 2012*, arXiv:1207.1158.

[13] LHCb, R. Aaij *et al.*, *Measurement of the $B_s^0 \to \mu^+\mu^-$ branching fraction and search for $B^0 \to \mu^+\mu^-$ decays at the LHCb experiment*, Phys. Rev. Lett. **111** (2013) 101805, arXiv:1307.5024.

[14] CMS, S. Chatrchyan *et al.*, *Measurement of the $B_s^0 \to \mu^+\mu^-$ branching fraction and search for $B^0 \to \mu^+\mu^-$ with the CMS Experiment*, Phys. Rev. Lett. **111** (2013) 101804, arXiv:1307.5025.

[15] CMS, LHCb, V. Khachatryan *et al.*, *Observation of the rare $B_s^0 \to \mu^+\mu^-$ decay from the combined analysis of CMS and LHCb data*, arXiv:1411.4413.

[16] UTfit Collaboration, Bevan, A. J. and others. http://www.utfit.org/UTfit/. Accessed: 2013-08-09.

[17] Particle Data Group, K. A. Olive *et al.*, *Review of Particle Physics*, Chin. Phys. **C38** (2014) 090001.

[18] ALEPH Collaboration, DELPHI Collaboration, L3 Collaboration, OPAL Collaboration, SLD Collaboration, LEP Electroweak Working Group, SLD Electroweak Group, SLD Heavy Flavour Group, S. Schael *et al.*, *Precision electroweak measurements on the Z resonance*, Phys. Rept. **427** (2006) 257, arXiv:hep-ex/0509008.

[19] Gfitter Group, M. Baak *et al.* http://gfitter.desy.de/Figures/Standard_Model/2013_05_29_ShowFullFitTable_large.gif. Accessed: 2014-08-18.

[20] Gfitter Group, M. Baak *et al.*, *The global electroweak fit at NNLO and prospects for the LHC and ILC*, Eur. Phys. J. **C74** (2014) 3046, arXiv:1407.3792.

[21] Muon G-2 Collaboration, G. W. Bennett *et al.*, *Final Report of the Muon E821 Anomalous Magnetic Moment Measurement at BNL*, Phys. Rev. **D73** (2006) 072003, arXiv:hep-ex/0602035.

[22] XENON100 Collaboration, E. Aprile *et al.*, *Dark Matter Results from 100 Live Days of XENON100 Data*, Phys. Rev. Lett. **107** (2011) 131302, arXiv:1104.2549.

[23] LUX Collaboration, D. S. Akerib *et al.*, *First results from the LUX dark matter experiment at the Sanford Underground Research Facility*, Phys. Rev. Lett. **112** (2014) 091303, arXiv:1310.8214.

[24] ATLAS, CMS, G. Aad *et al.*, *Combined Measurement of the Higgs Boson Mass in pp Collisions at $\sqrt{s} = 7$ and 8 TeV with the ATLAS and CMS Experiments*, arXiv:1503.07589.

[25] ATLAS Collaboration. https://twiki.cern.ch/twiki/bin/view/AtlasPublic/SupersymmetryPublicResults. Accessed: 2015-05-22.

[26] CMS Collaboration. https://twiki.cern.ch/twiki/bin/view/CMSPublic/PhysicsResultsSUS. Accessed: 2015-05-22.

[27] M. Baak *et al.*, *The Electroweak Fit of the Standard Model after the Discovery of a New Boson at the LHC*, Eur. Phys. J. **C72** (2012) 2205, arXiv:1209.2716.

[28] J. Charles *et al.*, *Current status of the Standard Model CKM fit and constraints on $\Delta F = 2$ New Physics*, Phys. Rev. **D91** (2015), no. 7 073007, arXiv:1501.05013.

[29] P. Bechtle, K. Desch, and P. Wienemann, *Fittino, a program for determining MSSM parameters from collider observables using an iterative method*, Comput. Phys. Commun. **174** (2006) 47, arXiv:hep-ph/0412012.

[30] P. Bechtle, K. Desch, W. Porod, and P. Wienemann, *Determination of MSSM parameters from LHC and ILC observables in a global fit*, Eur. Phys. J. **C46** (2006) 533, arXiv:hep-ph/0511006.

[31] P. Bechtle, K. Desch, M. Uhlenbrock, and P. Wienemann, *Constraining SUSY models with Fittino using measurements before, with and beyond the LHC*, Eur. Phys. J. **C66** (2010) 215, arXiv:0907.2589.

[32] P. Bechtle *et al.*, *Constrained Supersymmetry after two years of LHC data: a global view with Fittino*, JHEP **1206** (2012) 098, arXiv:1204.4199.

[33] O. Buchmueller *et al.*, *Prediction for the Lightest Higgs Boson Mass in the CMSSM using Indirect Experimental Constraints*, Phys. Lett. **B657** (2007) 87, arXiv:0707.3447.

[34] O. Buchmueller *et al.*, *Predictions for Supersymmetric Particle Masses using Indirect Experimental and Cosmological Constraints*, JHEP **0809** (2008) 117, arXiv:0808.4128.

[35] O. Buchmueller *et al.*, *Likelihood Functions for Supersymmetric Observables in Frequentist Analyses of the CMSSM and NUHM1*, Eur. Phys. J. **C64** (2009) 391, arXiv:0907.5568.

[36] O. Buchmueller *et al.*, *Predictions for m_t and M_W in Minimal Supersymmetric Models*, Phys. Rev. **D81** (2010) 035009, arXiv:0912.1036.

[37] O. Buchmueller *et al.*, *Frequentist Analysis of the Parameter Space of Minimal Supergravity*, Eur. Phys. J. **C71** (2011) 1583, arXiv:1011.6118.

[38] O. Buchmueller *et al.*, *Implications of Initial LHC Searches for Supersymmetry*, Eur. Phys. J. **C71** (2011) 1634, arXiv:1102.4585.

[39] O. Buchmueller *et al.*, *Supersymmetry and Dark Matter in Light of LHC 2010 and Xenon100 Data*, Eur. Phys. J. **C71** (2011) 1722, arXiv:1106.2529.

[40] O. Buchmueller *et al.*, *Supersymmetry in Light of 1/fb of LHC Data*, Eur. Phys. J. **C72** (2012) 1878, arXiv:1110.3568.

[41] O. Buchmueller *et al.*, *Higgs and Supersymmetry*, Eur. Phys. J. **C72** (2012) 2020, arXiv:1112.3564.

[42] O. Buchmueller *et al.*, *The CMSSM and NUHM1 in Light of 7 TeV LHC, $B_s \to \mu^+\mu^-$ and XENON100 Data*, Eur. Phys. J. **C72** (2012) 2243, arXiv:1207.7315.

[43] O. Buchmueller *et al.*, *The CMSSM and NUHM1 after LHC Run 1*, Eur. Phys. J. **C74** (2013) 2922, arXiv:1312.5250.

[44] O. Buchmueller *et al.*, *The NUHM2 after LHC Run 1*, arXiv:1408.4060.

[45] A. Fowlie *et al.*, *Bayesian Implications of Current LHC and XENON100 Search Limits for the Constrained MSSM*, Phys. Rev. **D85** (2012) 075012, arXiv:1111.6098.

[46] L. Roszkowski, E. M. Sessolo, and Y.-L. S. Tsai, *Bayesian Implications of Current LHC Supersymmetry and Dark Matter Detection Searches for the Constrained MSSM*, Phys. Rev. **D86** (2012) 095005, arXiv:1202.1503.

[47] A. Fowlie *et al.*, *The CMSSM Favoring New Territories: The Impact of New LHC Limits and a 125 GeV Higgs*, Phys. Rev. **D86** (2012) 075010, arXiv:1206.0264.

[48] K. Kowalska, L. Roszkowski, and E. M. Sessolo, *Two ultimate tests of constrained supersymmetry*, JHEP **1306** (2013) 078, arXiv:1302.5956.

[49] R. R. de Austri, R. Trotta, and L. Roszkowski, *A Markov chain Monte Carlo analysis of the CMSSM*, JHEP **0605** (2006) 002, arXiv:hep-ph/0602028.

[50] R. Trotta, R. R. de Austri, and L. Roszkowski, *Prospects for direct dark matter detection in the Constrained MSSM*, New Astron. Rev. **51** (2007) 316, arXiv:astro-ph/0609126.

[51] L. Roszkowski, R. R. de Austri, and R. Trotta, *On the detectability of the CMSSM light Higgs boson at the Tevatron*, JHEP **0704** (2007) 084, arXiv:hep-ph/0611173.

[52] L. Roszkowski, R. Ruiz de Austri, and R. Trotta, *Implications for the Constrained MSSM from a new prediction for $b \to s\gamma$*, JHEP **0707** (2007) 075, arXiv:0705.2012.

[53] R. Trotta *et al.*, *The Impact of priors and observables on parameter inferences in the Constrained MSSM*, JHEP **0812** (2008) 024, arXiv:0809.3792.

[54] R. Trotta, R. Ruiz de Austri, and C. Perez de los Heros, *Prospects for dark matter detection with IceCube in the context of the CMSSM*, JCAP **0908** (2009) 034, arXiv:0906.0366.

[55] F. Feroz *et al.*, *Challenges of Profile Likelihood Evaluation in Multi-Dimensional SUSY Scans*, JHEP **1106** (2011) 042, arXiv:1101.3296.

[56] C. Strege *et al.*, *Global Fits of the cMSSM and NUHM including the LHC Higgs discovery and new XENON100 constraints*, JCAP **1304** (2013) 013, arXiv:1212.2636.

[57] S. Henrot-Versill *et al.*, *Constraining Supersymmetry using the relic density and the Higgs boson*, Phys. Rev. **D89** (2014), no. 5 055017, arXiv:1309.6958.

[58] A. Fowlie *et al.*, *Dark matter and collider signatures of the MSSM*, Phys. Rev. **D88** (2013) 055012, arXiv:1306.1567.

[59] C. Strege *et al.*, *Profile likelihood maps of a 15-dimensional MSSM*, JHEP **1409** (2014) 081, arXiv:1405.0622.

[60] K. J. de Vries *et al.*, *The pMSSM10 after LHC Run 1*, arXiv:1504.03260.

[61] F. Feroz and M. P. Hobson, *Multimodal nested sampling: an efficient and robust alternative to MCMC methods for astronomical data analysis*, Mon. Not. Roy. Astron. Soc. **384** (2008) 449, arXiv:0704.3704.

[62] F. Feroz, M. P. Hobson, and M. Bridges, *MultiNest: an efficient and robust Bayesian inference tool for cosmology and particle physics*, Mon. Not. Roy. Astron. Soc. **398** (2009) 1601, arXiv:0809.3437.

[63] F. Feroz, M. P. Hobson, E. Cameron, and A. N. Pettitt, *Importance Nested Sampling and the MultiNest Algorithm*, arXiv:1306.2144.

[64] N. Metropolis *et al.*, *Equation of state calculations by fast computing machines*, The Journal of Chemical Physics **21** (1953), no. 6 1087.

[65] M. Citron *et al.*, *End of the CMSSM coannihilation strip is nigh*, Phys. Rev. **D87** (2013), no. 3 036012, arXiv:1212.2886.

[66] O. Buchmueller *et al.*, *Implications of Improved Higgs Mass Calculations for Supersymmetric Models*, Eur. Phys. J. **C74** (2014), no. 3 2809, arXiv:1312.5233.

[67] O. Buchmueller *et al.*, *Collider Interplay for Supersymmetry, Higgs and Dark Matter*, arXiv:1505.04702.

[68] S. P. Martin, *A Supersymmetry primer*, Adv. Ser. Direct. High Energy Phys. **21** (2010) 1, arXiv:hep-ph/9709356.

[69] S. Dimopoulos and D. W. Sutter, *The Supersymmetric flavor problem*, Nucl. Phys. **B452** (1995) 496, arXiv:hep-ph/9504415.

[70] F. Gabbiani, E. Gabrielli, A. Masiero, and L. Silvestrini, *A Complete analysis of FCNC and CP constraints in general SUSY extensions of the standard model*, Nucl. Phys. **B477** (1996) 321, arXiv:hep-ph/9604387.

[71] B. C. Allanach, *SOFTSUSY: a program for calculating supersymmetric spectra*, Comput. Phys. Commun. **143** (2002) 305, arXiv:hep-ph/0104145.

[72] J. R. Ellis, T. Falk, K. A. Olive, and Y. Santoso, *Exploration of the MSSM with nonuniversal Higgs masses*, Nucl. Phys. **B652** (2003) 259, arXiv:hep-ph/0210205.

[73] S. Heinemeyer, W. Hollik, and G. Weiglein, *Electroweak precision observables in the minimal supersymmetric standard model*, Phys. Rept. **425** (2006) 265, arXiv:hep-ph/0412214.

[74] J. R. Ellis, G. Ridolfi, and F. Zwirner, *Radiative corrections to the masses of supersymmetric Higgs bosons*, Phys. Lett. **B257** (1991) 83.

[75] G. Degrassi *et al.*, *Towards high precision predictions for the MSSM Higgs sector*, Eur. Phys. J. **C28** (2003) 133, arXiv:hep-ph/0212020.

[76] S. Heinemeyer, *MSSM Higgs physics at higher orders*, Int. J. Mod. Phys. **A21** (2006) 2659, arXiv:hep-ph/0407244.

[77] S. Heinemeyer *et al.*, *Precise prediction for M(W) in the MSSM*, JHEP **0608** (2006) 052, arXiv:hep-ph/0604147.

[78] G. Jungman, M. Kamionkowski, and K. Griest, *Supersymmetric dark matter*, Phys. Rept. **267** (1996) 195, arXiv:hep-ph/9506380.

[79] G. Belanger, F. Boudjema, A. Pukhov, and A. Semenov, *micrOMEGAs_3: A program for calculating dark matter observables*, Comput. Phys. Commun. **185** (2014) 960, arXiv:1305.0237.

[80] LEP 2 Joint SUSY Working Group ALEPH, DELPHI, L3, OPAL Experiments. http://lepsusy.web.cern.ch/lepsusy. Accessed: 2015-05-22.

[81] J. Ellis, K. A. Olive, and J. Zheng, *The Extent of the Stop Coannihilation Strip*, Eur. Phys. J. **C74** (2014) 2947, arXiv:1404.5571.

[82] J. L. Feng, K. T. Matchev, and T. Moroi, *Focus points and naturalness in supersymmetry*, Phys. Rev. **D61** (2000) 075005, arXiv:hep-ph/9909334.

[83] J. L. Feng and D. Sanford, *Heart of Darkness: The Significance of the Zeptobarn Scale for Neutralino Direct Detection*, JCAP **1105** (2011) 018, arXiv:1009.3934.

[84] J. R. Ellis, K. A. Olive, and C. Savage, *Hadronic Uncertainties in the Elastic Scattering of Supersymmetric Dark Matter*, Phys. Rev. **D77** (2008) 065026, arXiv:0801.3656.

[85] C. Savage, K. Freese, and P. Gondolo, *Annual Modulation of Dark Matter in the Presence of Streams*, Phys. Rev. **D74** (2006) 043531, arXiv:astro-ph/0607121.

[86] T. Piffl *et al.*, *The RAVE survey: the Galactic escape speed and the mass of the Milky Way*, Astron. Astrophys. **562** (2014) A91, arXiv:1309.4293.

[87] P. Agrawal, Z. Chacko, C. Kilic, and R. K. Mishra, *A Classification of Dark Matter Candidates with Primarily Spin-Dependent Interactions with Matter*, arXiv:1003.1912.

[88] J. S. Schwinger, *On Quantum electrodynamics and the magnetic moment of the electron*, Phys. Rev. **73** (1948) 416.

[89] D. Hanneke, S. F. Hoogerheide, and G. Gabrielse, *Cavity Control of a Single-Electron Quantum Cyclotron: Measuring the Electron Magnetic Moment*, Phys. Rev. **A83** (2011) 052122, arXiv:1009.4831.

[90] T. Aoyama, M. Hayakawa, T. Kinoshita, and M. Nio, *Tenth-Order Electron Anomalous Magnetic Moment — Contribution of Diagrams without Closed Lepton Loops*, Phys. Rev. **D91** (2015), no. 3 033006, arXiv:1412.8284.

[91] J. Bailey and K. Borer and F. Combley and H. Drumm and C. Eck and F. J. M. Farley and J. H. Field and W. Flegel and P. M. Hattersley and F. Krienen and F. Lange and G. Lebe and E. McMillan and G. Petrucci and E. Picasso and O. Rnolfsson and W. von Rden and R. W. Williams and S. Wojcicki, *Final report on the CERN muon storage ring including the anomalous magnetic moment and the electric dipole moment of the muon, and a direct test of relativistic time dilation*, Nuclear Physics B **150** (1979), no. 0 1 .

[92] M. Passera, W. J. Marciano, and A. Sirlin, *The Muon g-2 and the bounds on the Higgs boson mass*, Phys. Rev. **D78** (2008) 013009, arXiv:0804.1142.

[93] S. P. Martin and J. D. Wells, *Muon anomalous magnetic dipole moment in supersymmetric theories*, Phys. Rev. **D64** (2001) 035003, arXiv:hep-ph/0103067.

[94] C. Bobeth, A. J. Buras, and T. Ewerth, $\bar{B} \to X_s \ell^+ \ell^-$ *in the MSSM at NNLO*, Nucl. Phys. **B713** (2005) 522, arXiv:hep-ph/0409293.

[95] A. J. Buras *et al.*, ε'/ε *and rare K and B decays in the MSSM*, Nucl. Phys. **B592** (2001) 55, arXiv:hep-ph/0007313.

[96] G. Isidori and P. Paradisi, *Hints of large* $\tan\beta$ *in flavour physics*, Phys. Lett. **B639** (2006) 499, arXiv:hep-ph/0605012.

[97] G. Isidori, F. Mescia, P. Paradisi, and D. Temes, *Flavour physics at large* $\tan\beta$ *with a Bino-like LSP*, Phys. Rev. **D75** (2007) 115019, arXiv:hep-ph/0703035.

[98] A. Arbey, M. Battaglia, F. Mahmoudi, and D. Martnez Santos, *Supersymmetry confronts* ${B_s}^{+-}$ *: Present and future status*, Phys. Rev. **D87** (2013), no. 3 035026, arXiv:1212.4887.

[99] K. S. Babu and C. F. Kolda, *Higgs mediated* $B^0 \to \mu^+\mu^-$ *in minimal supersymmetry*, Phys. Rev. Lett. **84** (2000) 228, arXiv:hep-ph/9909476.

[100] J. Neyman, *Outline of a theory of statistical estimation based on the classical theory of probability*, Philosophical Transactions of the Royal Society of London. Series A, Mathematical and Physical Sciences **236** (1937), no. 767 pp. 333.

[101] ALEPH, A. Heister *et al.*, *Absolute mass lower limit for the lightest neutralino of the MSSM from* e^+e^- *data at* $\sqrt{s}$ *up to 209-GeV*, Phys. Lett. **B583** (2004) 247.

[102] S. Heinemeyer, W. Hollik, and G. Weiglein, *FeynHiggs: A Program for the calculation of the masses of the neutral CP even Higgs bosons in the MSSM*, Comput. Phys. Commun. **124** (2000) 76, arXiv:hep-ph/9812320.

[103] S. Heinemeyer, W. Hollik, and G. Weiglein, *The Masses of the neutral CP - even Higgs bosons in the MSSM: Accurate analysis at the two loop level*, Eur. Phys. J. **C9** (1999) 343, arXiv:hep-ph/9812472.

[104] M. Frank *et al.*, *The Higgs Boson Masses and Mixings of the Complex MSSM in the Feynman-Diagrammatic Approach*, JHEP **0702** (2007) 047, arXiv:hep-ph/0611326.

[105] T. Hahn *et al.*, *High-Precision Predictions for the Light CP -Even Higgs Boson Mass of the Minimal Supersymmetric Standard Model*, Phys. Rev. Lett. **112** (2014), no. 14 141801, arXiv:1312.4937.

[106] Heinemeyer, Sven and Hahn, Thomas and Rzehak, Heidi and Weiglein,Georg and Hollik, Wolfgang. http://www.feynhiggs.de. Accessed: 2015-05-22.

[107] P. Bechtle *et al.*, *HiggsSignals: Confronting arbitrary Higgs sectors with measurements at the Tevatron and the LHC*, Eur. Phys. J. **C74** (2014), no. 2 2711, arXiv:1305.1933.

[108] P. Bechtle *et al.*, *Probing the Standard Model with Higgs signal rates from the Tevatron, the LHC and a future ILC*, JHEP **1411** (2014) 039, arXiv:1403.1582.

[109] WMAP Collaboration, L. Page *et al.*, *First year Wilkinson Microwave Anisotropy Probe (WMAP) observations: Interpretation of the TT and TE angular power spectrum peaks*, Astrophys. J. Suppl. **148** (2003) 233, arXiv:astro-ph/0302220.

[110] Planck, P. A. R. Ade *et al.*, *Planck 2013 results. I. Overview of products and scientific results*, Astron. Astrophys. **571** (2014) A1, arXiv:1303.5062.

[111] S. Heinemeyer, D. Stockinger, and G. Weiglein, *Two loop SUSY corrections to the anomalous magnetic moment of the muon*, Nucl. Phys. **B690** (2004) 62, arXiv:hep-ph/0312264.

[112] S. Heinemeyer, W. Hollik, A. M. Weber, and G. Weiglein, *Z Pole Observables in the MSSM*, JHEP **0804** (2008) 039, arXiv:0710.2972.

[113] M. Misiak, *Rare B-Meson Decays*, arXiv:1112.5978.

[114] M. Misiak *et al.*, *Estimate of $\mathcal{B}(\bar{B} \to X_s\gamma)$ at $O(\alpha_s^2)$*, Phys. Rev. Lett. **98** (2007) 022002, arXiv:hep-ph/0609232.

[115] E949, A. V. Artamonov *et al.*, *New measurement of the $K^+ \to \pi^+\nu\bar{\nu}$ branching ratio*, Phys. Rev. Lett. **101** (2008) 191802, arXiv:0808.2459.

[116] A. Lenz *et al.*, *Constraints on new physics in $B - \bar{B}$ mixing in the light of recent LHCb data*, Phys. Rev. **D86** (2012) 033008, arXiv:1203.0238.

[117] A. Delgado *et al.*, *The light stop window*, Eur. Phys. J. **C73** (2013), no. 3 2370, arXiv:1212.6847.

[118] Belle, B. Kronenbitter *et al.*, *Measurement of the branching fraction of $B^+ \to \tau^+\nu_\tau$ decays with the semileptonic tagging method*, arXiv:1503.05613.

[119] Heavy Flavor Averaging Group (HFAG), Y. Amhis *et al.*, *Averages of b-hadron, c-hadron, and τ-lepton properties as of summer 2014*, arXiv:1412.7515.

[120] M. Misiak *et al.*, *Updated NNLO QCD predictions for the weak radiative B-meson decays*, arXiv:1503.01789.

[121] ATLAS Collaboration, G. Aad *et al.*, *Search for squarks and gluinos with the ATLAS detector in final states with jets and missing transverse momentum using* $\sqrt{s} = 8$ *TeV proton–proton collision data*, JHEP **1409** (2014) 176, arXiv:1405.7875.

[122] CMS, S. Chatrchyan *et al.*, *Search for new physics in the multijet and missing transverse momentum final state in proton-proton collisions at* $\sqrt{s}$*= 8 TeV*, JHEP **1406** (2014) 055, arXiv:1402.4770.

[123] ATLAS, G. Aad *et al.*, *Search for squarks and gluinos using final states with jets and missing transverse momentum with the ATLAS detector in* $\sqrt{s} = 7$ *TeV proton-proton collisions*, Phys. Lett. **B701** (2011) 186, arXiv:1102.5290.

[124] ATLAS, G. Aad *et al.*, *Search for squarks and gluinos with the ATLAS detector in final states with jets and missing transverse momentum using 4.7* fb^{-1} *of* $\sqrt{s} = 7$ *TeV proton-proton collision data*, Phys. Rev. **D87** (2013), no. 1 012008, arXiv:1208.0949.

[125] ATLAS Collaboration. https://cds.cern.ch/record/1744694/files/ATLAS-CONF-2014-049. Accessed: 2014-07-31.

[126] CMS, V. Khachatryan *et al.*, *Search for neutral MSSM Higgs bosons decaying to a pair of tau leptons in pp collisions*, JHEP **1410** (2014) 160, arXiv:1408.3316.

[127] P. Bechtle *et al.*, HiggsBounds – 4*: Improved Tests of Extended Higgs Sectors against Exclusion Bounds from LEP, the Tevatron and the LHC*, Eur. Phys. J. **C74** (2014), no. 3 2693, arXiv:1311.0055.

[128] G. J. Feldman and R. D. Cousins, *A Unified approach to the classical statistical analysis of small signals*, Phys. Rev. **D57** (1998) 3873, arXiv:physics/9711021.

[129] O. Buchmueller and J. Marrouche, *Universal mass limits on gluino and third-generation squarks in the context of Natural-like SUSY spectra*, Int. J. Mod. Phys. **A29** (2014) 1450032, arXiv:1304.2185.

[130] CMS, V. Khachatryan *et al.*, *Searches for supersymmetry using the* M_{T2} *variable in hadronic events produced in pp collisions at 8 TeV*, arXiv:1502.04358.

[131] T. Sjostrand, S. Mrenna, and P. Z. Skands, *PYTHIA 6.4 Physics and Manual*, JHEP **0605** (2006) 026, arXiv:hep-ph/0603175.

[132] P. Z. Skands *et al.*, *SUSY Les Houches accord: Interfacing SUSY spectrum calculators, decay packages, and event generators*, JHEP **0407** (2004) 036, arXiv:hep-ph/0311123.

[133] B. C. Allanach *et al.*, *SUSY Les Houches Accord 2*, Comput. Phys. Commun. **180** (2009) 8, arXiv:0801.0045.

[134] DELPHES 3, J. de Favereau *et al.*, *DELPHES 3, A modular framework for fast simulation of a generic collider experiment*, JHEP **1402** (2014) 057, arXiv:1307.6346.

[135] CMS Collaboration, S. Chatrchyan *et al.*, *Search for supersymmetry in final states with missing transverse energy and 0, 1, 2, or at least 3 b-quark jets in 7 TeV pp collisions using the variable* α_{T}, JHEP **1301** (2013) 077, arXiv:1210.8115.

[136] CMS Collaboration, S. Chatrchyan *et al.*, *Search for supersymmetry in pp collisions at* $\sqrt{s} = 7$ *TeV in events with a single lepton, jets, and missing transverse momentum*, Eur. Phys. J. **C73** (2013) 2404, arXiv:1212.6428.

[137] CMS Collaboration, S. Chatrchyan *et al.*, *Search for new physics in events with opposite-sign leptons, jets, and missing transverse energy in pp collisions at* $\sqrt{s} = 7$ *TeV*, Phys. Lett. **B718** (2013) 815, arXiv:1206.3949.

[138] CMS Collaboration, S. Chatrchyan *et al.*, *Search for new physics in events with same-sign dileptons and b-tagged jets in pp collisions at* $\sqrt{s} = 7$ *TeV*, JHEP **1208** (2012) 110, arXiv:1205.3933.

[139] M. Chen and A. Korytov, LandS *limits and signifcance*, http://mschen.web.cern.ch/mschen/LandS/. Accessed: 2015-05-22.

[140] CMS, V. Khachatryan *et al.*, *Search for dark matter, extra dimensions, and unparticles in monojet events in proton-proton collisions at* $\sqrt{s} = 8$ *TeV*, arXiv:1408.3583.

[141] CMS, S. Chatrchyan *et al.*, *Search for top-squark pair production in the single-lepton final state in pp collisions at* $\sqrt{s} = 8$ *TeV*, Eur. Phys. J. **C73** (2013), no. 12 2677, arXiv:1308.1586.

[142] CMS, S. Chatrchyan *et al.*, *Search for new physics in events with same-sign dileptons and jets in pp collisions at* $\sqrt{s} = 8$ *TeV*, JHEP **1401** (2014) 163, arXiv:1311.6736.

[143] CMS, S. Chatrchyan *et al.*, *Search for anomalous production of events with three or more leptons in pp collisions at* $\sqrt{s} = 8$ *TeV*, Phys. Rev. **D90** (2014), no. 3 032006, arXiv:1404.5801.

[144] Papucci, M. and Sakurai, Kazuki and Weiler, A. and Zeune, L. , Atom: *Automated Tests of Models*, in preparation.

[145] J. S. Kim, K. Rolbiecki, K. Sakurai, and J. Tattersall, *'Stop' that ambulance! New physics at the LHC?*, JHEP **1412** (2014) 010, arXiv:1406.0858.

[146] P. Grothaus, S. P. Liew, and K. Sakurai, *A closer look at a hint of SUSY at the 8 TeV LHC*, arXiv:1502.05712.

[147] A. Buckley *et al.*, *Rivet user manual*, Comput. Phys. Commun. **184** (2013) 2803, arXiv:1003.0694.

[148] M. Papucci, K. Sakurai, A. Weiler, and L. Zeune, *Fastlim: a fast LHC limit calculator*, Eur. Phys. J. **C74** (2014), no. 11 3163, arXiv:1402.0492.

[149] ATLAS, G. Aad *et al.*, *Search for direct third-generation squark pair production in final states with missing transverse momentum and two b-jets in* $\sqrt{s} = 8$ *TeV pp collisions with the ATLAS detector*, JHEP **1310** (2013) 189, arXiv:1308.2631.

[150] ATLAS, F. Meloni and P. Pani, *Search for direct top squark pair production in final states with one isolated lepton using* $21 fb^{-1}$ *of data collected with the ATLAS detector*, EPJ Web Conf. **71** (2014) 00103.

[151] ATLAS, G. Aad *et al.*, *Search for top squark pair production in final states with one isolated lepton, jets, and missing transverse momentum in* $\sqrt{s}$ *=8 TeV pp collisions with the ATLAS detector*, JHEP **1411** (2014) 118, arXiv:1407.0583.

[152] ATLAS, G. Aad *et al.*, *Search for direct top-squark pair production in final states with two leptons in pp collisions at* $\sqrt{s} = 8$ *TeV with the ATLAS detector*, JHEP **1406** (2014) 124, arXiv:1403.4853.

[153] ATLAS, G. Aad *et al.*, *Search for direct production of charginos, neutralinos and sleptons in final states with two leptons and missing transverse momentum in pp collisions at* $\sqrt{s} = 8$ *TeV with the ATLAS detector*, JHEP **1405** (2014) 071, arXiv:1403.5294.

[154] ATLAS, G. Aad *et al.*, *Search for direct production of charginos and neutralinos in events with three leptons and missing transverse momentum in $\sqrt{s} = 8$ TeV pp collisions with the ATLAS detector*, JHEP **1404** (2014) 169, arXiv:1402.7029.

[155] M. Kramer *et al.* https://twiki.cern.ch/twiki/bin/view/LHCPhysics/SUSYCrossSections8TeVstopsbottom. Accessed: 2015-05-22.

[156] M. Kramer *et al.*, *Supersymmetry production cross sections in pp collisions at $\sqrt{s} = 7$ TeV*, arXiv:1206.2892.

[157] ATLAS Collaboration. https://atlas.web.cern.ch/Atlas/GROUPS/PHYSICS/CombinedSummaryPlots/SUSY/ATLAS_SUSY_EWSummary/ATLAS_SUSY_EWSummary.png. Accessed: 2015-03-18.

[158] ATLAS, G. Aad *et al.*, *Search for the direct production of charginos, neutralinos and staus in final states with at least two hadronically decaying taus and missing transverse momentum in pp collisions at $\sqrt{s} = 8$ TeV with the ATLAS detector*, JHEP **1410** (2014) 96, arXiv:1407.0350.

[159] M. Muhlleitner, A. Djouadi, and Y. Mambrini, *SDECAY: A Fortran code for the decays of the supersymmetric particles in the MSSM*, Comput. Phys. Commun. **168** (2005) 46, arXiv:hep-ph/0311167.

[160] ATLAS Collaboration. https://atlas.web.cern.ch/Atlas/GROUPS/PHYSICS/CombinedSummaryPlots/SUSY/ATLAS_SUSY_Stop_tLSP/ATLAS_SUSY_Stop_tLSP.png. Accessed: 2015-03-18.

[161] WMAP, E. Komatsu *et al.*, *Seven-Year Wilkinson Microwave Anisotropy Probe (WMAP) Observations: Cosmological Interpretation*, Astrophys. J. Suppl. **192** (2011) 18, arXiv:1001.4538.

[162] WMAP, G. Hinshaw *et al.*, *Nine-Year Wilkinson Microwave Anisotropy Probe (WMAP) Observations: Cosmological Parameter Results*, Astrophys. J. Suppl. **208** (2013) 19, arXiv:1212.5226.

[163] Fermi-LAT, M. Ackermann *et al.*, *Constraining Dark Matter Models from a Combined Analysis of Milky Way Satellites with the Fermi Large Area Telescope*, Phys. Rev. Lett. **107** (2011) 241302, arXiv:1108.3546.

[164] HESS, A. Abramowski *et al.*, *H.E.S.S. constraints on Dark Matter annihilations towards the Sculptor and Carina Dwarf Galaxies*, Astropart. Phys. **34** (2011) 608, arXiv:1012.5602.

[165] ATLAS Collaboration. http://cds.cern.ch/record/1432199/files/ATLAS-CONF-2012-033. Accessed: 2015-05-22.

[166] CMS Collaboration. http://cds.cern.ch/record/1430715/files/SUS-12-005-pas. Accessed: 2015-05-22.

[167] CMS, S. Chatrchyan *et al.*, *Search for supersymmetry in hadronic final states with missing transverse energy using the variables α_T and b-quark multiplicity in pp collisions at $\sqrt{s} = 8$ TeV*, Eur. Phys. J. **C73** (2013), no. 9 2568, arXiv:1303.2985.

[168] ATLAS Collaboration. http://cds.cern.ch/record/1472710/files/ATLAS-CONF-2012-109. Accessed: 2015-05-22.

[169] CMS, *Cms-pas-sus-12-022*, http://cds.cern.ch/record/1546777/files/SUS-12-022-pas.pdf.

[170] ATLAS, G. Aad *et al.*, *Search for direct production of charginos and neutralinos in events with three leptons and missing transverse momentum in $\sqrt{s} = 7$ TeV pp collisions with the ATLAS detector*, Phys. Lett. **B718** (2013) 841, arXiv:1208.3144.

[171] E. A. Bagnaschi *et al.* http://mastercode.web.cern.ch/mastercode/. Accessed: 2015-05-22.

[172] J. Billard, L. Strigari, and E. Figueroa-Feliciano, *Implication of neutrino backgrounds on the reach of next generation dark matter direct detection experiments*, Phys. Rev. **D89** (2014), no. 2 023524, arXiv:1307.5458.

[173] J. R. Ellis *et al.*, *Against Tachyophobia*, Phys. Rev. **D78** (2008) 075006, arXiv:0806.3648.

[174] LHCb, R. Aaij *et al.*, *First Evidence for the Decay $B_s^0 \to \mu^+\mu^-$*, Phys. Rev. Lett. **110** (2013), no. 2 021801, arXiv:1211.2674.

[175] P. Cushman *et al.*, *Working Group Report: WIMP Dark Matter Direct Detection*, arXiv:1310.8327.

[176] ATLAS, *Atl-phys-pub-2013-011*, https://atlas.web.cern.ch/Atlas/GROUPS/PHYSICS/PUBNOTES/ATL-PHYS-PUB-2013-011/.

[177] ATLAS, *Atl-phys-pub-2014-010*, https://atlas.web.cern.ch/Atlas/GROUPS/PHYSICS/PUBNOTES/ATL-PHYS-PUB-2014-010/.

[178] ATLAS, *Atl-phys-pub-2014-010*, https://atlas.web.cern.ch/Atlas/GROUPS/PHYSICS/PUBNOTES/ATL-PHYS-PUB-2015-005/.

[179] ATLAS, *Physics at a High-Luminosity LHC with ATLAS*, arXiv:1307.7292.

[180] G. Salam and A. Weiler, collider-reach, http://collider-reach.web.cern.ch/. Accessed: 2015-04-12.

[181] P. Schwaller and J. Zurita, *Compressed electroweakino spectra at the LHC*, JHEP **1403** (2014) 060, arXiv:1312.7350.

[182] CMS Collaboration. https://twiki.cern.ch/twiki/bin/view/CMSPublic/PhysicsResultsPFT. Accessed: 2015-05-22.

[183] M. Kramer *et al.* https://twiki.cern.ch/twiki/bin/view/LHCPhysics/SUSYCrossSections. Accessed: 2015-05-22.

[184] O. Buchmueller, M. J. Dolan, S. A. Malik, and C. McCabe, *Characterising dark matter searches at colliders and direct detection experiments: Vector mediators*, JHEP **1501** (2015) 037, arXiv:1407.8257.